UNIVERSITAT POLITÈCNICA DE CATALUNYA BARCELONATECH

Time dependent flow of biolubricant and suspended particles behavior within total hip replacement

Alaleh Safari

DOCTORAL THESIS

Time Dependent Flow of Biolubricant and Suspended Particles Behavior Within Total Hip Replacement

Alaleh Safari

Machine Elements

This thesis is the result of a collaboration between Luleå University of Technology and Universitat Politècnica de Catalunya that aims toward a double degree

UNIVERSITAT POLITÈCNICA DE CATALUNYA

Time Dependent Flow of Biolubricant and Suspended Particles Behavior Within Total Hip Replacement

A thesis submitted to Luleå University of Technology and Universitat Politècnica de Catalunya for the double degree of Doctor of Philosophy by

Alaleh Safari

Luleå University of Technology
Department of Engineering Sciences and Mathematics
Division of Machine Elements

Universitat Politècnica de Catalunya
Department of Materials Science and Metallurgical Engineering

This thesis is the result of a collaboration between Luleå University of Technology and Universitat Politècnica de Catalunya that aims toward a double degree

February 2017

PREFACE

The work presented in this thesis has been carried out and funded under the Joint European Doctoral Programme in Material Science and Engineering (DocMASE) between July 2012 and January 2017. The project was collaboration between the division of Machine Elements of Luelå University of Technology, Luleå, Sweden and the division of Biomaterials, Biomechanics and Tissue Engineering of Universidad Politécnica de Cataluña (UPC), Barcelona, Spain.

I would like to express my sincere gratitude to my supervisor, Professor Nazanin Emami for all her guidance, kind supports and encouragements. She provided me the opportunity to peruse my research interest with her patience.

I sincerely acknowledge my co-supervisor Professor Michel Cervantes for all his attentions, valuable discussions and patience. I could have never gotten on correct research track without his guidance and support.

I also very much appreciate my co-supervisor Professor Maria-Pau Ginebra guidance, contributions and supports during my research in Barcelona.

I am really thankful to Dr. Montserrat Espanol for all her kindness and so much support during my work at UPC.

I would like to thank Professor Christian Poelma from TU Delft for all the valuable discussions and supports.

I am very thankfull to all my colleagues and friends at divisions of Machine Elements, Fluid and Experimental Mechanics and Material Science for the pleasant and enjoyable working environment especially Maria, Latifa, Joel and Mohammad. My special thanks also go to Martin Lund, Henrik Lycksam, Tore Serrander, Jan Granström, Lars Frisk and Johnny Grahn for all the help with laboratory works.

I would also like to thank all my colleagues at BBTE division in UPC especially Noelia, Priya and Erica.

I am truly thankful to all my friends in Luleå, especially Narges (Khanum Na), Sara, Ehsan, Saleh, Arash, Shokat, Dariush, Farnoosh, Golnaz, Mastaneh, Mana and Rezvaneh. You filled my life in Luleå with so many happy moments and unforgettable memories.

My heartfelt thanks go to my oldest friends Samira and Mahmoud. It is a blessing to have such kind and supportive friends around during tough times in life.

I could have never achieved my goals without the endless love, support and self-devotion of my parents. Thank you for always being there for me although it is impossible to thank you with words and I feel so blessed to have you. I love you.

I am also so grateful to all my family members, my brother (Hesam), my parents in law, my sisters in law (Sanaz, Vida and Parisa) and my brother in law (Meisam). No matter how far I was from them, they always supported me with love, encouragements and kindness.

Last but definitely not the least, I owe my success to Kaveh, his sincere love, patience, attention and support. Although he was not part of this project, he spent so much of his time helping me. Whenever I stuck in work, I was always benefited from precious discussions with him and his guidance in the lab works. Thank you for supporting me under all circumstances Kaveh and I would like to dedicate this thesis to you.

ABSTRACT

Total hip replacement (THR) has been one of the most successful surgeries in the 21st century. Ultra-high-molecular-weight-polyethylene (UHMWPE) shows favorable mechanical and tribological properties when used as a bearing surface material in THR. However, produced UHMWPE wear particles challenge increasing the THR lifetime. Bone loss (osteolysis) initiated by these wear particles is a major cause of total joint arthroplasty failure in both hip and knee prosthesis.

In addition to improving the wear resistance of bearing surfaces to reduce wear, wear debris distribution mechanisms within the joint gap must also be thoroughly investigated. These particles distribute within lubricant and across the implant gap. Synovial fluid (SF) lubricates natural joints which is a viscoelastic non-Newtonian shear thinning fluid. The non-Newtonian behavior of SF is attributed to its hyaluronic acid (HA) content which is a linear biopolymer. The distribution patterns of wear particles within total joint replacement are affected by the special rheological behaviors of the SF, geometrical parameters, particle size and shape and particle-fluid interactions. Therefore, understanding wear particles distribution pattern is pivotal to understand the mechanism and eventually minimizing third-body wear of the UHMWPE acetabular liner in THR.

According to fluid mechanics forces, the size and density of wear particles suggests that wear particles follow lubricant movements. However, over a matter of hours, such particles show specific behaviors within viscoelastic fluid (not visible in Newtonian fluid) such as particle migration and string formation along the flow direction.

The main aim of this project was to develop and validate an experimental method for assessing characteristics of HA and artificial SF solutions and behaviors of wear particles in a viscoelastic fluid flow. The effects of different parameters such as HA concentration, protein content, fluid flow types (steady, unsteady, etc.) and gap shapes on fluid behavior were quantified to fully understand such mechanisms.

In this project, micro particle image velocimetry (micro-PIV) was applied as the quantitative flow visualization method. Pin-on-disk tribo-measurement was performed as a complimentary study to investigate the tribological behaviors of a UHMWPE pin rotating against a cobalt chromium molybdenum (CoCrMo) disk in the presence of HA solutions of various concentrations. This study was conducted to understand the effects of dynamic loading on lubricant performance relative to those of static loading.

The results showed that under oscillatory flow conditions, strain amplitude, rate, and distribution are important parameters that affect the flow behaviors of HA solutions. Particle migration and alignment were affected by channel size, HA concentration, flow type and the elastic instability of the solution.

The tribological study results suggested that in the presence of HA, sinusoidal dynamic loading does not affect the frictional behaviors of UHMWPE moving against CoCrMo in comparison with static loading.

ABSTRACT

El reemplazo total de cadera (THR) ha sido una de las cirugías más exitosas en el siglo XXI. El polietileno de ultra alto peso molecular (UHMWPE) muestra propiedades mecánicas y tribológicas favorables cuando se utiliza como material de superficie de apoyo para implantes de cadera. Sin embargo, las partículas producidas por el desgaste del UHMWPE hacen que la vida útil de un THR sea un desafío clave. La pérdida ósea (osteólisis) producida por estas partículas de desgaste es una de las causas principales del fracaso total de la artroplastia articular.

Además de mejorar la resistencia al desgaste de las superficies de apoyo, a fin de reducir dicho desgaste, también deben investigarse a fondo los mecanismos de distribución de los restos de las partículas desgastadas en las juntas de la prótesis. Estas partículas se distribuyen a través del lubricante en los huecos del implante. El líquido sinovial (SF), un líquido viscoelástico no newtoniano no adelgazante, lubrifica las articulaciones naturales. El comportamiento no-newtoniano de SF se atribuye a su contenido de ácido hialurónico (HA), que es un biopolímero lineal. Los patrones de distribución de estas partículas de desgaste se ven afectados por los comportamientos reológicos especiales de la SF, por parámetros geométricos, por tamaños y formas de partículas y por interacciones entre partículas y fluidos. Por lo tanto, la comprensión de este patrón de distribución es fundamental para minimizar el desgaste del tercer cuerpo del UHMWPE.

Según las fuerzas mecánicas de los fluidos, el tamaño y la densidad de las partículas de desgaste sugiere que las partículas de desgaste siguen el movimiento del lubricante. Sin embargo, en cuestión de horas, estas partículas muestran comportamientos específicos dentro del fluido viscoelástico (no visible en el fluido newtoniano), tales como la migración de partículas y la formación de cordones a lo largo de la dirección del flujo.

El objetivo principal de este proyecto fue desarrollar y validar un método experimental para evaluar las características de HA y soluciones artificiales SF y el comportamiento de las partículas de desgaste en un flujo de fluido viscoelástico. Se cuantificaron los efectos de diferentes parámetros, tales como la concentración de HA, el contenido de proteína, los tipos de flujo de fluido (constante, inestable, etc.) y las formas de los huecos en el comportamiento de los fluidos, a fin de poder comprender plenamente dichos mecanismos.

La velocimetría de imagen de micropartículas (micro-PIV) se aplicó como el método de visualización cuantitativa del flujo en este proyecto. Se realizaron mediciones pin-on-disk como técnica complementaria, para investigar el comportamiento de fricción de una varilla de rotación de UHMWPE contra un disco de cobalto cromo molibdeno (CoCrMo) en presencia de soluciones HA de diversas concentraciones. Este estudio se llevó a cabo para comprender los efectos de la carga dinámica sobre el rendimiento del lubricante, en relación con los de carga estática.

Los resultados muestran que bajo condiciones de flujo oscilatorio, los niveles de deformación, las tasas y las distribuciones son parámetros importantes que afectan los comportamientos de flujo de las soluciones de HA. La migración de partículas y la alineación se vieron afectadas por los tamaños de canales, las concentraciones de HA, los tipos de flujo y la inestabilidad elástica de la solución.

Los resultados de la medición pin-on-disk sugieren que, en presencia de HA, la carga dinámica sinusoidal no afecta los comportamientos de fricción de UHMWPE con CoCrMo, en comparación con la carga estática.

NOMENCLATURE

$A_{channel}$	Area (channel cross section)
$A_{syringe}$	Area (syringe cross section area)
d	Diameter
D	Diffusion coefficient
D_h	Hydraulic diameter
f	Frequency (Hz)
F	Friction force
G'	Elastic modulus
G''	Viscous modulus
h	Channel width
H	Characteristic length
K	Boltzman constant
L	Channel length
L_e	Entrance length
m	Consistency index
n	Power law index
N_1	First normal stress difference
P	Pressure
Q	Volume flow rate
t	Time
T	Temperature
u	Flow velocity in x direction
u_0	Oscillatory velocity amplitude
$u_{cylinder}$	Cylinder velocity
$u_{syringe}$	Syringe velocity
U_{mean}	Flow mean velocity
v	Flow velocity in y direction
w	Channel height
ϕ	Phase of oscillatory motion
γ	Strain
$\dot{\gamma}$	Shear rate
$\dot{\gamma}_{critical}$	Critical shear rate
λ	Relaxation time
μ	Dynamic viscosity
ν	Kinematic viscosity
ω	Frequency (rad.s^{-1})
ρ	Density
σ_{xx}	Normal stress in the flow direction
σ_{yy}	Normal stress in the shear direction
τ	Response time
Abbreviations	
Amp	Amplitude
AC	Articular Cartilage

BCS	Bovine Calf Serum
CoC	Ceramic on Ceramic
CoCrMo	Cobalt Chromium Molybdenum
COF	Coefficient of Friction
CoP	Ceramic on Polymer
De	Deborah number
DSC	Differential Scanning Calorimetry
EC	Endothelial Cell
EDS	Energy-Dispersive X-ray Spectroscopy
HA	Hyaluronic Acid
Micro-PIV	Micro Particle Image Velocimetry
MoM	Metal-on-Metal
MoP	Metal-on-Polymer
MW	Molecular Weight
OA	Osteoarthritis
PBS	Phosphate Buffered Saline
PIV	Particle Image Velocimetry
POD	Pin on Disk
RA	Rheumatoid Arthritis
Re	Reynolds number
SEM	Scanning Electron Microcopy
SF	Synovial Fluid
SS-PF	Steady-state Poiseuille flow
THR	Total Hip Replacement
TiAlV	Titanium Aluminum Vanadium
TJA	Total Joint Arthroplasty
UH-CF	Unsteady Harmonic Couette Flow
UH-PF	Unsteady Harmonic Poiseuille Flow
UHMWPE	Ultra-High-Molecular-Weight-Polyethylene
W	Womersley number
Wi	Weissenberg number
Supscripts	
g	Gravity
l	Liquid
ND	Non-dimensional
os	Oscillatory
p	Particle

CONTENTS

APPENDED PAPERS

***Paper A:**
Safari, A., Emami, N., Cervantes, M.J. Bio-lubricant flow behavior in mini-channels. Lubr Sci. 2016; 28(4), 221-42.
The measurements were designed and performed by the author of the thesis. The data analysis part was performed by the author and the paper was written by the author of the thesis in discussion with Professor Cervantes and Professor Emami.

***Paper B:**
Safari, A., Cervantes, M. J., & Emami, N. Viscoelastic behavior effect of hyaluronic acid on reciprocating flow inside mini-channel. Lubr Sci. 2016; 28(8), 521-544.
The measurements were designed and performed by the author of the thesis. The data analysis part was performed by the author and the paper was written by the author of the thesis in discussion with Professor Cervantes and Professor Emami.

Paper C:
Safari, A., Emami, N., Cervantes, M.J. Viscoelasticity and shear thinning effects on bio-polymer solution and suspended particle behaviors under oscillatory curve Couette flow conditions. Submitted to Journal of non-Newtonian Fluid Mechanic
The measurements were designed and performed by the author of the thesis. The acquired data was analyzed by the author of the thesis. The CFD simulations were performed by Professor Cervantes. The paper was written by the author of the thesis in collaboration with Professor Cervantes and in discussion with Professor Emami.

Paper D:
Safari, A., Espanol, M., Ginebra, M.P., Cervantes M.J., Emami, N. Effect of dynamic loading versus static loading on the frictional behavior of a UHMEPW pin in artificial biolubricants. Submitted to Biosurface and Biotribology Journal
Pin on disc experiments were performed by the author of the thesis. SEM and EDS measurements were done by Dr. Espanol and the main author of the paper. DSC measurements were performed by professor Emami. The paper was written by the author of the thesis in collaboration with Professor Emami and in discussion with Professor Cervantes and Professor Ginebra.

LIST OF FIGURES

Chapter 1

INTRODUCTION

Joints are connections between individual bones [1]. Based on the degree of motion and connective material nature, natural joints are usually classified into three types: immovable joints (synarthroses or fibrous joints), slightly movable joints (amphiarthroses or cartilaginous joints), and movable joints (diarthroses (diarthrodial) or synovial joints) [1,2]. Most body movements are enabled by the synovial joints. These joints can be considered as ideal bearings with a very low coefficient of friction of 0.005-0.02 [3]. The design and configuration of articular joints are a trade-off between stability and freedom of motion [2]. Shoulder, hip and knee joints are three examples of articular joints [1].

The hip joint articulates the pelvis and femur bones with a configuration of a ball on socket. The ball part is the head of the femur, which rotates against the concave, cuplike acetabulum of the pelvis [4], Fig 1.1 (a). It is one of the largest joints in the body, and its configuration provides the hip joint with intrinsic stability. The construction and stability of the hip joint allows a variety of movements during daily activities [5]. The hip joint has three degrees of freedom and six types of movements in the three planes of the body: flexion-extension in the sagittal plane, abduction-adduction in the frontal plane and medial-lateral rotation in the transverse plane. Although the hip joint has wide range of movements, its main function is weight bearing [4]. The hip joint is exposed to 2.5-5.4 times the body weight during daily activities [6].

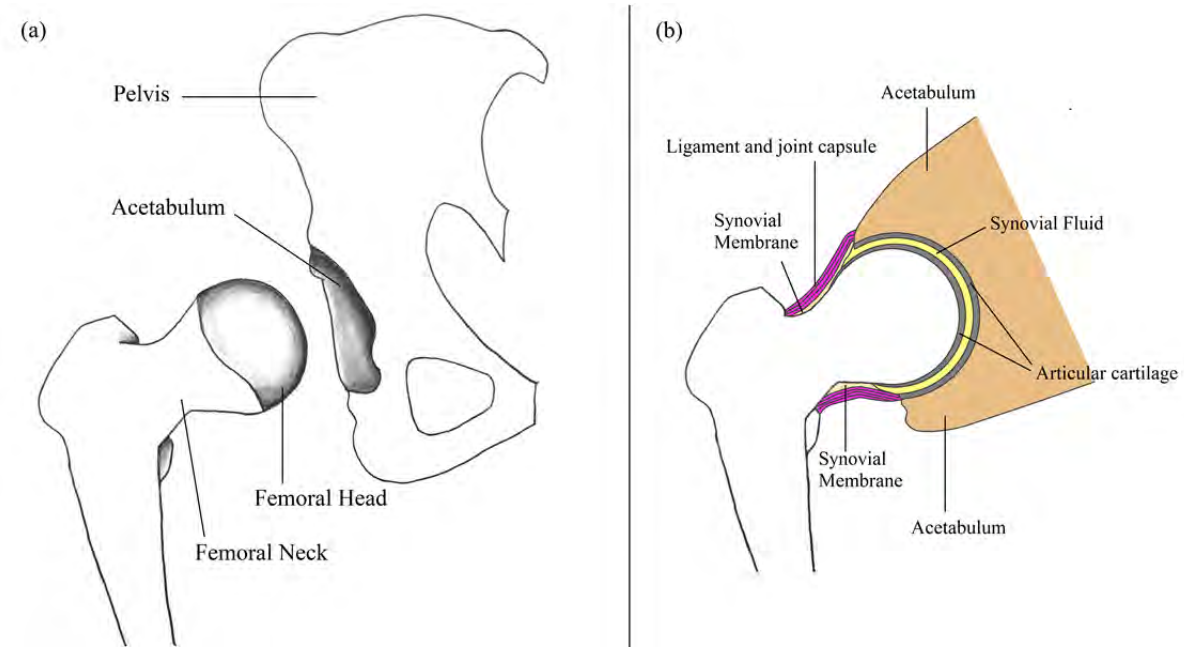

Fig 1.1. Natural hip joint (author's own figure)

Fig 1.1 (b) is a schematic image of the hip joint with the following main components: 1- Fibrous capsule made of dense connective tissue. This capsule is responsible for maintaining the joint integrity. The thick bands inside the capsule are called ligaments. 2- The inner metabolic active tissue layer inside the capsule, called the synovial membrane. The main responsibility of these tissues is to secrete synovial fluid (joint lubricant) inside the joint cavity and provide nutrients to the joint cells. 3- Articular cartilage, which is a soft porous composite material that covers the ends of the bones. [2,6,7].

1.1. Lubrication of natural hip joints

Synovial fluid and articular cartilage play the most important roles in joint lubrication.

1.1.1. Articular Cartilage

Articular cartilage (AC) has a smooth and shiny appearance [7]. It is actually a biphasic, nonlinear permeable viscoelastic solid [1]. Approximately 70% to 85% of the AC weight is water [8]. The strength of the AC is provided through collagen (50-75% of AC dry weight) and proteoglycan (15-30% of AC dry weight). Proteoglycan is responsible for the resiliency of this tissue [7,8]. The fibril nature of the AC makes it more resistant to tensile forces than compression [8].

The complex nature of the natural hip joint lubrication is attributed mainly to the biphasic and porous nature of the AC. Under loading, the AC deforms and distributes the loads and reduces the contact stresses. This behavior provides the possibility of achieving fluid film lubrication (condition when bearing surfaces are separated with a thin film of lubricant) in the natural hip joint [9].

1.1.2. Synovial Fluid

Synovial fluid (SF) is secreted by the synovial membrane inside the hip joint cavity. It is known to be the hip joint lubricant. It also provides nutrients for avascular cartilage cells and

disposes of waste. It exists in very small amounts (approximately 1-5 ml) inside the joint cavity [2,10].

SF is known to be a dialysate of blood plasma, but in healthy SF, the protein content is significantly lower than that of plasma (18-20 $mg.ml^{-1}$) [11,12]. In contrast to plasma, healthy SF does not coagulate due to the absence of fibrinogen and prothrombin [13]. This bio-fluid contains a special biopolymer called hyaluronic acid (HA). In healthy SF, the molecular weight (MW) and concentration of HA are 6.3-7.6 MDa and 1-4 $mg.ml^{-1}$, respectively [12,14]. The HA concentration is affected by age [13]. SF contains a variety of proteins. The main protein constituents of the SF are albumin (11.65-12.92 $mg.ml^{-1}$), globulin (6.84-7.58 $mg.ml^{-1}$) and glycoprotein lubricin (0.05-0.35 $mg.ml^{-1}$) [11,12]. The protein content of normal SF does not vary with age [13].

SF is a non-Newtonian shear-thinning fluid. It also has a viscoelastic nature. The shear-thinning and viscoelasticity of the SF is dependent on the HA content, the HA molecular weight and concentration, and the entanglement between HA polymer chains [13].

The shear-thinning behavior of the SF plays a significant role in enhancing the squeeze film effect and the entrapment of fluid during the fluid film lubrication [3].

Fig 1.2 shows the variation of the viscosity (μ) as a function of the shear rate ($\dot{\gamma}$) for a solution of HA (MW of 1.6-1.8 MDa and 5 $mg.ml^{-1}$ concentration in phosphate-buffered saline (PBS)). There exist three characteristic regions for this shear-thinning fluid; 1- Low shear rate plateau (at low shear rates, the fluid behaves as a Newtonian fluid), 2- Shear-thinning region 3- High shear rate plateau (at very high shear rates, the fluid behaves as a Newtonian fluid with a viscosity similar to the solvent viscosity) [15].

The intercept of the line fitted on the shear-thinning region in a double logarithmic plot with zero shear viscosity shows the value of the shear rate at the start of the shear-thinning, which is called the critical shear rate ($\dot{\gamma}_{critical}$)[16]. The HA polymer chains start to disentangle and slide along each other at this shear rate. The longest relaxation time (time required to damp the stress deformation and revert to the default configuration) of this polymeric solution is on the order of inverse of $\dot{\gamma}_{critical}$ [17].

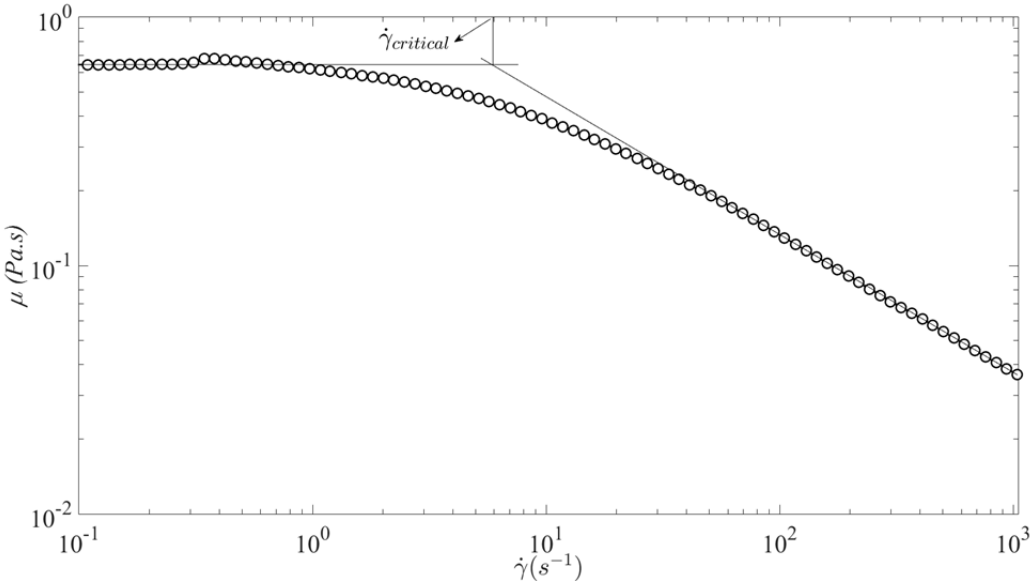

Fig 1.2. Viscosity (μ) function of the shear rate ($\dot{\gamma}$) for the HA solution (author's own figure)

The viscoelastic property of the synovial fluid was first discovered in 1950 [18]. At a low strain frequency (low speed joint activity), the HA chains have enough time to adapt to the applied stress, and the chains slip by each other and provide a viscous flow inside the joint gap. However, upon increasing the frequency (increasing the joint moving speed), the HA chains don't have enough time to deform during the short period of oscillating strain and instead store the mechanical energy. In this condition, the HA chains work as shock absorbers and protect the cartilage and synovial tissue from strong mechanical stresses [13].
The viscoelastic behavior of the SF is studied by deriving the two components of the dynamic rigidity of the SF: the viscous or loss modulus (G'') and the elastic or storage modulus (G') [13]. Fig 1.3 shows the variation of the dynamic moduli versus the strain rate for a HA solution (MW of 1.6-1.8 MDa and 5 $mg.ml^{-1}$ concentration) in BPS. At low strain frequencies, the viscous modulus controls the solution behavior, while upon increasing the frequency, the elastic modulus dominates; the transition point is called the crossover frequency, and the inverse of the crossover frequency is representative of the HA relaxation time [11].
Since the HA concentration varies with age, the shear-thinning and viscoelastic behaviors of normal SF are affected by age (the crossover frequency increases after the age of 27) [13].

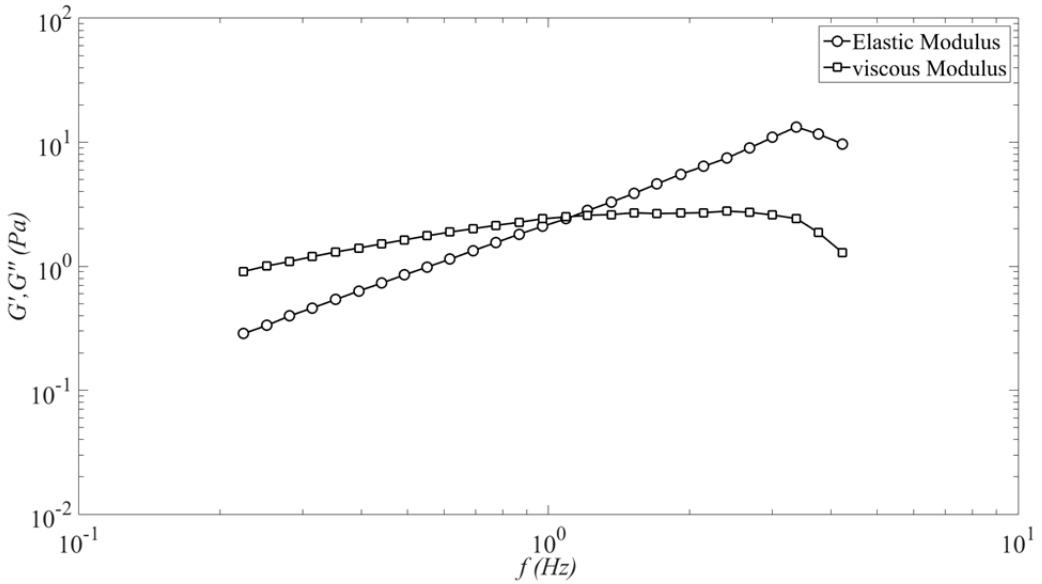

Fig 1.3. Viscous and elastic moduli (G' and G") versus strain frequency (f) for HA solution (author's own figure)

Until today the joint lubrication mechanism is not totally understood. There is no single theory that can totally explain the performance mechanism of the natural hip joints during daily activities. A variety of theories have been proposed until now to explain the lubrication system in human natural hip joints; some of them are hydrodynamic, hydrostatic, elastohydrodynamic, squeeze-film, boundary lubrication, mixed lubrication, weeping, boosted, and biphasic lubrication [10,19]. All of these theories try to explain the effective performance of the articular joint in providing almost frictionless motion. However, human joint performances are strongly affected by disease, accident and aging.

1.2. Joint defects

The most common type of the joint disease is osteoarthritis (OA). OA is a degenerative joint disease in which the AC is torn and worn off. In this disease, the cartilage surfaces are worn and degraded, and the bone surfaces are exposed and rub against each other. Although the origin of this disease is not totally understood, it is believed to be partly related to different wear mechanisms in the joints [6].
There are also other theories about the origin of this disease: 1- cartilage breakdown because of abnormal enzyme release from the cartilage cells, 2- defects in the cartilage or joint construction that people are born with that result in incorrect loading and the destruction of the cartilage [8].
Another type of joint arthritis is called rheumatoid arthritis (RA), and it occurs because of joint inflammation. It causes the cartilage tissue to thicken, erode and deform. Its origin is not well understood, but it seems that disorder in the immune system is an important factor [11]. The SF properties change due to these diseases, which affect the lubricity of the joint.

1.2.1. Pathological Synovial Fluid

In both degenerated and inflamed joints, the concentration and molecular weight of HA decrease [13].
In the SF of a patient with OA, the pH value increases compared to that of the normal SF. This higher pH decreases the stiffness of the HA chains and degrades their shear-thinning characteristic [12].
Joint diseases change and increase the protein content in the SF. In patients with OA disease, the concentrations of albumin and globulin in the SF increase to 17.75-18.45 $mg.ml^{-1}$ and 12.85-13.36 $mg.ml^{-1}$, respectively, with a total protein content of 30 $mg.ml^{-1}$, while the SF from patients with RA disease has a concentration of approximately 46 $mg.ml^{-1}$ [12,20]. The SF from a joint with inflammatory disease shows a plasma-like behavior. It contains fibrinogen and may clot if aspirated. However, for the SF of a degenerated joint, no plasma-like behavior is visible [13].
Changes in the HA characteristics of the pathological SF affect its rheological behavior. It seems that the inflammatory disease affects the SF rheological behavior more seriously. The shear-thinning behavior and viscosity of the SF from patients with RA are less than those of the SF from joints with OA, while the SF from patients with OA disease has less shear thinning compared to normal SF. In most cases, the SF from a joint with RA disease loses its shear-thinning behavior and behaves like a Newtonian fluid [11].
The viscoelastic behavior of the pathological SF is affected with the same trend as its shear-thinning behavior. While normal SF has a long relaxation time, the pathological SF may not show any elastic behavior for the usual strain frequencies of daily activities [11,13].
The lower shear-thinning and viscoelasticity of the pathological SF compared to the normal SF deteriorates the lubrication and increases the fatigue wear of the hip joint. Under such conditions, the hip joint may lose its capability of providing frictionless, painless movement and needs to be replaced with an artificial hip joint.

1.3. Artificial Hip Joint

Over the last 60 years, total hip joint replacement (THR) has been the most successful treatment method for patients with hip advanced joint diseases. Every year, over 1 million hip joint replacements are carried out worldwide [21].

Fig 1.4 shows a schematic view of a THR implant fixed in the body. It has the configuration of a ball on socket and consists of three main parts: the acetabular cup (socket), which is fixed in the acetabulum of the pelvis, the femoral head (ball), and the femoral stem, which is fixed inside the femur bone.

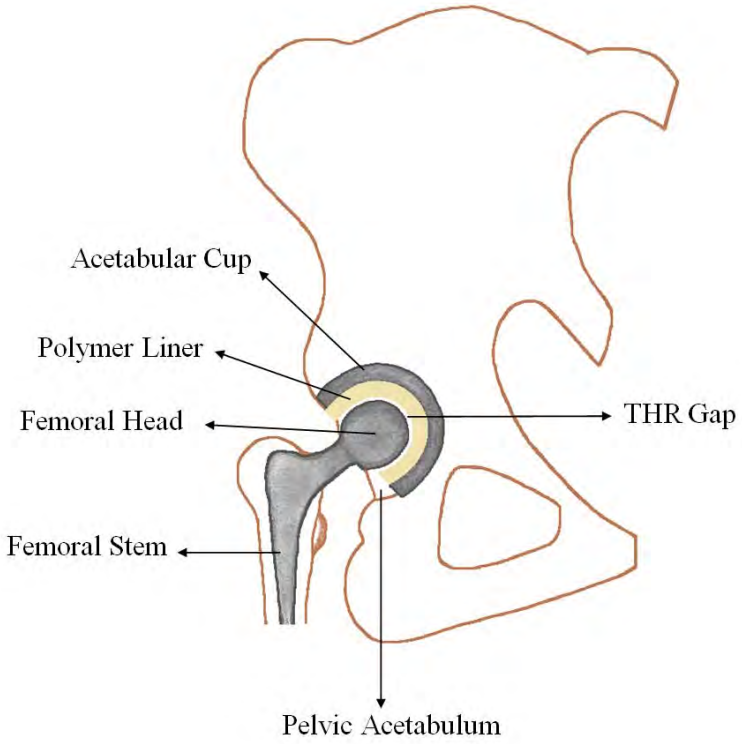

Fig 1.4. Schematic of hip implant (author's own figure)

Three main material combinations are usually used in an artificial hip joint; metal on metal (MoM), metal on polymer (MoP) or ceramic on polymer (CoP) and ceramic on ceramic (CoC) [8].

Previously THRs had the ball and socket produced from metal (MoM). The MoM implant is known as a McKee-Farrar joint. The ball and the socket were made from cobalt chromium (CoCr) alloy [8,22]. The equilateral contact in these THR implants produces high friction at the bearing surfaces, with a friction coefficient of approximately 0.18. The high friction also exposes the fixation interfaces to high torque and stresses [8,23,24].

To solve the problem of the high friction forces and other serious issues within MoM, Sir John Charnley introduced MoP, which reduced the coefficient of friction (COF) to 0.05 [8].

Currently, MoP/CoP hip implants are the most common configuration for THR. It consists of a metallic or ceramic ball rotating against a metallic cup with a polymer liner from ultra-high-molecular-weight-polyethylene (UHMWPE) [21]. UHMWPE shows favorable mechanical and tribological properties to be used as the bearing surfaces in THR such as a low COF, wear resistance, tensile impact and creep behavior [25]. The MoP/CoP implant also release much less of toxic metallic ions which MoM produces inside the body and does not have brittleness and fracture problems which the CoC implant shows [26]. However, its main drawback is the wear particles produced during the lifetime of the MoP implant. The migration of these wear particles to the periprosthetic tissues leads to osteolysis and implant loosening and failure [26]. The destructive oxidation behavior of the UHMWPE is one of the sources of polymeric wear particles [27]. The ingress of a third body into the implant gap can be mentioned as another source of wear. Third body wear contributes to the wear of the polymeric liner either directly or by roughening the metallic femoral head. The third body debris can originate from

different sources such as a metallic part of the implant or surgical instrument, bone or the cement for implant fixation [28-30].
In elderly patients, MoP hip implants may last up to 30 years. However, younger and more active patients apply more stresses on the implants, which results in more wear [31]. In some cases, a revision is required after only 10 years [21].
There have been many studies on improving the wear and mechanical characteristics of UHMWPE by cross-linking, adding antioxidants to the polymer, producing composites or adding reinforcements at nano and micron size [27].
Due to the high roughness of the polymer liner, the lubrication mode in the MoP hip implant is predominantly boundary lubrication (condition when most of the applied load is supported by asperities of the bearing surfaces) [23], which also increases the risk of high wear. Less friction does not correspond to less wear. However, it is suggested that the friction measurements are important for understanding the effect of surface traction on subsurface strains, orienting polymer molecules and affecting the wear mode [24].
There have been numerous numerical and experimental studies focused on understanding the frictional behavior of MoP hip implants and improving the design parameters. Most of the numerical studies did not take into account the special rheological behavior (shear-thinning and viscoelasticity) [32-37]. By considering the non-Newtonian viscoelastic behavior of the SF in numerical simulations, the estimates of the minimum film thickness and pressure distribution are improved [38-40]. These results show the necessity of understanding the non-Newtonian viscoelastic behavior of the THR implant's SF (called periprosthetic synovial fluid) and the parameters which affect the rheology.
At very high steady shear rates, the viscosity of the SF is constant. Shear rates within natural or artificial hip joint reaches a value of 10^5 s^{-1} [41]. Therefore, in most numerical simulations, the SF viscosity is considered to be constant. However, under real conditions, the shear is not steady inside the implant gap. It is necessary to understand the difference between the behaviors of the implant SF (non-Newtonian viscoelastic fluid) and a Newtonian fluid under different situations.
The non-Newtonian viscoelastic behavior of the SF also affects the random distribution of the suspended particles [42], and studying the particle synovial fluid interaction is crucial for carrying out investigations of the third body wear inside MoP hip implants.
Eventually, the first step to address the wear particle distribution pattern in the THR gap would be to understand the non-Newtonian viscoelastic characteristics of periprosthetic synovial fluid.

1.3.1. Properties of periprosthetic synovial fluid

The lubricant after total joint arthroplasty (TJA) is called periprosthetic synovial fluid, and there have been few studies investigating its composition and rheological behavior [11].
To understand how TJA changes the properties of the synovial fluid, the SF from patients before primary surgery (representative of the OA synovial fluid characteristic) was compared with samples taken from patients undergoing revision TJA. The OA and periprosthetic SFs have almost the same protein content. The HA concentration is found to be lower in the periprosthetic SF compared to in the SF of patients with OA [43-47]. However, there is not agreement regarding the molecular weight difference between the OA and periprosthetic SFs. Mazzucco et al. [43] and Yamada et al. [45] reported that the HA molecular weight in these two types of SF is the same. Saari [44], on the other hand, suggested that the molecular weight of the HA content in periprosthetic SF is higher than that of the SF from patients with OA. Guenther et al. [46] proposed that the distribution of the HA molecular weight should be

considered in the comparison. Their results showed that the fraction of high molecular weight HA is greater in the OA synovial fluid compared to in the periprosthetic synovial fluid.
Investigation of the rheological behavior of periprosthetic SF showed that the SFs from revision surgeries are degraded compared to those from the primary surgery. Therefore, the viscosity and shear-thinning behavior of the SF from revision is less compared to that of the SF from primary surgery [47-49]. Moreover, the SF from the revision surgery has a less elastic behavior, and its crossover frequency is higher [48].
To achieve reliable results from in vitro measurements of the wear and frictional behavior of MoP hip implants, it is crucial to have a lubricant capable of mimicking the periprosthetic SF characteristics. Its low availability, ethical issues and variability from patient to patient makes using natural SF in research experiments almost impossible [46]. Most studies replace the natural SF with a synthetic model for SF.

1.3.1.1. Frictional and rheological behavior of model synovial fluid

McKellop et al. [50] showed that when bovine blood serum was used as the lubricant in tribological measurements, the produced wear surfaces resembled the implant wear surfaces. Therefore, the ASTM standard proposes that bovine calf serum (BCS) is the best lubricant for bio-tribological measurements.
The protein content of SF is usually replaced with BCS in model SF. The normal protein content of the commercially available BCS is 40-80 $mg.ml^{-1}$ [20]. Therefore, the BCS is usually diluted to the desired concentration in distilled water or PBS [51]. Brandt et al. [51] stated that the protein composition fraction in the bovine calf serum (BCS) is different from that of SF. In some studies, the most abundant protein in the SF composition with its corresponding concentration is used in the lubricant composition (albumin and γ-globulin) [46,52]. To simulate the frictional behavior of an implant in the tribological measurements, many studies focused on recognizing the principal protein in providing the SF with lubrication characteristics. Lubricin is the most important protein in natural joint lubrication. However, the results of studies conducted by Mazzucco et al. [53] showed that lubricin is not the main protein in the lubrication of the joint implant. Their results also suggested that HA, phospholipid, albumin and γ-globulin do not play the role of the boundary lubricant in joint implants. Sawae et al. [54] investigated the effect of different lubricants on the wear and frictional behavior of UHMWPE and showed that the albumin solution produces much higher friction compared to the serum. However, both of these lubricants decrease the wear. Incorporating HA into the lubricant composition decreases the friction coefficient significantly. The protective role of the protein against wear for UHMWPE was shown by Schole et al. [55-57]. Their results showed that the adsorption of the protein on the implant surfaces protects them from direct contact and improves the wear characteristics of the implant. However, depending on the type of implant (MoM, CoC or MoP), the COF might increase or decrease in the presence of the protein layer. Other studies' results also verified that using diluted serum increased the friction coefficient [58-60]. Gispert et al. [61] also showed that the presence of protein in the lubricant composition prevents the transfer of the polymeric surface to the metallic surface and improves the wear. In contrast to Sawae et al. [54], their results show that adding HA to the solution does not have a considerable effect on the friction coefficient [61]. Fam [62] investigated the effect of the HA-containing lubricant on the friction coefficient of UHMWPE against CoCr. Their results showed that incorporating HA into the protein content solutions (serum or albumin) until a concentration of 1 $mg.ml^{-1}$ decreased the friction coefficient, and for higher HA concentration solutions, the friction coefficient stays constant.

Apart from the protein adsorption, the viscosity and shear-thinning characteristics of the SF also affect the squeezing effect and lubricant film thickness. Therefore, the SF rheological behavior has a direct effect on the frictional behavior of the implant.
The rheological behavior of the SF depends mostly on its HA content. Therefore, many studies have concentrated on understanding how different parameters affect the rheological behavior of HA solutions to produce an experimental model for the SF. These parameters include the HA molecular weight and concentration, HA segments, protein content, shear duration, and salt content in the solvent.
The HA degrades during joint disease, which suggests that HA segments appear in the synovial fluid [63]. Fujii et al. [63] showed that the effect of the HA segments on the viscoelastic behavior of the HA solution depends on the chain length. The viscosity of the HA solution is weakly affected by the temperature, and the HA molecular weight affects the non-Newtonian viscoelastic behavior of the HA solution more strongly than the concentration does [17,64,65]. Adding protein to the HA solution does not have any effect on the shear-thinning viscoelastic behavior of the solution [13,66]. However, Oates et al. [52] showed that the protein provides the HA solution with rheopexy behavior (where the shear stress increases upon applying a constant small shear rate for a long duration). Protein agglomerations increase the entanglement in the HA solution by providing a tight network around them [52].
Adding sodium chloride to the HA solution decreases the viscosity and increases the crossover frequency. The electrostatic repulsion between HA molecules is suppressed by adding sodium chloride to the solution [67].
The presence of both HA and protein seems to be crucial in a model SF. It is suggested by Brandt et al. [51] that PBS should be used as the solvent. The ions that are present in the PBS provide the solution with an osmolality level similar to that of the SF. When distilled water is used instead of PBS as the solvent, a non-clinical osmolality level is obtained [51].

1.4. Non-Newtonian viscoelastic fluid-particle interactions

Particles inside a non-Newtonian viscoelastic fluid have special behaviors that are not visible in a Newtonian fluid, including particle migration and particle string formation aligned with the flow direction. Michele et al. [42] showed for the first time that randomly distributed particles inside a non-Newtonian viscoelastic fluid that are subjected to shear flow form particle strings aligned with the flow direction. They attributed this special behavior to the normal stress differences that exist in the viscoelastic fluid. However, later studies suggested that many other factors affect the particles' special behavior. To understand the effects of different factors, some special characteristics of the non-Newtonian viscoelastic fluids (polymeric solutions) will be explained.

1.4.1. Non-Newtonian viscoelastic fluid characteristics

When shear forces a polymeric solution to flow, the polymer molecules tend to stretch and align themselves with the flow direction [68]. If the solution is entangled in the form of temporary networks, the applied strain and shear stresses on the fluid lead to network disentanglement. The Brownian motion acts to bring the polymer molecules toward their undeformed state or form new entanglements and to bring the polymer chains to their original conformation [13]. Therefore, a net force is applied on the polymer chain. The component of this force along the flow direction (x direction in Fig 1.5) is greater than its component along the shear direction (y direction in Fig 1.5) [68]. The shear stress applied on the viscoelastic fluid causes strain anisotropy and normal stress differences [69].

Fig 1.5 shows the shear and normal stresses applied on a fluid element when the fluid is subjected to shear.

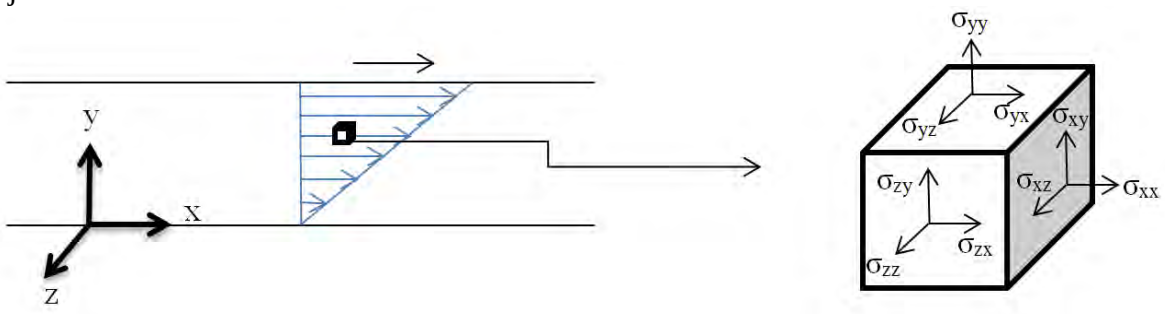

Fig 1.5. Shear and normal stresses applied on fluid element (author's own figure)

The difference between the normal stresses in the x and y directions is known as the *first normal stress difference* (Eq. (1-1)).

$$N_1 = \sigma_{xx} - \sigma_{yy} \qquad (1\text{-}1)$$

N_1, σ_{xx} and σ_{yy} represent the first normal stress difference, normal stress in the flow direction and normal stress in the shear direction, respectively.
The stress inequality is representative of the fluid elasticity. Therefore, a higher shear or strain enhances the stress and gives rise to the elasticity effect.
To characterize the effect of the fluid viscoelasticity on its behavior, two non-dimensional parameters are usually evaluated: the Deborah (De) and Weissenberg (Wi) numbers. The De number represents the ratio of the fluid relaxation time to the flow characteristic time (Eq. (1-2)). A small De number means that the fluid behaves mainly as a viscous fluid. A De number value of approximately 1 indicates that the fluid has viscoelastic behavior, and a high De number represents that the fluid behaves like an elastic solid material [70].
The Wi number defines the effect of the elastic forces compared to those of the viscous effects (Eq. (1-3)). Considerable non-Newtonian and non-linear viscoelastic behaviors are expected for flows with very high Wi numbers [71].

$$De = \lambda\omega \qquad (1\text{-}2)$$

$$Wi = \lambda\dot{\gamma} \qquad (1\text{-}3)$$

λ, ω and $\dot{\gamma}$ are the fluid relaxation time, flow frequency and shear rate, respectively.

1.4.2. Previous studies on Non-Newtonian viscoelastic fluid-particle interactions

The very early studies on particle alignment in non-Newtonian viscoelastic fluids suggested that alignment occurs if the elastic forces are significantly higher than the viscous forces (Wi > 10). This hypothesis was later challenged by Won and Kim [72]. The results of their studies on both shear-thinning and viscoelastic fluids showed that although elastic forces might be responsible for cross-flow particle migration, shear-thinning is the determinative parameter

for particle string formation. Scirocco et al. [73] also showed that strings start to form once a sufficient degree of shear-thinning is available. These results were recently confirmed by Van Loon et al. [74]. Particles in Newtonian fluid subjected to shear rotate to keep a zero torque balance on their surface [75]. To keep the particles in a string structure along the flow direction, each particle should keep its rotation and the zero torque condition on its surface [74]. Based on Van Loon et al. [74], in a Newtonian fluid, when two particles are getting close to each other, the fluid leaves the gap between them. The two particles then attach to each other, tumble and lose their rotation and zero torque. The applied net torque on the two particles results in their separation. When two particles are getting closer in a shear-thinning fluid, the small gap leads to the formation of a high shear rate and a decrease in the fluid viscosity. Therefore, a pressure builds-up and the squeezing effect prevents the particles from getting very close and keeps a thin fluid layer between them. This thin layer helps the particles to keep their rotation and the zero torque condition. Therefore, the formed string stays stable along flow direction.

The studies of Pasquino et al. [76] showed that in case of a very weak shear-thinning fluid, particle alignment only occurred near channel walls. They also concluded that a particle string forms only if the shear rate exceeds a critical value and the wall confinement enhances the string formation. Based on their results, the string length and alignment direction were affected by parameters such as the particle size, medium characteristics, colloidal and hydrodynamic forces, kinetics of string formation and particle migration. They also showed that the length of the particle strings increased upon increasing the shear rate or particle concentration [77].

Scirocco et al. [73] proposed that the particle string formation is a bulk phenomenon and does not necessarily occur at the walls. Moreover, if the particle size is small enough compared to the channel, there is no significant wall confinement effect on the particle string formation. However, the results of Van Loon et al. [74] showed that wall confinement up to some degree improves the collision probability and string formation.

Elastic forces drive the particles toward the lower shear rate region in a flow, while shear-thinning forces work in the opposite direction [75]. Jefri and Zahed [78] studied the particle migration in a shear-thinning viscoelastic Poiseuille flow. They showed that normal forces are responsible for the particle migration, but the migration behaviors of the particles depend on the interaction between the elastic and shear-thinning forces. Single-particle migration under Couette flow conditions between two concentric cylinders was studied numerically and experimentally by D'Avino et al. [79]. They showed that particles mainly migrate toward the outer cylinder due to the viscoelastic forces, except when they are very close to the inner cylinder. A higher angular velocity and shear-thinning increase the migration rate. The numerical simulation of particle migration under reciprocated confined simple shear flow showed that the particle migration is induced by the fluid viscoelasticity and wall confinement. However, increasing the frequency causes the migration to cease [80]. This result is partly in agreement with the results of Lormand and Phillips [81], who studied the migration of particles inside a viscoelastic shear-thinning fluid between concentric cylinders with oscillatory motion. Their results showed that the initial particle position plays a determinative role in the migration direction. Based on the particle initial positions, the migrations are toward the inner or outer cylinder. The inner migration velocity increased with the frequency, but the outer velocity reached a zero value with no migration toward the outer wall for frequencies larger than 1 Hz. They stated that the migration rate is affected by the elasticity parameter [81].

Lyon et al. [82] also showed that particles in a fluid flow with oscillatory motion cluster instead of forming long strings.

To investigate the particle-fluid interaction and effective parameters, applying a reliable fluid visualization method is crucial.

1.5. Micro Particle Image Velocimetry (Micro-PIV)

To study biological fluids, several methods have been applied, such as laser Doppler velocimetry, particle image velocimetry (PIV), double-slit photometry, and laser speckle techniques. Apart from PIV, the other techniques provide point information in the plane of study. Providing high spatial and temporal resolution over the whole plane of measurement is PIV's most important advantage over the other techniques. Moreover, PIV has quasi non-intrusive nature and is able to work at the milli- or microscales, which are very important features in studying biological fluids. The additional advantage of this method is its capability to be applied in both 2 and 3 dimensions [83-85].

1.5.1. General concept

Particle image velocimetry (PIV) is a quantitative flow visualization method. In this method, small tracer particles are added to the fluid and illuminated with a monochromatic light such as a laser in a light sheet to reduce the background noise. Successive one-frame or double-frame images are acquired from the flow. The plane of view is divided into numerous interrogation areas, and the displacement of the particles between successive images or two frames of a double-frame image in corresponding interrogation areas, divided by the time difference between the light exposures, gives the velocity of the particles, which is representative of the fluid velocity [86-88].
There are several parameters that affect the accuracy of the fluid measurement with PIV.
Since the fluid velocity is measured through particle movements, the quality of the results depends strongly on the accuracy of the particles following the fluid flow. Small particles follow the flow better, but particles smaller than 500 nm are more subject to Brownian motion.
To freeze the particle movement, the illumination duration must be short [86]. However, a long enough illumination duration must be provided so that there is enough light for the particles to be sharply visible.
The time between images must be defined reasonably to allow enough particle movement but at the same time avoid out-of-plane movement [86].
The interrogation area size is representative of the maximum velocity map spatial resolution. This size must be small to have the smallest effect possible on the velocity gradient but large enough to contain sufficient particles for the correlation procedure [86].
Based on the experimental situation, different processing methods can be applied, including auto/cross correlation, average correlation, and adaptive correlation, to obtain the greatest accuracy possible.
The maximal spatial resolution of PIV is 0.2-1 mm [89]. Hence, dealing with very small length scales, such as in studies on the cardiovascular system that contain arterioles and capillaries (with diameters on the order of microns) requires some modification to the conventional PIV method.
The micro-PIV working principle is the same as that of PIV. In this method, volume illumination is provided because of the microscopic length scale and optical access limitations. The focal depth of the recording lens defines the measurement plane [86,90].
The micro-PIV system consists of an illumination source and a CCD camera mounted on a microscope. The illumination source can be continuous or pulsed. Common pulsed illumination sources are Nd:YAG laser or LED system.

The main difference between these two methods is that in laser illumination, the particles' images are directly captured, while LED illumination provides images of the shadows of the particles.
The Nd:YAG laser emits two pulses with a duration of 5-10 ns and wavelength of 532 nm. The pulses are focused into the microfluidic device through a liquid-filled optical fiber and a dichroic mirror filter that reflects light with a wavelength of 532 nm and transmits light with a wavelength of 530-560 nm [89,90]. The filter prevents background and environmental noise light from entering the camera. Fig 1.6 shows a schematic view of the laser-illuminated micro-PIV system.

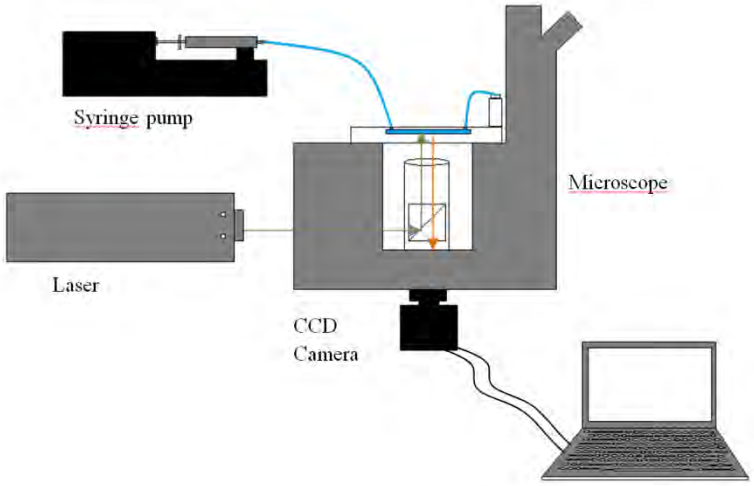

Fig 1.6. Schematic view of micro-PIV with laser illumination set up

1.5.2. Micro-PIV application in studying bio-fluids

To my best knowledge, the study of the blood behavior with the particle image velocimetry method started with the work of Sugii et al. [91], which was an in vivo study on the arteriole velocity profile in the rat mesentery to study microcirculation phenomena. RBCs were used as tracer particles and a velocity profile that was blunt at the center of the arteriole and sharp near the walls (a feature of non-Newtonian fluids) was observed.
Later, Hove et al. [92] applied digital PIV to study the intracardiac flow forces in zebrafish embryos using erythrocytes as tracer particles. Since previous studies showed that gen-expression profiles and endothelial cell arrangements change because of flow-induced forces, the final aim of this study was to quantify the shear stress and vertical flow forces in a developing heart. The results showed that the generated shear forces were greater than what was expected from the blood flow with such a low Reynolds number. These two early studies showed the suitability of PIV to be applied for studying the blood flow and rheology in the investigation of the microcirculation and blood hemodynamics (fluid mechanics of blood), RBC behaviors and flow around adherent and endothelial cells to investigate the shear stress effect on them.
Subsequently, other studies were conducted with micro-PIV, both in vivo and in vitro with different tracing particles.
Joeng et al. [93] studied the behavior of polymer-coated liposomes (as a carrier of a biological agent) in comparison with RBCs in vessels of the rat mesentery. Their results showed that the liposomes migrate toward the vessels walls under shear stress, in contrast with the RBC-depleted layer that forms near the vessel wall.

Vennemann et al. [94] studied the blood plasma in the beating heart of a chicken embryo. Fluorescent liposomes of a 400 nm diameter were used as tracer particles. The three error sources discussed in this work were that 1- the velocity measurement plane was not always parallel to the focal plane, 2- the velocity profile must be extrapolated to calculate the wall velocity and wall shear stress, and 3- the blood viscosity was not spatially constant, especially near the wall at very high shear rates where it showed very non-Newtonian behavior. In later studies, wall shear stress measurements were performed in the vitelline network of a chick embryo by Poelma [95,96], with small fluorescent particles of a 1 μm diameter used as tracer particles. A phase detection algorithm was developed that provided the capability for deriving the velocity of pulsatile blood flow at different cardiac phases. By conducting the measurement at different focal planes, a 2-component, 3-dimensional (2C-3D) velocity map was obtained.
In vivo micro-PIV studies were also performed to investigate the existence and effect of a glycocalyx layer on endothelial cells (ECs). An in vivo study by Domiano and co-workers [97] was conducted on ECs in cremaster muscle venules. This study confirmed the existence of a hydrodynamically effective glycocalyx endothelial surface layer that retarded plasma flow. As a consequence, the shear rate on the EC surface was effectively zero. However, the existence of such a layer for in vitro studies was not verified [98].
In vivo studies provide a complex situation in which the results are affected by many different factors and recognizing the effect of each individual parameter is very difficult or almost impossible. Therefore, numerous in vitro studies on bio-fluid behavior were performed with micro-PIV.
Lima and co-workers are among the leaders in performing in vitro studies on the blood with micro-PIV. They studied the red blood cell motion and interactions in microchannels with different configurations [99-102].
Voorhees et al. [103-105] conducted in vitro micro-PIV studies to investigate the steady and pulsatile flow effects on the EC responses. It was shown that the cell morphology changes based on the velocity of the fluid and the exerted shear stress, which results in changes to the shear stress itself (creating a cycle).
Rossi et al. [106-108] concentrated on deriving the effect of the cultured cell morphology on the behavior of fluid in the channel. They focused on optimizing the micro-PIV measurement parameters and conducting 2C-3D measurements.
The velocity information obtained by the PIV method was used as complementary data for studies related to the human knee or hip joint. PIV was used to provide validation information for the numerical simulation of the wear mechanisms in hip implants. This numerical simulation was developed based on a new hypothesis of third-body wear initialization after THR [30]. Micro-PIV together with birefringence was recently employed to develop a new diagnosis technique for joint diseases [109].

Compared to other fluids, biological fluid studies with micro-PIV have several limitations:

1- In vivo studies require dealing with complex situations. Therefore, the results are affected by many different factors, and recognizing the effect of each individual parameter is sometimes almost impossible. For example, the in vivo study of blood necessitates dealing with complex flows. The complexity originates from the non-Newtonian behavior of the blood, the complex vessel shapes and deformation because of the wall shear stresses, and the pulsatile and two-phase nature of the flow. In the case of wall shear stress measurements, for pulsating or moving organisms, defining the wall position is challenging and requires a special analysis procedure.
2- For in vitro studies, some parameters are kept constant to investigate the effect of a certain parameter. This may result in the underestimation of the velocities or shear

rates. The synthetic materials used for the fabrication of in vitro microchannels do not necessarily have the same properties and effects as biological tissues.

3- Natural particles are not always suitable for use as tracer particles. On the other hand, artificial particles can cause biological responses. Furthermore, because of bio-fluids' complex nature, special interactions between the fluid and tracer particles (either natural or artificial) might significantly affect the results.
4- Conventional micro-PIV is a 2D measurement method. However, it is possible to acquire 3D-3C velocities using different techniques. There are always unavoidable errors in the calculation of the out-of-plane velocity. For unsteady flow, which is usually the case in biological fluids, this limitation becomes even bolder.

1.6. Objective of the work

To my best knowledge, there has been no study that focused on investigating the implant's SF and wear particle distribution pattern inside the THR gap. Understanding the behavior of the wear particles and identifying the parameters that affect them provides the possibility to optimize the design parameters in THR implants to reduce the third body wear.
The main aim of the current work is to develop and validate an experimental method that provides the capability of quantitatively studying the behavior of HA and artificial SF solutions inside mini-channels and the special behavior of the particles in viscoelastic fluid flow. Quantifying the effects of different parameters such as the HA concentration or protein content, flow type (steady, unsteady, etc.) and gap shape and size on the fluid behavior is crucial to fully understand the particle distribution mechanisms.
In the current work, micro-PIV was applied as a flow visualization method to derive HA solution flow velocity profiles inside different mini-channels and under different flow conditions. The streamlines and shear stress information inside the flow are obtained from the velocity profiles.
In the first step, the simplest geometry (rectangular) was chosen for the mini-channel. The simplified geometry of the experimental model eliminated the geometric effect on the fluid flow. This allowed the investigation of different parameters such as the fluid composition, steady or unsteady flow and shear-thinning and viscoelastic non-Newtonian characteristic effects on the fluid behavior.
Next, the geometric effects were also studied by investigating the flow inside a curved mini-channel.
The fluid was subjected to different types of flow such as steady, unsteady harmonic pressure or shear-driven flow. The derived velocity profiles provided insight into the effect of parameters such as the pressure, strain amplitude or rate on the viscoelastic behavior of the flow and the interaction between the flow and the particles.
The final step in completing the experimental investigation was adding a normal load to the moving fluid. The simplest way is to add a steady load. However, THR implants are subjected to dynamic loading. To understand how different HA solutions perform under dynamic compere to static loading, a complementary study was conducted with a pin-on-disk on the frictional behavior of a UHMWPE pin rotating against a CoCrMo disk with different HA solutions.

1.6.1. Work plan

Based on the intended aim, this research project consisted of four main stages as follows, focused on complicating the flow condition and experimental model step by step to finally take measurements in an experimental model similar to the THR implants.

1- Steady-state Poiseuille flow (SS-PF): Study conducted on HA solution behavior under steady-state Poiseuille flow (pressure-driven flow) conditions inside a rectangular channel at different Newtonian Reynolds numbers with micro-PIV. The effects of different parameters including the channel size and material and HA and protein concentrations were investigated. This part consisted of assessing the effects of different measurement parameters such as the number of accumulated images and particle size on the micro-PIV results and building up measurement procedures. (Published as paper A).
2- Unsteady harmonic Poiseuille flow (UH-PF): Study conducted on HA solution behavior under unsteady harmonic oscillatory Poiseuille flow conditions inside a rectangular channel at different frequencies of oscillation with micro-PIV. The effects of different parameters including the channel size and material and HA and protein concentrations were investigated. Special particle behaviors were also investigated, in terms of if any migration or alignment was visible, which parameters affected these behaviors and how they affected the flow velocity profiles (Published as paper B).
3- Unsteady harmonic Couette flow (UH-CF): Study conducted on HA solution behavior under unsteady harmonic Couette flow conditions (flow induced by a moving surface) at three different frequencies of motion inside a curved channel with micro-PIV. Effects of HA and protein concentrations were studied. The pressure gradient effect was investigated by conducting measurements in two different channels (constant and variable cross-section channels). The particles' special behaviors were also investigated, in terms of possible visible migration or alignment, which parameters affected these behaviors and how they affected the flow velocity profiles (Presented in paper C).
4- Pin on disk (POD): The last step to provide an experimental model similar to the THR implant was to add a load. A complementary study was required to understand the effect of applying dynamic or static loading on the fluid performance. In the last stage, the frictional behavior of a UHMWPE pin rotating against a cobalt chromium molybdenum (CoCrMo) disk under static and dynamic loadings with different HA and protein content lubricants was studied with a pin-on-disk (Presented in paper D).

Chapter 2

THEORY

Theoretical solutions for a Newtonian fluid under three different flowing conditions are presented in this chapter. Comparison between these solutions with the experimental results of water was used to validate the experimental procedure. Moreover the theoretical equations provided insight to the effective parameters which were used for explaining and discussing the results (Chapter 5).

2.1. Steady-state Poiseuille flow

Laminar steady Poiseuille flow of a Newtonian fluid fully develops after a certain distance from the fluid inlet. The entrance length is calculated through Eq. (2-1) [110].

$$\frac{L_e}{D_h} = 0.06\,\mathrm{Re} \tag{2-1}$$

$$\mathrm{Re} = \rho U_{mean} D_h / \mu \tag{2-2}$$

ρ, U_{mean}, D_h, μ, L_e and Re represent the fluid density, flow mean velocity, hydraulic diameter, fluid dynamic viscosity, entrance length and Reynolds number, respectively.
The theoretical solution of Poiseuille flow in a rectangular channel where ($w>h$) (Fig 3.3) is obtained from Eqs. (2-3) and (2-4) [111]. The equations have been used to assess the quality of the measurements by comparison with theory.

$$Q = 2\int_0^{1/2w} dy \int_0^h dz\, u(y,z) = \frac{h^3 w \Delta p}{12\mu L}\left[1 - \sum_{n.odd}^{\infty} \frac{1}{n^5}\frac{192}{\pi^5}\frac{h}{w}\tanh\left(n\pi\frac{w}{2h}\right)\right] \tag{2-3}$$

$$u = \frac{4h^2 \Delta p}{\pi^3 \mu L} \sum_{n,odd}^{\infty} \frac{1}{n^3} \left[1 - \frac{\cosh\left(n\pi \frac{y}{h} \right)}{\cosh\left(n\pi \frac{w}{2h} \right)} \right] * \sin\left(n\pi \frac{z}{h} \right) \quad (2\text{-}4)$$

Q is the volume flow rate, h, w and L are channel width, height, and length, respectively (Fig 3.3), and Δp is the pressure difference.

2.2. Unsteady harmonic Poiseuille flow

The entrance length for laminar oscillatory flow was calculated based on Eq. (2-5) [112]:

$$L_{e(os)} = 0.03 D_h \mathrm{Re}_{os} \quad (2\text{-}5)$$

Re_{os} is the Reynolds number of the oscillatory flow, calculated as Eq. (2-6).

$$\mathrm{Re}_{os} = Amp_{fluid,mean} D_h / \nu \quad (2\text{-}6)$$

$Amp_{fluid,mean}$ and ν represent the amplitude of the cross-sectional mean velocity and kinematic viscosity, respectively.
The incompressible Navier-Stokes equation for flow along the x-direction is

$$\frac{\partial u}{\partial t} = \nu \nabla^2 u - \frac{1}{\rho} \frac{\partial p}{\partial x} \quad (2\text{-}7)$$

The variables of Eq. (2-7) are made dimensionless based on Eq. (2-8). ω, H, p represent the angular frequency of the oscillation, characteristic length and pressure, respectively.

$$x^* = \frac{x}{H}$$
$$u^* = \frac{u}{\omega H}$$
$$t^* = t * \omega \quad (2\text{-}8)$$
$$p^* = \frac{p}{\rho(\omega H)^2}$$

$$\frac{\partial u^*}{\partial t^*} = \frac{\nu}{\omega H^2} \nabla^2 u^* - \frac{\partial p^*}{\partial x^*} = \frac{1}{W^2} \nabla^2 u^* - \frac{\partial p^*}{\partial x^*} \quad (2\text{-}9)$$

Various numerical studies defined the characteristic length differently based on the channel shape (e.g., channel height and hydraulic diameter) [113-120]. In the current study, the hydraulic diameter was considered as the characteristic length so the effects of both the channel dimensions and geometry were taken into account.
Eq. (2-9) describes the relation among the viscous wave's penetration depth, flow pressure gradient along the channel, and velocity.
The non-dimensional parameter (W) that appears in Eq. (2-9) after making the parameters non-dimensional is known as the Womersley number (Eq. (2-10)).

$$W = H\sqrt{\frac{\omega}{\nu}} \tag{2-10}$$

This parameter is usually used to evaluate the oscillatory behavior of Newtonian fluids [112,113,121-123].
The Womersley number represents the ratio of the transient inertial to viscous forces and how deep the viscous waves generated at the wall penetrate into the flow.

2.3. Unsteady harmonic Couette flow

Shear flow near a flat plate with linear oscillatory motion is known as the Stokes second problem [124]. The equation of the motion is presented in Eq. (2-11). In the classical Stokes second problem, the flow reaches zero velocity at infinity. The extended situation of the Stokes second problem, in which shear flow is induced between two infinite parallel plates when one plate has a harmonic oscillatory motion and the other is at rest, was solved by Berker [125] (Fig 2.1).

$$\frac{\partial u}{\partial t} = \nu \frac{\partial^2 u}{\partial y^2} \tag{2-11}$$

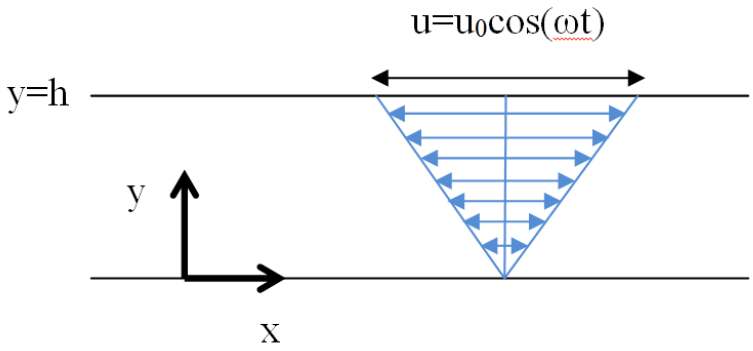

Fig 2.1. Schematic of flow-induced shear flow between two infinite parallel plates

Berker [125] solved the problem for the case in which the moving plane with sinusoidal harmonic motion is placed at y=0 and the fixed plane is placed at y=h (The general forms of the fluid velocity and boundary conditions are presented in Eq. (2-12) and (2-13)).

$$u(h,t) = 0$$
$$u(0,t) = u_0 \sin(\omega t) \qquad (2\text{-}12)$$

$$u = f(y)\sin(\omega t) + g(y)\cos(\omega t) \qquad (2\text{-}13)$$

He derived Eq. (2-14) for the fluid velocity.

$$u = \frac{u_0}{\sin(\beta_1 + \beta_2)}(e^{y\sqrt{\omega/2\nu}} \sin\beta_2. \sin(\omega t + y\sqrt{\omega/2\nu} + \beta_1) + e^{-y\sqrt{\omega/2\nu}} \sin\beta_1. \sin(\omega t - y\sqrt{\omega/2\nu} - \beta_2) \qquad (2\text{-}14)$$

β_1 and β_2 are arbitrary constants.
In the current study, the moving plane is placed at y=h with a harmonic cosine motion. The Berker solution was adapted for this case. Eqs (2-15) and (2-16) represent the boundary conditions and general form of the velocity, respectively.

$$u(h,t) = u_0 \cos(\omega t) = u_0 \sin(\omega t - \pi/2)$$
$$u(0,t) = 0 \qquad (2\text{-}15)$$

$$u = f(y)\sin(\omega t - \frac{\pi}{2}) + g(y)\cos(\omega t - \frac{\pi}{2}) \qquad (2\text{-}16)$$

This means that in the final general solution, a phase difference of $-\frac{\pi}{2}$ is required to be added to Berker's equation.

By replacing "*y*" with "*y-h*" in the general solution derived by Berker, the boundary conditions are satisfied. The final form of the fluid velocity is as Eq. (2-17):

$$u = \frac{-u_0}{\sin(\beta_1 + \beta_2)}(e^{(y-h)\sqrt{\omega/2\nu}} \sin\beta_2. \sin(\omega t + (y-h)\sqrt{\omega/2\nu} + \beta_1 - \frac{\pi}{2}) + e^{-(y-h)\sqrt{\omega/2\nu}} \sin\beta_1. \sin(\omega t - (y-h)\sqrt{\omega/2\nu} - \beta_2 - \frac{\pi}{2}) \qquad (2\text{-}17)$$

β_1 and β_2 are obtained by considering the zero velocity at *y*=0. Eqs. (2-18) and (2-19) present the final forms of the constants β_1 and β_2.

$$\beta_1 + \beta_2 = 2h\sqrt{\omega/2\nu} \tag{2-18}$$

$$\beta_1 = \tan^{-1}\left(\frac{-(\sin(2h\sqrt{\omega/2\nu})}{(e^{2h\sqrt{\omega/2\nu}} - \cos(2h\sqrt{\omega/2\nu})}\right) \tag{2-19}$$

The calculation procedures of β_1 and β_2 are presented in Eqs. (2-20) to (2-25).

$$y = 0 \Rightarrow u = 0$$

$$\Rightarrow u = \frac{-u_0}{\sin(\beta_1 + \beta_2)}(e^{-h\sqrt{\omega/2\nu}} \sin\beta_2.$$
$$\sin(\omega t - h\sqrt{\omega/2\nu} + \beta_1 - \frac{\pi}{2}) \tag{2-20}$$
$$+ e^{h\sqrt{\omega/2\nu}} \sin\beta_1.$$
$$\sin(\omega t + h\sqrt{\omega/2\nu} - \beta_2 - \frac{\pi}{2})$$

$$u = \frac{-u_0}{\sin(\beta_1 + \beta_2)}(e^{-h\sqrt{\omega/2\nu}}$$
$$\sin\beta_2.(\sin(\omega t).\cos(-h\sqrt{\omega/2\nu} + \beta_1 - \frac{\pi}{2}))$$
$$+\cos(\omega t).\sin(-h\sqrt{\omega/2\nu} + \beta_1 - \frac{\pi}{2})) \tag{2-21}$$
$$+ e^{h\sqrt{\omega/2\nu}} \sin\beta_1.$$
$$(\sin(\omega t).\cos(h\sqrt{\omega/2\nu} - \beta_2 - \frac{\pi}{2})$$
$$+\cos(\omega t).\sin(h\sqrt{\omega/2\nu} - \beta_2 - \frac{\pi}{2}))) = 0$$

To obtain a zero velocity at every instant, the coefficients of $\sin(\omega t)$ and $\cos(\omega t)$ should be zero, which provide us with Eqs. (2-22) to (2-24)

$$\begin{cases} 1)\ \ e^{-h\sqrt{\omega/2\nu}}\sin\beta_2.\cos(-h\sqrt{\omega/2\nu}+\beta_1-\dfrac{\pi}{2}) \\ \quad +e^{h\sqrt{\omega/2\nu}}\sin\beta_1.\cos(h\sqrt{\omega/2\nu}-\beta_2-\dfrac{\pi}{2})=0 \\ 2)\ \ e^{-h\sqrt{\omega/2\nu}}\sin\beta_2.\sin(-h\sqrt{\omega/2\nu}+\beta_1-\dfrac{\pi}{2}) \\ \quad +e^{h\sqrt{\omega/2\nu}}\sin\beta_1.\sin(h\sqrt{\omega/2\nu}-\beta_2-\dfrac{\pi}{2})=0 \end{cases}$$

$$\Rightarrow \begin{cases} 1)\ \ e^{-h\sqrt{\omega/2\nu}}\sin\beta_2.\cos(-h\sqrt{\omega/2\nu}+\beta_1-\dfrac{\pi}{2})= \\ \quad -e^{h\sqrt{\omega/2\nu}}\sin\beta_1.\cos(h\sqrt{\omega/2\nu}-\beta_2-\dfrac{\pi}{2}) \\ 2)\ \ e^{-h\sqrt{\omega/2\nu}}\sin\beta_2.\sin(-h\sqrt{\omega/2\nu}+\beta_1-\dfrac{\pi}{2})= \\ \quad -e^{h\sqrt{\omega/2\nu}}\sin\beta_1.\sin(h\sqrt{\omega/2\nu}-\beta_2-\dfrac{\pi}{2}) \end{cases} \qquad (2\text{-}22)$$

$$\Rightarrow \frac{e^{-h\sqrt{\omega/2\nu}}\sin\beta_2.\cos(-h\sqrt{\omega/2\nu}+\beta_1-\dfrac{\pi}{2})}{e^{-h\sqrt{\omega/2\nu}}\sin\beta_2.\sin(-h\sqrt{\omega/2\nu}+\beta_1-\dfrac{\pi}{2})}= \frac{-e^{h\sqrt{\omega/2\nu}}\sin\beta_1.\cos(h\sqrt{\omega/2\nu}-\beta_2-\dfrac{\pi}{2})}{-e^{h\sqrt{\omega/2\nu}}\sin\beta_1.\sin(h\sqrt{\omega/2\nu}-\beta_2-\dfrac{\pi}{2})}$$

$$\frac{\sin(-h\sqrt{\omega/2\nu}+\beta_1)}{-\cos(-h\sqrt{\omega/2\nu}+\beta_1)}=\frac{\sin(h\sqrt{\omega/2\nu}-\beta_2)}{-\cos(h\sqrt{\omega/2\nu}-\beta_2)} \qquad (2\text{-}23)$$

$$\tan(-h\sqrt{\omega/2\nu}+\beta_1)=\tan(h\sqrt{\omega/2\nu}-\beta_2)$$
$$\Rightarrow \beta_1+\beta_2=2h\sqrt{\omega/2\nu} \qquad (2\text{-}24)$$

β_1 is calculated from Eq. (2-25), which is obtained by replacing β_2 with $2h\sqrt{\omega/2\upsilon}-\beta_1$ in the second part of Eq. (2-22).

$$
\begin{aligned}
& e^{-h\sqrt{\omega/2\nu}} \sin\beta_2 . \sin(-h\sqrt{\omega/2\nu} + \beta_1 - \frac{\pi}{2}) + e^{h\sqrt{\omega/2\nu}} \\
& \sin\beta_1 . \sin(h\sqrt{\omega/2\nu} - \beta_2 - \frac{\pi}{2}) = 0 \\
& \Rightarrow -e^{-h\sqrt{\omega/2\nu}} \sin(2h\sqrt{\omega/2\nu} - \beta_1) \\
& \quad \cos(-h\sqrt{\omega/2\nu} + \beta_1) \\
& \quad - e^{h\sqrt{\omega/2\nu}} \sin\beta_1 \cos(-h\sqrt{\omega/2\nu} + \beta_1) = 0 \\
& \Rightarrow e^{-h\sqrt{\omega/2\nu}} \sin(2h\sqrt{\omega/2\nu} - \beta_1) = -e^{h\sqrt{\omega/2\nu}} \sin\beta_1 . \\
& \quad (\sin(2h\sqrt{\omega/2\nu}) \cos\beta_1 \\
& \quad - \cos(2h\sqrt{\omega/2\nu}) \sin\beta_1) = \\
& \quad - e^{2h\sqrt{\omega/2\nu}} \sin\beta_1 . \\
& \quad \sin\beta_1 (e^{2h\sqrt{\omega/2\nu}} + \cos(2h\sqrt{\omega/2\nu})) \\
& \quad = (\sin(2h\sqrt{\omega/2\nu}) \cos\beta_1 \\
& \Rightarrow \beta_1 = \tan^{-1}\left(\frac{-(\sin(2h\sqrt{\omega/2\nu})}{(e^{2h\sqrt{\omega/2\nu}} - \cos(2h\sqrt{\omega/2\nu})} \right)
\end{aligned}
\qquad (2\text{-}25)
$$

In comparison with this thesis experimental condition, this solution does not consider curvature effects and the finite channel condition.

Chapter 3

EXPERIMENTAL PROCEDURE

3.1. Micro-PIV

Fig 3.1 shows the schematic of the micro-PIV setup. The system consisted of a double-pulsed microstrobe (LED) and a high-speed double-frame CCD camera with a spatial resolution of 1280×1024 pixels per frame mounted on a microscope with four magnifications (5x, 10x, 20x and 40x). The two pulses had the same time duration, between 50 and 110 μs, based on the microstrobe power and the flow speed. The time between two pulses was set between 150 and 940 μs as a function of the flow rate and the type of fluid. The time between pulses was chosen to have the largest particle movement between each two frames of 16-20 pixels.

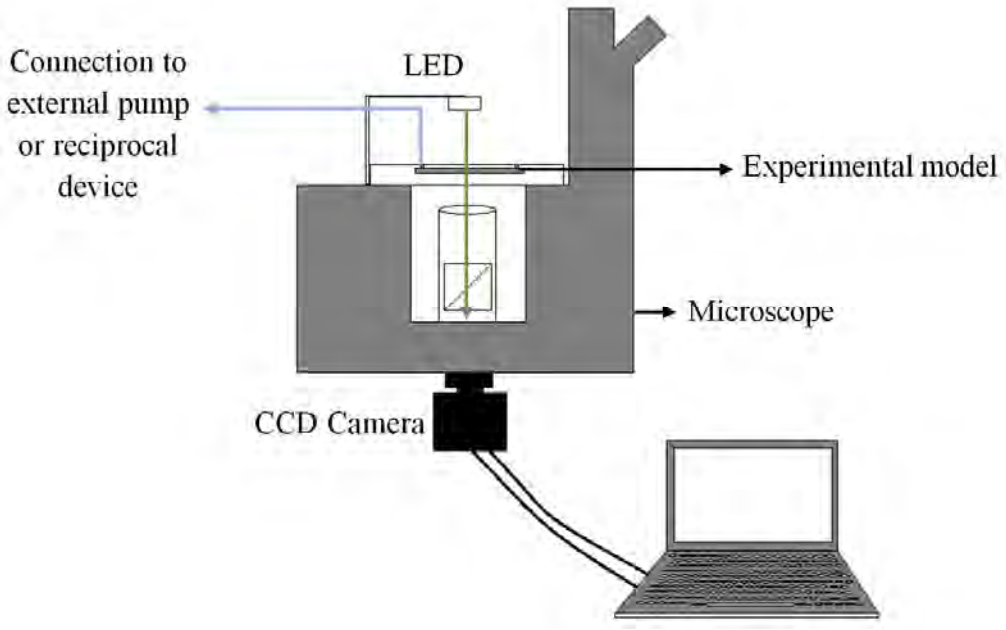

Fig 3.1. Schematic of micro-PIV set up

The seeding particle plays a major role in the quality of the acquired data from micro-PIV. The performance of the particles is affected by the visibility, size and density.
Suitable particles for micro-PIV measurements have a density similar to that of the fluid. Polystyrene particles, with a density of 1-1.05 g.cm^{-3}, are suitable for the study of water-based fluids.

3.1.1. Tracing particles

It has been suggested that for micro-PIV measurements, the particle size in the images should be on the order of 3-4 pixels [83]. The quality of the micro-PIV measurements depends strongly on how accurately the particles follow the fluid motion. Because of sedimentation or Brownian effects, the particles might not follow the fluid track. To minimize the sedimentation effect, the particle density must be close to the fluid density and the size of the particles must be kept reasonably small. However, Brownian motion affects small particles with a size between 50-500 nm at low velocities. In the current study, particles with diameters of 2 and 5 μm were chosen for magnifications of 20x and 10x, respectively.
According to Stokes' drag law, if the density of the particle is different from the liquid density, the induced velocity of the particle due to gravitational forces is (Eq. (3-1)) [83]

$$u_g = d_p^2 \frac{(\rho_p - \rho_l)}{18\mu} g \qquad (3\text{-}1)$$

where ρ is the density, d is the diameter and μ is the dynamic viscosity. The "p" index refers to particle, while "l" refers to liquid. The particle response time is (Eq.(3-2)) [83]

$$\tau_p = \frac{d_p^2 \rho_p}{18\mu_l} \qquad (3\text{-}2)$$

From the above equations, the response times of 2 and 5 μm diameter particles are approximately 2.3*10^{-7} s and 0.1*10^{-7} s, respectively. For steady-state conditions, these time scales are much smaller than the liquid time scale ($\frac{D_h}{U_{mean}} = 4.67*10^{-1}\ s$). Therefore, these particles follow the flow variations. The induced velocities due to gravitational forces of the 2 and 5 μm diameter particles were calculated to be 1.1*10^{-4} mm.s^{-1} and 6.9*10^{-4} mm.s^{-1}, respectively. Therefore, these particles do not face any sedimentation in the problem investigated.
For particles with diameters between 50 nm and 500 nm and velocities below 1 mm.s^{-1}, the Brownian effect is significant and causes errors in the estimation of the velocity. The error can be determined using Eq. (3-3)[83].

$$\varepsilon_x = \frac{1}{u}\sqrt{\frac{2D}{\Delta t}}$$
$$\varepsilon_y = \frac{1}{v}\sqrt{\frac{2D}{\Delta t}} \qquad (3\text{-}3)$$

u and *v* represent the fluid velocities in the x and y directions, respectively, Δt is the time interval (the time between frames or images) and D (diffusion coefficient of the particle) is calculated from the equation below [83].

$$D = \frac{KT_l}{3\pi\mu_l d_p} \tag{3-4}$$

K and T_l are the Boltzmann's constant and the liquid absolute temperature, respectively. The Brownian error equation shows that by increasing the time interval, the Brownian error decreases. This puts a lower limit on the time interval between frames [83].

3.1.2. Number of accumulated velocity maps

In micro-PIV measurements, to obtain a reliable velocity map, it is necessary to average several velocity maps. To determine the number of images required to obtain a stable mean value, 1000 images were captured, and the accumulated mean value was evaluated. Results showed that at least 300 images were required to obtain a variation of the mean velocity (calculated from Eq. (3-5)) below 0.5% (Fig 3.2).

$$Err\% = \frac{\left| \left(\sum_{i=1}^{n} u_i \right)/n - \left(\sum_{i=1}^{1000} u_i \right)/1000 \right|}{\left(\sum_{i=1}^{1000} u_i \right)/1000} * 100 \qquad 1 < n < 1000 \tag{3-5}$$

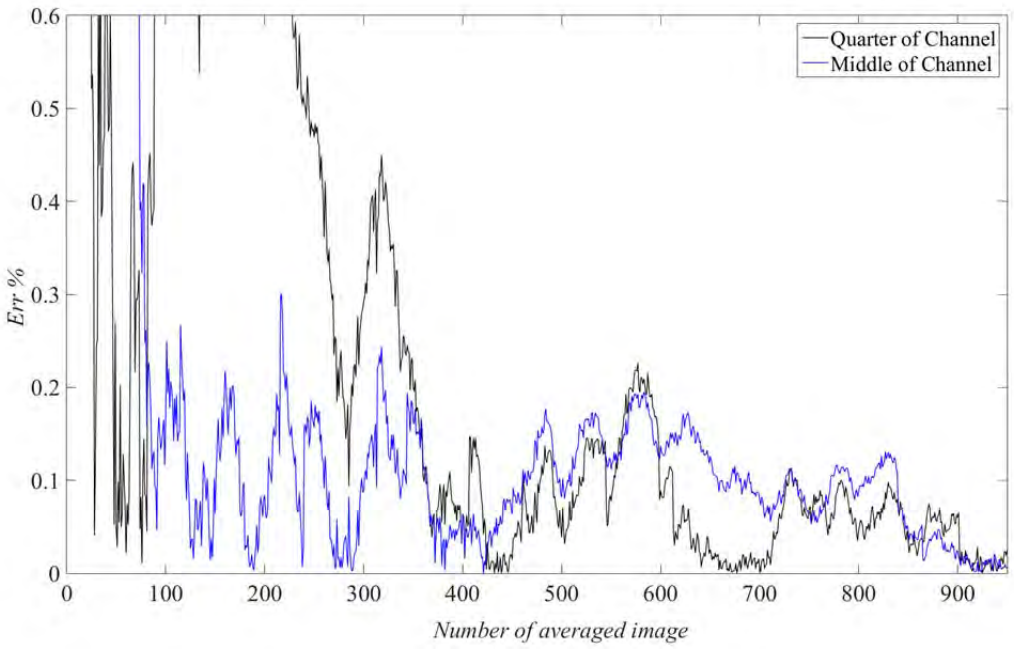

Fig 3.2. Variation of percentage of error vs. number of averaged images for water at Re of 23.33

3.2. Steady-state Poiseuille flow

One of the major problems with polystyrene particles is agglomeration in water. To assess the effects of different parameters on the experimental results, agglomeration should be avoided. For this stage, polystyrene particles with a density of 1-1.05 $g.cm^{-3}$ from Magsphere, Inc. (Pasadena, CA, USA) were chosen, which contained 0.05% anionic surfactant to prevent agglomeration.

3.2.1. Rectangular mini-channel

Mini-channels were designed and constructed to investigate the effects of different materials and channel sizes on the HA solution behavior. The channel consisted of four main parts, as shown in Fig 3.3: a Plexiglas plate (back plate) allowing light to travel through the model, a front plate with a glass window for providing optical access and a middle plate that was a steel frame capable of holding bars of different materials at a specific distance from each other. The steel frame provided two different channel widths, 1 mm (hydraulic diameter of 1.33 mm) and 1.5 mm (hydraulic diameter of 1.71 mm). The depth and length of both channels were 2 and 45 mm, respectively. Hereafter, the 1 mm width channel is named Channel 1, and the 1.5 mm width channel is named Channel 2.

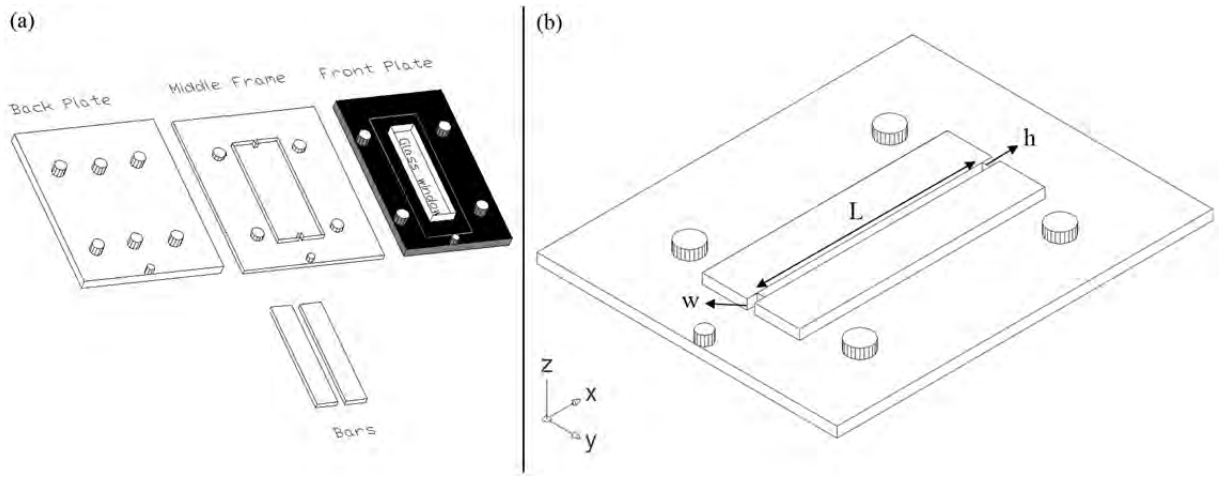

Fig 3.3. Schematic of rectangular mini-channel

The bars' material was chosen similar to that usually used in THR: UHMWPE, cobalt chromium molybdenum alloy (CoCrMo) and titanium aluminum vanadium alloy (TiAlV). The sides of the bars in contact with the fluid were polished to achieve at a mirror-like surface. Table 3.1 presents the surface roughness of the tested materials. Hereafter, the CoCrMo bars, UHMWPE bars and TiAlV bars are called Bar 1, Bar 2 and Bar 3, respectively. The largest entrance length (corresponding to the largest Re number and Channel 2) was 6.6 mm (Eq. (2-1)). The measurements were conducted at the middle of the rectangular channel with a 22 mm distance from the inlet and outlet at the middle depth of the channel (1 mm distance from top and bottom plates). Therefore, the boundary layer at that region was fully developed, and the velocity profiles were identical along the y-axis (3.2.1).

Table 3.1. Roughness of different material of the bars

Material	**Roughness (R_a in μm)**	
	1st bar	2nd bar
UHMWPE	0.362	0.342
CoCrMo	0.075	0.073
TiAlV	0.159	0.162

3.2.2. External pump

For steady flow, a kd Scientific Model 410 series syringe pump (KD Scientific Inc, Holliston, MA, USA) was used for injecting the fluid at different flow rates through the experimental model. It had 2% accuracy in providing a defined flow rate.
The flow rates in Channel 1 were chosen to produce the maximum fluid velocity in the same range as that in a hip implant based on published studies [41,126,127], and the flow rate in Channel 2 was chosen to have the same Re number (Eq. (2-2)) for a Newtonian fluid (water) as in Channel 1.
Three Reynolds numbers were chosen: 7.78 (called Re-1), 23.33 (Re-2) and 64.17 (Re-3). The flow rates corresponding to these Reynolds numbers were 0.7, 2.1 and 5.775 $ml.min^{-1}$, respectively, for Channel 1 and 0.82, 2.45 and 6.74 $ml.min^{-1}$ for Channel 2. For non-Newtonian fluids, the same flow rates were applied, although the Reynolds numbers were not identical. Each measurement was carried out three times to investigate the repeatability.
At this stage, the time between pulses was set to 200, 600 and 900 μs from the highest to lowest Re number, respectively.

3.2.3. Experimental fluid

Degassed water was used as the reference Newtonian fluid and to evaluate the experimental procedure. The criteria for the choices of the other fluids were to capture the periprosthetic rheological behavior with a simple composition and investigate the effects of the HA concentration and protein content at the same time. Three HA solutions were investigated. Table 3.2 contains information about the HA compositions and the names assigned to the experimental fluids

Table 3.2. Composition of the experimental fluid with assigned names

Experimental Fluid	**Fluid name**
Degassed water	**Fluid 1**
HA with 1.4-1.5 MDa molecular weight (Lifecore Biomedical, Minneapolis, Minnesota, USA) with concentration of 3 $mg.ml^{-1}$ in phosphate-buffered saline (PBS from Sigma Aldrich, St. Louis, Missouri, USA with 0.15 M concentration)	**Fluid 2**
HA with 3 $mg.ml^{-1}$ concentration in a mixture of 75% PBS and 25% bovine calf serum (BCS) (Sigma Aldrich 12133C)	**Fluid 3**
HA with concentration of 5 $mg.ml^{-1}$ in PBS.	**Fluid 4**

HA was dissolved in the liquid (PBS or 75% PBS+25% BCS) at room temperature by gently shaking it for 15 hours on a mini-shaker, which provided circular rocking and three-dimensional motion. For minimizing the bacterial activity, 0.1% (w/v) sodium azide (Sigma Aldrich 71289, St. Louis, Missouri, USA) was added.

3.2.4. Rheological measurements

The rheological behavior of the HA solutions was investigated by a Bohlin CVO rheometer at 25°C under shear rate control (0.05-1570 s^{-1}) with coaxial cylinders (C25) to obtain the variation of the viscosity versus the shear rate. The viscoelastic behavior of the HA with a 5 $mg.ml^{-1}$ concentration in PBS was investigated with the same rheometer and cone on a plate configuration consisting of a stainless steel cone of 1° and 20 mm in diameter. Frequency sweep measurements were performed with the strain value and frequency were set at 2% and 0.07-10 Hz, respectively. Investigating the viscoelastic behavior of the HA solutions with a concentration of 3 $mg.ml^{-1}$ was impossible due to the calibration range of the described rheometer.

3.3. Unsteady harmonic Poiseuille flow

Polystyrene particles with a density of 1-1.05 $g.cm^{-3}$ and diameter of 4.89 microns were chosen (microParticles GmbH, Berlin, Germany), along with a magnification of 10x.
The rectangular channel described in section 3.2.1 was used as the experimental channel in this stage as well.
The experimental fluids described in section 3.2.3 were used in the measurements of UH-PF.

3.3.1. Reciprocating pump

The unsteady Poiseuille flow was produced by an oscillatory pump consisting of a syringe and a homemade reciprocal device (Fig 3.4). The syringe oscillatory movement was obtained with a rotating disk coupled to an electrical motor. Fig 3.4 shows a schematic view of this oscillatory pump system. The angular position of the disk was determined through twelve steel teeth (knobs) equally spaced on the periphery of the disk and a magnetic encoder. The encoder signal allowed the synchronization of the micro-PIV and the LED, i.e., it acted as a trigger. With this system, images were captured at defined phases. Two rotating arms coupled the disk to the syringe to enable small syringe movements (up to 1 mm). Two different holes were used to attach the arm to the rotating disk. The hole that was closer to the center of the disk provided a smaller stroke amplitude for the syringe movement and a smaller flow rate amplitude, which is called S-1. The other hole with a larger stroke is called S-2. The frequency of the disk motion was controlled through a code developed in LabVIEW.
To achieve reliable velocity profiles from the micro-PIV measurements, image averaging was required. For unsteady measurements, the averaging was only possible if the phases of the velocity maps were the same. A total of 3200 images were captured for each measurement, i.e., 250 images at each phase.
The position of the syringe piston was determined by a distance laser. The angular position of the reciprocating disk in combination with the syringe piston position provided the phases of the captured images. The differentiation of the syringe piston position with time allowed the calculation of the syringe velocity.
Three frequencies of 0.37 (called F-0), 1.02 (F-1) and 2.03 (F-2) were applied during the measurements.
The lowest syringe motion frequency was chosen to be similar to the highest rotational frequency of a hip joint in a walking situation, 0.37 Hz (approximately 2 $rad.s^{-1}$). The highest frequency was 2.03 Hz, which is higher than the crossover frequency obtained for the HA solution with a 5 $mg.ml^{-1}$ concentration. A middle frequency of 1.02 Hz was also investigated. For the measurements with frequencies of 0.37 and 1.02 Hz, S-2 was used to attach the arms to the rotating disk. However, limitations in the micro-PIV system and LED did not allow

measurements of the maximum velocity for the frequency of 2.03 Hz with S-2; instead, S-1 was used. For S-1, the syringe stroke amplitude and flow rate amplitude were smaller compared to those of S-2. Therefore, the highest mass flow rate amplitude did not belong to the highest frequency. The maximum to minimum mass flow rates in this situation belonged to the measurements with frequencies of 1.02, 2.03 and 0.37 Hz, respectively.
The longest calculated entrance length belongs to the flow rate with the largest amplitude (F-1), which was 6 mm (Eqs. (2-5) and (2-6)). Therefore, at the middle of the channel (measurement section), the velocity profiles were fully developed.
The time between the two pulses was set between 150 and 600 μs as a function of the flow rate amplitude and the type of fluid.

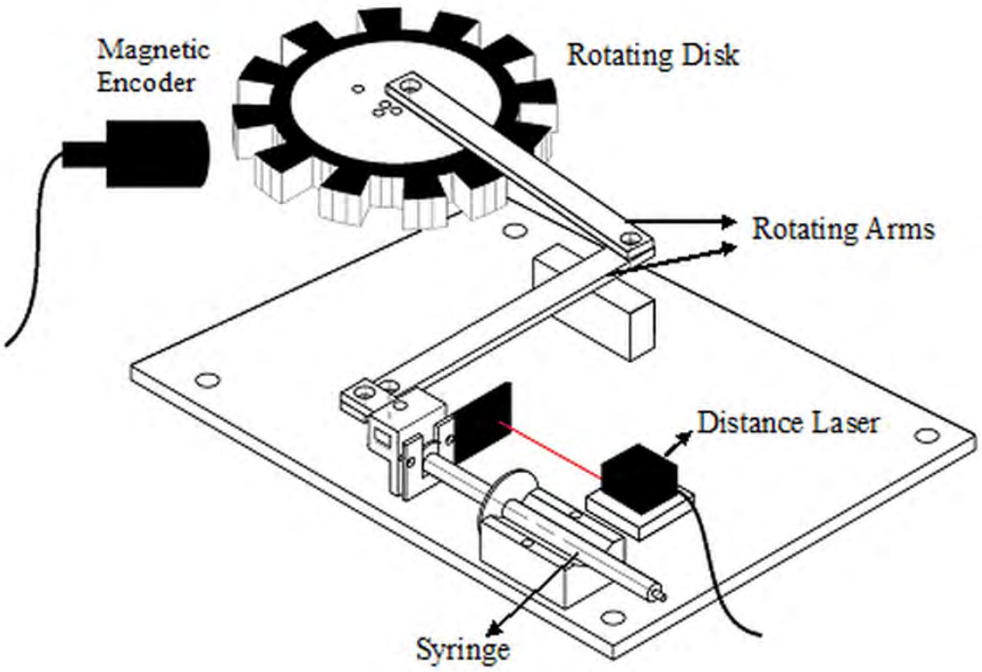

Fig 3.4. Schematic view of oscillatory pump

3.4. Unsteady harmonic Couette flow

Polystyrene particles with a density of 1-1.05 $g.cm^{-3}$ and average diameter of 4.89 microns were chosen (microParticles GmbH, Berlin, Germany), along with a magnification of 10x.
The experimental fluid concentrations and preparation procedures were the same as those described in section 3.2.3. However, HA with a 1.6-1.8 MDa molecular weight (Sigma Aldrich 53747, St. Louis, Missouri, USA) was used to produce the HA solutions.

3.4.1. Curved mini-channel

Two curved channels were designed to study the effect of shear-induced flow and the variation of the cross-section on the viscoelastic fluid behavior. The curved channel consisted of two concentric cylinders made from stainless steel. Optical access to the model was provided by placing the steel parts inside a Plexiglas frame. The constant-width channel had a width of 1.1 mm, while the converging-diverging channel width changed between 0.3 and 1.1 mm. The inner wall radius and depth of both channels were 21 and 3 mm, respectively.

Approximately 3 ml of fluid was stored in the rectangular storage of each model during the measurements (Fig 3.5), and the channels were sealed by an upper Plexiglas plate. The maximum curvature ratio (ratio of the channel width to the inner cylinder radius) of both channels was 0.05. The small field of view and the small curvature ratio suggest that the curvature effects were negligible.
Hereafter, the constant-width channel is called Const Channel, and the converging diverging channel is called Conv Channel.
The measurement location was selected to be at 45° with respect to the symmetrical axis of the model (Fig 3.5) and at the middle depth of the channel (with a 1.5 mm distance from the top and bottom plates). At this location and for the Conv Channel, the ratio of the largest to smallest measurement section width in a complete cycle was more than 2.

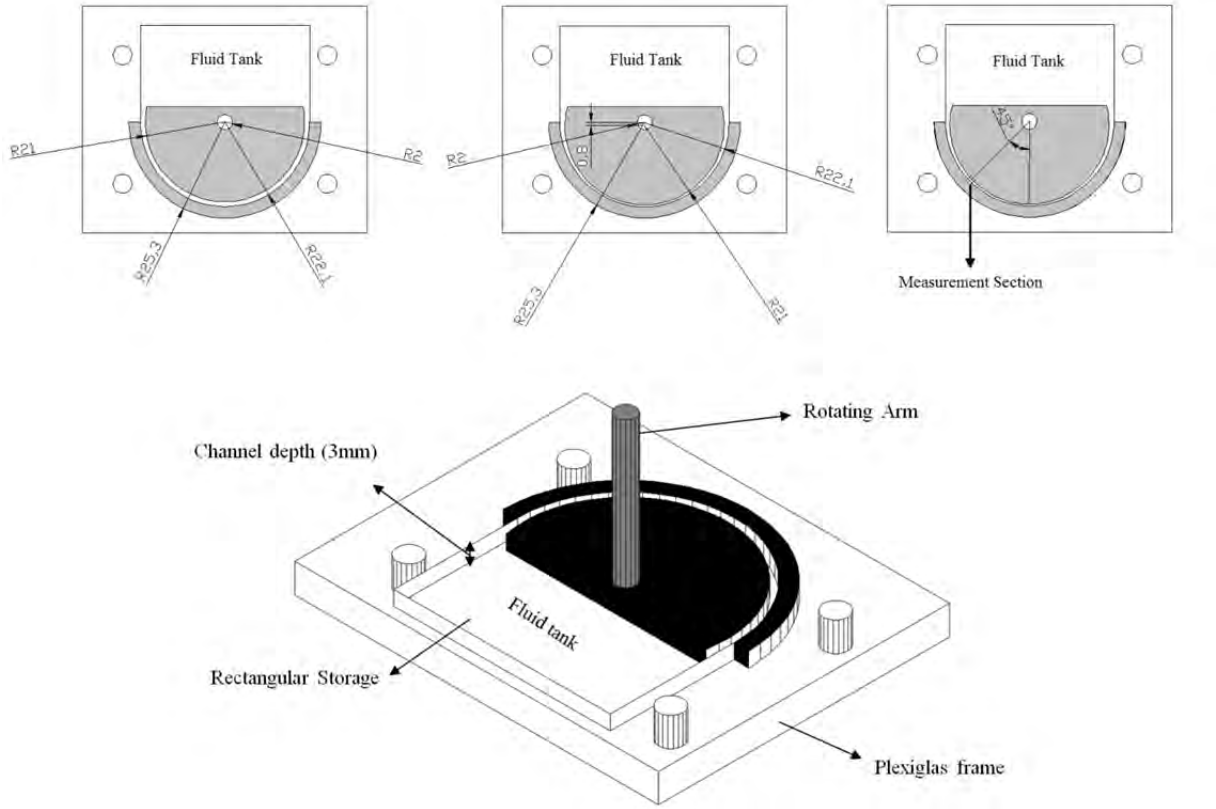

Fig 3.5. Schematic of curved mini-channel

3.4.2. Reciprocal device

In this stage, the shear-induced flow was provided by the inner cylinder oscillatory motion that was obtained by a rotating disk coupled to an electrical motor in combination with four rotating and one pushing arms. Fig 3.6 shows a schematic view of this oscillatory engine coupled with the experimental model. The working principle of this system was the same as that previously explained (Section 3.3.1). For UH-CF studies, all of the measurements were done by attaching the rotating arm to the rotating disk with S-2.
The amplitude of the rotation for the inner cylinder was set at 15° (total movement of 30°), which is the average hip joint rotation in the sagittal plane during walking [128].
Based on the frequency of the movement and the type of fluid, the time between pulses in the micro-PIV measurement was set between 150 and 940 μs, with the longest time corresponding to the lowest frequency and vice versa.

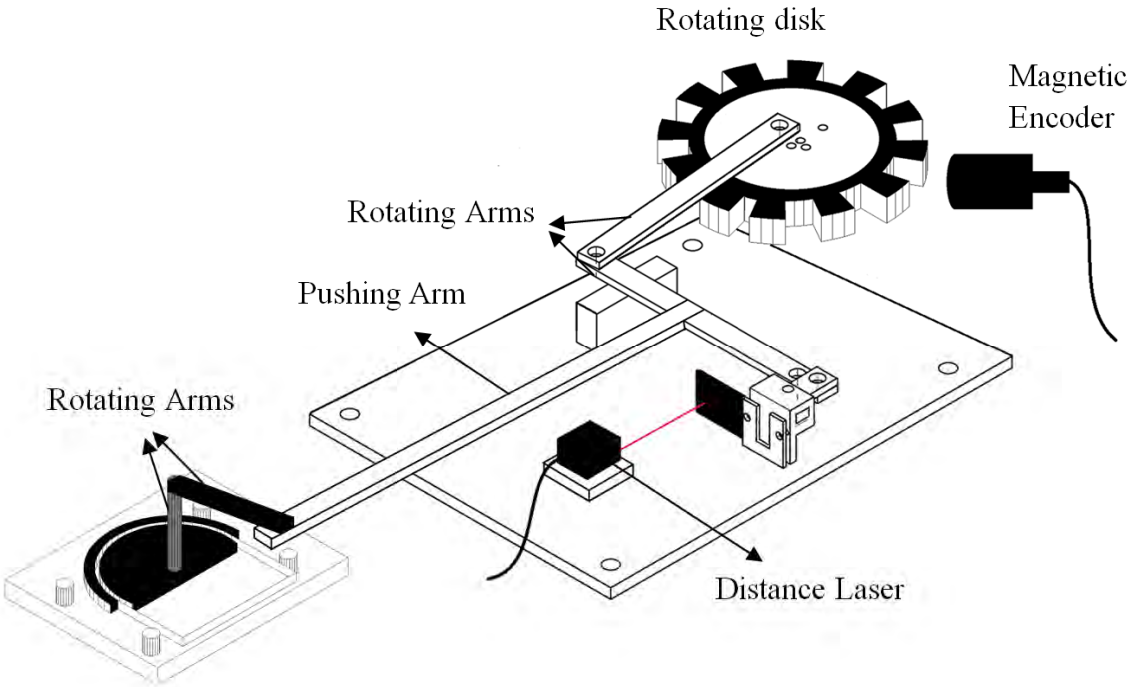

Fig 3.6. Schematic of oscillatory engine coupled with experimental model

As was mentioned earlier (section 3.1.2), at least 300 images are required to obtain a variation of the mean velocity below 0.5%. In this set of measurements, due to limitations of the CCD camera memory, 1500 images were captured with micro-PIV for each measurement (i.e., 120 images for each phase). The relative difference (*RD*) between the mean velocities obtained from 120 and 300 images was investigated (Eq. (3-6)). The *RD* is presented in Fig 3.7 along the channel width for the case of distilled water at a frequency of 2.03 Hz and at the phase with the cylinder maximum velocity.

$$RD = \frac{\left|\bar{u}_{120} - \bar{u}_{300}\right|}{u_{cylinder}} * 100 \qquad (3\text{-}6)$$

where $\bar{u}_{120}$ is the mean value of the velocity calculated using 120 images, $\bar{u}_{300}$ is the mean value calculated using 300 images and $\bar{u}_{cylinder}$ is the cylinder velocity at the specific phase. The maximum relative difference along the channel width in the measurement section is less than 1% of the cylinder velocity.

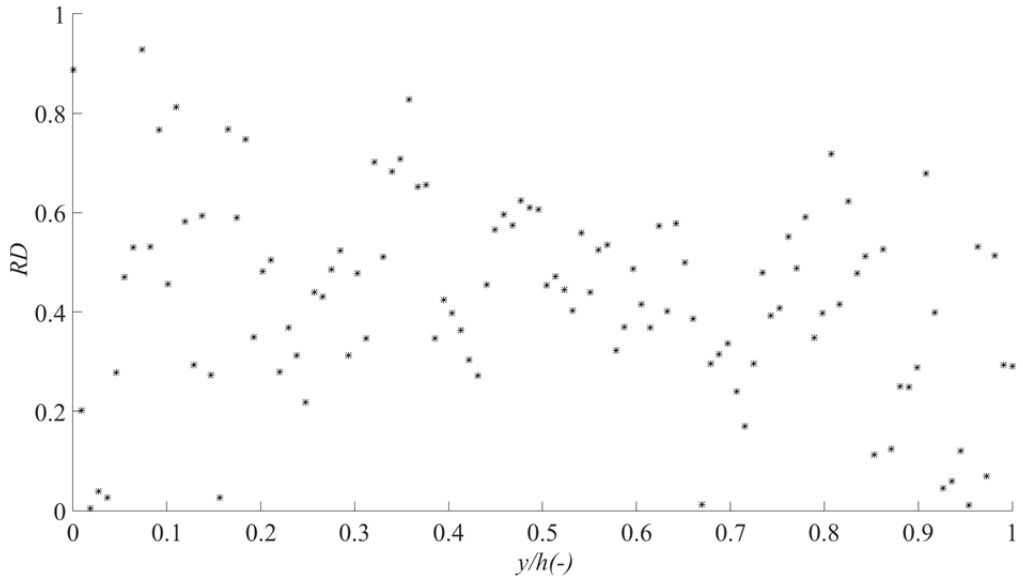

Fig 3.7. Relative difference between the mean velocity obtained with 120 and 300 images along the channel width at f=2.03 Hz.

3.5. Pin on disk

3.5.1. Material

Using the compression molding method, GUR 1020 UHMWPE (Ticona/Celanese, USA) blocks were prepared in our lab, and 4×4×4 mm^3 pins were cut out from a pressed UHMWPE block. Each pin was soaked in distilled water for a minimum of two weeks before the tribotest. The average roughness of the pin surface (derived from topographical analysis (section 3.5.4)) was approximately R_a=1.5-2 μm.

Chromium cobalt molybdenum alloy (CrCoMo) with a mirror-polished surface with an average roughness of R_a=0.005 μm was used as a counter-surface. The chemical composition of the CoCrMo discs was Co (65.74 wt%), Cr (27.11 wt%), Mo (5.52 wt%), Mn (0.78 wt%), N (0.194 wt%), Fe (0.07 wt%), Ni (0.06 wt%), Si (0.59 wt%), C (0.04 wt%), W (<0.02 wt%), Cu (<0.01 wt%), P (<0.003 wt%), S (<0.0005 wt%).

All samples were cleaned based on the procedure in the ASTM F732 - 00(2011) standard. Table 3.3 lists the lubricants used and the names assigned to them.

Table 3.3. Lubricants' composition

Lubricant Composition	**Lubricant name**
Distilled water	**DW**
Diluted BCS: 75% phosphate-buffered saline (PBS from Sigma Aldrich, St. Louis, Missouri, USA with 0.15 M concentration) and 25% BCS (Sigma Aldrich 12133C, St. Louis, Missouri, USA)	**DS**
HA with 1.6-1.8 MDa molecular weight (Sigma Aldrich 53747, St. Louis, Missouri, USA) with a concentration of 3 $mg.ml^{-1}$ in PBS	**HA**
HA with 3 a $mg.ml^{-1}$ concentration in a mixture of 75% PBS and 25% BCS	**HAS**

To minimize the bacterial activity, 0.1% (w/v) sodium azide (Sigma Aldrich 71289, St. Louis, Missouri, USA) was added to the HA solutions. Distilled water was used as the reference

lubricant to determine the influences of the HA and protein in the lubricant. Diluted BCS is the standard lubricant for the friction and wear measurements of joint implant materials. The criteria for choosing the other two lubricants were explained earlier in section 3.2.3.

3.5.2. Pin-on-disk set up

The frictional measurements under steady and dynamic loading were performed using a unidirectional Plint TE-67 pin-on-disk tribometer (Phoenix Tribology, Ltd., Kingsclere, England). For the steady-state condition, a 120 N load was applied on the pin, corresponding to a 7.5 MPa pressure. The dynamic load had a sinusoidal pattern with a frequency of 1 Hz, average load of 120 N, and amplitude of 40 N. The sinusoidal load was applied using a pneumatic system. The applied loads were chosen to keep the pressure in the range of 2-10 MPa based on the ASTM F732 - 00(2011) standard. Due to the high applied pressure, the polymeric pin underwent viscoelastic deformation. The pin thickness variation was measured by a displacement sensor coupled to the pin holder. Fig 3.8 provides a schematic view of the pin-on-disk setup. To reduce the hydrodynamic effects, the sliding velocity was kept constant at 34 $mm.s^{-1}$. This velocity lies in the typical velocity range for hip implants (0-50 $mm.s^{-1}$) [61]. Each measurement was performed for 50,000 cycles at room temperature (25-27° C). Distilled water was added gradually at a constant rate to the lubricant by a syringe pump (kd Scientific Model 410 series) to keep the concentration of the lubricants constant. Each set of measurements was performed at least three times. Hereafter, the measurements with steady and dynamic loading are referred to as Const and Sin, respectively.

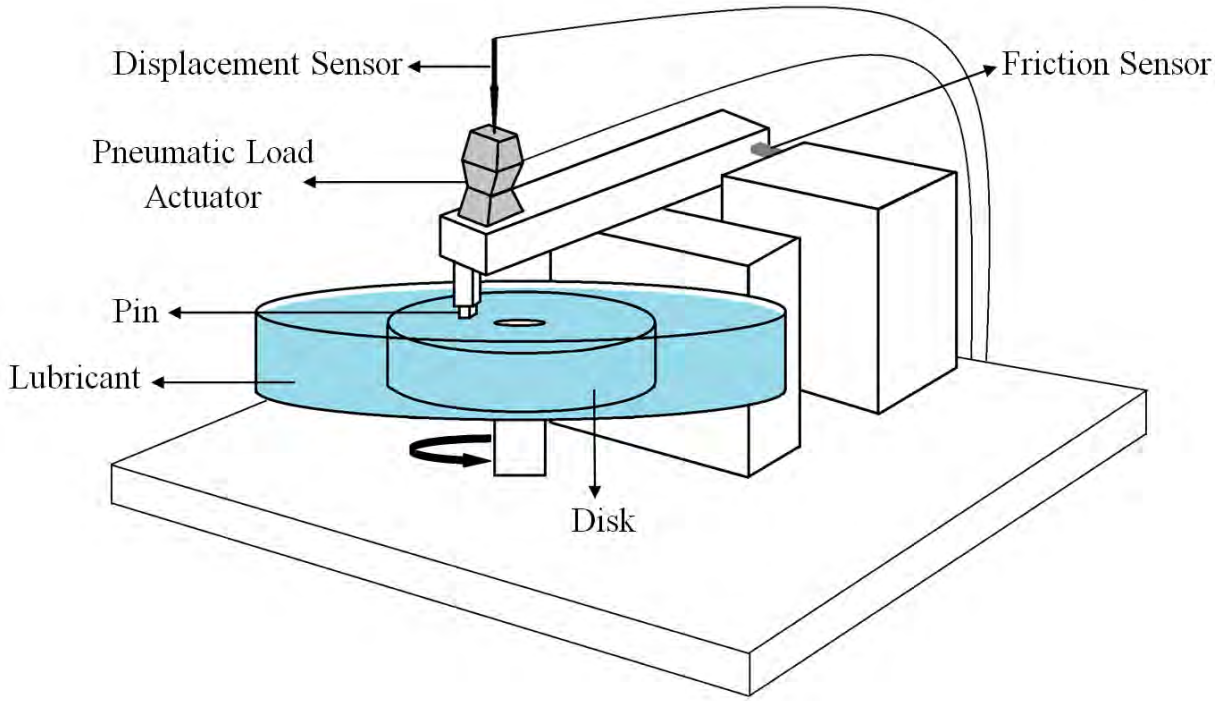

Fig 3.8. Schematic of pin on disk setup

Fig 3.9 shows the response and decay times of the friction sensor, which were approximately 0.7 and 1.2 s, respectively. The sensor characteristic times are considerably higher than the load cycle period (1 s). Therefore, the sensor could not capture the total range of friction under the dynamic loading condition. The decay time was larger than the response time. This suggests that the mean recorded friction forces had higher values compared to the real situation. Effectively, higher mean values for the recorded Sin friction force were obtained

compared to those Const. To correct the recorded friction mean value, sinusoidal loads at a frequency of 1 Hz with defined mean and amplitude values were applied on the friction sensor. By comparing the applied mean value with the recorded one, Eq. (3-7) was derived for correcting the friction mean value to obtain the modified value.

$$F_{\mathrm{mod}} = F_{record} - 0.13 * (F_{record\,\max} - F_{record\,\min})$$
$$F_{\mathrm{mod}(mean)} = Average(F_{\mathrm{mod}}) \qquad (3\text{-}7)$$

F represents the friction force. The above equation only corrects the recorded mean value. The mean COF (mean value for sinusoidal COF) was derived by dividing the modified mean friction by the mean applied load (120 N).

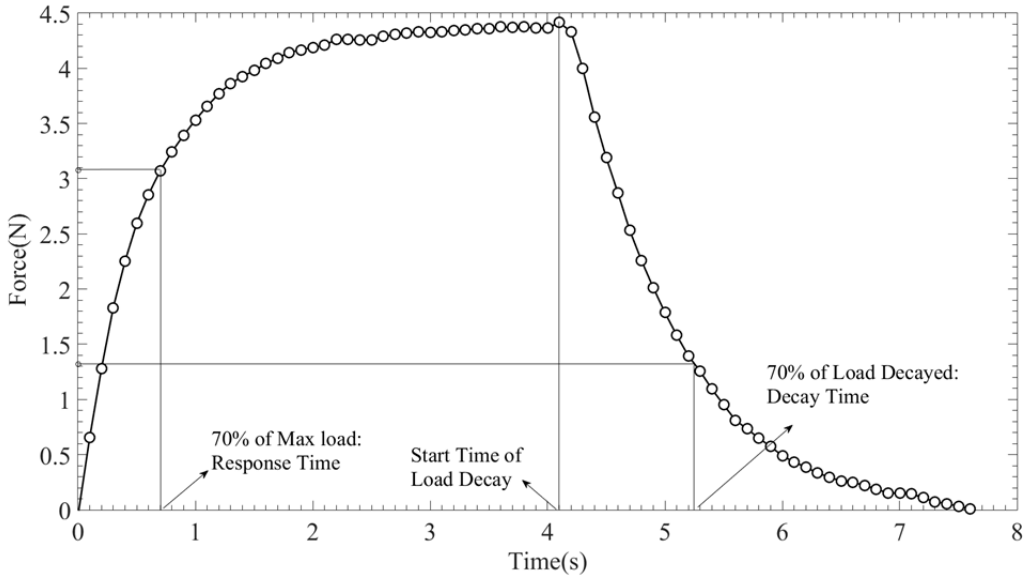

Fig 3.9. Step response and decay time of the friction load sensor

3.5.3. SEM and EDS

Scanning electron microcopy (SEM) images of the pins and the disks before and after the measurements were captured with a JEOL JSM-7001F microscope. No special treatment was performed on the disk surfaces, but the pin surfaces were coated with platinum/palladium (80/20). The pins' surfaces were also analyzed with energy-dispersive X-ray spectroscopy (EDS) to investigate the chemical elemental composition.

3.5.4. Topographical analysis

The topography of the pin and disk surfaces were captured and analyzed by optical interferometry (Zygo NewView 7300) before and after the tribotest.

3.5.5. Crystallinity

Differential scanning calorimetry (DSC) was used to investigate whether or not the tribotesting affected the degree of crystallinity of the UHMWPE pins (tested in different lubricants). The degree of crystallinity was also measured on aged UHMWPE pins (aged in distilled water at 37°C for 2 months)

Chapter 4

DATA ANALYSIS

4.1. Micro-PIV

To investigate the different fluids' flow behaviors, the velocity profiles are derived by applying cross-correlation between two frames of a micro-PIV double-frame image. The plane of view in the micro-PIV images was divided into numerous interrogation areas. The particle displacements between the two frames of a double-frame image in the corresponding interrogation areas divided by the time between pulses was used to obtain the velocity of the particles.

To obtain reliable results for the velocity profile, each interrogation area must contain 6 to 8 particles [83]. The sizes of the interrogation areas used for the data analysis were 16×128 and 32×128 pixels for magnifications of 10 and 20, respectively. These sizes were selected to have at least 6 particles in the frame and to get as close as possible to the wall. For water and distances less than 15 microns from the wall, the velocity had a value as small as 0.47 $mm.s^{-1}$. In that region and for the smallest time interval (200 μs), the Brownian error was 5% (Eqs. (3-3) and (3-4)). This suggests that the Brownian error was larger than 5% for the near-wall velocity. However, since the particles near the wall are influenced by the no-slip boundary condition, these equations are not valid in that distance and correction factors are required. Brenner et al. solved the Navier-Stokes equation for creeping flow and provided a correction factor for normal Brownian diffusion [129]. Goldman et al. also derived a correction factor for tangential Brownian motion [130]. The combination of these two factors suggests that Brownian motions cease at the wall [131].

An analytical solution showed that in Couette flow, the particle motions always have a lag compared to that of the fluid [132]. The particles do not follow the flow close to the wall due to particle-wall hydrodynamic interactions. The velocity lag is below 1% for distances greater than two times the particle diameter. To avoid the high-error region, the analysis plane borders were placed at a distance twice the particle diameter from each sidewall. Therefore,

the first velocity vector is placed at least approximately 20 and 14 microns away from the wall for the 10 and 20 magnifications, respectively.
In micro-PIV measurements, due to the small field of view and high noise to signal ratio, successive velocity profiles must be averaged to obtain stable mean velocity profiles.

4.1.1. Steady-state Poiseuille flow

To increase the statistic of data collected near the wall, the velocity profiles of the SS-PF are the average of 10 middle velocity profiles along the channel width. The distance between every two neighbor profiles is 80 microns. To compare different measurements, the velocity profiles were made non-dimensional by the fluid flow rate (Eq. (4-1)).

$$u_{ND} = \frac{uA_{channel}}{Q} \qquad (4\text{-}1)$$

u and $A_{channel}$ represent the measured velocity and channel cross-section area, respectively.

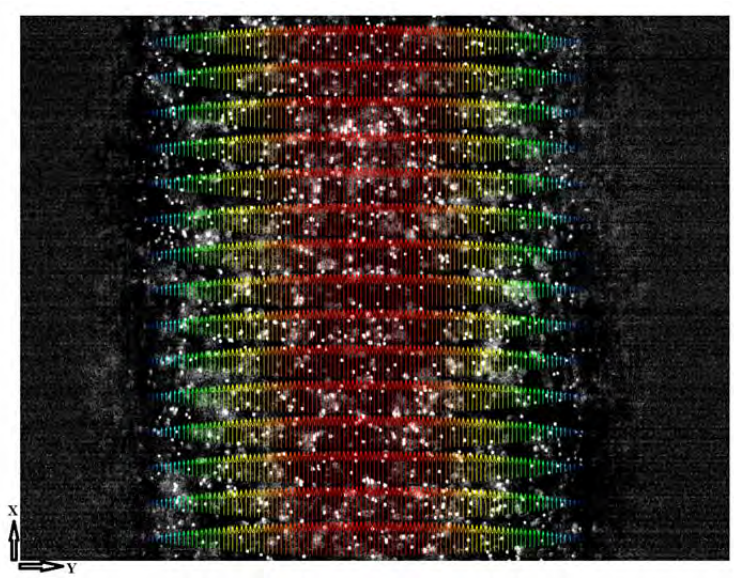

Fig 4.1. Velocity map of Channel 1, CoCrMo bars, Re-2

4.1.2. Unsteady harmonic Poiseuille flow

Micro-PIV used as a two-dimensional measurement technique in this thesis. Therefore, the measurements are performed in a plane (xy plane). The derived velocity maps for UH-PF indicate that the fluid motion was only along the direction perpendicular to the channel width (x-axis in Fig 4.1).
In oscillatory flow, when averaging velocity maps, it is necessary for the maps to have similar phases. Therefore, for UH-PF, the derived velocity maps were phase-resolved and averaged out for each phase. Sinus curves were fitted to the pump velocity and the velocity of each interrogation area along the channel width, providing the phase and amplitude of the fluid velocities.
To compare the different experimental conditions, the velocity profiles were made dimensionless according to Eq.(4-2).

$$u_{ND} = \frac{uA_{channel}}{Amp_{u_{syringe}} A_{syringe}} \tag{4-2}$$

u, $A_{channel}$, $A_{syringe}$ and Amp represent the velocity measured, channel cross-section area, syringe cross-section area and velocity amplitude, respectively.
The definitions of the parameters presented in Eq. (4-2) are provided in Eq. (4-3)

$$\begin{aligned} u_{syringe} &= Amp_{u_{syringe}} \sin(2\pi f + \phi_{syring}) \\ u &= Amp_{fluid} \sin(2\pi f + \phi_{flow}) \\ u_{ND} &= Amp_{ND} \sin(2\pi f + \phi_{flow}) \\ \Delta\phi &= \phi_{syring} - \phi_{flow} \end{aligned} \tag{4-3}$$

f is the frequency in Hz, and ϕ represent the phase of oscillatory motion, respectively.

4.1.3. Unsteady harmonic Couette flow

Sinus curves were fitted to the velocity data obtained from the distance laser.
The derived velocity maps were phase-resolved and averaged at each phase, i.e., angular-resolved. Sinus curves were fitted to the angular-resolved velocities of each interrogation area along the channel width, describing the profile in time for the Const Channel. The amplitude and phase of the fluid velocity were derived from the sinus curves. The phase difference between the moving wall and the fluid was calculated from Eq. (4-4).

$$\begin{aligned} u_{cylinder} &= Amp_{u_{cylinder}} \sin(2\pi f + \phi_{cylinder}) \\ u &= Amp_{fluid} \sin(2\pi f + \phi_{flow}) \\ \Delta\phi &= \phi_{cylinder} - \phi_{flow} \end{aligned} \tag{4-4}$$

u, Amp, f and ϕ represent the measured velocity, calculated amplitude, frequency and phase of the oscillatory motion, respectively. The velocity amplitudes were made dimensionless by dividing by the maximum amplitude to make the results comparable at different frequencies. The obtained phase for the moving wall was ϕ = -90°. Therefore, the cylinder velocity could be written in Cos form (Eq. (4-5)).

$$u_{cylinder} = -Amp_{u_{cylinder}} \cos(2\pi f) \tag{4-5}$$

The variation of the channel width in the Conv Channel made it impossible to follow the same procedure for the data analysis.

Chapter 5

RESULTS AND DISCUSSION

In this section, the most important findings of the current work are presented. This chapter contains three main parts. In the first section, the HA solution rheology is presented. The second section contains micro-PIV results for steady-state and unsteady Poiseuille flow and unsteady Couette flow, and the third section includes the results of the tribotest measurements.

5.1. HA solution rheology

The most frequent equation applied for quantifying polymer behavior in the shear-thinning region is the power law model as Eq. (5-1) [133].

$$\mu = m\gamma^{n-1} \qquad (5\text{-}1)$$

The above equation is a line fitted on the shear-thinning region of the double-logarithmic plot of the viscosity-shear rate. “n-1” is the slope of the line, and “n” is called the power law index. “m” is the consistency index, which is the intercept of the fitted line with a shear rate of 1 s^{-1}. In the SS-PF and UH-PF studies, HA with a molecular weight of 1.4-1.5 MDa was used, while the molecular weight of the HA used in the UH-CF and POD studies was 1.6-1.8 MDa. Fig 5.1 (a and b) shows the variation of the viscosity as a function of the shear rate for the HA solutions used for the UH-PF and UH-CF studies, respectively. Power law indices of the HA solutions with 3 and 5 $mg.ml^{-1}$ concentrations are presented in Table 5.1. The Table includes value of different rheological propertied for HA solutions with 3 and 5 $mg.ml^{-1}$ concentration with two different MW. These values were used to discuss the HA solutions behaviors.

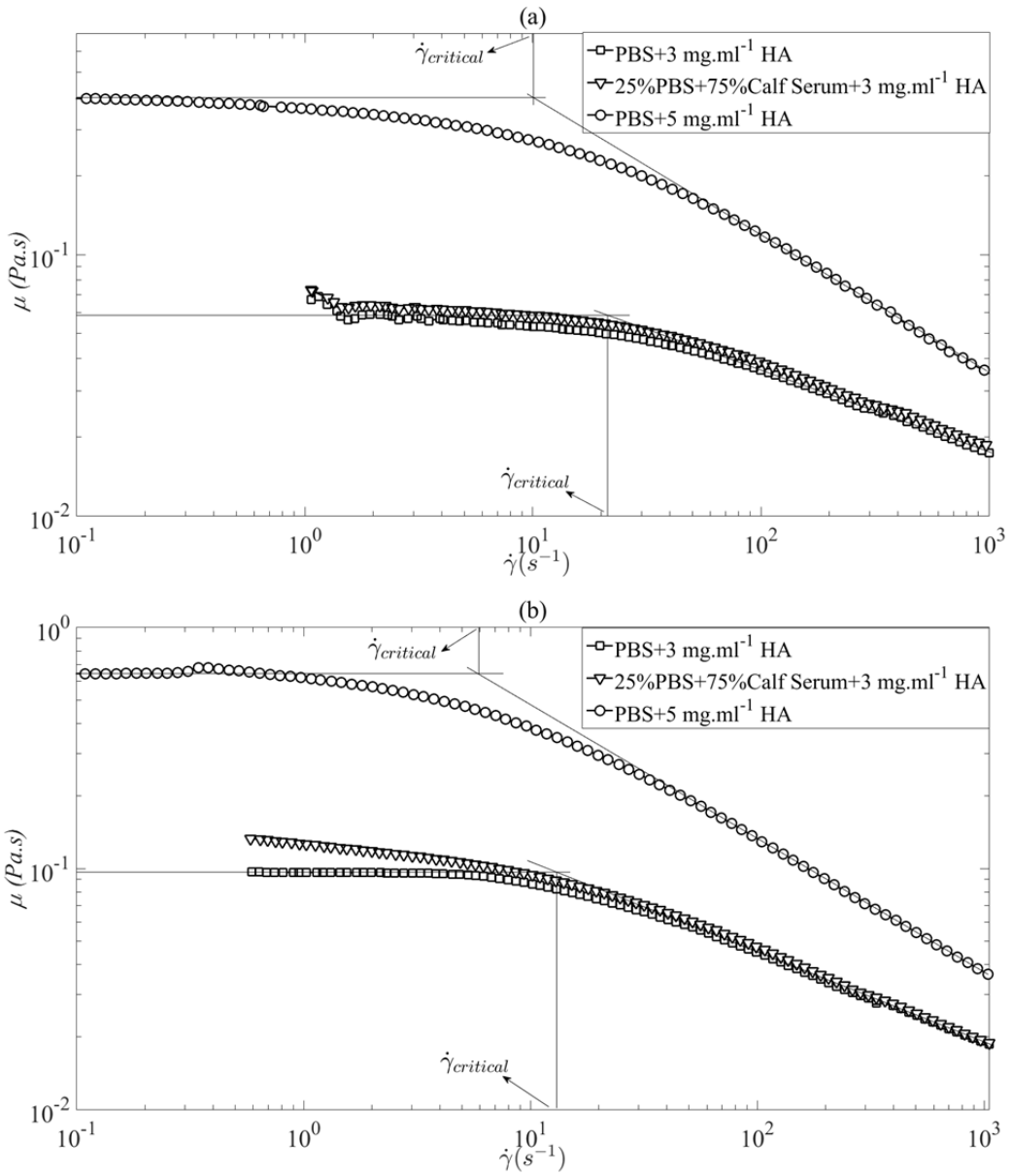

Fig 5.1. Viscosity (μ) function of the shear rate (γ) for the HA solutions with (a) MW of 1.4-1.5 MDa and (b) MW of 1.6-1.8 MDa

Fig 5.1 shows the shear rate at which the shear-thinning behavior starts ($\dot{\gamma}_{critical}$). The intersection of the fitted line on the shear-thinning region with the zero shear viscosity is the transition shear that represents the start of the polymer shear-thinning behavior and is called the critical shear rate [16,134]. Table 5.1 provides the critical shear rates for different HA solutions.

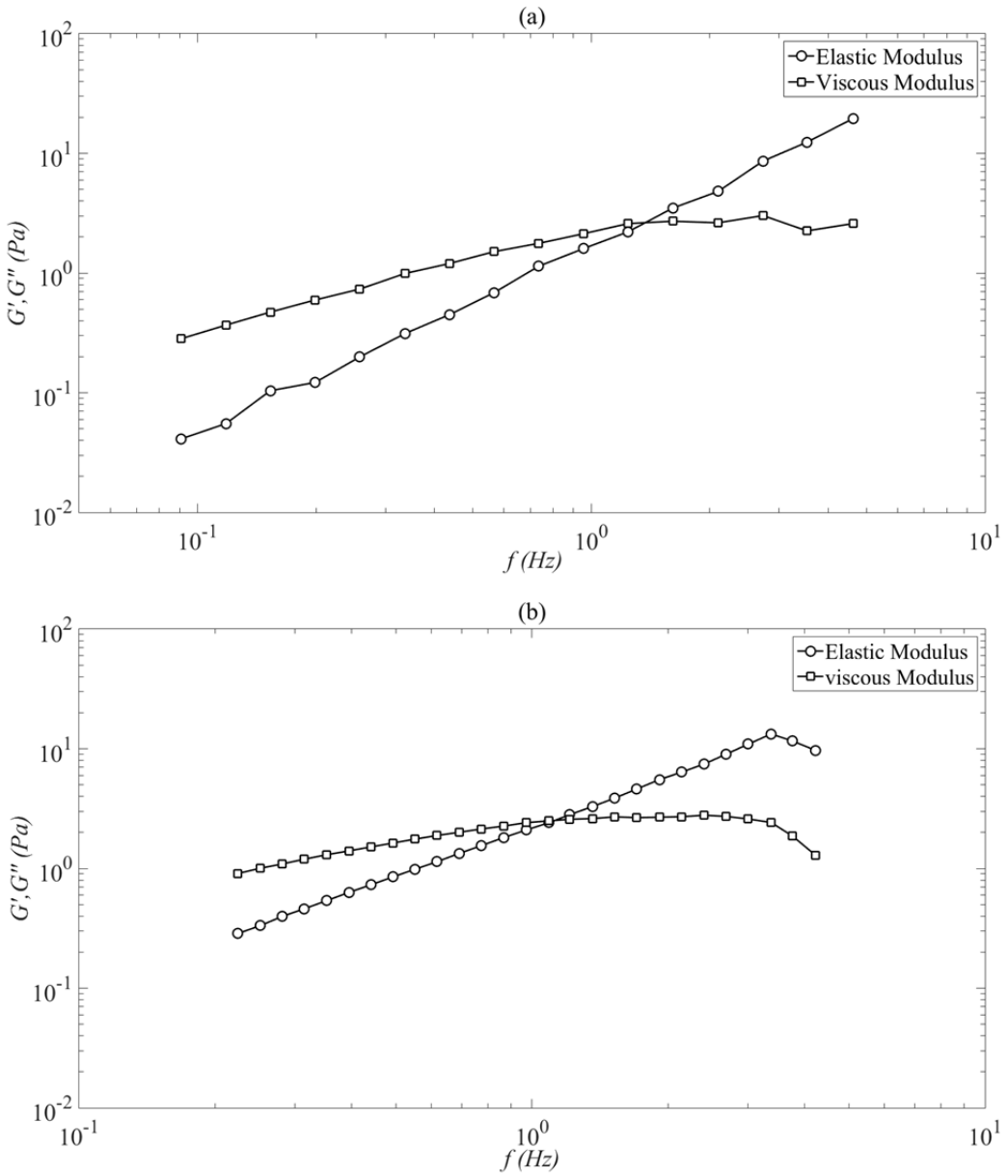

Fig 5.2. Viscous and elastic moduli (G' and G") versus strain frequency (f) for HA with 5 mg.ml^{-1} concentration in PBS with (a) MW of 1.4-1.5 MDa and (b) MW of 1.6-1.8 MDa

Fig 5.2 (a and b) shows the dynamic moduli versus strain frequency for HA solutions with a 5 mg.ml^{-1} concentration. Table 5.1 includes the crossover frequencies for the different high-concentration HA solutions. At frequencies lower than the crossover frequency, the viscous modulus controls the fluid flow behavior, but upon increasing the frequency, the elastic modulus dominates, and so the HA solution shows more elastic behavior than viscous. The dynamic moduli of HA solutions with 3 mg.ml^{-1} were not measurable due to instrument limitations, but previous studies indicated that upon decreasing the HA concentration, the crossover frequency increases [64]. The dynamic moduli were measured in the linear viscoelastic region. Fig 5.3 shows the dynamic moduli variation as a function of strain at frequency of 1.02 Hz. In linear viscoelastic region the dynamic moduli stay constant as the strain increases. The dynamic moduli decrease as the strain increases in non-linear viscoelastic region.

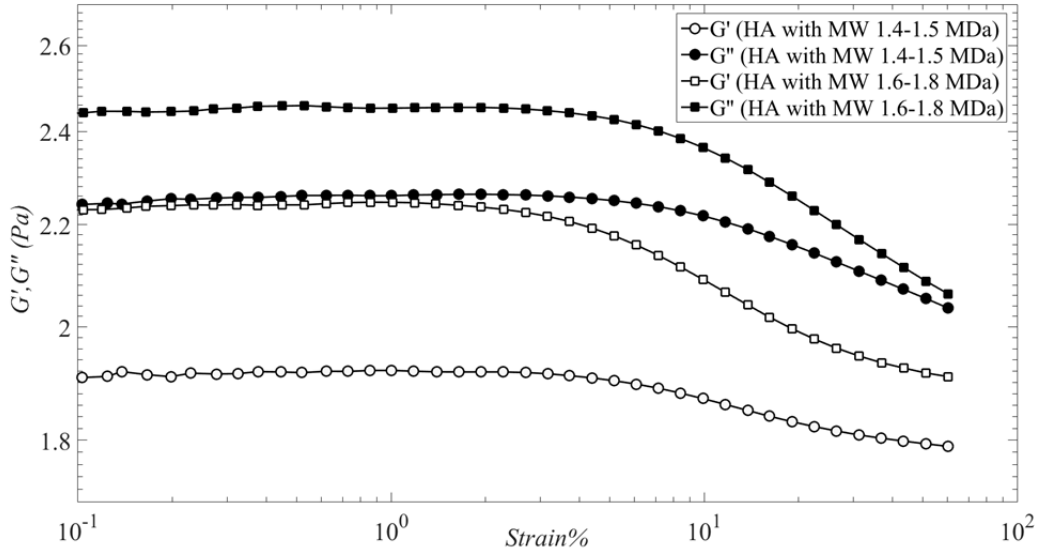

Fig 5.3. Viscous (filled marks) and elastic (hollow marks) moduli versus strain% at frequency of 1.02 Hz for HA with 5 mg.ml^{-1} concentration in PBS for HA solution with MW of 1.4-1.5 MDa (circle) and MW of 1.6-1.8 MDa (square)

Table 5.1. Rheological parameters for HA solutions

Molecular weight	**n (power law index)**		$\dot{\gamma}_{critical}$ **(s^{-1})**		**Crossover Frequency (Hz)**	
	Fluid 2	Fluid 4	Fluid 2	Fluid 4	Fluid 2	Fluid 4
1.4-1.5 MDa	0.685 ± 0.015	0.460 ± 0.013	21.3	10	NA	1.4 ± 0.08
1.6-1.8 MDa	0.618 ± 0.011	0.443 ± 0.012	13	6	NA	1.1 ± 0.05

5.2. Micro-PIV

5.2.1. Steady-state Poiseuille flow

5.2.1.1. HA solution composition effect

Fig 5.4 shows the velocity profiles and shear rates along a non-dimensional channel within Channel 1 using Bar 1 for degassed water and HA solutions with concentrations of 3 and 5 mg.ml^{-1}. The HA solution is a non-Newtonian fluid with a higher viscosity than that of water (Fig 5.1). Therefore, the HA solution velocity profiles have blunter shapes compare to those of water, and the bluntness increases with the HA concentration and Re number. For the Newtonian fluid, all of the non-dimensional velocity profiles are compatible with each other, and the differences are in the range of the pump accuracy (2%). However, by increasing the flow rate for the non-Newtonian fluid, the non-dimensional velocity profile becomes blunter. This is indicative of the spatial variation of the HA solution viscosity. For the Newtonian fluid, the velocity profile has a parabolic shape, and the shear rate along the channel width changes linearly. However, there is a non-linear trend for the non-Newtonian fluid, and upon decreasing the flow rate, the non-Newtonian shear rate profile becomes more linear (Fig 5.4 (b) and (c)).

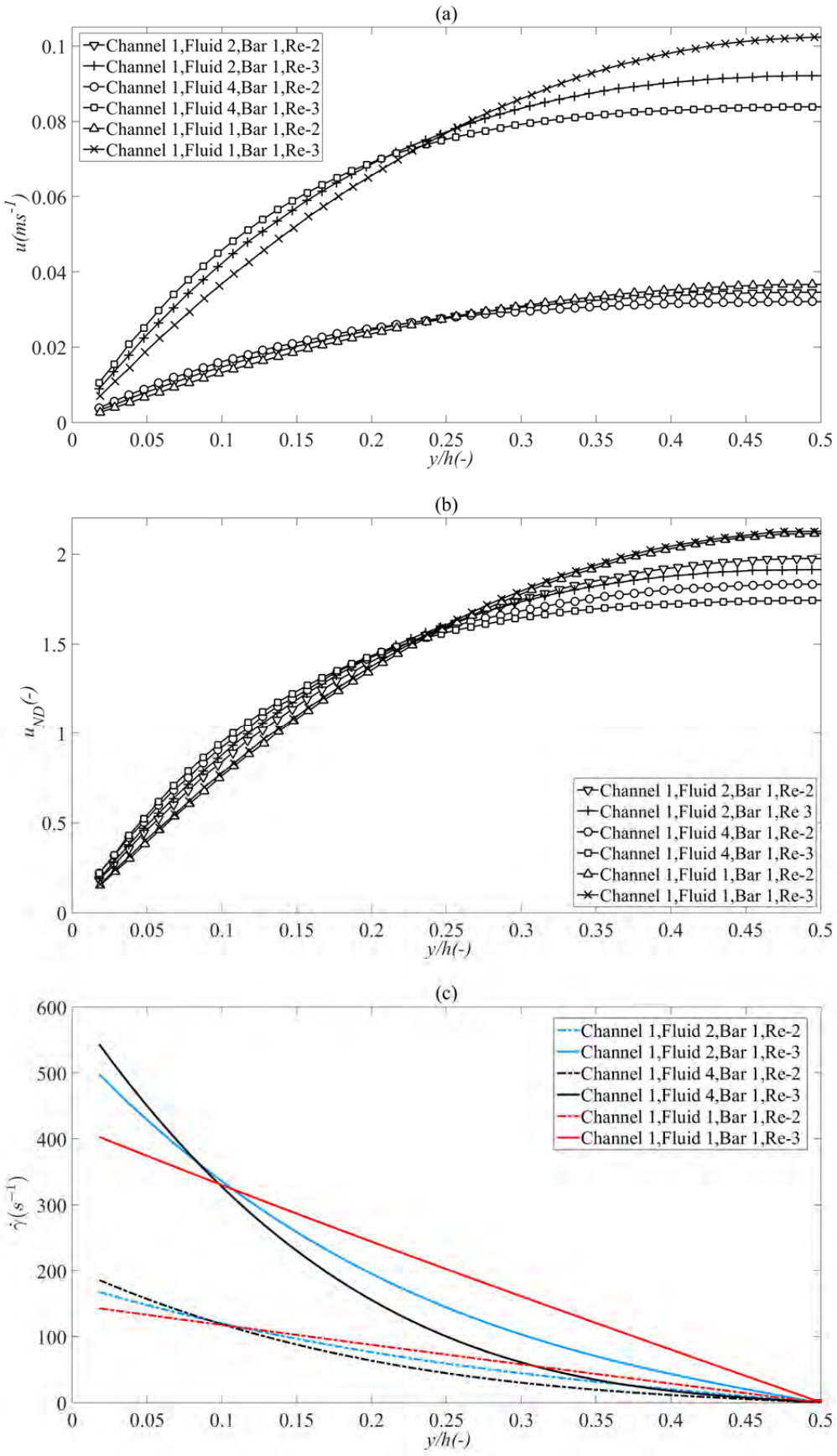

Fig 5.4. (a) Velocity profiles, (b) non-dimensional velocity profiles and (c) shear rate along non-dimensional channel width for degassed water, HA solutions with concentration of 3 and 5 mg.ml^{-1} in PBS

Fig 5.5 shows the non-dimensional velocity profiles along the non-dimensional channel width for the HA solutions with a concentration of 3 mg.ml^{-1} with and without protein content. The duration of each measurement was approximately 45 s. Oates et al. [52] showed that adding protein to the HA solution provides the solution with rheopectic behavior, which is time-dependent. The protein-containing solution exhibits structure-building behavior under small shear rates. The aggregation of the protein around the HA chains contributes to the formation of the structures and rheopexy.
There is good compatibility between the velocity profiles of Fig 5.5, which suggests that under the current unidirectional measurement conditions (shear rate and duration), adding protein did not affect the HA solution behavior.

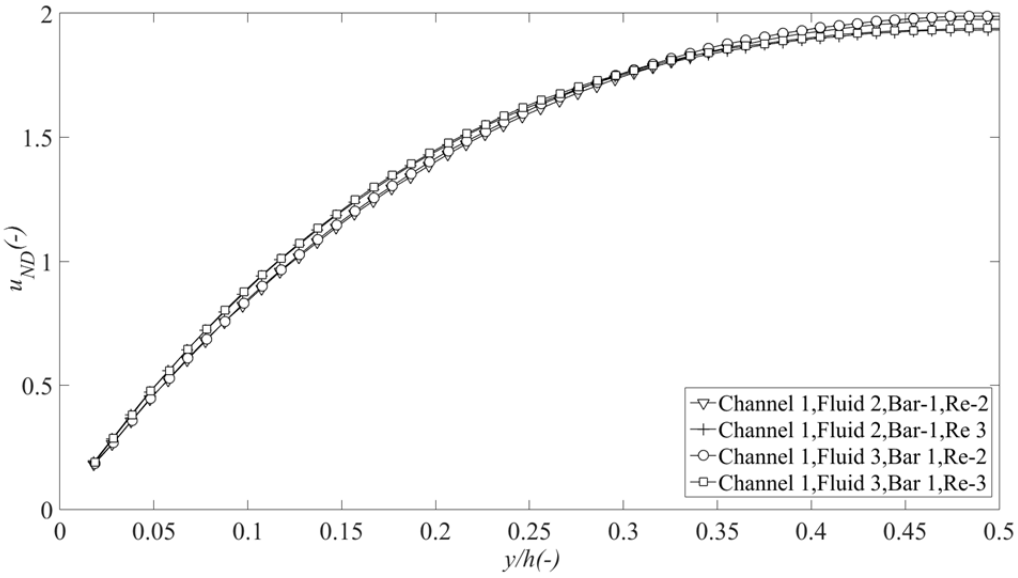

Fig 5.5. Non-dimensional velocity profiles along non-dimensional channel width for HA solutions with concentration of 3 mg.ml^{-1} in PBS and 25% PBS+75% BCS

5.2.1.2. Channel size effect

Fig 5.6 shows the non-dimensional velocity profiles along the non-dimensional channel width for a HA solution with a concentration of 3 mg.ml^{-1} in PBS. The differences between the profiles are very insignificant. Although the Newtonian Re numbers were kept constant for the two channels, the Re numbers of the non-Newtonian fluids in the two channels were different. However, because of the very small Re numbers, the differences in the fluid behavior and velocity profiles are insignificant.

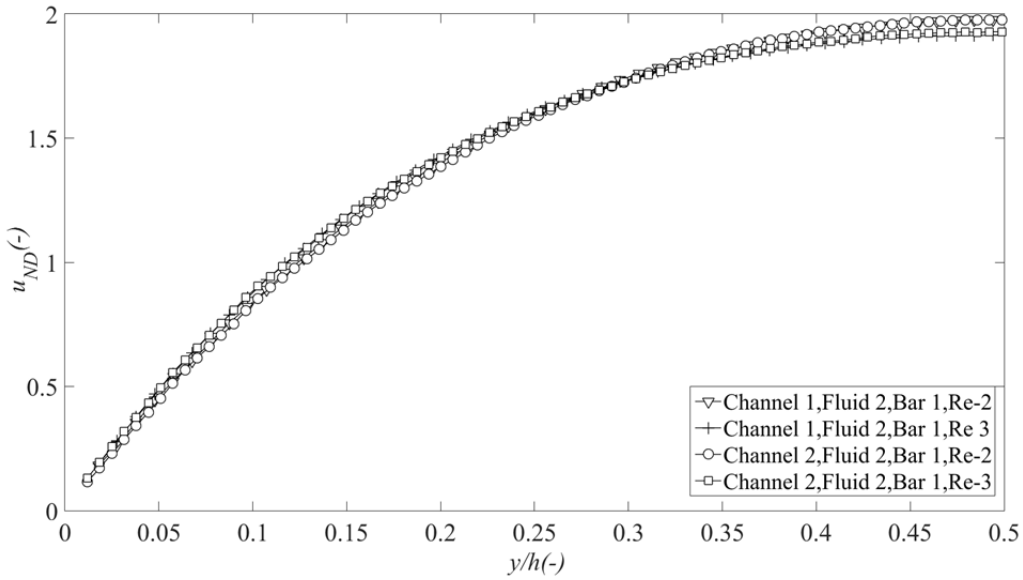

Fig 5.6. Non-dimensional velocity profiles along non-dimensional channel width for HA solutions with concentration of 3 mg.ml^{-1} in PBS for Channel 1 and Channel 2

For a fluid following the power law behavior, Delplace derived Eq. (5-2) as a generalized Re number for flow inside a duct with an arbitrary cross-section [135].

$$\mathrm{Re}_{general} = \frac{\varphi U_{mean}^{2-n} D_h^n}{m\{(24n+\xi)/(24+\xi)n\}^n \xi^{n-1}} \qquad (5\text{-}2)$$

ξ is a geometric parameter that depends only on the cross-sectional shape. For Channel 1 and Channel 2, this parameter has values of 7.774 and 7.238, respectively.
For a Newtonian Re of 64.17 (Re-3), the Re numbers of Fluid 2 calculated from Eq. (5-2) for Channel 1 and Channel 2 were 3.88 and 3.42, respectively. The Fluid 4 flow inside Channel 1 and Channel 2 had Re numbers of 1.68 and 1.26, respectively. The differences between the Re numbers of Fluid 4 (with a higher HA concentration and shear-thinning characteristic) in the two channels are greater than those for Fluid 2.

5.2.2. Unsteady harmonic Poiseuille flow

It was explained in section 1.1.2 that at very high steady shear rates, the HA solution shows Newtonian behavior with a viscosity similar to that of its solvent. Because of the very small gap size in natural joints, the shear rate values are high. It is usually assumed that at high shear rates inside natural joints, SF behaves as a Newtonian fluid. However, the nature of the flow inside the joint is not steady. Therefore, understanding the effect of the unsteadiness on the viscoelastic non-Newtonian fluid flow behavior is required.
The main aim of this section of the work was to investigate the effect of the unsteadiness on the polymer solution behavior in comparison with those under steady flow and Newtonian fluid flow.
To provide reference behavior for a Newtonian fluid, the degassed water behavior under unsteady Poiseuille flow was investigated experimentally and discussed based on the theory explained in section 2.2. The behaviors of HA solutions with different concentrations and

protein contents were studied and compared with those under steady condition and Newtonian fluid.

5.2.2.1. Degassed water behavior

At the lowest frequency and smallest channel cross-section, the velocity profiles have a parabolic shape at each phase and exhibit quasi-steady behavior (similar to the steady flow velocity profiles). However, upon increasing the frequency, the velocity profiles deviate from keeping their parabolic shapes at each phase, and the maximum velocity did not occur in the middle of the channel but close to the walls. This behavior is known as the Richardson annular effect, and it depends on the penetration depth of the viscous waves. Fig 5.7 shows the non-dimensional velocity profiles along the non-dimensional channel width for degassed water and F-2 in Channel 2.

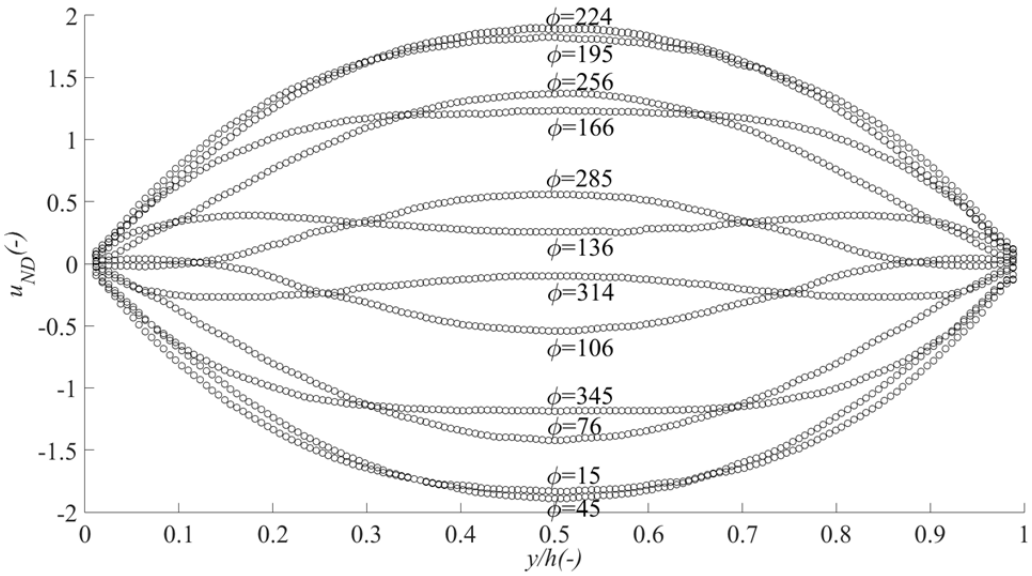

Fig 5.7. Non-dimensional velocity profiles along the non-dimensional channel width for water in Channel 2 at F-2

The depths of penetration of the viscous waves are proportional to $\sqrt{\frac{\nu}{\omega}}$ [116]. The Womersley number (W in Eq. (2-10)) is representative of the viscous wave penetration depth compared to the channel characteristic length. Table 5.2 includes the W values for different fluids and experimental conditions of UH-PF. At high W values, the waves did not cross the whole channel width, and the viscous forces were confined near the channel walls. At the center of the channel, the inertial forces dominated the viscous forces, and the fluid was not affected by the friction. In this situation and based on Eq. (2-9), the pressure gradient distribution ($\frac{\partial p^*}{\partial x^*}$) and unsteady term ($\frac{\partial u^*}{\partial t^*}$) had the same order of magnitude in the middle of the channel. The time derivative of the velocity resulted in the creation of a phase lag between the pressure gradient and the fluid motion [116].

Table 5.2. Womersley number of different experimental conditions.

Fluid 1	***W* (Channel 1)**	***W* (Channel 2)**
F-0	2.02	2.6
F-1	3.37	4.33
F-2	4.76	6.12
Fluid 2	***W* (Channel 1)**	***W* (Channel 2)**
F-0	0.27	0.38
F-1	0.47	0.6
F-2	0.68	0.87
Fluid 3	***W* (Channel 1)**	***W* (Channel 2)**
F-0	0.24	0.34
F-1	0.43	0.54
F-2	0.61	0.79
Fluid 4	***W* (Channel 1)**	***W* (Channel 2)**
F-0	0.09	0.14
F-1	0.17	0.23
F-2	0.25	0.33

Fig 5.8 shows the non-dimensional amplitudes and phase differences of degassed water along the non-dimensional channel width inside Channels 1 and 2 at different frequencies of motion in comparison with the steady state non-dimensional velocity profiles. The phase differences between the velocities at different positions along the channel width and the bulk velocity are shown in Fig 5.8(b) in Channels 1 and 2 at different frequencies. The random variation of the phase differences near the wall is the result of the small velocity magnitude and high standard deviation of the velocity at that region (above 10% of the absolute velocity).

By increasing the *W* value, the non-dimensional unsteady amplitude profiles deviate from the steady-state velocity profile, and the increase in the phase difference along the channel width is enhanced. These are representative of the Richardson annular effect. The annular effect appears on the velocity profiles for *W* above 4.3 for both channels, regardless of the aspect ratio (ratio of channel width to channel depth, which is 0.5 for Channel 1 and 0.75 for Channel 2).

The phase difference depends on the penetration depth of the viscous waves and *W* value. For low *W* values, the increase in the phase difference between the bulk velocity and the fluid velocity across the channel was negligible. By increasing *W*, this phase difference increased (Fig 5.8 (b)).

One of the parameters that affects the velocity amplitude and phase difference values is the aspect ratio of the channel. For experimental conditions with close *W* values, by decreasing

the aspect ratio, the amplitude is reduced and the phase difference is enhanced because of the higher friction forces [120,136].

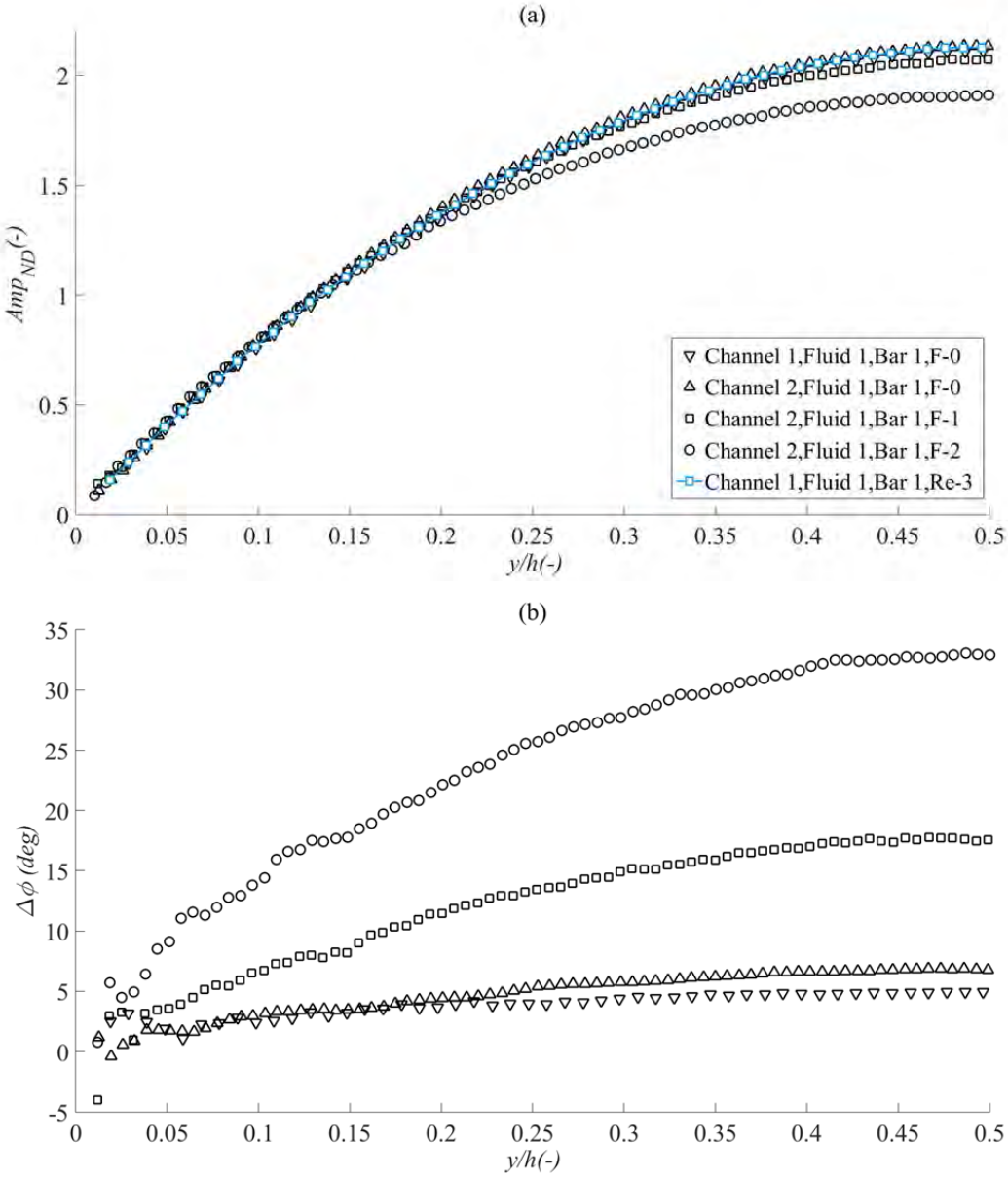

Fig 5.8. (a) Non-dimensional amplitude (Amp_{ND}) and (b) Phase difference ($\Delta\phi$) of water in Channel 1 and Channel 2 at different frequencies in comparison to non-dimensional steady state Poiseuille flow velocity profile in Channel 1

5.2.2.2. HA behavior

Fluid 2, Fluid 3 and Fluid 4 had much higher viscosities in comparison with degassed water (between 20 to 45 times). The very high viscosity value and low *W* suggest that the HA solutions should show a quasi-steady behavior. Fig 5.9 shows the non-dimensional velocity profiles along the non-dimensional channel width for the HA solution with the highest *W* value (Fluid 2 in Channel 2 at F-2). At all phases, the velocity profiles keep their blunt shapes. Because of the small *W* value, under unsteady oscillatory movement, similar behavior to the steady condition was expected. HA solutions contain transient networks of HA entanglements under low shear rates [137]. If the UH-PF of the HA solutions was similar to SS-PF, the

available transient networks should be disentangled and produce a spatial viscosity distribution along the channel width. Therefore, the non-dimensional velocity profiles at each phase (or amplitude profiles) along the channel width should become blunter upon increasing the frequency (or bulk flow rate).

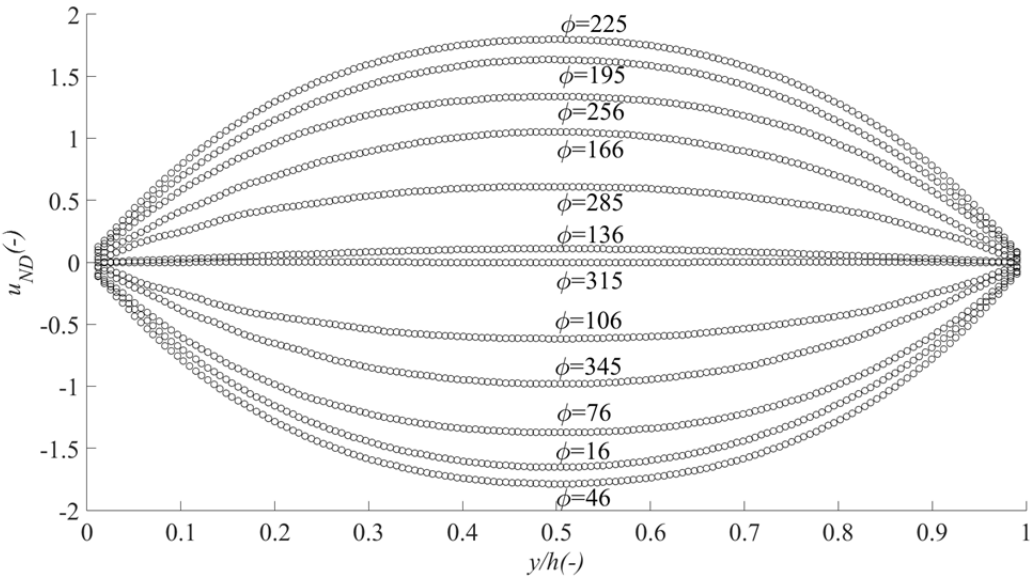

Fig 5.9. Non-dimensional velocity profiles along the non-dimensional channel width for HA solution with 3 mg.ml^{-1} concentration in PBS in Channel 2, F-2

Fig 5.10 shows the behavior of HA solutions with concentrations of 3 and 5 mg.ml^{-1} in PBS. Fig 5.10(a) shows the non-dimensional amplitude variation along the non-dimensional channel width for Channel 1 at different frequencies. Based on the steady behavior of HA solutions, it was expected that upon increasing the frequency or HA concentration, the amplitude profiles would become blunter. However, this trend was not followed under quasi-steady behavior. As explained in section 3.3.1 of the "experimental procedure" chapter, in UH-PF measurements, because of experimental limitations, the maximum flow rate did not belong to the maximum frequency, and the maximum to minimum flow rates corresponded to the frequencies of 1.02, 2.03 and 0.37 Hz, respectively. For Fluid 2 (low HA concentration), the amplitude profile of F-1 is slightly blunter than that of F-0. However, at F-2, the amplitude profile is not blunter than that of F-0. Fluid 4 at F-0 has a slightly blunter amplitude profile compared to Fluid 2 at F-0. However, for Fluid 4 (high HA concentration), the amplitude profiles do not get blunter upon increasing the frequency.

This behavior could be explained based on the relaxation time of the polymer contents. Physically, the "relaxation time" is the required time for the stress in polymers to reach e^{-1} of its initial value [138]. The relaxation time (λ) is actually the required time to damp the stress deformation and reach the default configuration or form new networks or entanglements between polymer chains [134]. The longest relaxation time for polymers is on the order of the inverse of the critical shear rate. The relaxation times of Fluid 2 and Fluid 4 were 0.047 s and 0.1 s, respectively (Fig 5.1(a)). To assess the rheological behavior of the polymeric solutions according to the stress relaxation time, the non-dimensional "Deborah number" (De) was evaluated (Eq. (1-2)) [139,140].

A small De number means that the fluid behaves mainly as a viscous material. A De number of approximately 1 indicates that the fluid does not have enough time to be released from all of its previously applied deformations and has viscoelastic behavior. In this situation, the previous polymer chain state influences the present behavior. A high De number represents

more elastic or solid behavior [70]. To evaluate the De number value (Eq. (1-2)), half of each cycle period was considered as the characteristic time for the flow. In the middle of each cycle, the flow direction changed, and thus so did the direction of the stress applied to the fluid. The polymers needed some time to be released from their previously applied stresses to revert to their default configuration. Then, they disentangled and took their new orientation. Based on the Cox-Merz rule, the data from steady shear measurements in Hz is used for the relaxation time estimation, while for the calculation of characteristic time, half of the frequency in rad.s^{-1} was considered (ω/2) [141].

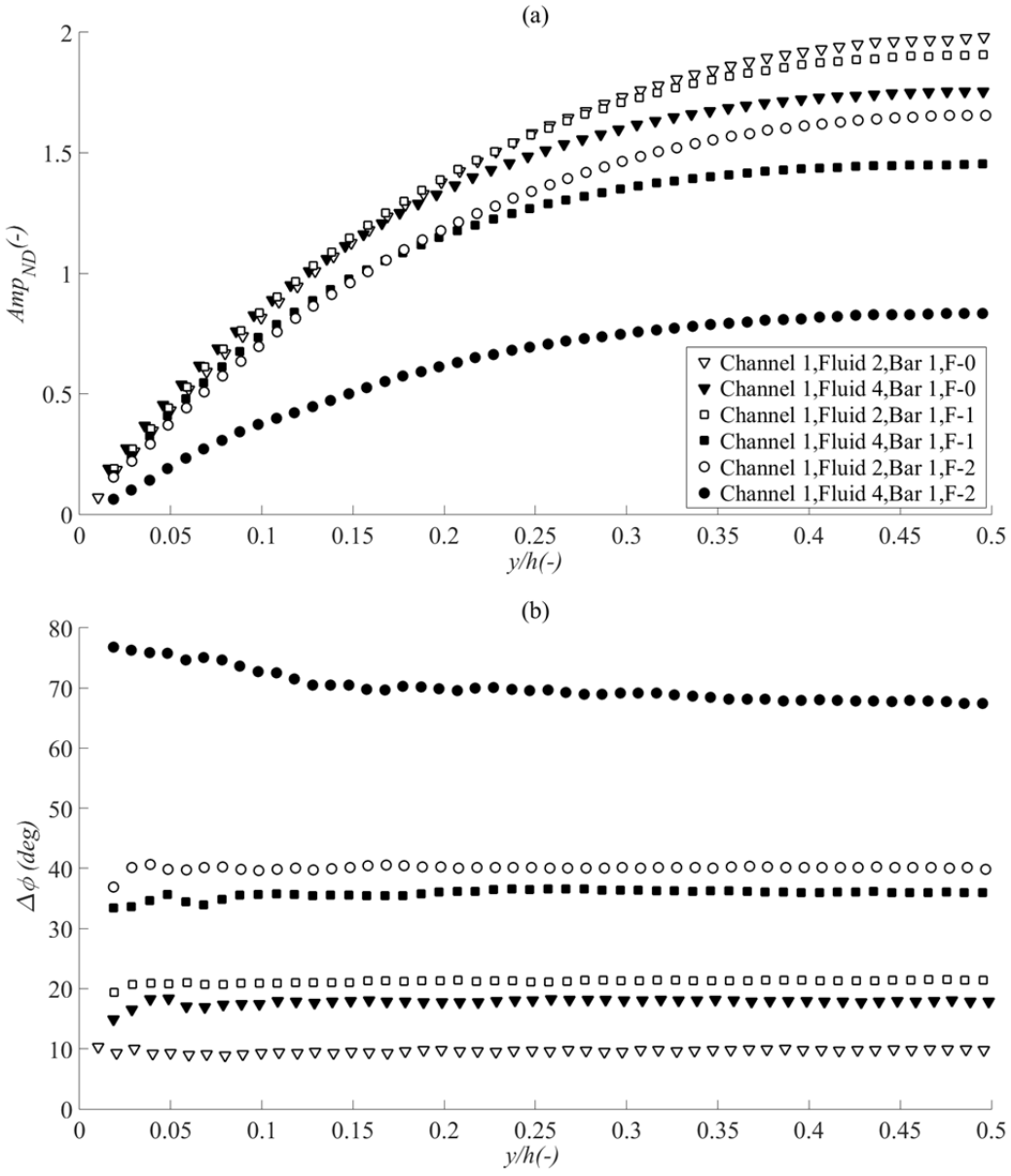

Fig 5.10. (a) Non-dimensional amplitude (Amp_{ND}) and (b) Phase difference ($\Delta\phi$) of 3 mg.ml^{-1} HA in PBS (empty marker) and 5 mg.ml^{-1} HA in PBS (full marker) for F-0 (triangle), F-1 (square) and F-2 (circle)

Table 5.3 shows the De number values for Fluids 2 and 4. Upon increasing the De number, the deviation of the HA solution velocity profiles from the expected blunt profiles increases. At low strain frequencies, the fluid had enough time to damp the stresses applied from the

opposite direction. Upon increasing the frequency, there were still deformations from the stresses applied in the opposite direction remaining in the polymer network, which prevented the fluid from reaching the highest possible amplitude and provided the fluid with partially elastic behavior. The amplitude dropped significantly compared to the other cases for Fluid 4 at F-2. The viscoelastic behavior of the HA solution was explained in section 1.1.2. The crossover frequency at which the HA behavior changes from a viscous material to an elastic one is representative of the disentanglement rate or HA chain mobility. F-2 (frequency of 2.03 Hz) is higher than the crossover frequency of Fluid 4 (1.4 Hz). Therefore, at this frequency, the polymer solution behaved as an elastic material, absorbing the applied stresses and reducing the mobility and velocity of the flow.

Table 5.3. De number values for Fluid 2 and 4

Fluid	**Frequency**	**De**
Fluid 2	F-0	0.21
	F-1	0.6
	F-2	1.2
Fluid 4	F-0	0.46
	F-1	1.28
	F-2	2.56

Fig 5.10 (b) shows the phase differences between the syringe velocities and fluid velocities along the channel width for Fluids 2 and 4. It is observed that the phase difference increases upon increasing the frequency and HA concentration in the solution. The disentanglement process is a time-dependent process, and more disentanglement takes a longer time. Therefore, in channels with higher shear rates, the disentanglement density and phase difference increased. The quantity of this phase difference could also be estimated from the relaxation time and the frequency of the motion. At each frequency, the phase difference value was between one to two relaxation times.

The phase difference had a constant value along the channel width for the HA solutions except for Fluid 4 at F-2, which showed an increasing phase difference trend close to the channel walls. Since the frequency of the motion was higher than the crossover frequency, the disentanglement degree was low for this measurement condition. By getting closer to the channel wall, because of the high value of the wall shear rate, the disentanglement degree and phase difference increased.

Fig 5.11 shows the non-dimensional amplitude profiles of HA solutions with a concentration of 3 $mg.ml^{-1}$ in PBS and 75% PBS + 25% BCS. Almost the same behavior is observed for the two HA solutions at F-0 and F-2. The difference in the profiles at F-1 could be due to the non-linear viscoelastic behavior of the solutions (Fig 5.3). The shear strains at different frequencies are calculated from Eq. (5-3).

$$\dot{\gamma} = \omega\gamma \qquad (5\text{-}3)$$

γ, $\dot{\gamma}$ and ω are the shear strain, shear rate and strain frequency in rad.s^{-1}, respectively. The strain amplitudes for Fluid 3 at F-0, F-1 and F-2 were 65.4, 53 and 23, respectively. A high value for the maximum strain suggests that the measurements lay in the non-linear viscoelastic behavior region of the solutions. The measurements at F-1 compared to those at the other frequencies had both the highest strain amplitude and high value of the strain rate at the same time. This could explain the different behavior of the solution at this frequency.

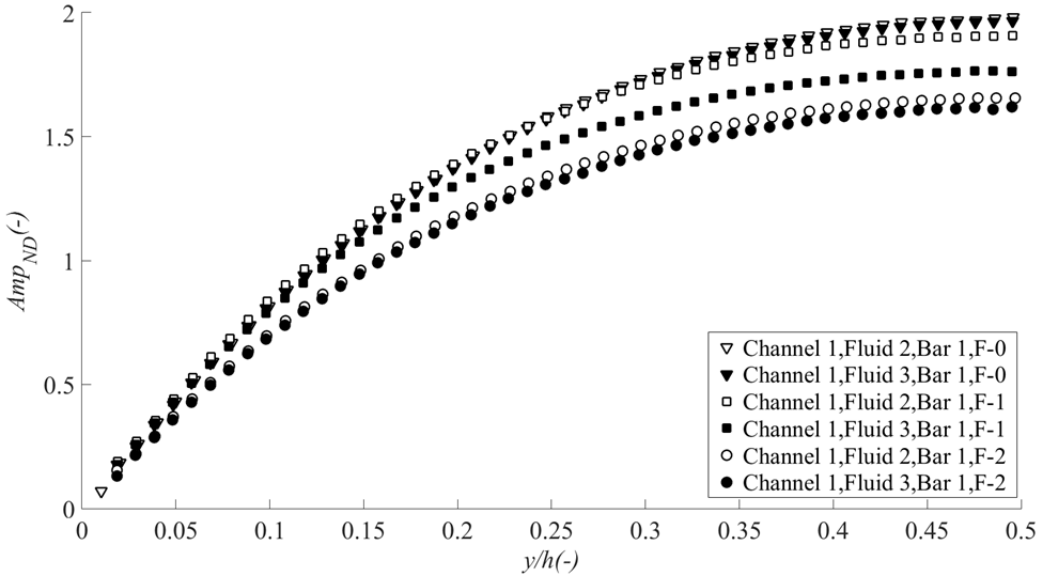

Fig 5.11. Non-dimensional amplitude (Amp_{ND}) of 3 mg.ml^{-1} HA in PBS (empty marker) and 3 mg.ml^{-1} HA in 75% PBS+25% calf serum (full marker) for F-0 (triangle), F-1 (square) and F-2 (circle)

Non-Brownian particles suspended in a non-Newtonian viscoelastic fluid show special migration and string formation behaviors that were explained in section 1.4.2. No special behavior was detected for Fluids 2 or 3 or Fluid 4 at F-0 during the measurements of UH-PF. However, the particles formed alignments in Fluid 4 at frequencies of 1.02 and 2.04 Hz. Fig 5.12 shows the particle distribution at the start and end of the measurements. Fig 5.12 (a) shows that the particles were randomly distributed at the start of each measurement, and Fig 5.12 (b) shows the small number of string structures that were formed at the end of the measurements at F-2. Few strings were visible in all of the phases. Fig 5.12 (c) and (d) show the string-structures formed at the end of the measurement at F-1 for the maximum velocity and 60 degrees after the maximum velocity during each cycle, respectively. The mechanism of the particle string formation was explained in section 1.4.2, and it was noted that the formation of the string-structures depends on the shear-thinning degree of the fluid. The current results are in agreement with the idea that shear-thinning plays the critical role in the formation of the particle strings. The amplitude of the shear rate depends on the flow rate amplitude. Therefore, the maximum to minimum shear rate and shear-thinning degree corresponded to F-1, F-2 and F-0. At F-0, with the smallest degrees of shear rate and shear-thinning, no string structures were visible, and at F-2, the density of string-structures and their length were small. The formation of long particle strings occurred at F-1, with the highest

shear rate amplitude and shear-thinning degree. Comparing Fig 5.12 (c) and (d) showed that the strings were distributed along the whole channel width at the maximum velocity phases (corresponding to the maximum shear rate), and at 60 degrees after, the particle alignments were only visible near the walls, which were the high shear rate regions. This suggests that the shear rate and shear-thinning differences between the phases were the reason that the particle alignment density was different at various phases. Previous studies showed that the formation of the string-structures is time-consuming, and after some minutes a dynamic equilibrium is obtained under reciprocating motion [72,82].

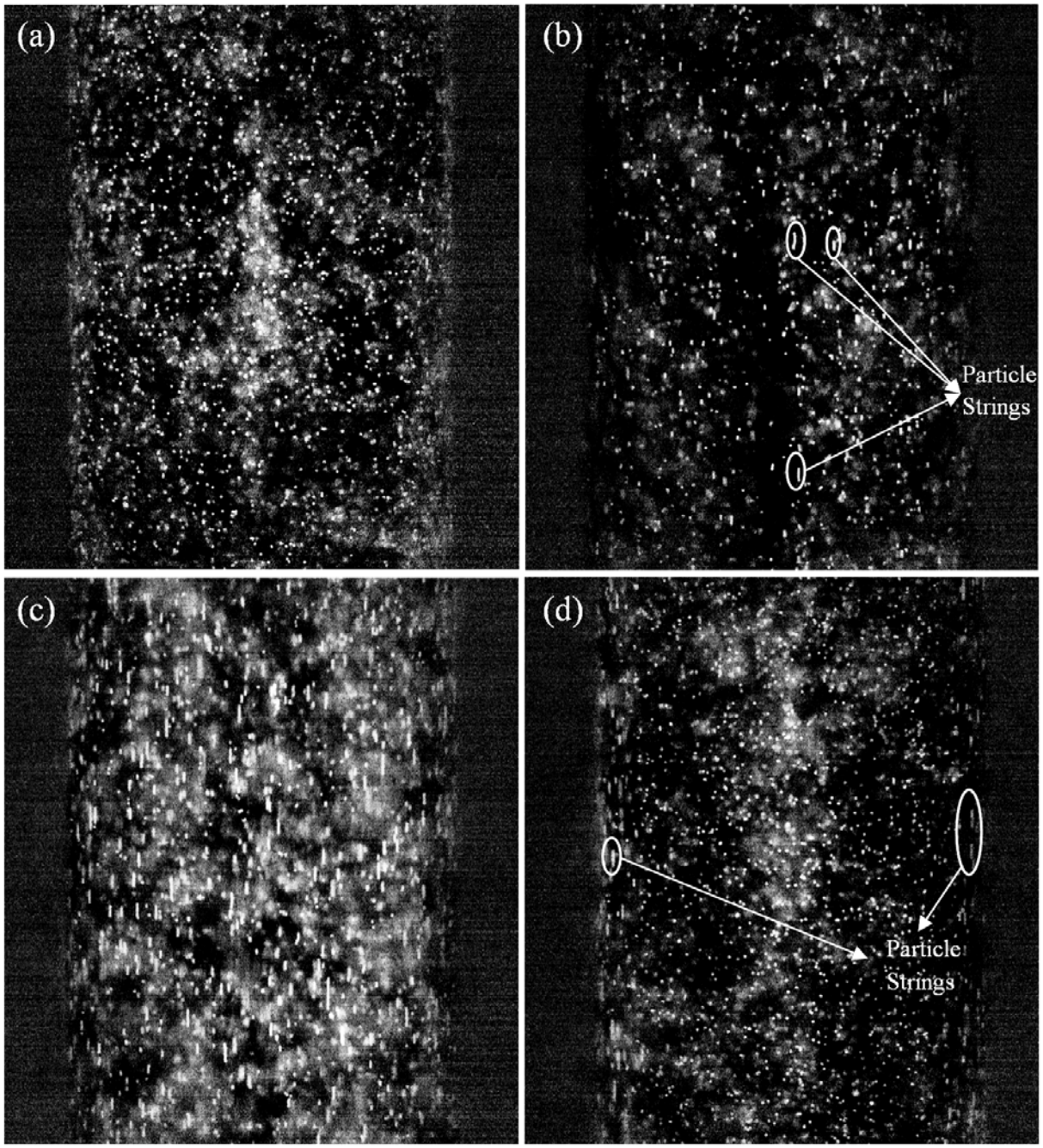

Fig 5.12. (a) Fluid 4 particle distributions in Channel 1 at the start of measurement, (b) string-structure formed at the end of measurement at F-2, (c) string-structure formed at the end of measurement at F-1 at the phase of maximum fluid velocity and (d) at 60 degrees after maximum velocity

No particle migration was observed for the UH-PF measurements. The shear rate amplitude and shear-thinning degree had rather high values. Therefore, the lack of particle migration could be due to a balance between the shear-thinning and elastic forces. The elastic forces drive particles to the lower shear rate region (channel center for Poiseuille flow), while shear-thinning works in the opposite direction and moves the particles toward regions with higher shear rates (channel wall) [75,78]. Moreover, it should be noted that these measurements were performed in non-linear viscoelastic region of the solutions which could also have certain effects on the particle-fluid interactions.

5.2.3. Unsteady harmonic Couette flow

During the SS-PF and UH-PF measurements, the simplest geometry and flow were chosen to focus on investigating the unsteadiness effect on the viscoelastic non-Newtonian flow behavior. For the UH-CF studies, a similar geometry and flow to the hip implant were chosen. At the first step, the distilled water behavior was investigated and compared with the theory to obtain a Newtonian reference flow behavior and to evaluate the performance of the experimental setup. The behaviors of HA solutions with different concentrations and protein contents were then investigated inside constant and variable cross-section channels.

5.2.3.1. Distilled water behavior

Fig 5.13 shows the velocity profiles along the Const channel width for different phases at F-2 and F-0. The viscous waves generated at the moving wall penetrate into the fluid with a velocity perpendicular to the wall and a penetration depth calculated from Eq. (5-4).

$$\delta = \sqrt{\frac{2\nu}{\omega}} \qquad (5\text{-}4)$$

δ, ν and ω represent the penetration depth or Stokes boundary layer thickness, kinematic viscosity and frequency of oscillation, respectively. For frequencies of 2.03, 1.02 and 0.37 Hz, the Stokes length is 0.4, 0.56 and 0.93 mm, respectively. At F-2, the Stokes length was smaller than the channel width, and the generated viscous waves at the moving wall only controlled the fluid in that region. By moving away from the inner cylinder, the phase difference increased. At some phases (e.g. $\phi = 303°$), the flow direction varied between the middle of the channel and the moving wall, which occurred due to the small Stokes length at F-2 compared to the channel width. However, the experimental conditions enhanced this phenomenon. (Fig 5.13(a)).

At F-0, the Stokes length is comparable to the channel size. Therefore, the viscous waves generated at the moving wall could control the flow over the whole channel width. However, the velocity profiles from Fig 5.13(b) show that at each phase, the absolute values of the experimental velocity profiles along the channel width have lower values compared to the theoretical velocity profiles.

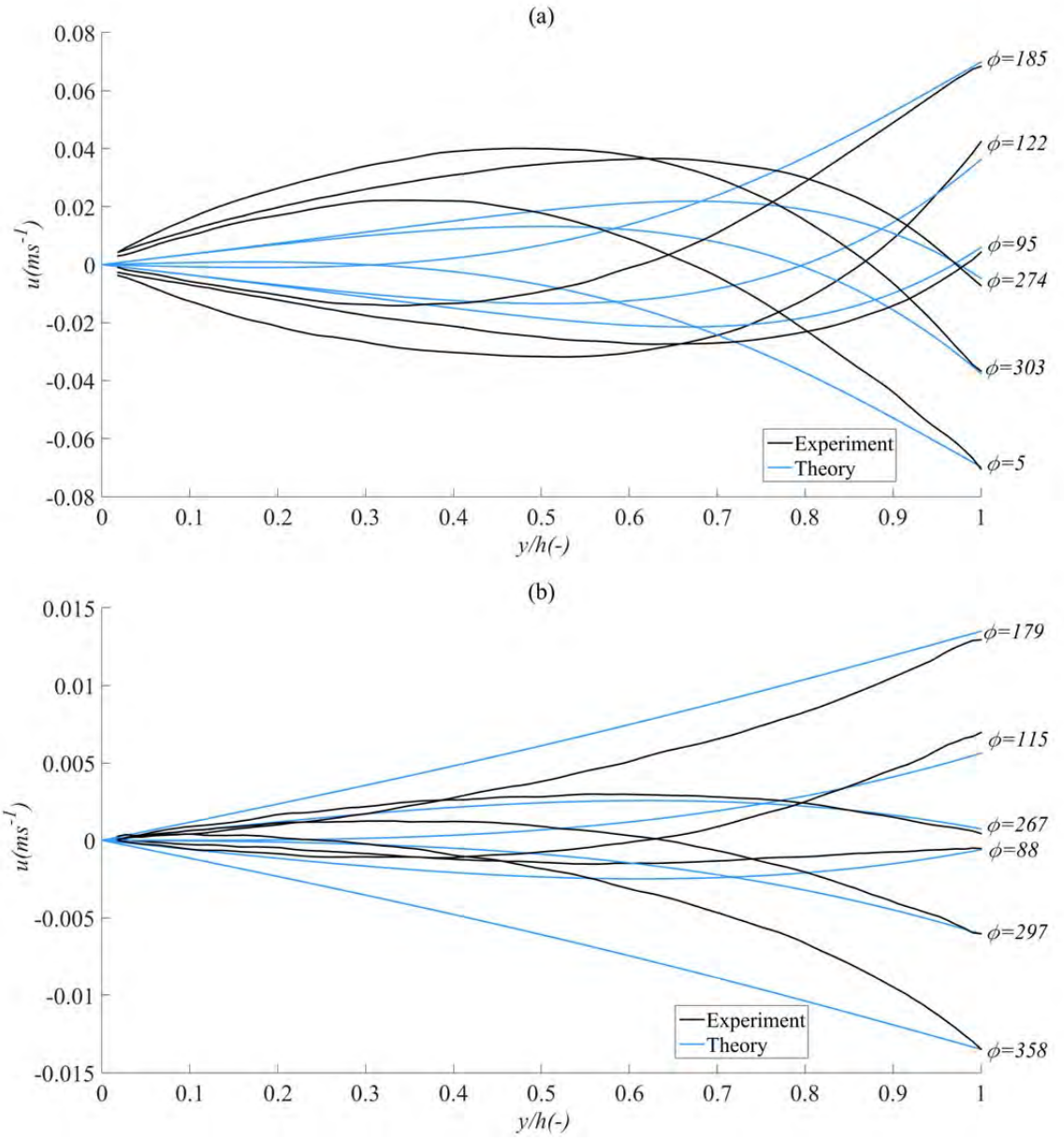

Fig 5.13. Experimental (black lines) and theoretical (blue lines) velocity profiles along Const Channel width for distilled water at frequency of (a) 2.04 Hz and (b) 0.37 Hz

Fig 5.14 shows the amplitude and phase difference profiles along the non-dimensional channel width from the experimental results and theoretical analysis for distilled water at different frequencies. The experimental and theoretical results are not in agreement. The theoretical solution belongs to the induced flow between two infinite parallel plates condition (Eq. (2-17)), while the experiments were performed inside a closed channel. To investigate the effect of the curvature and confining walls, a CFD model was developed in Ansys CFX. The model included only the curved channel, i.e., the fluid tank visible in Figure 2 was not included in the numerical domain. A hexahedral mesh consisting of more than 200 000 elements was used to discretize the space with a time step of 0.02 s. The amplitude profile along the channel width at F-2 from the numerical model is presented in Fig 5.14(a). The agreement between the theoretical and numerical results suggests that the difference between

the experimental and theoretical results does not originate from the sidewalls or the curvature effects.

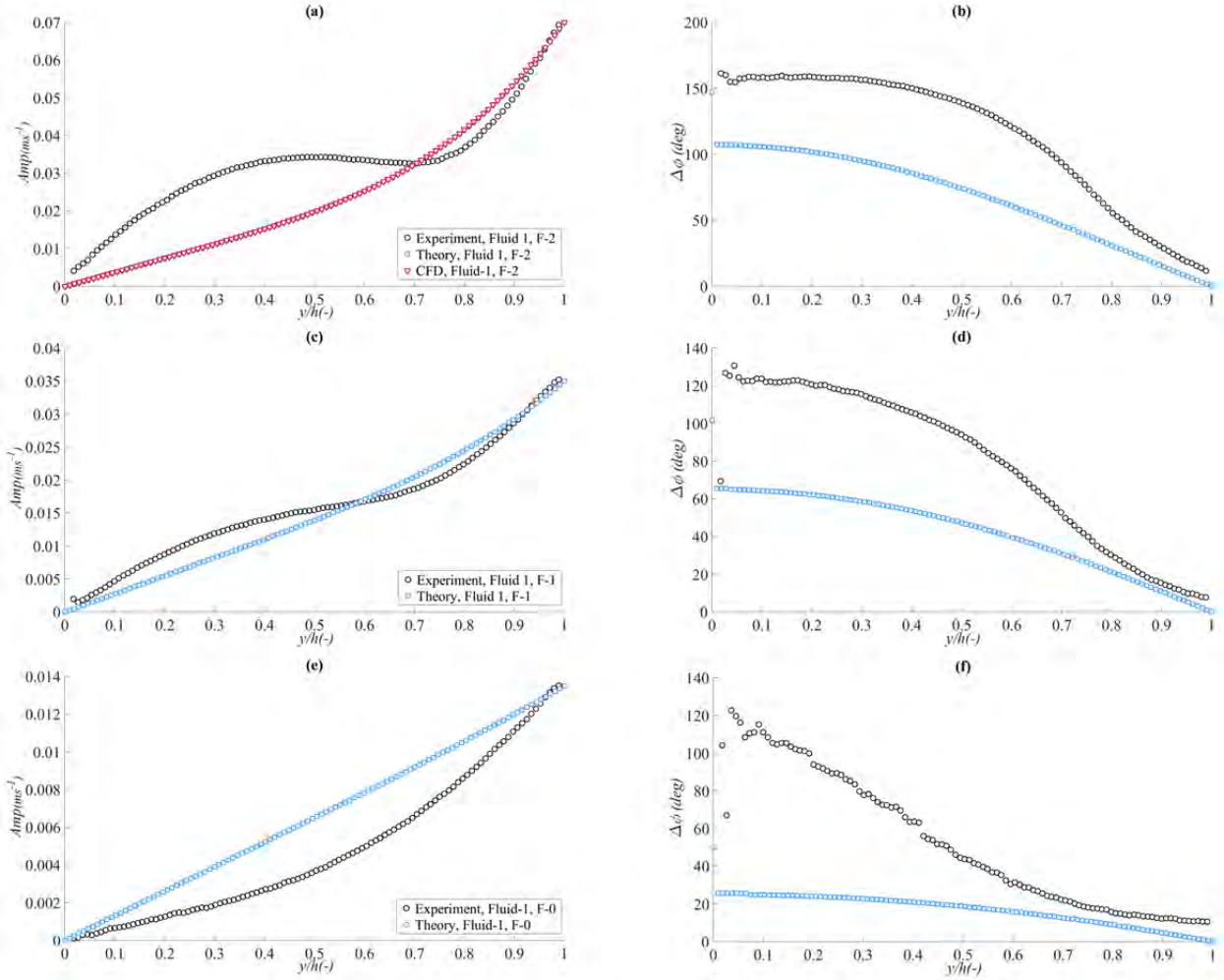

Fig 5.14. Amplitude (Amp) and Phase difference ($\Delta\phi$) of distilled water in Const Channel of experiment (black circle) and theory (blue square) and CFD (red triangle) for (a) and (b) F-2, (c) and (d) F-1, (e) and (f) F-0

Because the flow inside the fluid tank were not of interest for this study, no micro-PIV data was collected in that region, and so there are no velocity maps for the inside of the fluid tank. However, it is speculated that the difference between the experimental and theoretical results is due to the creation of a reverse flow as the inner disk moves back and forth in the fluid tank. Fig 5.15 shows a schematic of the experimental model and the fluid rotations inside the model. The rotation of the inner disk created fluid rotation inside the fluid tank. It was expected that the fluid moved based on the rotation direction shown in Fig 5.15 with black arrow number 1. However, the fluid might also move and rotate as the red arrows that are marked with number 2. Therefore, a reverse flow was generated inside the channel, which was actually a pressure-driven flow.

At F-2, the Stokes boundary layer thickness was smaller compared to the channel width. Therefore, the viscous waves generated at the moving wall controlled the fluid near the moving wall, while the pressure-driven reverse flow controlled the fluid behavior near the fixed outer wall. This explains the different behaviors in the experimental and theoretical results and the enhanced variation of the velocity between the region near the moving wall and the middle of the channel (Fig 5.13 (a)). At F-0, the Stokes length was comparable to the

channel width. Therefore, the viscous waves generated at both the moving and fixed walls could control the fluid behavior across the whole channel width. The final flow was the superposition of the two flows. The reverse flow reduced the absolute value of the velocities that were induced by the moving surface along the channel width. This reduction is visible in Fig 5.13 (b) and Fig 5.14 (e).

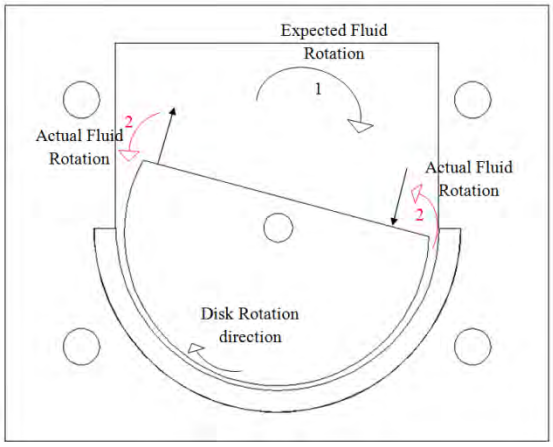

Fig 5.15. Fluid Motion inside the experimental model

5.2.3.2. HA behavior

As explained in section 5.2.2.2, because of the high viscosity of the HA solutions, the viscous wave penetration depth covers the whole channel width for the HA solutions, and the viscosity controls the behavior of the flow. It was expected that the time-dependent nature of the HA behavior and the frequency of the motion affect the HA solutions (the same as in section 5.2.2.2). Fig 5.16 shows the non-dimensional velocity profiles' amplitudes along the non-dimensional channel width for different HA solutions at different frequencies along the Const Channel. Similar behavior with a less than 1% difference is visible for the different experimental conditions, except for Fluid 4 at frequency of 2.03 Hz, with a 4% difference. The amplitudes of Fluid 3 were similar to those of Fluid 2.

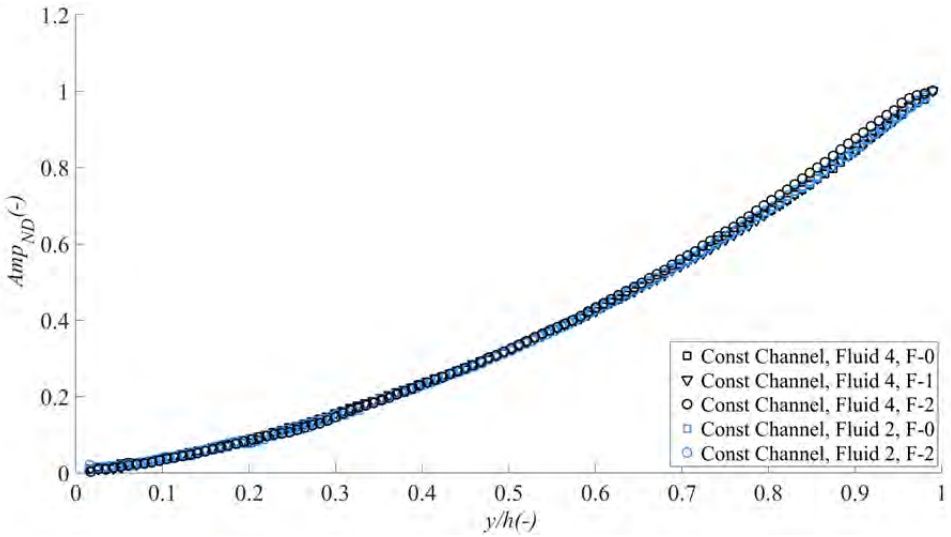

Fig 5.16. Non-dimensional amplitude (Amp_{ND}) in Const Channel width for HA solution with 3 mg.ml^{-1} concentration at F-2 (blue circle), and F-0 (blue square), HA solution with 5 mg.ml^{-1} concentration at F-0 (black square), F-1 (downward black triangle), F-2 (black circle); Moving wall is at 1

Because of the high De numbers (Table 5.4), it was expected that the frequency affected the HA solution flow behavior. However, in contrast to the HA solution behavior under UH-PF, the velocity profiles were not affected by the frequency of motion or the HA concentration.
Such disagreement is related to the difference between strain amplitudes. The strain amplitude under the UH-CF was 8, which is much smaller than the 23-60 of the UH-PF. Based on Eq (1-3), the Wi number is directly proportional to the strain value. Therefore, the UH-CF measurements had significantly smaller Wi numbers compared to the UH-PF measurements. The concentration at which entanglement formation starts for the HA solution with a molecular weight of 1.5 MDa in PBS was reported to be 2.4 $mg.ml^{-1}$ [65]. Therefore, all of the polymeric solutions in the current work were entangled. As explained earlier in section 1.4.1, smaller strain and Wi numbers are representative of a small disentanglement density and as a result less velocity variation as a function of the frequency. Moreover, in Poiseuille flow, the distribution of the strain along the channel width resulted in a spatial distribution of the viscosity in the channel and different non-dimensional velocity profiles. Such a variation for the current study of the UH-CF was much smaller compared to that of the UH-PF. The strain amplitude at the fixed and moving walls had values of 1.5 and 8, respectively, for UH-CF. Therefore, there was no considerable strain distribution that would cause a considerable velocity deviation between the different measurement conditions.

Table 5.4. Weissenberg and Deborah number values for Fluid 2 and 4

Fluid	Frequency	Wi	De
Fluid 2	F-0	0.23	0.35
	F-1	0.63	0.99
	F-2	1.25	1.97
Fluid 4	F-0	0.49	0.77
	F-1	1.36	2.16
	F-2	2.72	4.30

For Fluid 4 at F-2, the particles migrated to the outer wall gradually. At the same time, some of the particles formed string structures. Fig 5.17 shows the depleted region near the moving wall at the end of the measurements and the trajectory of the particles away from the moving wall. Fig 5.17 (b) was derived by extracting the maximum pixel values for a series of images (image accumulation). The migrated particles formed a depleted layer in the vicinity of the moving wall. This layer formed gradually and resulted in a gradual decrease in the velocity values. The velocity profiles were derived based on an averaging of several velocity maps to obtain reliable velocity fields at each phase. The variation of the velocity because of the particle-depleted region near the moving wall is the reason for the different behavior of Fluid 4 in Fig 5.16.
As stated by Scirocco [73], particle string structures start to form once a sufficient degree of shear-thinning is obtained. Then, the elasticity or wall confinement intensifies the string formation. Since the critical shear rate value of Fluid 4 was the lowest compared to that of the

other fluids, it shows shear-thinning behavior at lower shear rates. Upon moving toward the moving wall, the shear rate increased. This provides a sufficient degree of shear-thinning and a suitable condition for particle string formation inside Fluid 4 at F-2 at some point near the moving wall.

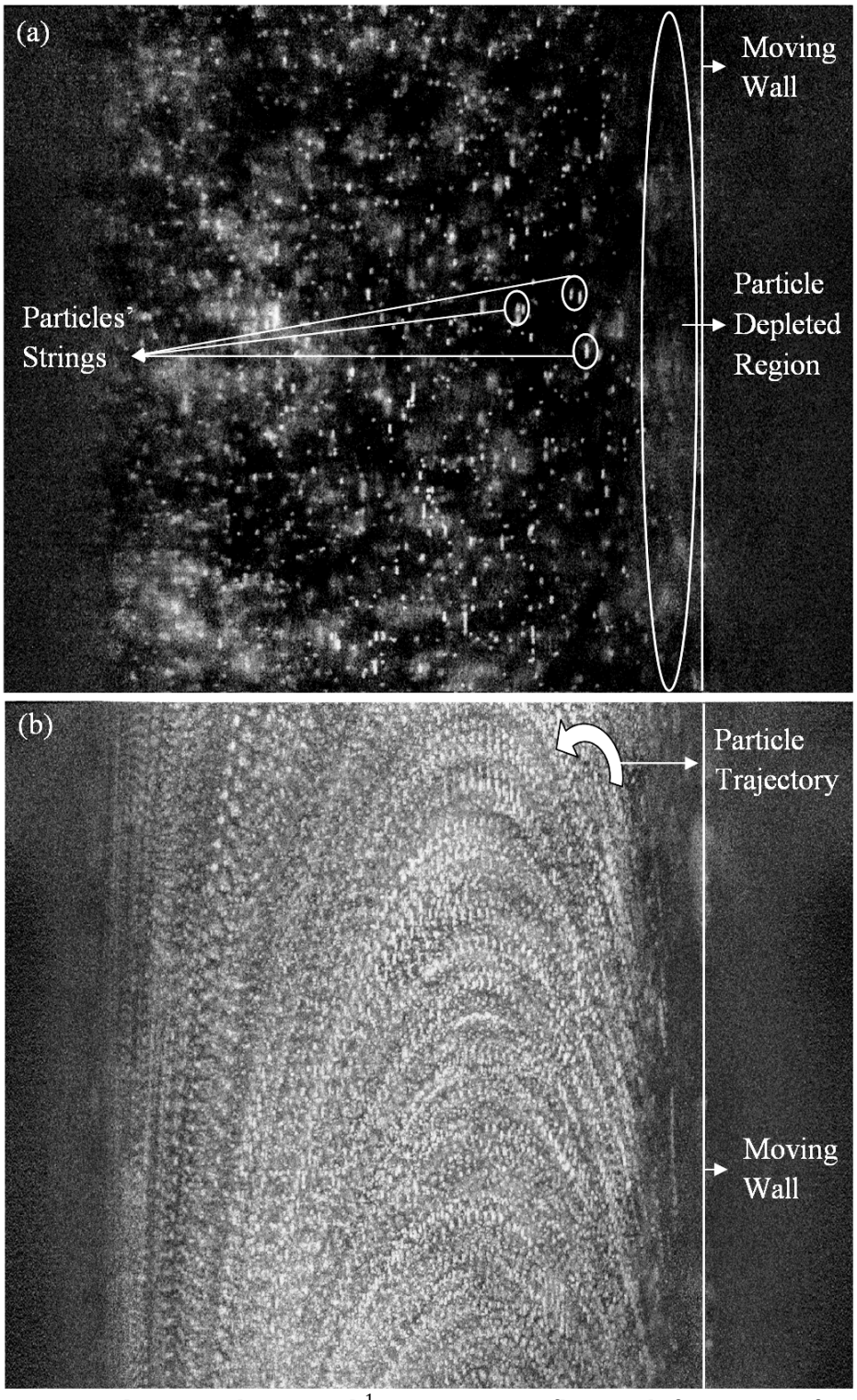

Fig 5.17. HA solution with 5 mg.ml^{-1} concentration flow with frequency of 2.03 Hz. (a) particle depleted layer and particle alignment (b) particle trajectories in the plane of view

The migrations of particles were enhanced upon decreasing the channel width. It was observed that in Conv Channel, at all frequencies for Fluid 2 and Fluid 3 and at F-0 and F-1 for Fluid 4, the particles migrated if the measurement section width was smaller than 0.4 mm. To evaluate the width of the depleted region at the end of the measurements, the last five images of each measurement were image-accumulated (by deriving the maximum pixel values extracted). Fig 5.18 shows examples of the depleted region width of Fluid 2 at F-2 and F-1 and Fluid 4 at F-0.

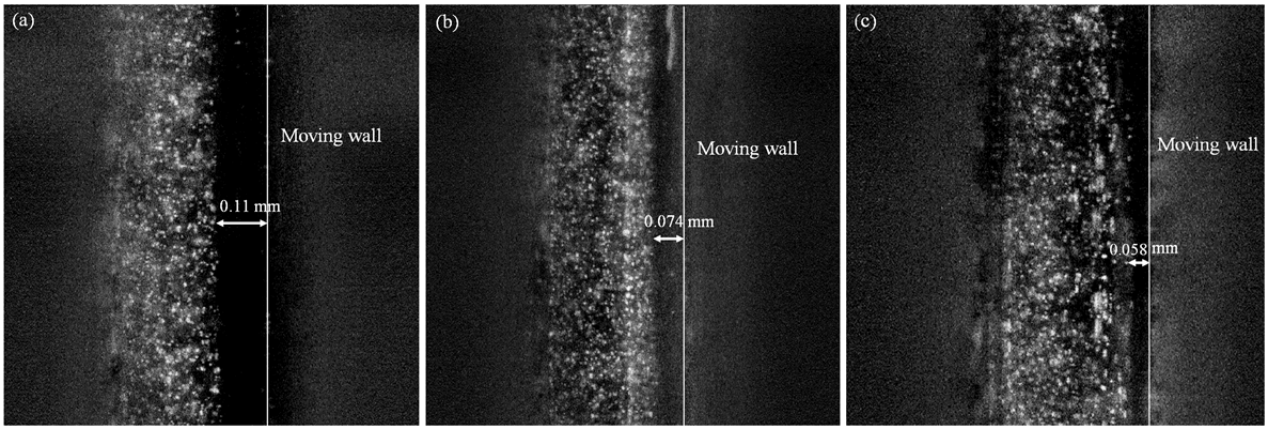

Fig 5.18. Width of particle depletion region for (a) Fluid 2 at F-2, measurement section width of 0.37 mm, (b) Fluid 2 at F-1, measurement section width of 0.36 mm and (c) Fluid 4 at F-0, measurement section width of 0.35 mm

It was shown by D'Avino et al. [79] and Van Loon et al. [74] that wall confinement has a significant effect on the particle migration and string structure formation. A smaller gap size and more confinement enhance the migration and string formation. Particles are placed with different distances from the confinement walls inside the channel. Therefore, they are exposed to different shear rates from the walls. The variations of the shear rates around the particles produce a normal force imbalance and particle cross-streamline migration. By decreasing the channel size in UH-CF by keeping the frequency of the moving wall constant, the shear rate variation around the particles increased and the particle migration was enhanced. Therefore, in Conv Channel, a depleted region formed in the vicinity of the moving wall for almost all of the measurement conditions, which was not the case in Const Channel.

To compare the depleted region width at different experimental conditions, the measurements were performed at least three times, and the precision error at the 90% confidence interval was estimated. Fig 5.19 shows the wall depletion width of the different measurement conditions for two different phases of motion. For different experimental conditions, the mean width of the depletion layer varied between 0.031 and 0.105 mm.

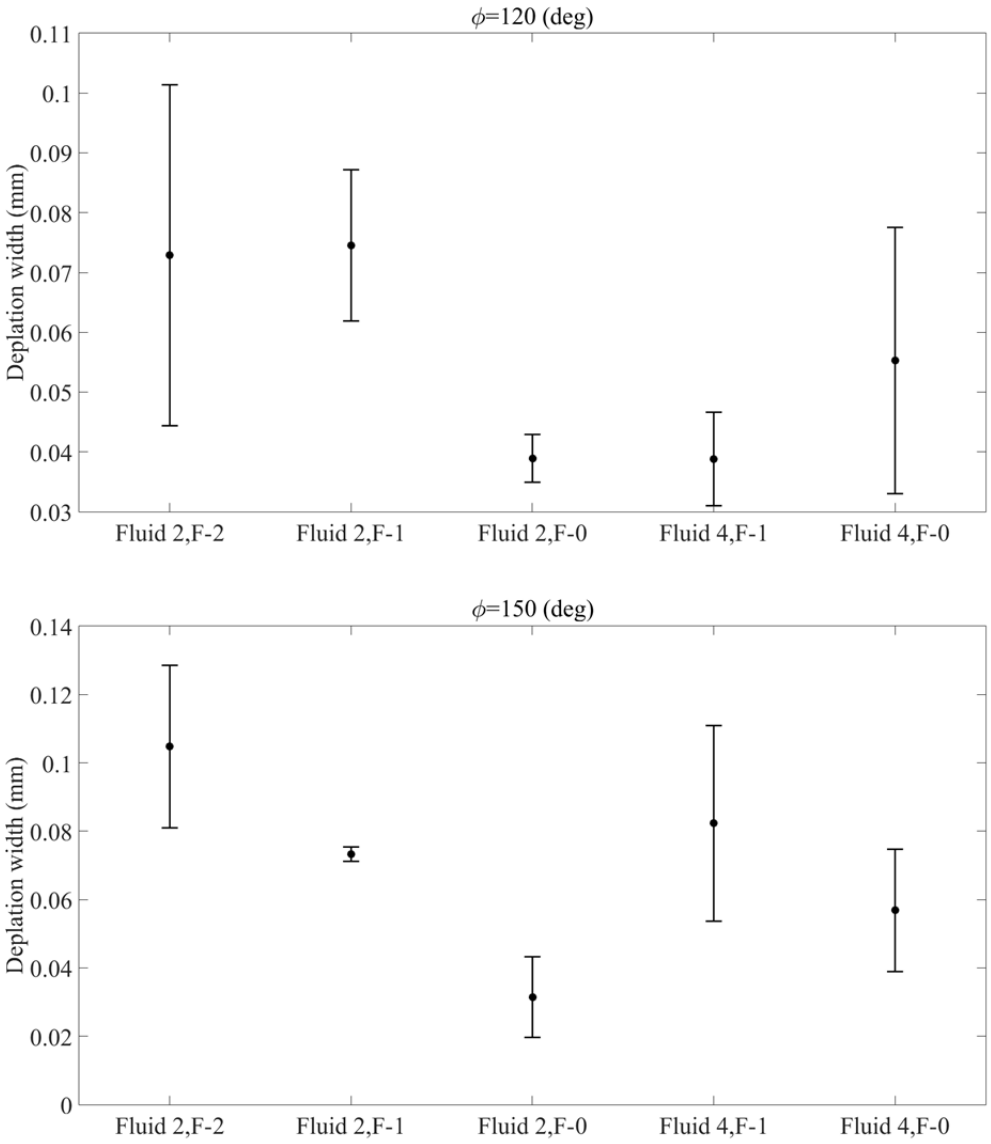

Fig 5.19. Wall depletion width of different measurement condition at two different phases of motion

The particle behavior at the start and end of the measurement for Fluid 4 at F-2 is shown in Fig 5.20. A random particle distribution is visible at the start of the measurement in Fig 5.20(a). For all of the measurement sections, the particles gradually formed strings and migrated to the inner or outer channel walls during the measurements. Fig 5.20 (b) and (c) show the particle distributions for measurement sections of 0.7 and 0.36 mm, respectively. All of the particles participated in the string structures.

The Conv Channel had a smaller width compared to the Const channel. Upon decreasing the channel size, the string structure formation was increased because the shear rate increased, which enhanced the shear-thinning characteristic of the fluid. The string formation was also improved because of more particle collisions. Therefore, for Fluid 4, string formation also occurred at F-1, although the length and number of the strings at F-1 were considerably lower than at F-2. Fig 5.20(d) shows the particle distribution inside Fluid 4 at F-1 at the end of the measurement in the measurement section of 0.32 mm. A depleted region with a 0.04 mm width is visible.

Lormand and Philips [81] studied particle migration in a viscoelastic fluid subjected to flow in concentric cylinders. Their viscoelastic fluid's viscosity was higher than the HA solutions'

viscosity of the current study. However, it had a similar shear-thinning characteristic to that of Fluid 4. They observed that for frequencies smaller than 1 Hz, the particles migrated to either the inner or outer wall. However, this behavior strongly depended on the characteristics of the flow. The migration direction also depended on the particle initial position. For frequencies higher than 1 Hz, the outward migration of the particles ceased, and the particles stayed at regions close to the outer cylinder. However, this behavior was not captured for Fluid 4 of the current study.

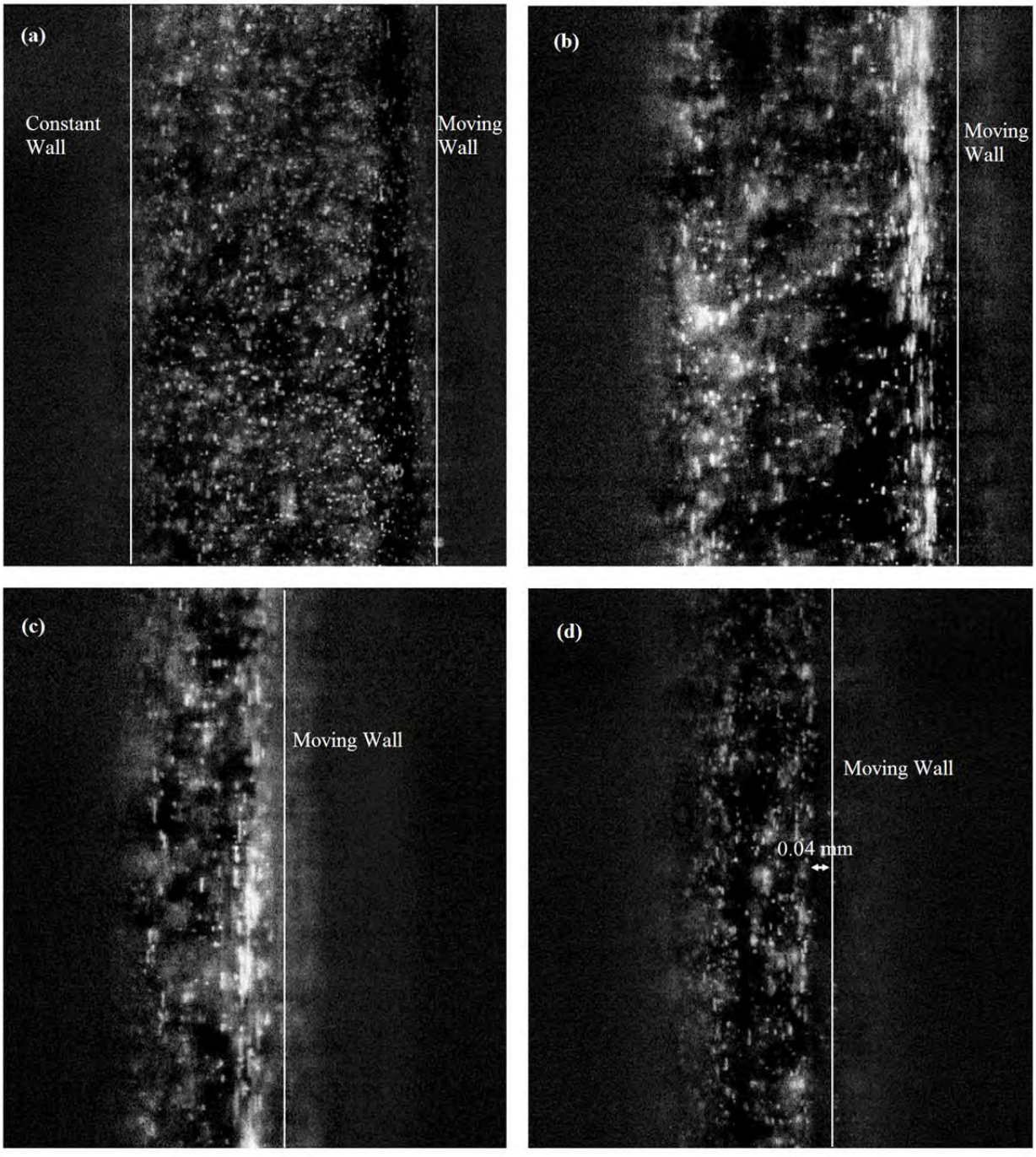

Fig 5.20. Particle distribution along Conv Channel for HA solution with 5 mg.ml^{-1} Concentration along 0.7 mm measurement section width at frequency of 2.03 Hz at (a) start and (b) end of the measurement (c) 0.36 mm measurement section width at frequency of 2.03 at the end of the measurement (d) 0.32 mm measurement section width at frequency of 1.02 at the end of the measurement

To consider the applicability of the findings of current study, it should be noted that the highest angular velocity inside the hip joint is 0.37 Hz [142].

5.3. Pin on disk

The frictional behavior of a UHMWPE pin rotating against a CoCrMo disk was investigated. The effect of dynamic loading in comparison with static loading on the lubrication performance of different lubricants was studied. Fig 5.21 shows the mean COF for the Sin load and the COF of the Const load at the last hour of measurements and the error bars (standard deviation from 3 measurements).
The value of the COF suggests that the active lubrication mechanism was mixed lubrication [61].
The difference between the steady-state and dynamic COFs was significant for the non-HA-containing lubricants. A statistical analysis (one-way ANOVA) performed on the COF values of the Sin and Const loads in the case of the non-HA solution lubricants led to a value of $p<0.03$. However, for the HA-containing lubricants, the difference between the COFs of the static and dynamic loadings was not significant.

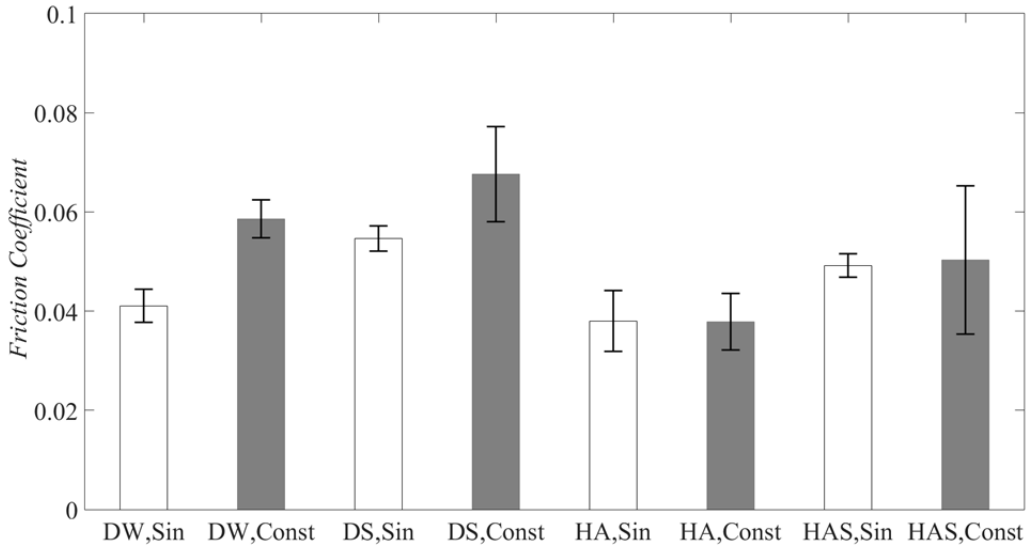

Fig 5.21. Average friction coefficients after a sliding distance of 1700 meters for all test conditions

In the presence of DW as the lubricant, applying a dynamic load decreased the COF. When the load was increased in the Sin load, the surface asperities came close to each other and water was entrapped between the asperities. The water gradually depleted which built up pressure and produced a micro-squeeze effect. The COF decreased because of the contribution of the built-up pressure to the load supported by the fluid film.
The friction condition improved under dynamic loading in presence of DW as the lubricant. However, the SEM images presented in Fig 5.22 shows that the surface of the CoCrMo disk confronted more severe wear under the Sin load in comparison with Const load. Fig 5.21(a) and (c) correspond to the CoCrMo surface after the measurement with the Sin and Const loads, respectively. Grooves of the 2-body abrasive wear are visible for both loading conditions, which suggest that abrasive wear was the dominant wear mechanism for both loading conditions. For the Sin load, wear tracks are observed, which are absent for the Const load. Based on the hypothesis suggested by Barbour et al. [143], under a high stress condition

and constant load, the produced wear particles were trapped between the surface asperities and were prevented from deteriorating the wear condition. However, under a dynamic load and during the load-decreasing phase, the asperities were separated, thereby providing the opportunity for the wear debris to slide along the surfaces and contribute to the wear.
In contrast to the DW, the micro-squeeze effect did not result in a decreased COF in the presence of HA. The HA solution had a significantly higher viscosity than the water, and the higher viscosity improved the hydrodynamic effect and decreased the COF. Other authors also reported a decrease in the COF upon adding HA to the lubricant [54,61,62]. Therefore, during the running-in period and in the presence of HA, the surfaces were effectively separated and stayed smooth. The squeeze effect became negligible because of the lower roughness and asperity. This decreased the variation in the COF under the Sin and Const loads.

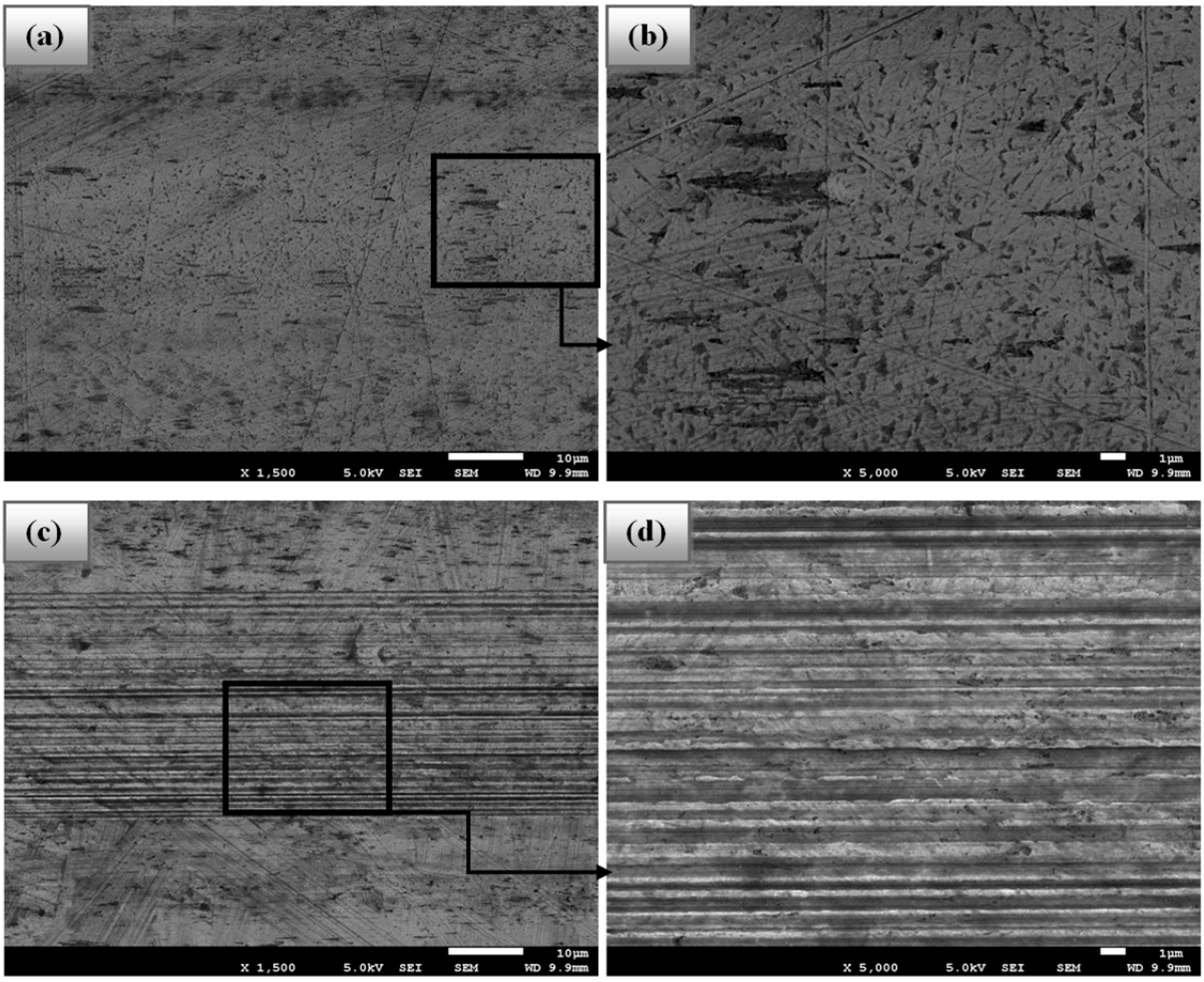

Fig 5.22. SEM images of CoCrMo disk surfaces after tribotesting with distilled water as the lubricant (a) under constant load conditions at a magnification of 1500×, (b) under constant load conditions at a magnification of 5000×, (c) under sinusoidal load conditions at a magnification of 1500×, and (d) under sinusoidal load conditions at a magnification of 5000×

The diluted BCS had the highest COF. The results of many tribological studies suggest that when UHMWPE moves against CoCrMo in the presence of a protein-containing solution, the protein is adsorbed on both surfaces [56,58,60]. The adsorbed protein formed a bridge between the surfaces by the rubbing of protein on protein. This increased the attraction

between the surfaces and the friction. In the current study, by applying a dynamic load and in the load-increasing duration, the surfaces' asperities came closer to each other, which broke the adsorbed protein layer and decreased the COF.

Fig 5.23 shows SEM images of the pin surfaces before and after the pin-on-disk measurements. Fig 5.23(b), (c) and (d) show the pin surface after the pin-on-disk measurements under constant load conditions with lubricants of DW, HA solution in PBS and diluted BCS, respectively. Fig 5.22(d) shows that in the presence of protein, the pin surface was totally protected. However, for the DW or HA solution in PBS, the tracks of the sliding direction are visible. The ripple-shaped tracks could be created via abrasive wear or, as mentioned by other authors, as a result of plastic strain accumulation [144]. As stated by other theory under unidirectional motion, these ripples formed a result of polymer chains orientation due to exerted friction forces at the polymer surface [145,146]. This suggests that the pin and disk surfaces made contact.

In the presence of HA in the diluted BCS, the COF was significantly decreased compared to without the HA, and the variation between the COFs of the Const and Sin loads disappeared. Results of a Study by Serro et al. [147] showed that in presence of HA, albumin adsorption on UHMWPE surface decreased. Therefore, by adding HA to diluted BCS, the friction behavior moved towards HA solution in PBS frictional behavior and COF decreased.

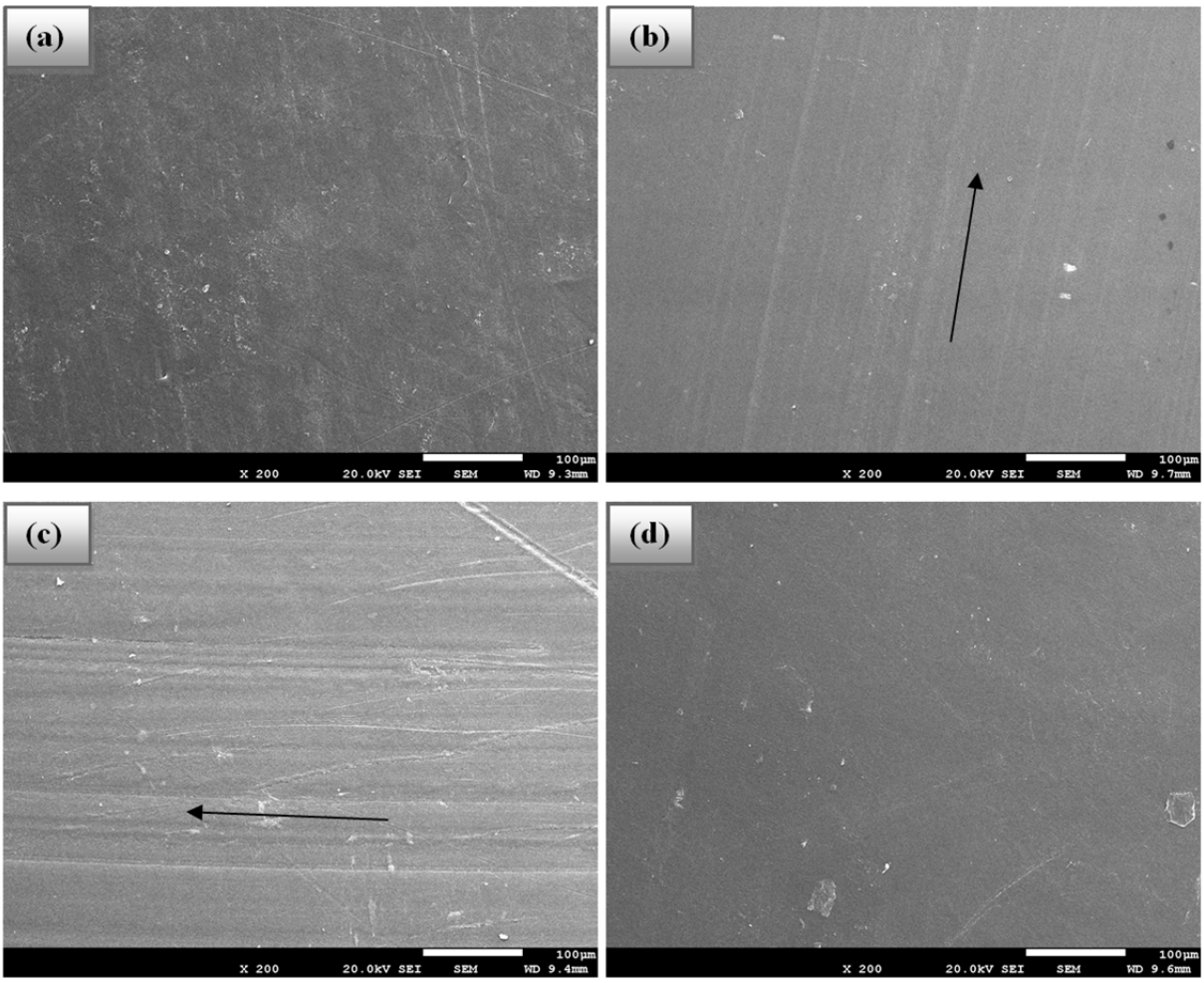

Fig 5.23. SEM images of the UHMWPE pin surface (a) before pin-on-disk measurements and after pin-on-disk measurements under constant load conditions with (b) distilled water, (c) HA solution 3 $mg.ml^{-1}$ concentration in PBS and (d) diluted BCS; the arrows show the sliding direction

Chapter 6

CONCLUSION

Studying wear particle distribution patterns in hip implants can help uncover solutions for minimizing third-body wear and improve the implant design. The present study focused on developing and validating an experimental procedure for investigating artificial SF behavior and effective parameters on polymeric particle distributions within non-Newtonian viscoelastic bio-fluid. The most important findings of the present work are as follows.

- A comparison between steady-state Poiseuille flow velocity profiles with unsteady harmonic Poiseuille amplitudes of velocity profiles shows that laws applied to the steady condition for non-Newtonian fluid are not applicable for oscillatory conditions. Flows within hip implants are subjected to oscillatory motion. Due to the time dependent behavior of the HA polymeric chain, it is not possible to estimate SF behavior based on its steady state rheological behavior.
- Strain amplitudes, distributions and rates affect HA solution behavior under oscillatory conditions. Strain amplitudes and distributions have stronger effects on non-Newtonian viscoelastic flow behaviors than strain rates. The time dependent behaviors of HA solutions are enhanced at high strain values corresponding to non-linear viscoelasticity.
- Increasing HA concentrations directly increases particle alignment and migration.
- Adding proteins to the HA solution did not affect steady state flow behaviors. Under unsteady oscillatory conditions, the effects of protein were only visible under non-linear viscoelastic conditions.
- Competition between elastic and shear-thinning forces of HA solutions determine particle migration behavior in linear viscoelastic condition.
- Wall confinement has significant effects on particle migration and alignment, as it increases fluid shear-thinning and elasticity.
- Under oscillatory Couette flow, particles migrated to either both walls or to the outer wall. The migration behaviors of particles are dependent on the HA concentration and motion frequency. For strain rates in hip implants (0-0.37 Hz), particles always migrated towards the outer wall. This suggests that inside hip implants, wear particles are mostly concentrated close to the polymeric liner rather than to the metallic ball.

- Under oscillatory Couette flow condition, the results showed that the movement of articulating surfaces within tank of fluid significantly affects flow inside the channel. The joint capsule acts as a fluid tank. When examining SF behavior within a joint gap, considering the effects of fluid stored in the capsule is crucial.
- The friction behaviors of the UHMWPE under dynamic and static loads were studied using the pin-on-disk. Dynamic loading did not affect friction when the lubricant contains HA and for lubricants without HA, coefficients of friction increase under static loading compared to dynamic loading.

Chapter 7

FUTURE WORKS

Present study focused on developing a procedure for investigating bio-fluid behaviors and bio-fluid-particle interactions and on characterizing effective parameters. To obtain practical results from such measurements, a number of parameters must be considered in future work.

As our results reveal the importance of geometrical parameters, it is necessary to improve the experimental model towards more spherical shapes (similar to hip implants geometry).

While we performed 2-dimensional measurements, to fully understand particle-specific behavior within non-Newtonian viscoelastic fluid, 3-dimensional measurements must be conducted.

In micro-PIV model to simplify our experimental conditions, effects of loads were not considered in the present work. However, normal forces play a key role in implant performance. It is vital to consider normal loads in the future measurements to obtain more realistic results.

The main purpose of designing the present experimental work was to understand particle in correct size range behavior within hip implants. Wear particles within hip implants are mostly derived from UHMWPE. It would be interesting to investigate the effects of *in-vivo* produced particles on particle-fluid interactions (or particles produced by hip simulators).

Effects of the fluid tank on channel flows during Unsteady Harmonic Couette Flow measurement were not proved through experimental evidence. As the micro-PIV could not generate data for that region, a numerical simulation must be carried out to validate the experimental results. Moreover, by complicating the experimental conditions in future works, a numerical simulation would be beneficial for more thoroughly understanding the physics of fluid and particle behaviors.

REFERENCES

[1] V.C. Mow, W.M. Lai. Recent developments in synovial joint biomechanics, SIAM Rev. 22 (1980) 275-317.

[2] P.H. Wooley, M.J. Grimm, E.L. Radin. The structure and function of joints, Arthritis and Allied Conditions.A Textbook of Rheumatology, Lippincott Williams & Wilkins, Philadelphia. (2005) 149-173.

[3] T. MURAKAMI. The lubrication in natural synovial joints and joint prostheses. JSME international journal.Ser.3, Vibration, control engineering, engineering for industry. 33 (1990) 465-474.

[4] P.K. Levangie, C.C. Norkin, Joint structure and function: a comprehensive analysis, FA Davis 2011.

[5] M. Nordin, V.H. Frankel, Basic biomechanics of the musculoskeletal system, Lippincott Williams & Wilkins 2001.

[6] C.P. Neu, K. Komvopoulos, A.H. Reddi. The interface of functional biotribology and regenerative medicine in synovial joints, Tissue Engineering Part B: Reviews. 14 (2008) 235-247.

[7] A. Neville, A. Morina, T. Liskiewicz, Y. Yan. Synovial joint lubrication—does nature teach more effective engineering lubrication strategies? Proc.Inst.Mech.Eng.Part C. 221 (2007) 1223-1230.

[8] A.Z. Szeri, Fluid film lubrication, Cambridge University Press 2010.

[9] T. Stewart. Tribology of artificial joints, Orthopaedics and Trauma. 24 (2010) 435-440.

[10] V.C. Mow, R. Huiskes, Basic orthopaedic biomechanics & mechano-biology, Lippincott Williams & Wilkins 2005.

[11] H. Fam, J.T. Bryant, M. Kontopoulou. Rheological properties of synovial fluids, Biorheology. 44 (2007) 59-74.

[12] S. Ghosh, D. Choudhury, N.S. Das, B. Pingguan-Murphy. Tribological role of synovial fluid compositions on artificial joints—a systematic review of the last 10 years, Lubr Sci. 26 (2014) 387-410.

[13] E.A. Balazs. The Physical Properties of Synovial Fluid and the Special Role of Hyaluronic Acid, Disorders of the Knee, JB LippincoU Co., Philadelphia. (1974) 63-75.

[14] L.B. Dahl, I.M. Dahl, A. Engstrom-Laurent, K. Granath. Concentration and molecular weight of sodium hyaluronate in synovial fluid from patients with rheumatoid arthritis and other arthropathies, Ann.Rheum.Dis. 44 (1985) 817-822.

[15] L. Ambrosio, A. Borzacchiello, P. Netti, L. Nicolais. Rheological study on hyaluronic acid and its derivative solutions, Journal of MACROMOLECULAR SCIENCE—PURE AND APPLIED CHEMISTRY. 36 (1999) 991-1000.

[16] A. Bingöl, D. Lohmann, K. Püschel, W. Kulicke. Characterization and comparison of shear and extensional flow of sodium hyaluronate and human synovial fluid, Biorheology. 47 (2010) 205-224.

[17] E. Fouissac, M. Milas, M. Rinaudo. Shear-rate, concentration, molecular weight, and temperature viscosity dependences of hyaluronate, a wormlike polyelectrolyte, Macromolecules. 26 (1993) 6945-6951.

[18] P. Seller, D. Dowson, V. Wright. The rheology of synovial fluid, Rheologica Acta. 10 (1971) 2-7.

[19] M.J. Furey, B.M. Burkhardt. Biotribology: Friction, wear, and lubrication of natural synovial joints, Lubr Sci. 9 (1997) 255-271.

[20] A.P. Harsha, T.J. Joyce. Challenges associated with using bovine serum in wear testing orthopaedic biopolymers, Proc.Inst.Mech.Eng.H. 225 (2011) 948-958.

[21] Z.M. Jin, J. Fisher, E. Ingham, Biotribology: material, design, lubrication and wear in artificial hip joints in: G.E. Totten (Ed.), Handbook of Lubrication and Tribology: Volume I Application and Maintenance, CRC Press, New York, 2006,.

[22] A. Unsworth. Tribology of human and artificial joints, Proc.Inst.Mech.Eng.H. 205 (1991) 163-172.

[23] Z. Jin, M. Stone, E. Ingham, J. Fisher. (v) Biotribology, Current Orthopaedics. 20 (2006) 32-40.

[24] R. Hall, A. Unsworth. Friction in hip prostheses, Biomaterials. 18 (1997) 1017-1026.

[25] M. Slouf, S. Eklova, J. Kumstatova, S. Berger, H. Synkova, A. Sosna, et al. Isolation, characterization and quantification of polyethylene wear debris from periprosthetic tissues around total joint replacements, Wear. 262 (2007) 1171-1181.

[26] I. Catelas, M.A. Wimmer, S. Utzschneider, Polyethylene and metal wear particles: characteristics and biological effects, 33 (2011) 257-271.

[27] S. Suñer, J. Tipper, N. Emami. Biological effects of wear particles generated in total joint replacements: trends and future prospects, Tribology-Materials, Surfaces & Interfaces. 6 (2012) 39-52.

[28] H.J. Lundberg, D.R. Pedersen, T.E. Baer, M. Muste, J.J. Callaghan, T.D. Brown. Effects of implant design parameters on fluid convection, potentiating third-body debris ingress into the bearing surface during THA impingement/subluxation, J.Biomech. 40 (2007) 1676-1685.

[29] A.D. Heiner, H.J. Lundberg, T.E. Baer, D.R. Pedersen, J.J. Callaghan, T.D. Brown. Effects of episodic subluxation events on third body ingress and embedment in the THA bearing surface, J.Biomech. 41 (2008) 2090-2096.

[30] T. Brown, H. Lundberg, D. Pedersen, J. Callaghan. 2009 Nicolas Andry Award: Clinical Biomechanics of Third Body Acceleration of Total Hip Wear, Clinical Orthopaedics and Related ResearchÂ®. 467 (2009) 1885-1897.

[31] S.S. Brown, I.C. Clarke. A review of lubrication conditions for wear simulation in artificial hip replacements, Tribol.Trans. 49 (2006) 72-78.

[32] F. Wang, Z. Jin. Elastohydrodynamic lubrication modeling of artificial hip joints under steady-state conditions, Journal of tribology. 127 (2005) 729-739.

[33] D. Jalali-Vahid, M. Jagatia, Z. Jin, D. Dowson. Prediction of lubricating film thickness in UHMWPE hip joint replacements, J.Biomech. 34 (2001) 261-266.

[34] Z.M. Jin, D. Dowson, J. Fisher. Analysis of fluid film lubrication in artificial hip joint replacements with surfaces of high elastic modulus, Proc.Inst.Mech.Eng.H. 211 (1997) 247-256.

[35] D. Jalali-Vahid, Z. Jin. Transient elastohydrodynamic lubrication analysis of ultra-high molecular weight polyethylene hip joint replacements, Proc.Inst.Mech.Eng.Part C. 216 (2002) 409-420.

[36] D. Jalali-Vahid, Z. Jin, D. Dowson. Elastohydrodynamic lubrication analysis of hip implants with ultra high molecular weight polyethylene cups under transient conditions, Proc.Inst.Mech.Eng.Part C. 217 (2003) 767-777.

[37] A.F. Quinonez, J. Fisher, Z. Jin. A steady-state elastohydrodynamic lubrication model aimed at natural hip joints with physiological loading and anatomical position, Proc.Inst.Mech.Eng.Part J. 222 (2008) 503-512.

[38] J. Tichy, B. Bou-SaĂŻd. The Phan-Thien and Tanner model applied to thin film spherical coordinates: applications for lubrication of hip joint replacement, J.Biomech.Eng. 130 (2008) 021012.

[39] A. Meziane, B. Bou-Saïd, J. Tichy. Modelling human hip joint lubrication subject to walking cycle, Lubr Sci. 20 (2008) 205-222.

[40] L. Gao, D. Dowson, R.W. Hewson. A numerical study of non-Newtonian transient elastohydrodynamic lubrication of metal-on-metal hip prostheses, Tribol.Int. 93 (2016) 486-494.

[41] Z.M. Jin, D. Dowson, J. Fisher. Analysis of fluid film lubrication in artificial hip joint replacements with surfaces of high elastic modulus, Proc.Inst.Mech.Eng.H. 211 (1997) 247-256.

[42] J. Michele, R. Pätzold, R. Donis. Alignment and aggregation effects in suspensions of spheres in non-Newtonian media, Rheologica Acta. 16 (1977) 317-321.

[43] D. Mazzucco, R. Scott, M. Spector. Composition of joint fluid in patients undergoing total knee replacement and revision arthroplasty: correlation with flow properties, Biomaterials. 25 (2004) 4433-4445.

[44] H. Saari, S. Santavirta, D. Nordstrom, P. Paavolainen, Y.T. Konttinen. Hyaluronate in total hip replacement, J.Rheumatol. 20 (1993) 87-90.

[45] H. Yamada, M. Morita, O. Henmi, S. Miyauchi, Y. Yoshida, T. Kikuchi, et al. Hyaluronan in synovial fluid of patients with loose total hip prosthesis, Arch.Orthop.Trauma Surg. 120 (2000) 521-524.

[46] L.E. Guenther, B.W. Pyle, T.R. Turgeon, E.R. Bohm, U.P. Wyss, T.A. Schmidt, et al. Biochemical analyses of human osteoarthritic and periprosthetic synovial fluid, Proc.Inst.Mech.Eng.H. 228 (2014) 127-139.

[47] A. Galandáková, J. Ulrichová, K. Langová, A. Hanáková, M. Vrbka, M. Hartl, et al. Characteristics of synovial fluid required for optimization of lubrication fluid for biotribological experiments, Journal of Biomedical Materials Research Part B: Applied Biomaterials. (2016).

[48] D. Mazzucco, G. McKinley, R.D. Scott, M. Spector. Rheology of joint fluid in total knee arthroplasty patients, Journal of orthopaedic research. 20 (2002) 1157-1163.

[49] J. DesJardins, A. Aurora, S.L. Tanner, T.B. Pace, K.B. Acampora, M. Laberge. Increased total knee arthroplasty ultra-high molecular weight polyethylene wear using a clinically relevant hyaluronic acid simulator lubricant, Proc.Inst.Mech.Eng.H. 220 (2006) 609-623.

[50] H. McKellop, I. Clarke, K. Markolf, H. Amstutz. Wear characteristics of UHMW polyethylene: a method for accurately measuring extremely low wear rates, J.Biomed.Mater.Res. 12 (1978) 895-927.

[51] J. Brandt, L. Brière, J. Marr, S. MacDonald, R. Bourne, J. Medley. Biochemical comparisons of osteoarthritic human synovial fluid with calf sera used in knee simulator wear testing, Journal of Biomedical Materials Research Part A. 94 (2010) 961-971.

[52] K.M. Oates, W.E. Krause, R.L. Jones, R.H. Colby. Rheopexy of synovial fluid and protein aggregation, J.R.Soc.Interface. 3 (2006) 167-174.

[53] D. Mazzucco, M. Spector. THE JOHN CHARNLEY AWARD PAPER: The Role of Joint Fluid in the Tribology of Total Joint Arthroplasty. Clin.Orthop. 429 (2004) 17-32.

[54] Y. Sawae, T. Murakami, J. Chen. Effect of synovia constituents on friction and wear of ultra-high molecular weight polyethylene sliding against prosthetic joint materials, Wear. 216 (1998) 213-219.

[55] S. Scholes, A. Unsworth, R. Hall, R. Scott. The effects of material combination and lubricant on the friction of total hip prostheses, Wear. 241 (2000) 209-213.

[56] S.C. Scholes, A. Unsworth. The effects of proteins on the friction and lubrication of artificial joints, Proc.Inst.Mech.Eng.H. 220 (2006) 687-693.

[57] S.C. Scholes, A. Unsworth. Comparison of friction and lubrication of different hip prostheses, Proc.Inst.Mech.Eng.H. 214 (2000) 49-57.

[58] J. Yao, M. Laurent, T. Johnson, C. Blanchard, R. Crowninshield. The influences of lubricant and material on polymer/CoCr sliding friction, Wear. 255 (2003) 780-784.

[59] X. Chen, Z. Jin, J. Fisher. Effect of albumin adsorption on friction between artificial joint materials, Proc.Inst.Mech.Eng.Part J. 222 (2008) 513-521.

[60] M. Flannery, E. Jones, C. Birkinshaw. Analysis of wear and friction of total knee replacements part II: Friction and lubrication as a function of wear, Wear. 265 (2008) 1009-1016.

[61] M. Gispert, A. Serro, R. Colaco, B. Saramago. Friction and wear mechanisms in hip prosthesis: Comparison of joint materials behaviour in several lubricants, Wear. 260 (2006) 149-158.

[62] H. Fam. Effect of composition on periprosthetic fluid rheology and friction in total knee arthroplasty, (2010).

[63] K. Fujii, M. Kawata, Y. Kobayashi, A. Okamoto, K. Nishinari. Effects of the addition of hyaluronate segments with different chain lengths on the viscoelasticity of hyaluronic acid solutions, Biopolymers. 38 (1996) 583-591.

[64] H. Fam, M. Kontopoulou, J. Bryant. Effect of concentration and molecular weight on the rheology of hyaluronic acid/bovine calf serum solutions, Biorheology. 46 (2009) 31-43.

[65] W.E. Krause, E.G. Bellomo, R.H. Colby. Rheology of sodium hyaluronate under physiological conditions, Biomacromolecules. 2 (2001) 65-69.

[66] Z. Zhang, S. Barman, G. Christopher. The role of protein content on the steady and oscillatory shear rheology of model synovial fluids, Soft matter. 10 (2014) 5965-5973.

[67] Y. Mo, T. Takaya, K. Nishinari, K. Kubota, A. Okamoto. Effects of sodium chloride, guanidine hydrochloride, and sucrose on the viscoelastic properties of sodium hyaluronate solutions, Biopolymers. 50 (1999) 23-34.

[68] R.K. Gupta, Polymer and composite rheology, CRC Press 2000.

[69] J.M. Dealy, J. Wang, Viscosity and Normal Stress Differences, Melt Rheology and its Applications in the Plastics Industry, Springer, 2013, pp. 19-47.

[70] P. Partal, J.M. Franco, Non-Newtonian fluids, in: Crispulo Gallegos (Ed.), Rheology - Volume I, Eolss Publisher, 2010, pp. 96-119.

[71] N. Phan-Thien, Understanding viscoelasticity: basics of rheology, Springer Science & Business Media 2013.

[72] D. Won, C. Kim. Alignment and aggregation of spherical particles in viscoelastic fluid under shear flow, J.Non Newtonian Fluid Mech. 117 (2004) 141-146.

[73] R. Scirocco, J. Vermant, J. Mewis. Effect of the viscoelasticity of the suspending fluid on structure formation in suspensions, J.Non Newtonian Fluid Mech. 117 (2004) 183-192.

[74] S. Van Loon, J. Fransaer, C. Clasen, J. Vermant. String formation in sheared suspensions in rheologically complex media: The essential role of shear thinning, Journal of Rheology (1978-present). 58 (2014) 237-254.

[75] G. D'Avino, P. Maffettone. Particle dynamics in viscoelastic liquids, J.Non Newtonian Fluid Mech. 215 (2015) 80-104.

[76] R. Pasquino, F. Snijkers, N. Grizzuti, J. Vermant. The effect of particle size and migration on the formation of flow-induced structures in viscoelastic suspensions, Rheologica acta. 49 (2010) 993-1001.

[77] R. Pasquino, D. Panariello, N. Grizzuti. Migration and alignment of spherical particles in sheared viscoelastic suspensions. A quantitative determination of the flow-induced self-assembly kinetics, J.Colloid Interface Sci. 394 (2013) 49-54.

[78] M. Jefri, A. Zahed. Elastic and Viscous Effects on Particle Migration in Plane-Poiseuille Flow, Journal of Rheology (1978-present). 33 (1989) 691-708.

[79] G. D'Avino, F. Snijkers, R. Pasquino, M. Hulsen, F. Greco, P. Maffettone, et al. Migration of a sphere suspended in viscoelastic liquids in Couette flow: experiments and simulations, Rheologica acta. 51 (2012) 215-234.

[80] G. d'Avino, P. Maffettone, F. Greco, M. Hulsen. Viscoelasticity-induced migration of a rigid sphere in confined shear flow, J.Non Newtonian Fluid Mech. 165 (2010) 466-474.

[81] B.M. Lormand, R.J. Phillips. Sphere migration in oscillatory Couette flow of a viscoelastic fluid, Journal of Rheology (1978-present). 48 (2004) 551-570.

[82] M. Lyon, D. Mead, R. Elliott, L. Leal. Structure formation in moderately concentrated viscoelastic suspensions in simple shear flow, Journal of Rheology (1978-present). 45 (2001) 881-890.

[83] M. Raffel, C.E. Willert, S.T. Wereley, J. Kompenhans, Particle Image Velocimetry A Practical Guide, 2nd ed., Springer, 2007.

[84] P. Vennemann, R. Lindken, J. Westerweel. In vivo whole-field blood velocity measurement techniques, Exp.Fluids. 42 (2007) 495-511.

[85] R. Lindken, M. Rossi, S. Grobe, J. Westerweel. Micro-Particle Image Velocimetry (micro-PIV): Recent developments, applications, and guidelines, Lab Chip. (2009) 2551.

[86] M. Raffel, C.E. Willert, S.T. Wereley, J. Kompenhans, Particle Image Velocimetry A Practical Guide, 2nd ed., Springer, 2007.

[87] P. Vennemann, R. Lindken, J. Westerweel. In vivo whole-field blood velocity measurement techniques, Exp.Fluids. 42 (2007) 495-511.

[88] R. Lindken, M. Rossi, S. Grobe, J. Westerweel. Micro-Particle Image Velocimetry (micro-PIV): Recent developments, applications, and guidelines, Lab Chip. (2009) 2551.

[89] S.T. Wereley, C.D. Meinhart, Micron-Resolution Particle Image Velocimetry, in: K.S. Breuer (Ed.), Microscale Diagnostic Techniques, Springer, 2005, pp. 51-112.

[90] S.T. Wereley, C.D. Meinhart. Recent Advances in Micro-Particle Image Velocimetry, Annual Review of Fluid Mechanics. 42 (2010) 557-576.

[91] Y. Sugii, S. Nishio, K. Okamoto. *In vivo* PIV measurement of red blood cell velocity field in microvessels considering mesentery motion, Physiological Measurement. 23 (2002) 403-416.

[92] J.R. Hove, R.W. Köster, A.S. Forouhar, G. Acevedo-Bolton, S.E. Fraser, M. Gharib. Intracardiac fluid forces are an essential epigenetic factor for embryonic cardiogenesis, Letters to Nature. 421 (2003) 172-177.

[93] J.H. Jeong, Y. Sugii, M. Minamiyama, H. Takeuchi, K. Okamoto. Interaction between liposomes and RBC in microvessels in vivo, Microvasc.Res. 73 (2007) 39-47.

[94] P. Vennemann, K.T. Kiger, R. Lindken, B.C.W. Groenendijk, S. Stekelenburg-de Vos, T.L.M. ten Hagen, et al. In vivo micro particle image velocimetry measurements of blood-plasma in the embryonic avian heart, J.Biomech. 39 (2006) 1191-1200.

[95] C. Poelma, K. Van der Heiden, B.P. Hierck, R.E. Poelmann, J. Westerweel. Measurements of the wall shear stress distribution in the outflow tract of an embryonic chicken heart, Journal of the Royal Society Interface. 7 (2010) 91-103.

[96] C. Poelma, P. Vennemann, R. Lindken, J. Westerweel. In vivo blood flow and wall shear stress measurements in the vitelline network, Experiments in Fluids. 45 (2008) 703-713.

[97] M.L. Smith, D.S. Long, E.R. Damiano, K. Ley. Near-wall micro-PIV reveals a hydrodynamically relevant endothelial surface layer in venules in vivo, Biophys.J. 85 (2003) 637-645.

[98] D.R. Potter, E.R. Damiano. The Hydrodynamically Relevant Endothelial Cell Glycocalyx Observed In Vivo Is Absent In Vitro, Circulation Research. 102 (2008) 770-776.

[99] R. Lima, M.S. Oliveira, T. Ishikawa, H. Kaji, S. Tanaka, M. Nishizawa, et al. Axisymmetric polydimethysiloxane microchannels for in vitro hemodynamic studies, Biofabrication. 1 (2009) 035005.

[100] V. Garcia, R. Dias, R. Lima, In Vitro Blood Flow Behaviour in Microchannels with Simple and Complex Geometries, in: G.R. Naik (Ed.), Applied Biological Engineering - Principles and Practice, InTech, 2012, pp. 393-416.

[101] R. Lima, S. Wada, S. Tanaka, M. Takeda, T. Ishikawa, K. Tsubota, et al. In vitro blood flow in a rectangular PDMS microchannel: experimental observations using a confocal micro-PIV system, Biomed.Microdevices. 10 (2008) 153-167.

[102] R. Lima, T. Ishikawa, Y. Imai, M. Takeda, S. Wada, T. Yamaguchi. Measurement of Individual Red Blood Cell Motions Under High Hematocrit Conditions Using a Confocal Micro-PTV System, Ann.Biomed.Eng. 37 (2009) 1546-1559.

[103] C.M. Leong. In Vitro Measurements of Flow Over Endothelial Cells, Rensselaer Polytechnic Institute, PhD thesis, 2008.

[104] C.M. Leong, A. Voorhees, G.B. Nackman, T. Wei. Flow bioreactor design for quantitative measurements over endothelial cells using micro-particle image velocimetry, Rev.Sci.Instrum. 84 (2013).

[105] A. Voorhees, G.B. Nackman, T. Wei. Experiments show importance of flow-induced pressure on endothelial cell shape and alignment, Proceedings of thr Royal Society A. 463 (2007) 1409-1419.

[106] M. Rossi, I. Ekeberg, P. Vennemann, R. Lindken, J. Westerweel, B.P. Hierck, et al., In vitro study of shear stress over endothelial cells by Micro Particle Image Velocimetry (μPIV), (2006).

[107] M. Rossi, R. Lindken, J. Westerweel. Optimization of multiplane μPIV for wall shear stress and wall topography characterization, Experiments in Fluids. 48 (2010) 211-223.

[108] M. Rossi, R. Lindken, B.P. Hierck, J. Westerweel, Tapered microfluidic chip for the study of biochemical and mechanical response at subcellular level of endothelial cells to shear flow, Lab Chip. (2009) 1403.

[109] S.J. Haward, A. Jaishankar, M.S.N. Oliveira, M.A. Alves, G.H. McKinley. Extensional flow of hyaluronic acid solutions in an optimized microfluidic cross-slot devicea), Biomicrofluidics. 7 (2013).

[110] P.K. Kundu, I.M. Cohen. Fluid Mechanics 4th, (2008).

[111] H. Bruus, Theoretical Microfluidics., New York: Oxford University Press 2008.

[112] M.Ö Çarpinlioğlu, M.Y. Gündoğdu. A critical review on pulsatile pipe flow studies directing towards future research topics, Flow Meas.Instrum. 12 (2001) 163-174.

[113] S. Uchida. The pulsating viscous flow superposed on the steady laminar motion of incompressible fluid in a circular pipe, Zeitschrift für angewandte Mathematik und Physik ZAMP. 7 (1956) 403-422.

[114] V. O'Brien. Pulsatile fully developed flow in rectangular channels, Journal of the Franklin Institute. 300 (1975) 225-230.

[115] C. Fan, B. Chao. Unsteady, laminar, incompressible flow through rectangular ducts, Zeitschrift für angewandte Mathematik und Physik ZAMP. 16 (1965) 351-360.

[116] A. Yakhot, M. Arad, G. Ben-Dor. Numerical investigation of a laminar pulsating flow in a rectangular duct, Int.J.Numer.Methods Fluids. 29 (1999) 935-950.

[117] D. Drake. On the flow in a channel due to a periodic pressure gradient, The Quarterly Journal of Mechanics and Applied Mathematics. 18 (1965) 1-10.

[118] E. Urata. The frequency response of rectangular ducts, Proc.Inst.Mech.Eng.Part C. (2014) 0954406214542037.

[119] M. Franke, E. Moore. Dynamic response approximation for noncircular fluid lines, Journal of Dynamic Systems, Measurement, and Control. 98 (1976) 421-424.

[120] S. Ray, F. Durst. Semianalytical solutions of laminar fully developed pulsating flows through ducts of arbitrary cross sections, Physics of Fluids (1994-present). 16 (2004) 4371-4385.

[121] T. MUTO, K. NAKANE. Unsteady Flow in Circular Tube: Velocity Distribution of Pulsating Flow, Bulletin of JSME. 23 (1980) 1990-1996.

[122] E.B. Denison, W.H. Stevenson, R.W. Fox. Pulsating laminar flow measurements with a directionally sensitive laser velocimeter, AIChE J. 17 (1971) 781-787.

[123] C. Sert, A. Beskok. Numerical simulation of reciprocating flow forced convection in two-dimensional channels, TRANSACTIONS-AMERICAN SOCIETY OF MECHANICAL ENGINEERS JOURNAL OF HEAT TRANSFER. 125 (2003) 403-412.

[124] L. Ai, K. Vafai. An investigation of Stokes' second problem for non-Newtonian fluids, Numerical Heat Transfer, Part A. 47 (2005) 955-980.

[125] R. Berker. Intégration des équations du mouvement d'un fluide visqueux incompressible, Handbuch der physik. 2 (1963) 1-384.

[126] D. Jalali-Vahid, M. Jagatia, Z. Jin, D. Dowson. Prediction of lubricating film thickness in UHMWPE hip joint replacements, J.Biomech. 34 (2001) 261-266.

[127] D. Dowson, C. McNie, A. Goldsmith. Direct experimental evidence of lubrication in a metal-on-metal total hip replacement tested in a joint simulator, Proc.Inst.Mech.Eng.Part C. 214 (2000) 75-86.

[128] R.C. JOHNSTON, G.L. Smidt. Measurement of hip-joint motion during walking, J.Bone Joint Surg.Am. 51 (1969) 1083-1094.

[129] H. Brenner. The slow motion of a sphere through a viscous fluid towards a plane surface, Chemical engineering science. 16 (1961) 242-251.

[130] A.J. Goldman, R.G. Cox, H. Brenner. Slow viscous motion of a sphere parallel to a plane wall—I Motion through a quiescent fluid, Chemical Engineering Science. 22 (1967) 637-651.

[131] K.D. Kihm, Near-field characterization of micro/nano-scaled fluid flows, Springer 2011.

[132] A. Goldman, R. Cox, H. Brenner. Slow viscous motion of a sphere parallel to a plane wall—II Couette flow, Chemical engineering science. 22 (1967) 653-660.

[133] M. Kontopoulou, Applied polymer rheology: polymeric fluids with industrial applications, John Wiley & Sons 2011.

[134] M. Vazquez, D. Schmalzing, P. Matsudaira, D. Ehrlich, G. McKinley. Shear-induced degradation of linear polyacrylamide solutions during pre-electrophoretic loading, Anal.Chem. 73 (2001) 3035-3044.

[135] F. Delplace, J.C. Leuliet. Generalized Reynolds number for the flow of power law fluids in cylindrical ducts of arbitrary cross-section, The Chemical Engineering Journal and the Biochemical Engineering Journal. 56 (1995) 33-37.

[136] S. Ray, B. Ünsal, F. Durst, Ö Ertunc, O. Bayoumi. Mass flow rate controlled fully developed laminar pulsating pipe flows, Journal of fluids engineering. 127 (2005) 405-418.

[137] H. Fam. Effect of composition on periprosthetic fluid rheology and friction in total knee arthroplasty, Queen's University, PhD thesis, 2010.

[138] D. Roylance. Engineering viscoelasticity, Department of Materials Science and Engineering–Massachusetts Institute of Technology, Cambridge MA. 2139 (2001) 1-37.

[139] M.T. Shaw, Introduction to polymer rheology, John Wiley & Sons 2012.

[140] C.W. Macosko, R.G. Larson. Rheology: principles, measurements, and applications, (1994).

[141] W.P. Cox, E.H. Merz. Correlation of dynamic and steady flow viscosities, Journal of Polymer Science. 28 (1958) 619-622.

[142] R. Ferber, I.M. Davis, D.S. Williams Iii. Gender differences in lower extremity mechanics during running, Clin.Biomech. 18 (2003) 350-357.

[143] P.M. BARBOUR, D. Barton, J. Fisher. The influence of stress conditions on the wear of UHMWPE for total joint replacements, J.Mater.Sci.Mater.Med. 8 (1997) 603-611.

[144] M. Gispert, A. Serro, R. Colaço, E. Pires, B. Saramago. The effect of roughness on the tribological behavior of the prosthetic pair UHMWPE/TiN-coated stainless steel, Journal of Biomedical Materials Research Part B: Applied Biomaterials. 84 (2008) 98-107.

[145] H. Marrs, D. Barton, R. Jones, I. Ward, J. Fisher, C. Doyle. Comparative wear under four different tribological conditions of acetylene enhanced cross-linked ultra high molecular weight polyethylene, J.Mater.Sci.Mater.Med. 10 (1999) 333-342.

[146] C. Bragdon, D. O'Connor, J. Lowenstein, M. Jasty, W. Syniuta. The importance of multidirectional motion on the wear of polyethylene, Proc.Inst.Mech.Eng.Part H J.Eng.Med. 210 (1996) 157-165.

[147] A. Serro, K. Degiampietro, R. Colaço, B. Saramago. Adsorption of albumin and sodium hyaluronate on UHMWPE: a QCM-D and AFM study, Colloids and Surfaces B: Biointerfaces. 78 (2010) 1-7.

Paper A

Bio-Lubricant Flow Behavior in Mini-Channels

Reprinted with permission

LUBRICATION SCIENCE
Lubrication Science 2016; **28**:221–242
Published online 1 December 2015 in Wiley Online Library (wileyonlinelibrary.com). DOI: 10.1002/ls.1328

Bio-lubricant flow behaviour in mini-channels

Alaleh Safari[1], Nazanin Emami[1] and Michel J. Cervantes[2,3,*,†]

[1]*Biotribology group, Division of Machine Element, Luleå University of Technology, 97187 Luleå, Sweden*
[2]*Division of Fluid and Experimental Mechanics, Luleå University of Technology, 97187Luleå, Sweden*
[3]*Water Power Laboratory, Norwegian University of Science and Technology, 7491 Trondheim, Norway*

ABSTRACT

One of the most common causes of failures in total joint replacements is the generation of wear particles within the joint. This contributes to bone lost and aseptic loosening of the implant, eventually requiring its replacement. Many studies have been carried out to improve the wear characteristics of bearing surfaces in total joint replacement. From the lubrication point of view, the friction behaviour of surfaces and rheology of the joint lubricant (synovial fluid) have been extensively studied. However, little attention has been paid to the interaction between the lubricant and the bearing surfaces. The aim of this study is to develop a methodology for studying the behaviour of bio-based lubricant in mini-channels. For this purpose, micro-particle image velocimetry was used in order to characterise the lubricant behaviour. Channels made of relevant materials such as ultra-high molecular weight polyethylene, cobalt–chromium–molybdenum alloy and titanium–aluminium–vanadium alloy with 1 and 1.5 mm width, 45 mm length and 2 mm depth were experimentally investigated. Results suggested that the used polymeric solution interaction with solid surfaces is very sensitive to the polymer concentration in the lubricant. Moreover, it was observed that there exist differences between water (Newtonian reference fluid) and the polymeric solution behaviour even at very simple movements; although usually, the properties of this lubricant at high shear rates are estimated by water properties.

Received 26 March 2015; Revised 18 October 2015; Accepted 2 November 2015

KEY WORDS: TJR; synovial fluid; wear particles; micro-PIV; hyaluronic acid

INTRODUCTION

Total joint replacement (TJR) is one of the most successful surgical procedures of the 21st century. In a conventional hip implant, ultra-high molecular weight polyethylene (UHMWPE) is used as polymeric liner in acetabular cup, and the counter surface (femoral head) is made of hard materials such as cobalt–chromium alloy or ceramics such as alumina. Wear particles are produced during the lifetime of the implant when the polymeric liner meets the hard surface of the femoral head, which makes increasing TJR lifetime an important challenge. One of the major causes of failure in total joint

*Correspondence to: Michel J. Cervantes, Division of Fluid and Experimental Mechanics, Luleå University of Technology, 97187 Luleå, Sweden.
†E-mail: Michel.Cervantes@ltu.se

arthroplasty is bone lost (osteolysis) initiated by these wear particles.[1] In addition to improving the wear resistance of the bearing surfaces to reduce wear, wear debris distribution mechanism within the joint gap should also be thoroughly investigated. These particles are distributed through the joint lubricant called synovial fluid; a non-Newtonian viscoelastic shear thinning fluid[2,3] and the distribution mechanism totally depend on behaviour of this fluid.

Synovial fluid is dialysate of blood plasma. Its composition consists of water, protein and hyaluronic acid (HA). Synovial fluid contains less protein compared with plasma. In healthy synovial fluid, the main proteins are usually albumin ($7\,mg\,ml^{-1}$) and γ-globulins ($11\,mg\,ml^{-1}$). Other proteins exist in very small amounts. However, the concentration increases in diseased synovial fluid.[2,3] Key molecules of synovial fluid for lubrication are lubricin proteoglycan ($0.05–0.35\,mg\,ml^{-1}$), hyaluronan ($1–4\,mg\,ml^{-1}$) and surface active phospholipids ($0.1\,mg\,ml^{-1}$).[3–5] HA controls the water content and viscosity in the synovial fluid.[6] The molecular weight of HA in a healthy synovial fluid is 6.3–7.6 MDa[7] and exists at a concentration of $1.45–4.22\,mg\,ml^{-1}$. However, its molecular weight and concentration decreases to the order of 1.06–6.8 MDa and $0.19–3.61\,mg\,ml^{-1}$, respectively, for diseased synovial fluid of osteoarthritis or rheumatoid arthritis.[3] The rheological properties of synovial fluid depend on molecular weight and concentration of HA content plus interactions between HA and protein chains.

Sodium hyaluronate (NaHA) is a sodium salt of HA and a linear biopolymer.[6] To understand the behaviour and rheological properties (non-Newtonian and viscoelasticity) of HA, different studies were carried out on NaHA in solution form.[8–14] Results contained plots of viscosity versus shear rate for different solution concentration and plots of viscous and elastic dynamic modulus versus frequency that quantify non-Newtonian and viscoelasticity behaviour, respectively.[8–11] The results suggested that viscoelastic behaviour of HA in synovial fluid is not significantly affected by its protein content. However, the rheopexy of HA is related to complex interaction between HA and protein chains.[14] Studies also show that at very high shear rates, HA content solution properties are similar to water properties.[8–11] In most numerical simulations of joints and implants, synovial fluid properties are thus replaced with water properties.[15–17]

Therefore, suitable method to investigate the behaviour and influence of HA on water-based solution behaviour in comparison with water in channels is of importance from a fluid rheological and the surface liquid interaction point of view.

Several methods have been applied for studying biological fluids such as laser Doppler velocimetry, double-slit photometric, laser speckle techniques, etc.[18] These techniques provide point information in the plane of study. Particle image velocimetry (PIV) is capable of providing high spatial and temporal resolution for the whole measurement volume. Furthermore, PIV is able to work at milli-scales or micro-scales, an important feature for studies in biological fields. The quasi non-intrusive nature of micro-PIV method and the capability of applying it in both two-dimensional and three-dimensional studies are additional advantages of this measurement method.[18–20] Blood was the first biofluid to be extensively studied by PIV or micro-PIV methods.[18,20,21] Another recent application of PIV is the study of human joint lubricant behaviour. PIV was used to provide validation information for numerical simulation of wear mechanisms in hip implants. This numerical simulation was developed based on a new hypothesis of wear initialization after TJR.[22] Micro-PIV together with birefringence was recently employed in order to develop a new diagnosis technique for joint diseases.[12] Based on these studies, the PIV method can be applied as a reliable technique for providing information regarding joints, joint implant fluid flow and fluid–solid surface interactions in these implants.

One of the areas of interest in the subject of fluid–solid surface interaction is flow slip on solid surface phenomenon. Although no-slip condition is accepted to be valid at macro scale for Newtonian

DOI: 10.1002/ls

fluid, recent studies have challenged the validity of this condition at micro-scales. For a review on the studies of slip condition of Newtonian fluid, refer to the literature.[23,24] These studies focused on the behaviour of water against hydrophobic and hydrophilic surfaces. This method was later applied to investigate the rheology of a non-Newtonian fluid solution of polyethylene oxide in deionised water to investigate the slip and shear stress behaviour of complex fluids near hydrophobic and hydrophilic surfaces.[25,26]

In the present study, the effect of HA on the fluid behaviour versus water in mini-channels with walls of different materials (similar to materials used in TJR) was investigated in the milli-scale.

As a first step, degassed water flowing in a straight mini-channel was studied with micro-PIV method and the velocity profiles compared with analytical solution as a validation process. Several issues to assess the quality of the measurements were addressed. The validated methodology was used to study the behaviour of HA content solutions and different parameters affecting this behaviour.

MATERIAL AND METHOD

Experimental set-up

Micro-PIV working principle is the same as PIV, apply at small length scale. In PIV method, tracing particles are added to the fluid and illuminated with a monochromatic light such as laser in a light sheet to reduce the background noise. By acquiring and cross-correlating sequences of images from the tracing particles in the light sheet, the velocity distribution within the plane of study can be estimated. In micro-PIV, volume illumination is required due to the microscopic length scale and optical access limitation. The system consists of an illumination source and a charge-coupled device camera mounted on a microscope. The illumination source can be continuous or pulsed. Pulsed illumination sources are usually Nd:YAG laser or LED system.[19,27]

The system used consisted of a double pulsed micro-strobe, a high-speed double frame charge-coupled device camera with spatial resolution of 1280×1024 pixel per frame mounted on a microscope with four magnifications (5×, 10×, 20× and 40×). Figure 1 shows a schematic view of the micro-PIV system used

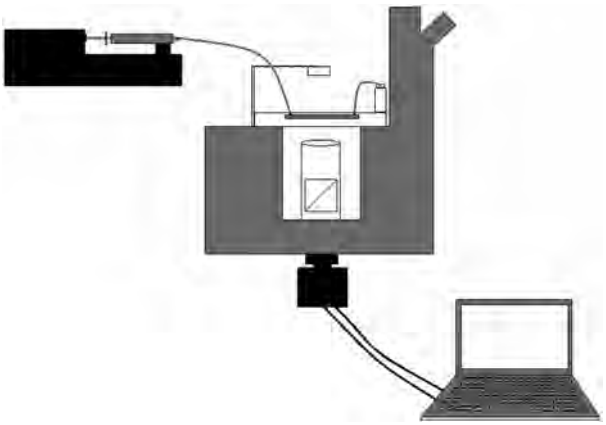

Figure 1. Schematic view of a micro-particle image velocimetry set-up.

DOI: 10.1002/ls

for the measurements. The two pulses had the same time duration, between 50 and 90 μs, based on the micro-strobe power and the fluid speed. The time between two pulses was set as a function of the Reynolds number (Re) (Equation (1)), 200, 600 and 900 μs from the highest Re number to the lowest, respectively.

$$\mathrm{Re} = \rho U D_h / \mu \tag{1}$$

where ρ is the density, U is the mean velocity, μ is the dynamic viscosity of the fluid and D_h is the hydraulic diameter.

A syringe pump 'KDS 410 (KD Scientific Inc. Holliston, Massachusetts, USA)' was used for pumping the liquid with different flow rates through the experimental model. It has 2% accuracy in providing defined flow rate.

A mini-channel was designed and constructed to investigate the effects of different materials and channel sizes on HA behaviour. The channel consisted of three different parts as shown in Figure 2; a Plexiglas plate (back plate) allowing light to travel through the model, a front plate with a glass window for optical access and a middle plate consisting of a steel frame capable of holding bars of different materials. Two different channel widths, 1 mm (hydraulic diameter of 1.33 mm) and 1.5 mm (hydraulic diameter of 1.71 mm), were manufactured and investigated. The depth and length of both channels are 2 and 45 mm, respectively. Hereafter, the 1 mm width channel is named Channel 1 and the 1.5 mm width channel is named Channel 2.

Bars' material was chosen similarly to the one usually used in TJR: UHMWPE, cobalt–chromium–molybdenum alloy and titanium–aluminium–vanadium alloy. The sides of the bars in contact with the fluid were polished to achieve a mirror-like surface. Table I presents the surface roughness of the tested materials.

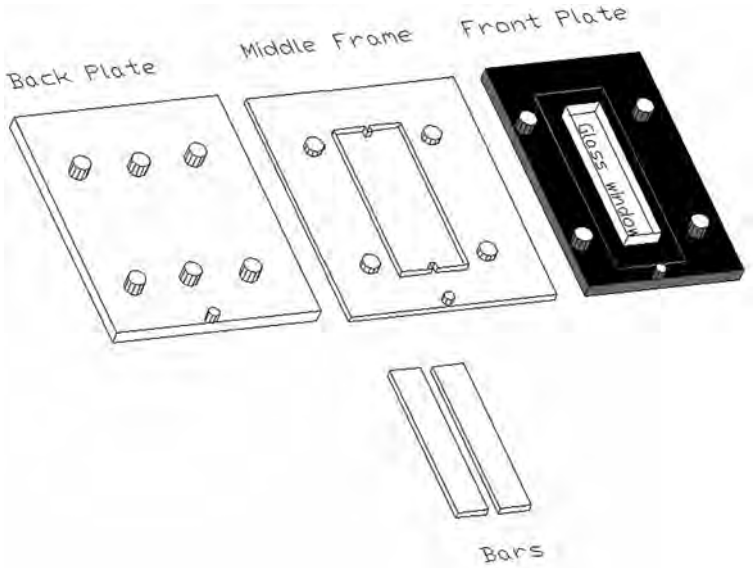

Figure 2. Experimental model.

DOI: 10.1002/ls

Table I. Roughness of different material of the bars.

	Roughness (Ra in μm)	
Material	1st bar	2nd bar
UHMWPE	0.362	0.342
Cobalt–chromium	0.075	0.073
Titanium	0.159	0.162

UHMWPE, ultra-high molecular weight polyethylene.

Experimental fluids and particles

As mentioned earlier, degassed water was tested first. The other experimental fluids were selected to characterise a simplified and similar composition as the joint lubricant.

After the TJR surgery, joint lubricant is called periprosthetic fluid. Although there are not many studies on the composition of this lubricant, available studies suggest that the composition of this liquid is similar to the synovial fluid.[3] In order to have a simple fluid composition with similar viscosity to the periprosthetic fluid, two solutions of HA with molecular weight of 1.5 MDa (Lifecore Biomedical, Mineapolis, Minnesota, USA) and concentration of $3\,\mathrm{mg\,ml^{-1}}$ in phosphate buffer saline (PBS) with 0.15 M concentration (Sigma Aldrich, St. Louis, Missouri, USA) and mixture of 75% PBS and 25% bovine calf serum (Sigma Aldrich 12133C) were studied. For investigating the polymeric behaviour of HA, a more concentrated solution of $5\,\mathrm{mg\,ml^{-1}}$ HA solution in PBS was also tested. HA was dissolved in the liquid (PBS or 75% PBS + 25% serum) at room temperature by gently shaking it for 15 h on a mini-shaker, which provided circular rocking and three-dimensional motion.

The fluids were characterised in a rheometer (Bohlin CVO, Malvern Instruments Ltd., Malvern, Worcestershire, United Kingdom) at 25°C under shear rate control ($0.05–1570\,1\,\mathrm{s^{-1}}$) to obtain the variation of the viscosity versus the shear rate which can be used to derive the shear stress distribution based on following equation:

$$\tau = \mu * \gamma \tag{2}$$

where τ and γ represent shear stress and shear rate, respectively. Figure 3 shows the viscosity versus the shear rate profile.

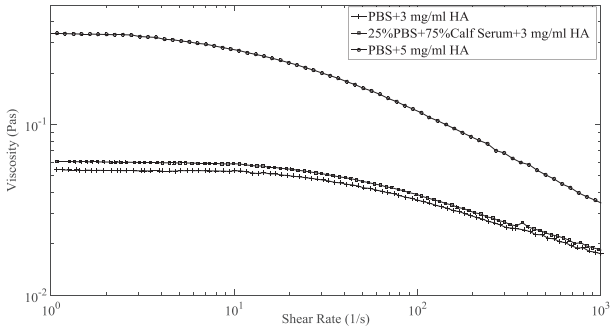

Figure 3. Viscosity changes versus shear rate profile for hyaluronic acid (HA) solutions derived from rheometer measurements. PBS, phosphate-buffer saline.

DOI: 10.1002/ls

The flow rates in Channel 1 were chosen to produce maximum fluid velocity in the same range as in a hip implant based on published studies.[16,17,28] The flow rate in Channel 2 was chosen to have the same Re as the Newtonian fluid (water) in Channel 1. Three Reynolds numbers were chosen: 7.78, 23.33 and 64.17. Flow rates corresponding to these Re are respectively 0.7, 2.1 and 5.775 ml min^{-1} for Channel 1 and 0.82, 2.45 and 6.74 ml min^{-1} for Channel 2. For non-Newtonian fluids, these flow rates were applied, although the Reynolds numbers are not identical. Each measurement was carried out three times to investigate the repeatability. Table II presents a summary of the different cases investigated.

The quality of the acquired data from micro-PIV strongly depends on the seeding particles. The following parameters affect the performances of the particles: visibility, size and density of the particles.

Suitable particles for water are polystyrene particles, which have a density of 1–1.05 g cm^{-3}. Magsphere particles were chosen for this study (Magsphere, Inc., Pasadena, California, USA). These particles contain 0.05% anionic surfactant, which prevents them from agglomeration, a major problem with these types of particles.

A requirement for good micro-PIV measurements is that particles must follow the fluid motion, which could be challenging if due to sedimentation or Brownian effects, particles do not follow the fluid track. In order to solve the sedimentation effect, particle density must be close to the fluid density, and the size of the particles must be kept reasonably small. However, small particles between 50 and 500 nm at low velocities will be affected by Brownian motion. On the other hand, the particle size should be in the order of 3–4 pixels. In the current study, particles with sizes of 2 and 5 μm were chosen for magnification of 20 and 10, respectively.

According to Stoke's drag law, if the density of the particle is different from the liquid density, the induced velocity of the particle due to gravitational forces is[19]

$$V_g = d_p^2 \frac{\left(\rho_p - \rho_l\right)}{18\mu} g \tag{3}$$

Table II. Different measurements conditions.

Fluid	Fluid Name
Water	Fluid-1
PBS + HA 3 mg ml^{-1} solution	Fluid-2
75% PBS + 25% serum + HA 3 mg ml^{-1} solution	Fluid-3
PBS + HA 5 mg ml^{-1} Solution	Fluid-4
Channel width	Channel name
1 mm channel width	Channel 1
1.5 mm channel width	Channel 2
Bar material	Bar name
CoCrMo	Bar-1
UHMWPE	Bar-2
TiAlV	Bar-3
Flow Reynolds number (Newtonian)	Flow name
Re = 7.78	Re-1
Re = 23.33	Re-2
Re = 64.17	Re-3

PBS, phosphate buffer saline; HA, hyaluronic acid; CoCr, MoCobalt Chromium Molybdenum alloy; UHMWPE, ultra-high molecular weight polyethylene; TiAlV, titanium aluminium vanadium alloy.

DOI: 10.1002/ls

where ρ is the density, d is the diameter and μ is the dynamic viscosity. The p index refers to particle, while l refers to liquid. The particle response time is[19]

$$\tau_p = \frac{d_p^2 \rho_p}{18\mu_l} \tag{4}$$

From the aforementioned equations, the response time of a 2 and 5 μm diameter particle is about 2.3×10^{-7} and 0.1×10^{-7} s, respectively. These time scales are much smaller than the liquid time scale $\left(\frac{D_h}{U} = 4.67.10^{-1}\ s\right)$. Therefore, these particles will follow the flow variations. The induced velocity of a 2 and 5 μm diameter particle was calculated to be 1.1×10^{-4} and 6.9×10^{-4} mm s^{-1}, respectively. Therefore, these particles will not face any sedimentation problems.

As mentioned in Raffel *et al.*,[19] the Brownian effect will become significant for particles with diameters of 50 to 500 nm and velocities below 1 mm s^{-1}. This effect will cause an error in the estimation of the velocity. The error can be determined using the following equations:[19]

$$\begin{aligned} \varepsilon_x &= \frac{1}{u}\sqrt{\frac{2D}{\Delta t}} \\ \varepsilon_y &= \frac{1}{v}\sqrt{\frac{2D}{\Delta t}} \end{aligned} \tag{5}$$

where u and v are the fluid velocities in the x and y directions, respectively (Figure 5). Δt is the time interval (the time between frames or images) and D (diffusion coefficient of the particle) is calculated from the following equation:[19]

$$D = \frac{KT_l}{3\pi\mu_l d_p} \tag{6}$$

where K is the Boltzmann's constant and T_l is the liquid absolute temperature. The Brownian error equation shows that by increasing the time interval, the Brownian error decreases. This puts a lower limit for the time interval.[19] The smallest time interval in the current measurements was 200 μs (for highest flow rate). By having the velocity as small as 0.47 mm s^{-1}, which happens for water within less than 15 μm distance to the wall, the Brownian error is 5%. Therefore, the Brownian error should be larger than 5% for near-wall velocity. However, since particles near wall are influenced by the no-slip boundary condition, these equations are not valid in that distance, and correction factors are required. Brenner *et al.* solved the Navier–Stokes equation for creeping flow and provided a correction factor for normal Brownian diffusion.[29] Goldman *et al.* also derived a correction factor for tangential Brownian motion.[30] Combination of these two factors suggests Brownian motions cease at wall.[31]

Measured water velocity profiles in the experimental model were validated with the theoretical solution of Poiseuille flow in a rectangular channel where ($w > h$), obtained from the following equations:[32]

$$\begin{aligned} Q &= 2\int_0^{1/2w} dy \int_0^h dz\, v_x(y,z) \\ &= \frac{h^3 w \Delta p}{12\mu L}\left[1 - \sum_{n.odd}^{\infty} \frac{1}{n^5}\frac{192}{\pi^5}\frac{h}{w}\ \tanh\left(n\pi\ \frac{w}{2h}\right)\right] \end{aligned} \tag{7}$$

DOI: 10.1002/ls

$$v_x = \frac{4h^2\Delta p}{\pi^3 \mu L} \sum_{n,odd}^{\infty} \frac{1}{n^3} \left[1 - \frac{\cosh\left(n\pi \frac{y}{h}\right)}{\cosh\left(n\pi \frac{w}{2h}\right)} \right] * \sin\left(n\pi \frac{z}{h}\right) \tag{8}$$

where Q is the flow rate, h, w and L are channel width, height and length, respectively, (Figure 4) and Δp is pressure difference. The error percentage for the current dimension of $w/h = 2$ is 0.2%.

RESULTS

Water measurements

The size of the interrogation areas used for the data analysis was 16×128 and 32×128 pixels for a magnification of 10 and 20, respectively. The interrogation area size was selected to have at least eight particles in the frame[19] and also to get as close as possible to the wall.[33] Analytical solution showed that in Couette flow, particles motions always have a lag compared with the fluid. This phenomenon is enhanced near the wall, and particles do not follow the fluid movement near the surface. For distances larger than two times the particle diameter, the velocity lag is below 1%. The analysis plane borders were placed at a distance twice that of the particle diameter from each side wall to avoid the high error region. Therefore, the first velocity vector is placed about 20 and 14 μm away from the wall for 10 and 20 magnifications, respectively.

For the frame size of 1280×1024 pixels (1.54×1.24 mm), 15 velocity profiles were derived along the channel as shown in Figure 5. In order to increase the statistic near the wall, the velocity profiles shown later are the average of 10 middle velocity profiles along the channel width. Distance between each two neighbour profiles is 80 μm.

Several aspects of the method were investigated in order to develop a reliable methodology: minimum number of images to get a reliable value of the velocity, repeatability of the results, influence of the magnification and comparison of the experiment to the exact analytical solution.

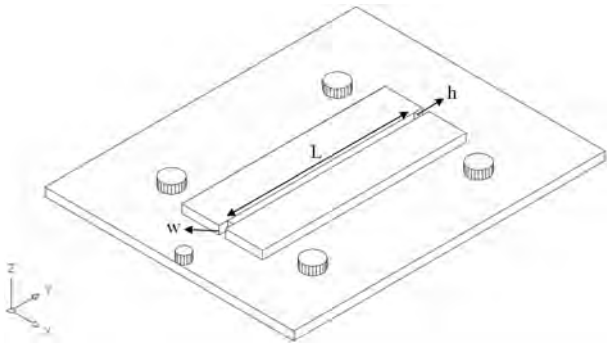

Figure 4. Schematic view of the rectangular channel, L, h and w represents channel length, width and height, respectively.

DOI: 10.1002/ls

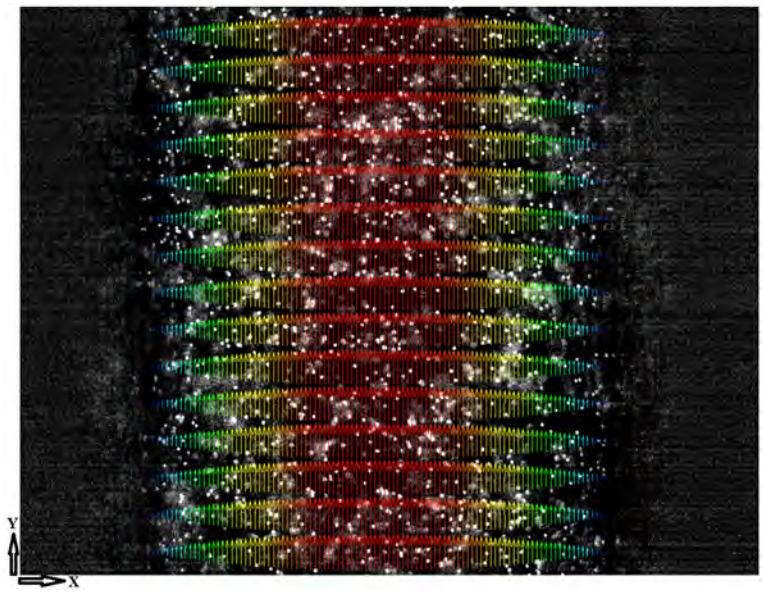

Figure 5. Velocity map of Channel 1, cobalt–chromium–molybdenum alloy bars, Reynolds number 23.33.

To determine the number of images required to get a stable mean value, 1000 images were captured, and the accumulated mean value was evaluated. Comparison of the results for most middle velocity profile with theoretical results showed that at least 300 images were required to get a variation of the mean velocity below 0.5%.

In order to assess the quality of the measurements, a comparison with theory was performed. Velocity profiles along the channel width were made non-dimensional by dividing them with each profile maximum velocity. Figure 6 shows the experimental and theoretical dimensionless profiles;

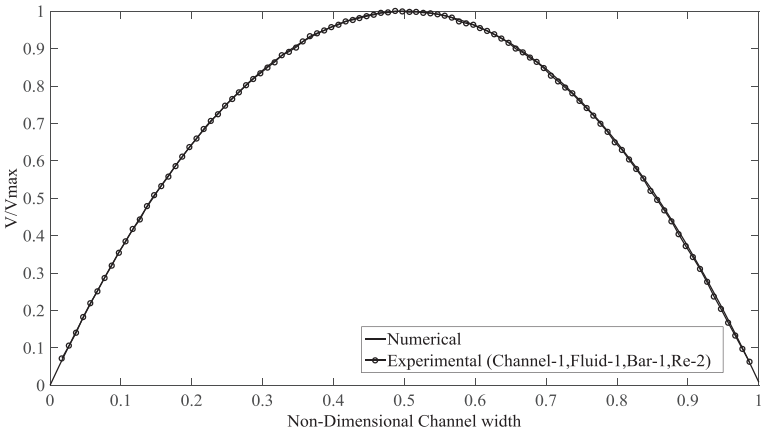

Figure 6. Channel 1, cobalt–chromium–molybdenum alloy bars, Reynolds number (Re) 23.33: non-dimensional velocity profile theory–experiment adjustment.

DOI: 10.1002/ls

the difference is below 1%. In order to investigate fluid behaviour on the solid surface, velocity profiles need to be extrapolated. However, according to Neto *et al.*,[25] the slip length of deionised water near a hydrophobic surface is around 100 nm; this length is lower for water flow on hydrophilic surfaces. These dimensions are far beyond the accuracy of our measurements, so no special behaviour is visible for water measurements.

The compatibility of the results between different magnifications was also addressed. Figure 7 presents results with two magnifications: 10 and 20. The difference is about 1%. This shows that there exists reliable compatibility between different magnifications' results, and for closer look at fluid behaviour near wall, velocity profiles derived from measurements with 20 magnification will be considered.

Hyaluronic acid behaviour

The following section contains velocity profiles of different HA solutions. The object is to investigate the effect of the channel dimension, bar material, HA–protein interaction and HA concentration on the velocity profiles.

Newtonian versus non-Newtonian fluid

Measurements of the velocity with micro-PIV are repeated three times with magnifications of 10 and 20 for Channels 1 and 2 with different materials. Four hundred acquired images were used to derive the velocity profiles.

Figures 8 and 9 present velocity and shear rate profiles, respectively, in the middle of the channel along its width for both water and a HA solution of 3 mg ml^{-1} in PBS. The shear rates are derived from a fourth-order polynomial fit on the experimental results. The HA solution is a non-Newtonian liquid with higher viscosity compare with water, producing a blunter velocity profile. For the Newtonian

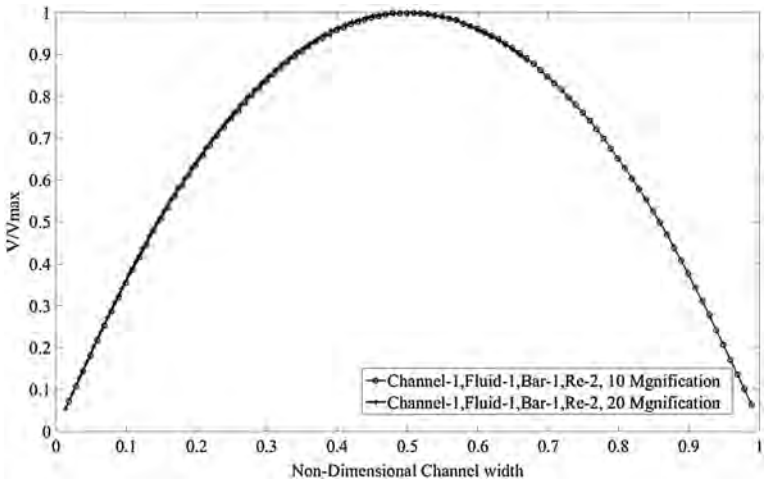

Figure 7. Channel 1, cobalt–chromium–molybdenum alloy bars, Reynolds number (Re) 23.33: average velocity profile of 10 and 20 magnification adjustment.

DOI: 10.1002/ls

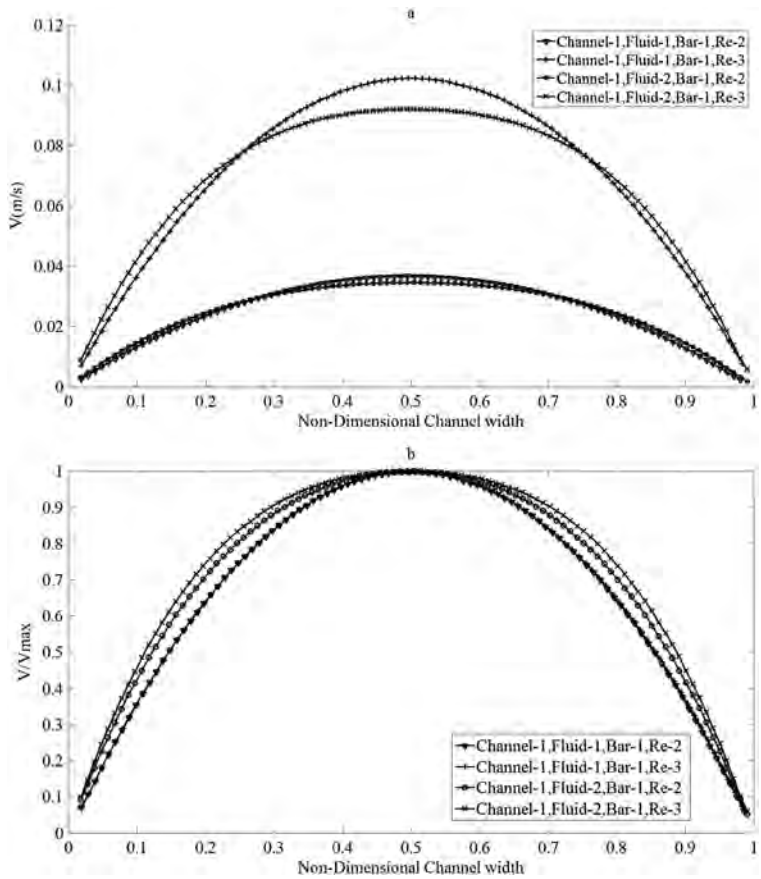

Figure 8. Channel 1: cobalt–chromium–molybdenum alloy bars average velocity profiles of water and hyaluronic acid solution in phosphate buffer saline with 3 mg/ml concentration at Reynolds number (Re) 23.33 and 64.17, (a) velocity profiles in $m\,s^{-1}$ and (b) non-dimensional velocity profiles.

fluid, all non-dimensional velocity profiles are compatible with each other. However, increasing the flow rate for the non-Newtonian fluid gives a blunter non-dimensional velocity profile.

This result illustrates the spatial variation of the HA solution viscosity. For the Newtonian fluid, the shear rate along the channel width changes linearly. This is representative of its parabolic velocity profile. However, there is a non-linear trend for the non-Newtonian fluid, and by decreasing the flow rate, the non-Newtonian shear rate profile leads towards possessing a more linear profile. The experiments were designed to have a maximum fluid velocity similar to hip joint maximum fluid velocity; acquired shear rates are smaller compared with what is usually considered for the real hip joints. At very high shear rates, the synovial fluid shows Newtonian behaviour with constant viscosity at a value close to water. As the main goal of the present study is to investigate the non-Newtonian fluid characteristic on the flow behaviour and the fluid–solid surface interaction, very high shear rates near solid surface are not favourable and avoided.

DOI: 10.1002/ls

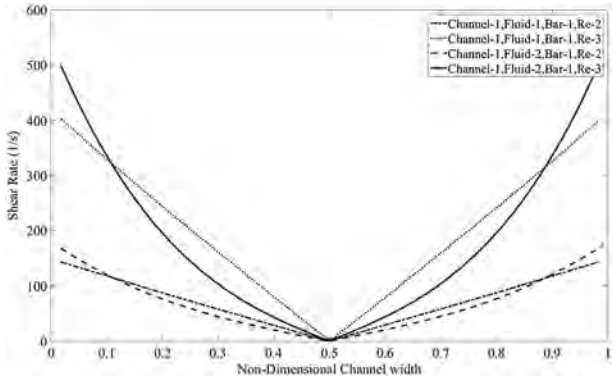

Figure 9. Channel 1: cobalt–chromium–molybdenum alloy bars average shear rate profiles of water and hyaluronic acid solution in phosphate buffer saline with 3 mg ml^{-1} concentration at Reynolds number (Re) 23.33 and 64.17.

HA–protein interaction

As stated in previous studies, complex interactions between the HA chain and the protein provides the rheopectic behaviour for synovial fluid.[14] In order to investigate whether this interaction has an effect on the behaviour of HA solution in the channel, velocity profiles of HA solution in PBS and HA solution in 75% PBS and 25% calf serum are presented dimensionless at different flow rates in Figure 10.

The capturing time for 400 images is about 45 s. Adding protein to the HA solution with concentration of 3 mg ml^{-1} does not change its flowing behaviour and shear stresses during this small amount of time.

Channel size effect

Since the viscosity of non-Newtonian fluids is shear dependent, under constant measurement condition, Re of these fluids are different from Newtonian one. Calculating Re of a non-Newtonian fluid is a complex procedure.[34] As explained earlier in this study, the Newtonian Re is kept constant for the measurements conducted in different channel sizes, and flow rates corresponding to these Reynolds numbers for Newtonian fluids are also applied for non-Newtonian fluids. Therefore the Re of the non-Newtonian fluid is not the same for different channel sizes. Figure 11 shows non-dimensional velocity profiles along the non-dimensional channel width for Channels 1 and 2.

Channel 1 shows blunter non-dimensional velocity profiles. This difference is very insignificant. However, it suggests that under this situation, the non-Newtonian fluid does not have same behaviour in two channels.

Bar material effect

Slip of the flow near hydrophobic surfaces increases, which can cause an increase in flow rate compared with Poiseuille flow and consequently increment in velocity profile.[31] Therefore, changes in velocity profile derived from channels with different degree of hydrophobicity (UHMWPE or

DOI: 10.1002/ls

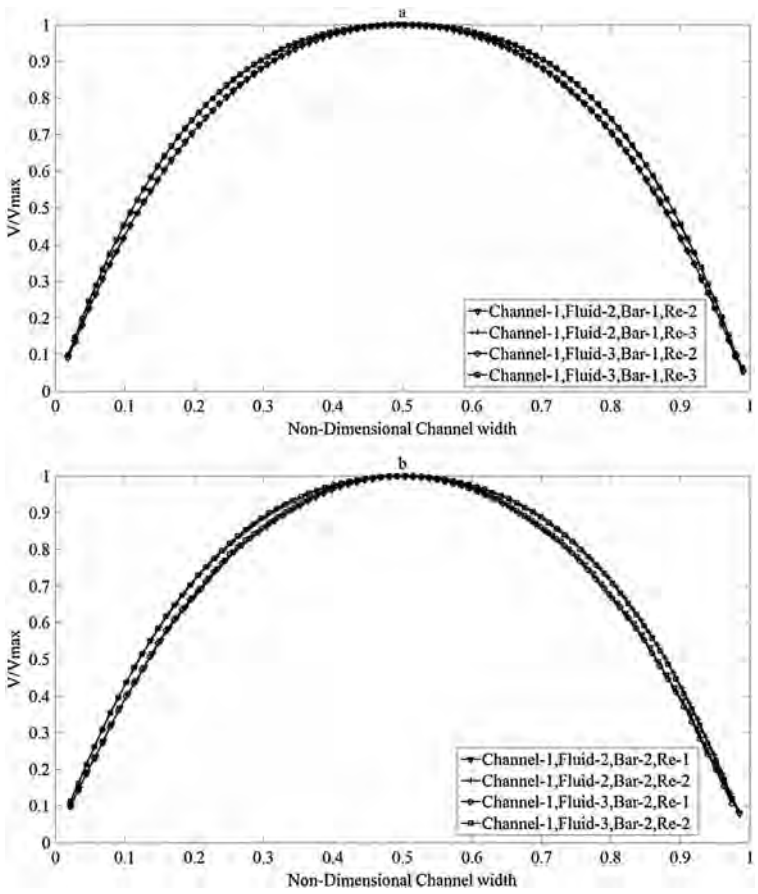

Figure 10. Channel 1: (a) cobalt–chromium–molybdenum alloy bars and (b) ultra-high molecular weight polyethylene bars, non-dimensional average velocity profiles of hyaluronic acid solutions with 3 mg ml^{-1} concentration in phosphate buffer saline and mixture of 75% PBS + 25% calf serum at different Reynolds number.

cobalt–chromium–molybdenum alloy)[35] surfaces show the effectiveness of the slip on different surface materials. Figure 12 shows the velocity profiles in channels with different material bar.

Results present a difference below 1% in velocity magnitude for channels with UHMWPE bars compared with the other two channels bars. This suggests that the slip flow effect is negligible compared with the channel size.

HA concentration effect

Polymer solution behaviour strongly depend on the concentration of the polymer in the solution as mentioned in the literature;[25,26] increasing the concentration provides more slip flow behaviour.

DOI: 10.1002/ls

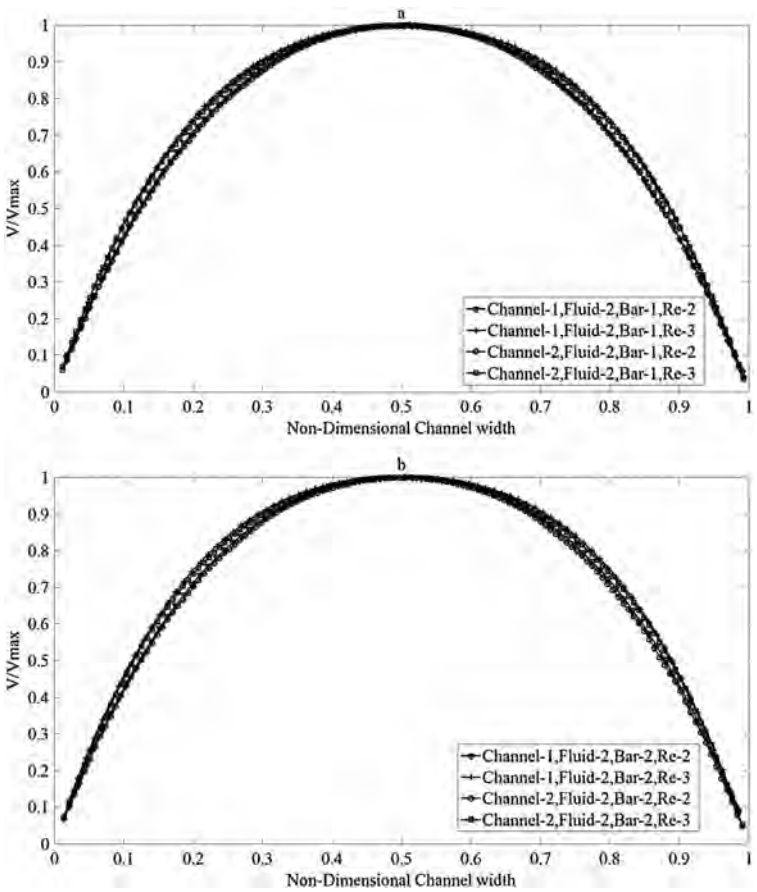

Figure 11. Channel 1 and 2: (a) cobalt–chromium–molybdenum alloy bars and (b) ultra-high molecular weight polyethylene, non-dimensional average velocity profiles of hyaluronic acid solution with 3 mg ml^{-1} concentration in phosphate buffer saline at Reynolds number (Re) 23.33 and 64.17.

More concentrated solutions enhances the special polymeric behaviour of the HA. HA solution of 5 mg ml^{-1} in PBS was tested and compared with that of 3 mg ml^{-1} concentration one. This increment in concentration may specifically lead to slip flow on the walls. Figure 13 presents velocity profiles of HA solutions in PBS for Channel 1 and two different channel bar materials. By extrapolating the velocity profiles, behaviour of the fluid near the wall can be investigated. These results show that the behaviour of higher concentrated HA solution near solid wall is different from the lower one and the velocity does not reach zero at the wall. This situation is enhanced near UHMWPE, which is both hydrophobic and rougher.

Figures 14 and 15 provide a closer look at the situation near the wall for two different HA concentration solutions and water. These velocity profiles are derived with magnification 20×, which improves the spatial resolution by a factor of 2.

DOI: 10.1002/ls

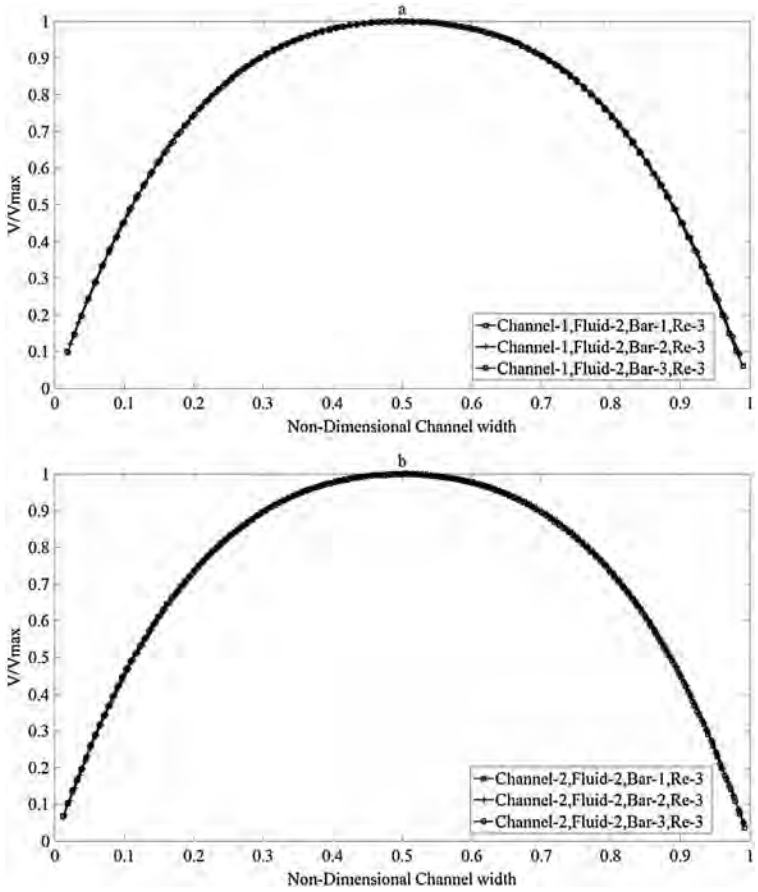

Figure 12. (a) Channel 1: different material bars, Reynolds number (Re) 64.17 and (b) Channel 2: different material bar, Re 23.33 non-dimensional average velocity profile.

Figures 13–15 results show that the wall slip is an apparent phenomenon for the higher concentration HA solution especially near a hydrophobic surface. For the HA solution with 3 mg/ml concentration, the wall slip near the most hydrophobic (UHMWPE) surface is negligible. Near other surfaces, this HA solution behaves mostly like water, and the slip phenomenon may occur; however, its magnitude is beyond the accuracy of our measurement set-up and could not be captured.

Figures 16 and 17 show shear rates along channel width for two different concentrations of HA solution in channels with two different bar materials.

These two figures show that although for higher concentration of the polymeric solution, slip behaviour enhances, slip length is still negligible compare with channel length and the velocity profiles in channels with different bar materials are not different significantly. Both the shear rate and the

DOI: 10.1002/ls

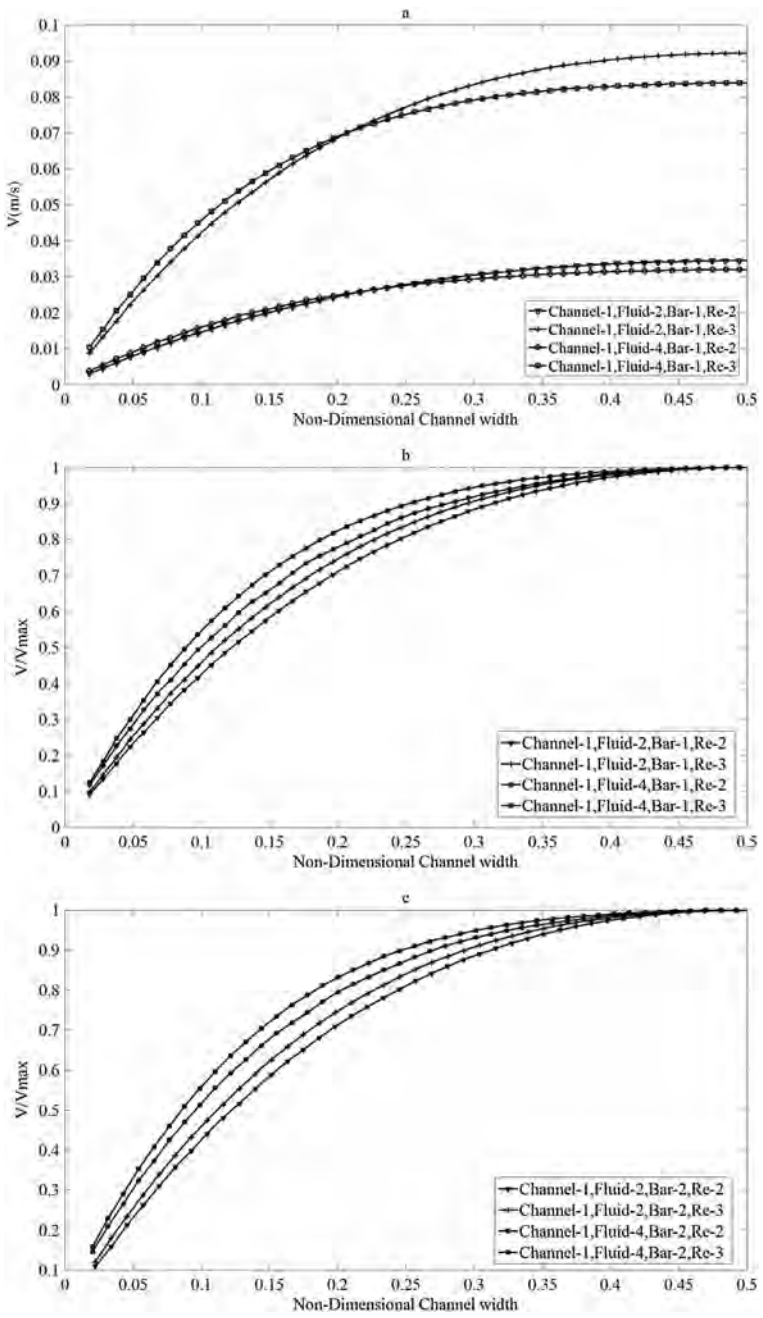

Figure 13. Channel 1: average velocity profiles of hyaluronic acid solutions in phosphate buffer saline with 3 mg ml^{-1} and 5 mg ml^{-1} concentration at Reynolds number (Re) 23.33 and 64.17, (a) cobalt–chromium–molybdenum bars velocity profiles in m s^{-1}, (b) cobalt–chromium–molybdenum bars non-dimensional velocity profiles and (c) ultra-high molecular weight polyethylene bars non-dimensional velocity profiles.

DOI: 10.1002/ls

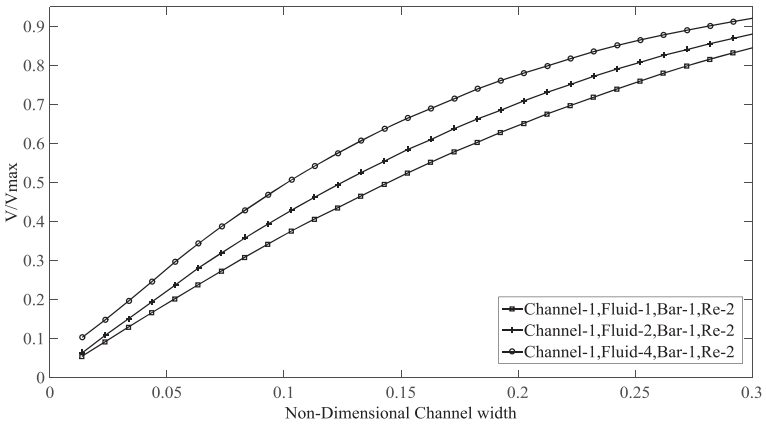

Figure 14. Channel 1: cobalt–chromium–molybdenum alloy bars Reynolds number (Re) 23.33, non-dimensional average velocity profile.

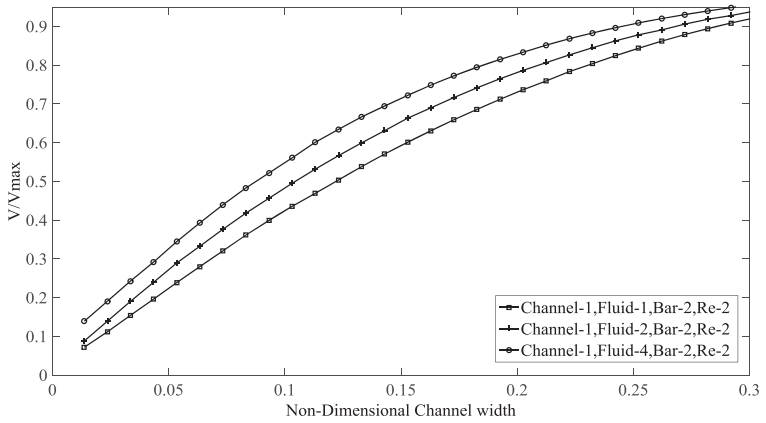

Figure 15. Channel 1: ultra-high molecular weight polyethylene bars Reynolds number (Re) 23.33, non-dimensional average velocity profile.

corresponding viscosity are higher near channel walls for higher concentration solution, resulting in higher wall shear stress.

DISCUSSION

This study focused on steady state flow behaviour of biopolymer solution inside a mini-channel. Composition of this solution is similar to artificial joints' lubricant. The final goal is to investigate the fluid non-Newtonian characteristic effect on velocity distribution and fluid–solid interaction inside the channel.

DOI: 10.1002/ls

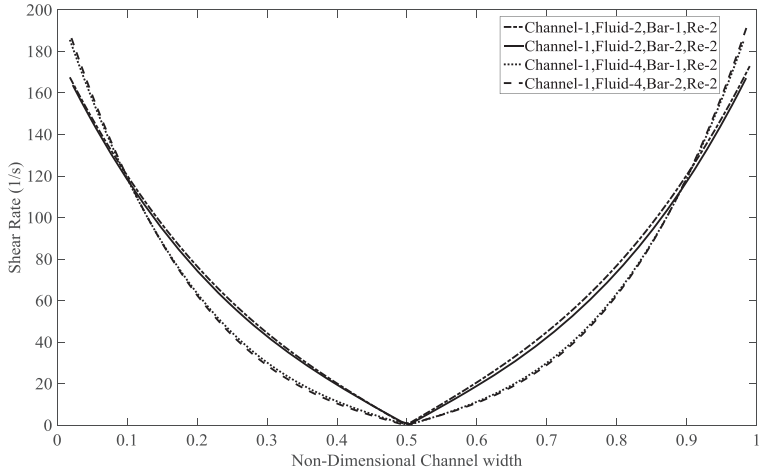

Figure 16. Channel 1: Reynolds number (Re) 23.33, average shear rate profiles along channel width of cobalt–chromium–molybdenum alloy and ultra-high molecular weight polyethylene bars.

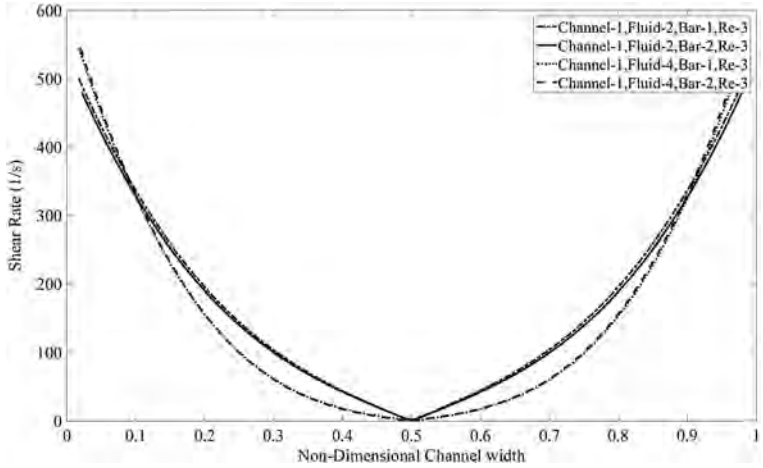

Figure 17. Channel 1: Reynolds number (Re) 64.17, average shear rate profiles along channel width of cobalt–chromium–molybdenum alloy and ultra-high molecular weight polyethylene bars.

Dependency of the viscosity on shear rate in HA solutions is the key factor in different behaviour between Fluid 1, 2 and 4. These shear thinning fluids have three characteristic regions:[36]

- low shear rate plateau where at low shear rates the fluid behaves as Newtonian;
- shear thinning region where the viscosity decreases by increasing shear rate; and
- high shear rate plateau where at very high shear rate, the fluid behaves as Newtonian again with viscosity similar to the solvent viscosity.

DOI: 10.1002/ls

Figure 3 shows low shear rate plateau and shear thinning region. Most frequent equation applied for quantifying the polymer behaviour in shear thinning region is the power law model as Equation (9).[37]

$$\mu = m\dot{\gamma}^{n-1} \tag{9}$$

The aforementioned equation is a line fitted on the shear thinning region of the double logarithmic plot of the viscosity–shear rate. $n-1$ is the slop of the line, and n is called the power law index. m is the consistency index, the intercept of the line with the shear rate of 1 1/s. Power law indices of the Fluid 2 and Fluids 4 are 0.685 and 0.469, respectively.

In a circular tube, the Newtonian shear rate distribution is known as an apparent shear rate of a non-Newtonian fluid with the same flow rate. The relation between an apparent and true wall shear rate in a rectangular cross section is as in Equation (10):[38]

$$\dot{\gamma}_{true} = \frac{2n+1}{3n}\dot{\gamma}_{apparent} \tag{10}$$

Since in current study the first velocity vector is placed 20 μm away from the wall, wall shear rate is unknown. However, comparing the nearest shear rate to the wall presented in Figure 9 with the shear rate calculated from Equation (10) shows if this relation is applicable for near wall shear rates or not. Closest shear rate to the channel wall for Channel 1 and Fluid 1 at Re-2 and Re-3 are 142.8 and 402.6 1/s, respectively. At Re-2, the true shear rates for Fluid 2 and Fluid 4 derived from Equation (10) are 159 and 180.3 1/s respectively. These values have 2% for Fluid 2 and 5% for Fluid 4 differences from the values showed in Figure 16. At Re-3, the differences between the predicted shear rates from Equation (10) with the shear rates shown in Figure 17 are 6% and 5% for Fluid 2 and Fluid 4, respectively. Since the pump accuracy is 2%, parts of these differences are related to the systematic errors.

To investigate the effect of the channel size on the non-Newtonian behaviour of the solution, non-Newtonian Re should be quantified. For the fluid following the power law behaviour, Delplace derived Equation (11) as a generalised Re number for flow inside a duct with arbitrary cross section:[39]

$$\mathrm{Re}_{general} = \frac{\varphi U^{2-n} D_H^n}{m\{(24n+\xi)/(24+\xi)n\}^n \xi^{n-1}} \tag{11}$$

where ξ is geometrical parameter that depends only on the cross-sectional shape. For Channel 1 and Channel 2, this parameter has values of 7.774 and 7.238, respectively.

Based on aforementioned equation, Fluid 2 has Re of 0.74 and 0.63 for Channel 1 and Channel 2, respectively, while these values for Fluid 4 are 0.26 and 0.2. This suggests that keeping Newtonian Re constant for different geometries results in higher Re discrepancy for shear thinner fluids (smaller n value).

The entanglement conditions of the current HA solutions were not studies. However based on a previous study, for HA solutions in PBS with molecular weight of 1.5 MDa, the entanglement concentration is 2.4 mg ml^{-1}.[11] Therefore, it can be concluded that there are entanglements between HA chains of both Fluid 2 and Fluid 4. Results of adding protein to HA solution show that under steady-state situation, the biopolymer solution behaviour relies mostly on the HA concentration rather than the solvent–polymer interaction. This behaviour was also reported before that protein content

DOI: 10.1002/ls

effect on the rheological behaviour of the HA solutions is considerable at HA solutions with concentration lower than entanglement concentration.[40] Oates *et al.* showed that different HA solution rheological behaviour in the presence of protein is due to the protein agglomeration. Protein agglomeration form at quiescent condition and high shear rates retard this procedure.[14] Therefore, under shear rates of this experiment, these structures do not form.

To investigate the slip behaviour near channel wall, most studies extrapolated the velocity profiles to the channel walls.[25,26,41] However, this method is not found accurate enough and applicable in the current study to investigate the wall-slip behaviour. The nearest reliable velocity vector distance from the wall is placed 14 to 20 μm away from the wall. Therefore, it is not possible to judge based on the available data what is the velocity situation at the wall.

CONCLUSION

A methodology for studying bio-based fluid in mini-channels was developed by investigating different factors such as tracing particles, repeatability, theory-experiment and different magnifications adjustment. The HA solution behaviour away from the wall is irrelevant to the material of the solid walls. Moreover, although protein interaction with the HA chain changes the viscosity of the non-Newtonian fluid, it does not affect the behaviour of the HA solution in a duct channel. Increasing the solution concentration from 3 to 5 mg ml^{-1} considerably enhances the polymeric behaviour of the solution. For the flow in channel, there are definite differences between water and the HA solution behaviours especially at small scales (micro scales) even at low concentration.

ACKNOWLEDGEMENTS

The authors' gratitude goes to the Doctoral Program DocMASE for the financial support and SANDVIK and CELANESE/TICONA for providing test materials.

REFERENCES

1. Ingham E, Fisher J. Biological reactions to wear debris in total joint replacement. *Proceedings of the Institution of Mechanical Engineers. Part H, Journal of Engineering in Medicine* 2000; **214**(1):21–37. DOI:10.1243/0954411001535219.
2. Balazs EA. The physical properties of synovial fluid and the special role of hyaluronic acid, in *Disorders of the Knee*, A Helfet (ed.), T. B. Lippincott Co., Philadelphia 1974: 63–75.
3. Fam H, Bryant JT, Kontopoulou M. Rheological properties of synovial fluids. *Biorheology* 2007; **44**(2):59–74.
4. Mazzucco D, Scott R, Spector M. Composition of joint fluid in patients undergoing total knee replacement and revision arthroplasty: correlation with flow properties. *Biomaterials* 2004; **25**(18):4433–4445. DOI:10.1016/j.biomaterials.2003.11.023.
5. Chiroiu V, Mosneguţu V, Munteanu L, Ioan R. On a micromorphic model for the synovial fluid in the human knee. *Mechanic Research Communications* 2010; **37**(2):246–255. DOI:10.1016/j.mechrescom.2009.12.003.
6. Neville A, Morina A, Liskiewicz T, Yan Y. Synovial joint lubrication — does nature teach more effective engineering lubrication strategies? *Proceedings of the Institution of Mechanical Engineers, Part C* 2007; **221**(10):1223–1230.
7. Dahl LB, Dahl IM, Engstrom-Laurent A, Granath K. Concentration and molecular weight of sodium hyaluronate in synovial fluid from patients with rheumatoid arthritis and other arthropathies. *Annals of the Rheumatic Diseases* 1985; **44**(12):817–822.
8. Fouissac E, Milas M, Rinaudo M. Shear-rate, concentration, molecular weight, and temperature viscosity dependences of hyaluronate, a wormlike polyelectrolyte. *Macromolecules* 1993; **26**(25):6945–6951.
9. Meyer F, Lohmann D, Kulicke W. Determination of the viscoelastic behavior of sodium hyaluronate in phosphate buffered saline with rheo-mechanical and rheo-optical methods. *Journal of Rheology (1978-present)* 2009; **53**(4):799–818.

10. Bingöl A, Lohmann D, Püschel K, Kulicke WM. Characterization and comparison of shear and extensional flow of sodium hyaluronate and human synovial fluid. *Biorheology* 2010; **47**(3):205–224.
11. Krause WE, Bellomo EG, Colby RH. Rheology of sodium hyaluronate under physiological conditions. *Biomacromolecules* 2001; **2**(1):65–69.
12. Haward SJ, Jaishankar A, Oliveira MSN, Alves MA, McKinley GH. Extensional flow of hyaluronic acid solutions in an optimized microfluidic cross-slot device[a]. *Biomicrofluidics* 2013; **7**:044108 (2013). DOI: 10.1063/1.4816708
13. Mendichi R, Šoltés L, Giacometti Schieroni A. Evaluation of radius of gyration and intrinsic viscosity molar mass dependence and stiffness of hyaluronan. *Biomacromolecules* 2003; **4**(6):1805–1810.
14. Oates KM, Krause WE, Jones RL, Colby RH. Rheopexy of synovial fluid and protein aggregation. *Journal of the Royal Society Interface* 2006; **3**(6):167–174. DOI:10.1098/rsif.2005.0086.
15. Jin Z, Dowson D. A full numerical analysis of hydrodynamic lubrication in artificial hip joint replacements constructed from hard materials. *Proceedings of the Institution of Mechanical Engineers, Part C* 1999; **213**(4):355–370.
16. Jin ZM, Dowson D, Fisher J. Analysis of fluid film lubrication in artificial hip joint replacements with surfaces of high elastic modulus. *Proceedings of the Institution of Mechanical Engineers. Part H* 1997; **211**(3):247–256.
17. Jalali-Vahid D, Jagatia M, Jin Z, Dowson D. Prediction of lubricating film thickness in UHMWPE hip joint replacements. *Journal of Biomechanics* 2001; **34**(2):261–266.
18. Vennemann P, Lindken R, Westerweel J. *In vivo* whole-field blood velocity measurement techniques. *Experiments in Fluids* 2007; **42**(4):495–511. DOI:10.1007/s00348-007-0276-4.
19. Raffel M, Willert CE, Wereley ST, Kompenhans J. *Particle Image Velocimetry: A Practical Guide*. Springer: Berlin, 2007.
20. Lindken R, Rossi M, Grobe S, Westerweel J. Micro-particle image velocimetry (micro-PIV): recent developments, applications, and guidelines. *Lab on a Chip* 2009; **9**(17):2551. DOI:10.1039/B906558J.
21. Garcia V, Dias R, Lima R. Vitro blood flow behaviour in microchannels with simple and complex geometries, in *Applied Biological Engineering — Principles and Practice*, INTECH 2012: 393–416. DOI: 10.5772/2101.
22. Brown TD, Lundberg HJ, Pedersen DR, Callaghan JJ. Nicolas Andry Award: clinical biomechanics of third body acceleration of total hip wear. *Clinical Orthopaedics and Related ResearchÂ®* 2009; **467**(7):1885–1897. DOI:10.1007/s11999-009-0854-2.
23. Rothstein JP. Slip on superhydrophobic surfaces. *Annual Review of Fluid Mechanics* 2010; **42**:89–109.
24. Neto C, Evans DR, Bonaccurso E, Butt HJ, Craig VSJ. Boundary slip in Newtonian liquids: a review of experimental studies. *Reports on Progress in Physics* 2005; **68**(12):2859.
25. Joseph P, Tabeling P. Direct measurement of the apparent slip length. *Physical Review E* 2005; **71**(3)**:**035303. DOI: 10.1103/PhysRevE.71.035303
26. Degré G, Joseph P, Tabeling P, Lerouge S, Cloitre M, Ajdari A. Rheology of complex fluids by particle image velocimetry in microchannels. *Applied Physics Letters* 2006; **89**(2). DOI:10.1063/1.2221501.
27. Wereley ST, Meinhart CD. Recent advances in micro-particle image velocimetry. *Annual Review of Fluid Mechanics* 2010; **42**:557–576. DOI:10.1146/annurev-fluid-121108-145427.
28. Dowson D, McNie C, Goldsmith A. Direct experimental evidence of lubrication in a metal-on-metal total hip replacement tested in a joint simulator. *Proceedings of the Institution of Mechanical Engineers, Part C* 2000; **214**(1):75–86.
29. Brenner H. The slow motion of a sphere through a viscous fluid towards a plane surface. *Chemical Engineering Science* 1961; **16**(3):242–251.
30. Goldman AJ, Cox RG, Brenner H. Slow viscous motion of a sphere parallel to a plane wall — I Motion through a quiescent fluid. *Chemical Engineering Science* 1967; **22**(4):637–651. DOI:10.1016/0009-2509(67)80047-2.
31. Kihm KD. *Near-field Characterization of Micro/Nano-scaled Fluid Flows*. Springer: Berlin, 2011.
32. Bruus H. *Theoretical Microfluidics*. Oxford University Press, New York 2008.
33. Goldman A, Cox R, Brenner H. Slow viscous motion of a sphere parallel to a plane wall — II Couette flow. *Chemical Engineering Science* 1967; **22**(4):653–660.
34. Madlener K, Frey B, Ciezki H. Generalized Reynolds number for non-Newtonian fluids. *Progress in Propulsion Physics* 2009; **1**:237–250.
35. Fam H. Effect of composition on periprosthetic fluid rheology and friction in total knee arthroplasty. PhDThesis, Queen's University: Kingston, 2010.
36. Vazquez M, Schmalzing D, Matsudaira P, Ehrlich D, McKinley G. Shear-induced degradation of linear polyacrylamide solutions during pre-electrophoretic loading. *Analytical Chemistry* 2001; **73**(13):3035–3044.
37. Kontopoulou M. *Applied Polymer Rheology: Polymeric Fluids with Industrial Applications*. John Wiley & Sons: Hoboken, 2011.
38. Pipe CJ, Majmudar TS, McKinley GH. High shear rate viscometry. *Rheologica Acta* 2008; **47**(5):621–642.

39. Delplace F, Leuliet JC. Generalized Reynolds number for the flow of power law fluids in cylindrical ducts of arbitrary cross-section. *The Chemical Engineering Journal and the Biochemical Engineering Journal* 1995; **56**(2):33–37. DOI:10.1016/0923-0467(94)02849-6.
40. Tirtaatmadja V, Boger D, Fraser J. The dynamic and steady shear properties of synovial fluid and of the components making up synovial fluid. *Rheologica Acta* 1984; **23**(3):311–321.
41. Poelma C, Vennemann P, Lindken R, Westerweel J. *In vivo* blood flow and wall shear stress measurements in the vitelline network. *Experiments in Fluids* 2008; **45**(4):703–713. DOI:10.1007/s00348-008-0476-6.

Paper B

Viscoelastic Behavior Effect of Hyaluronic Acid on Reciprocating Flow inside Mini-Channel

Reprinted with permission

LUBRICATION SCIENCE
Lubrication Science (2016)
Published online in Wiley Online Library (wileyonlinelibrary.com). DOI: 10.1002/ls.1344

Viscoelastic behaviour effect of hyaluronic acid on reciprocating flow inside mini-channel

Alaleh Safari[1,*,†], Michel J. Cervantes[2,3] and Nazanin Emami[1,*,†]

[1]*Biotribology group, Division of Machine Element, Luleå University of Technology, 97187, Luleå, Sweden*
[2]*Division of Fluid and Experimental Mechanics, Luleå University of Technology, 97187, Luleå, Sweden*
[3]*Water Power Laboratory, Norwegian University of Science and Technology, 7491, Trondheim, Norway*

ABSTRACT

One of the most successful surgeries during the 21st century is total joint replacement (TJR) with material combination of polymer-on-metal (PoM). Despite its success, wear particle generation at the interface of the polymer and metal causes eventually implant loosening. Investigating and understanding the wear particles distribution should help in designing implants with better performances. First step towards characterising wear particle distribution is deriving the lubricant behaviour and velocity distribution inside implant gap.

Different hyaluronic acid (HA) solutions were subjected to a sinusoidal movement in straight rectangular channels. The velocity profiles along the channel width were measured with Micro Particle Image Velocimetry. HA solution behaviour was found to be dependent on the concentration. Results showed significant differences between the water (Newtonian) and HA behaviour in unsteady flow. The unsteady behaviour of the lubricant depended strongly on its non-Newtonian viscoelastic behaviour which was due to the time dependent nature of HA solution. Copyright © 2016 John Wiley & Sons, Ltd.

Received 1 February 2016; Revised 26 May 2016; Accepted 11 June 2016

KEY WORDS: viscoelasticity; reciprocating motion; hyaluronic acid; joint lubricant

INTRODUCTION

Synovial fluid (SF) is a lubricant found in natural joints. This fluid acts as a lubricant and mechanical stress absorber during joint movements. Two of the most important joint diseases (osteoarthritis or rheumatoid arthritis) originate with a change in this fluid's chemical and/or physical composition.[1] Moreover during total joint replacement (TJR) surgery, the fluid composition changes as well. Any change in the composition of SF directly affects its performance; this is especially important in TJR. In the most conventional combination of hip prosthesis, a polymeric acetabular cup moves against a

*Correspondence to: Alaleh Safari and Nazanin Emami, Machine Element, Luleå University of Technology, 97187 Luleå, Sweden.
†E-mail: Alaleh.safari@ltu.se; Nazanin.Emami@ltu.se

metal/ceramic counter surface (PoM combination). The lubrication regime for this joint implant is in the range of elastohydrodynamic (EHL) to boundary lubrication.

One of the major sources of failure in TJR is the generated wear particles at the interface of the implant. Many studies have been focused on improving the wear characteristic of the implant materials or the lubrication of joint implants in order to reduce the wear particles generation.[2–4] However, there is a lack of knowledge on the distribution pattern of these particles. These particle releases in the implant lubricant and their size and density suggest that they follow the fluid movements.[5] The fluid dynamic behaviour and velocity distribution of the lubricant inside the implant gap are thus of primary importance to understand the particle movement. SF behaviour, velocity and pressure distribution inside the joints gap are strongly affected by its non-Newtonian shear-thinning and viscoelastic characteristics.[6,7] The viscoelasticity and shear-thinning of SF depend mainly on the molecular weight and concentration of HA content inside the lubricant.

Different studies have focused on the composition and rheological behaviour of SF from diseased joints (osteoarthritis or rheumatoid arthritis) and periprosthetic fluid (generated SF after TJR surgery).[8–10] Results show that HA molecular weight, concentration and SF viscoelasticity and shear thinning decrease in a diseased joint compared to a healthy one, for a review refer to.[1] SF is a dialysate of blood plasma. The lubricity characteristic of SF is dependent on proteoglycan (0.05–0.35 mg ml^{-1}), hyaluronan (1–4 mg ml^{-1}) and surface active phospholipids (0.1 mg ml^{-1}).[1,8,11] The non-Newtonian shear thinning and viscoelastic behaviour of SF are attributed to the hyaluronic acid (HA) content. HA is the commercial name for sodium hyaluronate (NaHA) which is a linear biopolymer.[12] In normal SF, the concentration of HA is 1.45–4.22 mg ml^{-1} with molecular weight of 6.7–7.6 MDa.[13] These parameters decrease in pathological SF.[1,14] Oates et al.[15] showed that protein aggregation provides SF with the rheopectic behaviour. The common result of studies on the composition of normal and pathological SF showed that in pathological SF (compared to normal SF), both concentration and molecular weight of HA decreased and the proportionality of the HA concentration to the protein also changed.[1,8,13,16]

The viscoelastic property of SF was discovered in 1950.[1,17] SF has both viscous (at low strain rate or slow joint activity) and elastic characteristics (at high strain rate or higher joint activity). Later, several studies were conducted to characterise the viscoelastic behaviour of normal and pathological SF.[8,18–20] The frequency at which elastic (storage) module dominate the viscous (loss) module is called the crossover frequency.[16,21] Studies on different SFs showed that the crossover frequency increased for pathological SF and in elderly people compared to healthy and young people, respectively. In some extreme cases, e.g. after TJR surgery, there is no crossover frequency in the normal frequency range of joint motion; the SF acts only as a viscous liquid.[1,9]

There are several studies on the rheological properties of HA and most of them study viscosity or viscoelasticity of HA solutions at different concentrations, molecular weight or type of solvent.[22–27] These studies mostly concentrated on deriving viscosity-shear rate dependencies, viscoelastic behaviour regarding concentration and molecular weight of HA solutions, intrinsic viscosity relationships to the concentration and molecular weight of HA, effect of HA chain interaction with other molecules (e.g. proteins or sodium chloride), temperature and solution pH on the rheological behaviour. Results of the viscoelastic behaviour characterisation show that by increasing molecular weight or concentration of HA in the solution, the crossover frequency decreases and the viscoelastic behaviour improves. However, the effect of higher molecular weight on the elastic behaviour of HA is stronger than the concentration.[23,26] Lower pH also makes the HA stiffer and enhances the elastic behaviour of the solution.[27] Adding sodium chloride to the HA solution suppresses the electrostatic repulsion between

DOI: 10.1002/ls

HA molecules, resulting in lower viscosity and increments of cross over frequency in dynamic viscoelasticity measurements.[22] Protein agglomerations provide a tight network around the HA chains and increase the entanglements between HA macromolecules in the solution.[15] However, it was stated that the viscoelasticity of SF is not affected by change in its protein content.[16]

The viscoelastic and shear-thinning behaviour of HA or SF has mostly been studied through measurements conducted with rheometers. However, to the best of our knowledge there is no investigation on how these characteristics affect the fluid flow behaviour in the joint gap. Quantification of the effect of different parameters such as the HA concentration or protein content, fluid flow type (steady, unsteady, etc.) and the gap shape on the fluid behaviour are necessary to fully understand the mechanisms. In this study, HA solutions (with similar composition to periprosthetic fluid) subjected to unsteady (sinusoidal) movements in a straight rectangular channel, mimicking the reciprocal flow within a joint during movement, were investigated. The viscoelastic effect on flow behaviour, velocity profile distribution and the effect of concentration or protein content on the behaviour were investigated and compared to measurements with water. The simplified geometry of the experimental model eliminated the geometrical effect on the lubricant flow allowing investigating the lubricant composition, unsteadiness and viscoelastic non-Newtonian characteristic effect on the lubricant behaviour. The results provided an overview of the flow behaviour inside the joint gap of TJR. Potential effect on the wear debris movement and distribution pattern may be deduced. Micro Particle Image Velocimetry (Micro-PIV) was used in order to visualise the oscillatory flow behaviour of HA solutions and degassed water in a rectangular mini channel (for reference 5).

MATERIALS AND METHOD

Experimental setup

Previous study showed the suitability of micro-PIV to study biopolymer solution flow behaviour at small scales.[5] The working principle of micro-PIV is the same as the PIV method for small scales. In the PIV method, tracing particles are added to the fluid. Particles are illuminated with a pulsed light, which is usually a Nd:YAG laser or LED.[28,29] Sequences of images are captured by a charge coupled device (CCD) camera through a microscope and cross-correlated to derive the particles' velocity distribution. If the density and size of these particles are suitable they will follow the fluid motion and the particle behaviour is representative of the fluid behaviour (details on particle suitability evaluation could be found in previous study[5]).

Figure 1 shows a schematic view of the setup. The system consisted of a double pulsed micro-strobe (LED), a high speed double frame CCD camera with a spatial resolution of 1280×1024 pixels per frame mounted on a microscope with four magnifications (5×, 10×, 20× and 40×). The two pulses had the same time duration, between 50 and 90 μs, based on the micro-strobe power and the flow speed. The time between two pulses was set between 150 and 600 μs as a function of the flow rate amplitude and the type of fluid. Polystyrene particles, with a density of 1–1.05 $g\,cm^{-3}$ and diameter of 4.89 microns, were chosen for this study (microParticles GmbH, Berlin, Germany) with a magnification of 10×.

The oscillatory movement of the fluid was imposed by a syringe (Figure 1). The syringe oscillatory movement was obtained with a rotating disk coupled to an electrical motor. Figure 2 shows a schematic view of this oscillatory pump system. Twelve steel teeth (knobs) equally spaced on the periphery of the disk were installed. A magnetic encoder allowed these knobs to determine the angular position of the disk.

DOI: 10.1002/ls

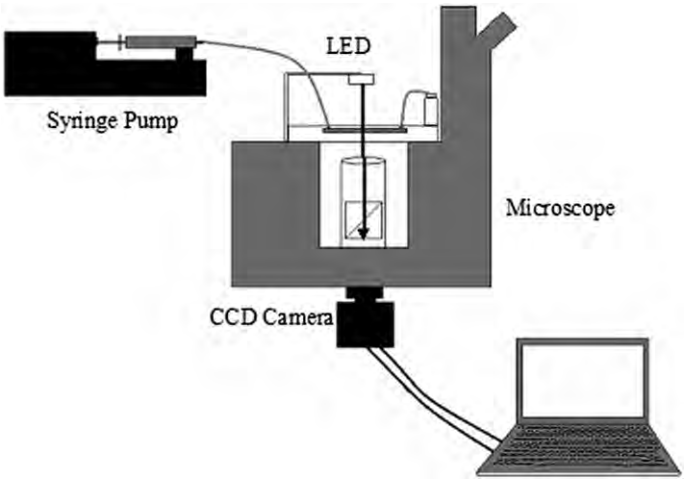

Figure 1. Schematic view of micro-PIV setup.

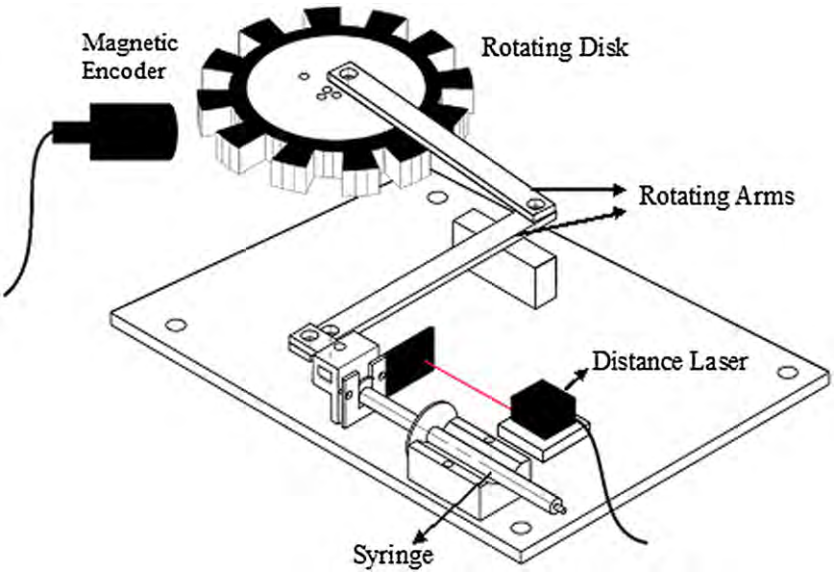

Figure 2. Schematic view of oscillatory pump.

The encoder signal allowed the synchronisation of the micro-PIV and the LED, i.e. it acted as a trigger. With this system, images were captured at defined phases. Two arms coupled the disk to the syringe to provide small syringe movements—up to 1 mm. Two different holes were available to attach the arm to the rotating disk. The closer hole to the centre of the disk provided a smaller stroke amplitude for the syringe movement (S-1) and a smaller flow rate amplitude. The other hole with larger stroke was called S-2. The frequency of the disk motion was controlled through a developed code with LabVIEW.

DOI: 10.1002/ls

As mentioned in previous work,[5] at least 300 images are required in the present setup to get a mean velocity with less than 0.5% variation. In reciprocating measurement, the averaging was only possible if the phases of the velocity maps were the same.

The phases of the images were defined based on the position of the syringe piston and the phase of the reciprocating movement. A distance laser provided information on the syringe piston position. This data allowed determination of the syringe motion, which gives the syringe velocity after derivation with time.

Mini channels were manufactured from Chromium Cobalt Molybdenum (CrCoMo) alloy and Ultra High Molecular Weight Polyethylene (UHMWPE), both are used in TJR. The model consisted of four different parts as shown in Figure 3; a Plexiglas plate (back plate) allowing light to travel through the model, a front plate with a glass window providing optical access, a middle plate consisting of a steel frame capable of holding bars at specific distances from one another and the bars themselves, either CoCrMo or UHMWPE. The steel frame provided channels with two different widths; 1 mm (hydraulic diameter of 1.33 mm) and 1.5 mm (hydraulic diameter of 1.71 mm). The depth and length of both channels were 2 and 45 mm, respectively. Hereafter, the 1 mm wide channel is named Channel 1 and the 1.5 mm wide channel is named Channel 2.

The sides of the bars in contact with the fluid were polished to achieve a mirror-like surface. Table I presents the surface roughness of the tested materials.

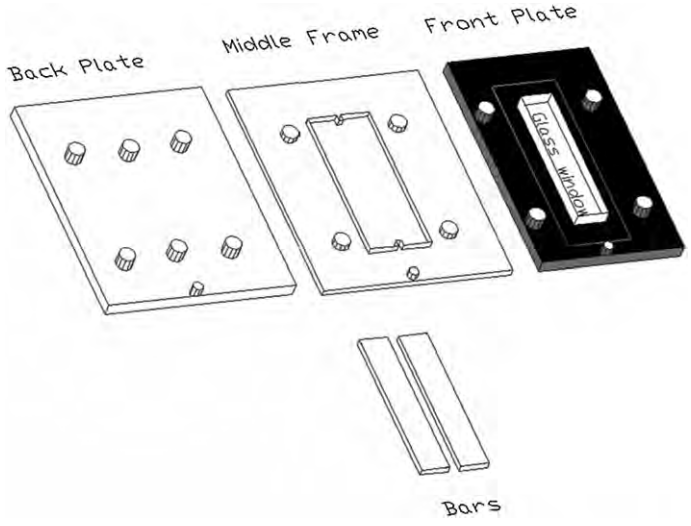

Figure 3. Experimental model.

Table I. Roughness (Ra) of different bar materials used in the channel.

	Ra [μm]	
Material	Bar 1	Bar 2
UHMWPE	0.362	0.342
Cobalt chromium	0.075	0.073

DOI: 10.1002/ls

Experimental fluid

Velocity fields of degassed water were measured to evaluate the test rig/procedure and provide a reference behaviour for Newtonian fluids. The HA solutions investigated were chosen to capture the periprosthetic fluid characteristics through a simple composition. Available data suggests that the periprosthetic fluid has similar composition to normal SF with lower viscosity, shear thinning and viscoelastic behaviour.[1] To capture the periprosthetic fluid characteristic and investigate the effect of different parameters on flow behaviour, three solutions of HA were studied:

1 HA with 1.5 MDa molecular weight (Lifecore Biomedical, Minneapolis, Minnesota, USA) with concentration of $3\,\mathrm{mg\,ml^{-1}}$ in Phosphate Buffer Saline (PBS from Sigma Aldrich, St. Louis, Missouri, USA with 0.15 M concentration)
2 HA with $3\,\mathrm{mg\,ml^{-1}}$ concentration in a mixture of 75% PBS and 25% bovine calf serum (Sigma Aldrich 12133C)
3 HA with concentration of $5\,\mathrm{mg\,ml^{-1}}$ in PBS. For all solutions, the blending procedure has been published.[5]

The fluids were characterised in a rheometer (Bohlin CVO) at 25°C under shear rate control ($0.05–1570\,\mathrm{l\,s^{-1}}$) to obtain the variation of the viscosity versus the shear rate in order to derive the shear stress distribution based on the following equation.

$$\sigma = \mu \times \dot{\gamma} \tag{1}$$

σ, μ and $\dot{\gamma}$ are shear stress, dynamic viscosity and shear rate, respectively.

The viscoelastic behaviour of the HA with $5\,\mathrm{mg\,ml^{-1}}$ concentration in PBS was investigated with a rheometer and cone on plate configuration consisting of a stainless steel cone of 1° and 20 mm diameter, strain rate of 1–3% and strain frequency between 0.07 and 10 Hz. The results of the other solution (HA with $3\,\mathrm{mg\,ml^{-1}}$ concentration) were noisy and out of the range of the rheometer calibration.

For the micro-PIV measurements, lowest syringe motion frequency was chosen similar to the highest rotational frequency of a hip joint in a walking situation; 0.37 Hz (22 rpm) in our study. The highest frequency was 2.03 Hz (122 rpm), higher than the crossover frequency obtained for the HA solution with $5\,\mathrm{mg\,ml^{-1}}$ concentration. A middle frequency of 1.02 Hz (61 rpm) was also investigated.

Table II provides an overview of the different experimental cases. For measurements with frequencies of 0.37 and 1.02 Hz, S-2 was used to attach the arms to the rotating disk. However, limitations in the micro-PIV system and LED did not allow measurements of maximum velocity for an angular velocity of 2.03 Hz with S-2. S-1 was used for measurements with the frequency of 2.03 Hz. For S-1, the syringe stroke amplitude was smaller compared to S-2. Therefore, the highest mass flow rate amplitude did not belong to the highest frequency and the maximum to minimum mass flow rates in this situation belonged to measurements with frequencies of 1.02, 2.03 and 0.37 Hz, respectively.

DATA ANALYSIS

Cross-correlation was applied on double frame images. The interrogation area size chosen was 16×64 pixels, having at least eight particles in each interrogation area.[28,30] Particle lag

DOI: 10.1002/ls

Table II. Different measurement condition.

Fluid	Fluid name
Water	Fluid 1
PBS + HA 3 mg ml^{-1} solution	Fluid 2
75% PBS + 25% serum + HA 3 mg ml^{-1} solution	Fluid 3
PBS + HA 5 mg ml^{-1} solution	Fluid 4
Channel width (*h*)	**Channel name**
1 mm channel width	Channel 1
1.5 mm channel width	Channel 2
Bar material	**Bar name**
CoCrMo	Bar 1
UHMWPE	Bar 2
Flow frequency (Hz)	**Frequency acronym**
f = 0.37 Hz	*F*-0
f = 1.02 Hz	*F*-1
f = 2.03 Hz	*F*-3
Stroke length	**Stroke acronym**
Channel 1: 3.4 mm Channel 2: 3.8 mm	S-1
Channel 1: 10 mm Channel 2: 11.5 mm	S-2

movement compared to the fluid in Couette flow was evaluated with an analytical solution. The lag increased near the solid surfaces. However, for distances larger than two times the particle diameter, the lag was below 1%.[30] Therefore, the borders of the analytical plane along the channel width were put at a distance twice the particle diameters to avoid high uncertainty in the results.

The piston syringe motion and velocity pattern were derived from the distance laser data. The zero phase of each cycle was defined at the piston syringe position in the middle of the stroke when the stroke starts to increase. Images were captured at 12 different phases during each period. A total of 3200 images were captured for each measurement, i.e. about 250 images at each phase. The derived velocity maps were phase resolved and averaged out for each phase. Sinus curves were fitted to the pump velocity and the velocity of each interrogation area along the channel width, providing the phase and amplitude of the fluid velocities.

The velocity profiles were made dimensionless according to Eq. 2 to compare the different experimental conditions.

$$V_{ND} = \frac{V_{fluid} A_{channel}}{Amp_{V_{syringe}} A_{syringe}} \tag{2}$$

V, $A_{channel}$, $A_{syringe}$ and Amp represent the velocity measured, channel cross-section area, syringe cross-section area and velocity amplitude, respectively.

Eq. 3 provides definition for the parameters used in Eq. 2.

DOI: 10.1002/ls

$$\begin{aligned} V_{syringe} &= Amp_{V_{syringe}} \sin(2\pi f + \phi) \\ V_{fluid} &= Amp_{fluid} \sin\left(2\pi f + \phi^{'}\right) \\ V_{ND} &= Amp_{ND} \sin\left(2\pi f + \phi^{'}\right) \\ \Delta\phi &= \phi - \phi^{'} \end{aligned} \tag{3}$$

f is the frequency in Hz. ϕ and ϕ' represent the phase of the syringe and fluid velocity in radians, respectively. The measurements indicate that the fluid motion is only in one direction (y axis) perpendicular to channel width (x axis is along channel width). The entrance length for laminar oscillatory flow was calculated based on Eq. 4[31]

$$Le = 0.03H\mathrm{Re}_{os} \tag{4}$$

Le and H are the entrance length and hydraulic diameter respectively. Re_{os} is the Reynolds number of the oscillatory flow calculated as

$$\mathrm{Re}_{os} = Amp_{fluid,mean} H/\nu \tag{5}$$

$Amp_{fluid,mean}$ and ν are amplitude of cross-sectional mean velocity and kinematic viscosity respectively. The longest calculated entrance length was 6 mm. Since the measurements were conducted at the middle of the channel with 22 mm distance from inlet and exit and the measured velocity profiles are identical along the y axis, the boundary layer is fully developed.

A dimensionless analysis of the incompressible Navier–Stokes equation, differential form of the variation of momentum, for oscillatory flow reveals the importance of the Womersley number ($W = H\sqrt{\frac{\omega}{\nu}}$), see.[32] The Womersley number is the ratio of the transient inertial to viscous forces. W represents how deep the viscous waves generated at the wall penetrate into the flow. This dimensionless number is usually used to evaluate the oscillatory behaviour of Newtonian fluids,[31,33–36] the derivation follows. The incompressible Navier–Stokes equation for flow along the y-direction is given by:

$$\frac{\partial u}{\partial t} = \nu\nabla^2 u - \frac{1}{\rho}\frac{\partial p}{\partial y}. \tag{6}$$

Eq. 7 represents non-dimensionless variables of Eq. 6 assuming ω, ρ, ν, H and p representative of the angular frequency of the oscillation, fluid density, kinematic viscosity, characteristic length and the pressure, respectively.

$$\begin{aligned} y^* &= \frac{y}{H_u} \\ u^* &= \frac{}{\omega H} \\ t^* &= t^*\omega \\ p^* &= \frac{p}{\rho(\omega H)^2} \end{aligned} \tag{7}$$

$$\frac{\partial u^*}{\partial t^*} = \frac{\nu}{\omega H^2}\nabla^2 u^* - \frac{\partial p^*}{\partial y^*} = \frac{1}{W^2}\nabla^2 u^* - \frac{\partial p^*}{\partial y^*} \tag{8}$$

In numerical studies, the characteristic length is defined based on the channel shape (e.g. channel height, hydraulic diameter, etc.).[32,35,37–42] In this study, the hydraulic diameter was considered as the characteristic length so both the effect of channel dimension and geometry were taken into account.

DOI: 10.1002/ls

Eq. 8 describes the relation between viscous waves' penetration depth, flow pressure gradient and velocity. The consequences of this relation will be presented later in the results.

Table III presents the Womersley number for the fluids and experimental conditions investigated.

A non-Newtonian shear thinning fluid has three characteristic regions[43]:

- Low shear rate plateau where the fluid behaves like a Newtonian fluid
- Shear thinning region where the viscosity decreases by shear rate increment
- High shear rate plateau where the viscosity stays constant similar to solvent viscosity and the fluid becomes Newtonian again.

To study the oscillatory flow of a shear thinning fluid and calculation of *W*, in most studies, the defined characteristic dynamic viscosity is similar to high shear rate Newtonian viscosity.[44] However, in this study the highest shear rate was about $600\,s^{-1}$; water dynamic viscosity was not a good estimation for HA characteristic viscosity. Instead, the complex viscosity (frequency-dependent viscosity under oscillatory strain condition) of the fluid at the oscillation frequency was considered as the viscosity. Based on Cox–Merz rule, the complex viscosity is equal to the dynamic steady shear viscosity if the shear rate is equal to the frequency in rad s^{-1} or $\mu(\dot{\gamma}) = \mu^*(\omega)$ if $\dot{\gamma} = \omega(rad/s)$. The variables η, η^*, ω and $\dot{\gamma}$ are dynamic and complex viscosities, oscillation frequency and steady shear rate, respectively.[45]

RESULTS AND DISCUSSION

HA rheology

Figure 4 shows the viscosity versus the shear rate profile. The line fitted on the double logarithmic shear thinning region follows the power law model which is the most frequent model of describing polymeric non-Newtonian behaviour (Eq. 9)

Table III. Womersley number for the different fluids and experimental conditions investigated.

Fluid 1		***W* (Channel 1)**	***W* (Channel 2)**
F-0	**W-0**	2.02	2.6
F-1	**W-1**	3.37	4.33
F-2	**W-2**	4.76	6.12
Fluid 2		***W* (Channel 1)**	***W* (Channel 2)**
F-0	**W-0**	0.27	0.38
F-1	**W-1**	0.47	0.6
F-2	**W-2**	0.68	0.87
Fluid 3		***W* (Channel 1)**	***W* (Channel 2)**
F-0	**W-0**	0.24	0.34
F-1	**W-1**	0.43	0.54
F-2	**W-2**	0.61	0.79
Fluid 4		***W* (Channel 1)**	***W* (Channel 2)**
F-0	**W-0**	0.09	0.14
F-1	**W-1**	0.17	0.23
F-2	**W-2**	0.25	0.33

DOI: 10.1002/ls

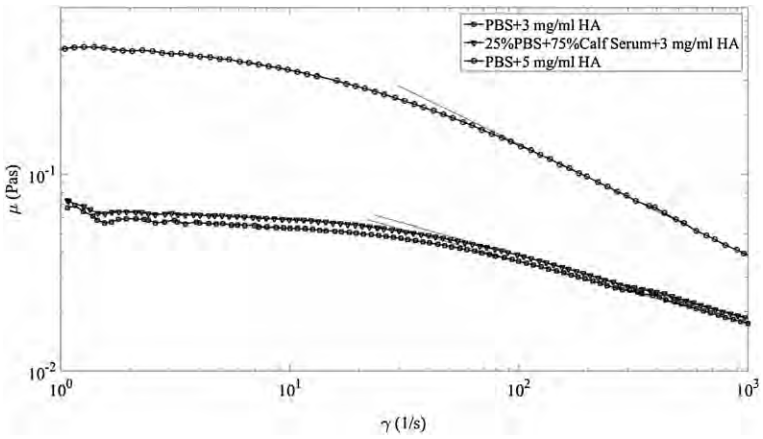

Figure 4. Viscosity (μ) function of the shear rate (γ) for the HA solutions investigated.

$$\mu = m\dot{\gamma}^{n-1} \tag{9}$$

$n - 1$ is the slop of the line and n is called the power law index. m is the consistency index which is the intersection of the line with the shear rate of $\gamma = 1$ Hz. The slopes of the lines fitted on the shear thinning regions of Figure 4 are 0.687, 0.681 and 0.445 for Fluids 2, 3 and 4, respectively. The intersection of this line with the zero shear viscosity is the transition shear where the shear thinning behaviour of the polymer starts and is called the critical shear rate ($\dot{\gamma}_{critical}$).[10,43]

At low shear rates, the polymeric fluids were expected to behave as Newtonian fluids with constant viscosity. However, an unexpected increment in viscosity of Fluid 2 and 3 at very low shear rates, visible in Figure 4, was obtained. This effect was also reported by Zhang et al.[46] They explained this phenomenon based on interfacial effects. They also mentioned that the differences in HA solutions with and without protein content behaviours are also related to interface effect; otherwise, the HA solutions rheology are identical with and without protein content.

Figure 5 shows the elastic and viscous module versus strain frequency. At low frequencies, the viscous module was higher and the fluid exhibited viscous behaviour. By increasing the frequency, the elastic module dominated the viscous one. The crossover frequency was about 1.4 Hz. The crossover frequencies for the HA solutions with 3 mg ml^{-1} concentration were not measured. However, previous studies indicate that the crossover frequency increases with decreasing HA concentration.[26]

Reciprocating motion measurements

Water behaviour. Figure 6 shows the non-dimensional velocity profiles as a function of the non-dimensional channel width (x/h) for Channel 1 and 2 at two different frequencies (different Womersley numbers).

At low W, the velocity variation over time was slow; the term $\frac{\partial u^*}{\partial t^*}$ in Eq. 8 was negligible. Therefore, the fluid had enough time to adapt itself to the applied changes on the imposed pressure gradient and behaved as steady at every instant; the fluid had a quasi-steady behaviour. In Figure. 6 (a) (Channel 1 and W-0), W had value of 2.02, with a parabolic shape for the velocity profiles at each phase. The measurement for W-0 in Channel 2 had a higher Womersley number of 2.6; the velocity profiles deviated

DOI: 10.1002/ls

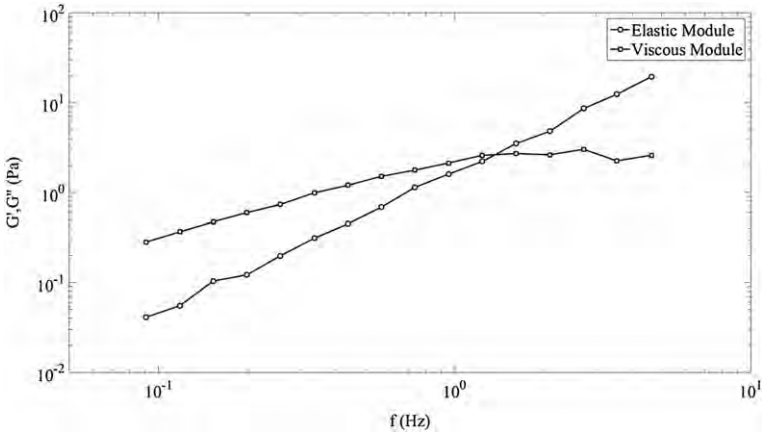

Figure 5. Viscous and elastic modules (G' and G'') versus strain frequency (f) for HA with 5 mg ml^{-1} concentration in PBS.

from the parabolic shape. By increasing the Womersley number (either by increasing the frequency or channel width) deviation from the parabolic shape was enhanced.

The depth of penetration of the viscous waves was proportional to $\sqrt{\frac{\nu}{\omega}}$ [32] Increasing W decreased the penetration depth of the viscous waves. At a high W value, the waves did not reach the whole channel width and the inertia forces dominated the viscous forces. The viscous forces were confined near the walls and the fluid at the channel centre was frozen, not affected by friction. In this situation the pressure gradient distribution ($\frac{\partial p^*}{\partial y^*}$) and unsteady term ($\frac{\partial u^*}{\partial t^*}$) had the same order of magnitude in the middle of the channel. A phase lag between the pressure gradient and the fluid motion was present in this part of the channel resulting from the time derivation of the velocity.[32] Therefore the maximum velocity did not occur in the middle of the channel but close to the wall (Figure 6 (b)). This phenomenon is known as the Richardson annular effect. In our measurements, the annular effect appeared on the velocity profiles for W above 4.3 for both channels, regardless of the aspect ratio (ratio of channel width to channel depth which is 0.5 for Channel 1 and 0.75 for Channel 2).

The amplitude and phase difference (Eq. 3) of the sinusoidal flow at different channel positions along the width for Channel 1 and 2 and different Womersley numbers are shown in Figure 7 a and b, respectively.

In similar cases (e.g. Channel 1 at W-2 and Channel 2 at W-1), the non-dimensional amplitude of oscillation was always lower for the channel with a lower aspect ratio. This lower amplitude was the effect of a higher relative friction in the smaller channels (Figure 7(a)).

The phase differences contain some random variation near the walls, as the standard deviation of the velocity was significant, above 10% of the absolute velocity.

For the lowest W, $W = 2.02$, the increment of the phase difference between the bulk velocity and fluid velocity across the channel was negligible. By increasing W, this phase difference increased (Figure 7 (b)). Phase difference depended on the penetration depth of the viscous waves, i.e. the W number. For two similar cases, the phase difference was expected to be comparable. However from Figure 7(b), there was a significant difference between phase differences in cases with similar W values. The aspect ratio of the channel was the responsible parameter for the difference in phase shift. By decreasing the aspect ratio, friction forces and inertial effect increased which enhanced the phase difference.[42,47]

DOI: 10.1002/ls

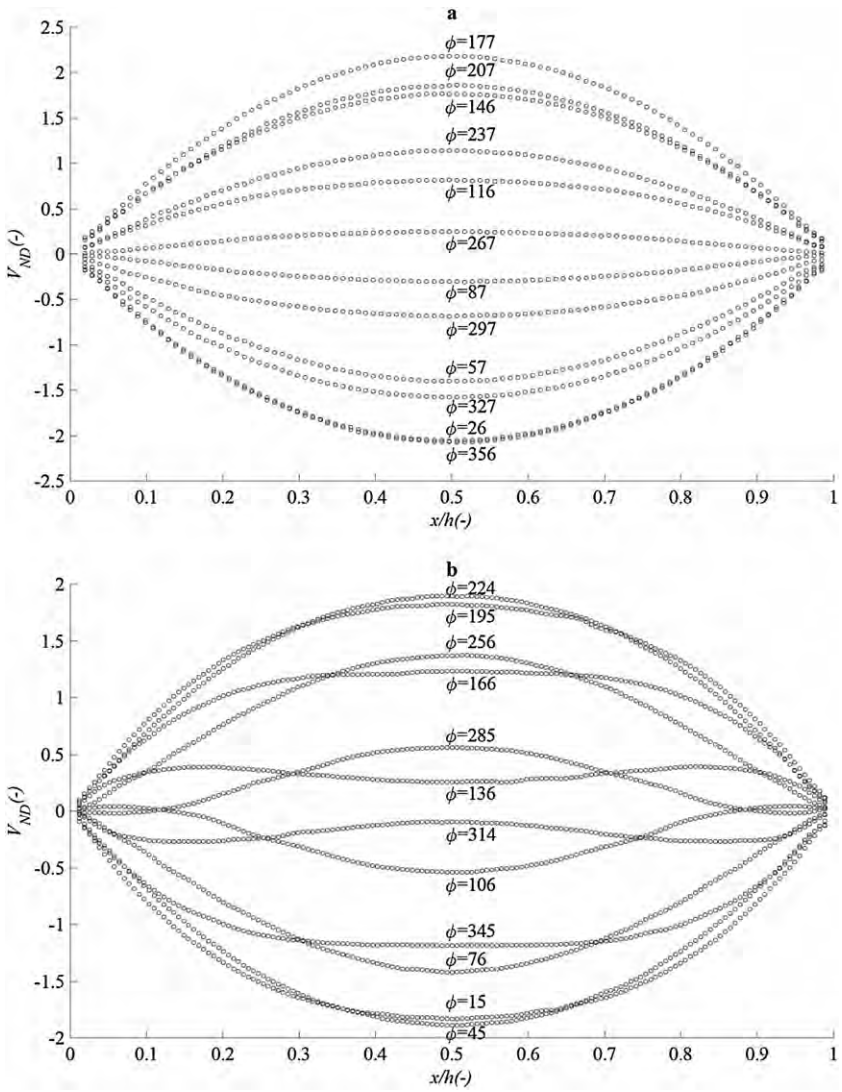

Figure 6. Non-dimensional velocity (V_{ND}) profiles along the non-dimensional channel width (x/h) for water, a) Channel 1, W-0, b) Channel 2, W-2.

HA solution behaviour

1) 3mg ml^{-1} HA in PBS. Figure 8 shows the oscillatory behaviour of HA solution with 3 mg ml^{-1} concentration in PBS (Fluid 2) together with the results obtained from water. The polymeric solution exhibited shear thinning behaviour. Based on previous study in one-directional movement, the velocity profile along the channel width deviated from a parabolic shape to a blunt profile by increasing the flow rate.[5] At low shear rates, the transient entanglements between HA polymer chains could be observed.[48] By increasing the local shear rate along the channel width from centre to wall, these networks were

DOI: 10.1002/ls

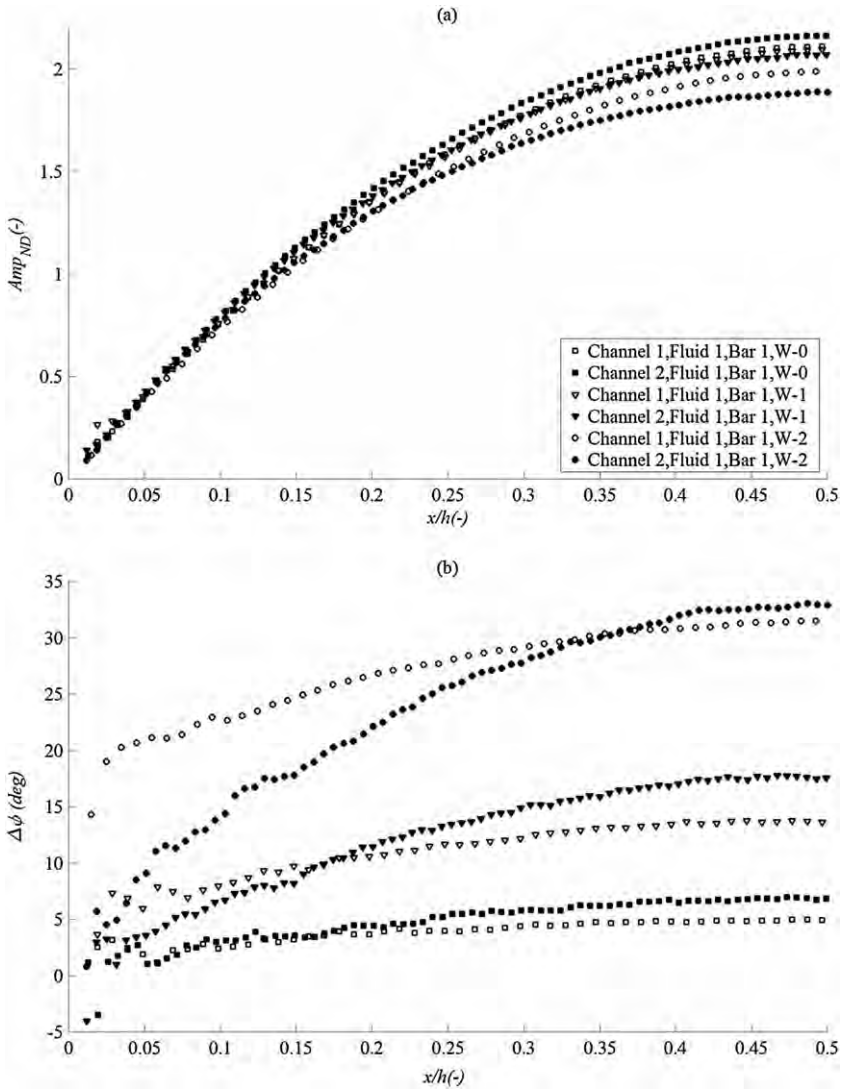

Figure 7. Non-dimensional amplitude (Amp_{ND}) (a), phase difference ($\Delta\phi$) (b) of water in Channel 1 (empty marker) and Channel 2 (full marker) for W-0 (square), W-1 (triangle) and W-2 (circle).

disentangled and produced spatial viscosity distribution along the channel width.[5] Figure 8 (a) shows that this behaviour was also obtained during reciprocal movement. The viscosity of Fluid 2 along the channel width during reciprocal motion was at least 20 times that of the water viscosity and the calculated Womersley values were very small (Table IV). Therefore, this fluid was expected to have a quasi-steady behaviour without any effect of the unsteadiness in the velocity profiles along the channel width, which was true based on velocity profiles of Figure 9. This signified that by increasing the frequency (bulk flow rate), the local velocity amplitude profile should have tended towards a blunter one. This

DOI: 10.1002/ls

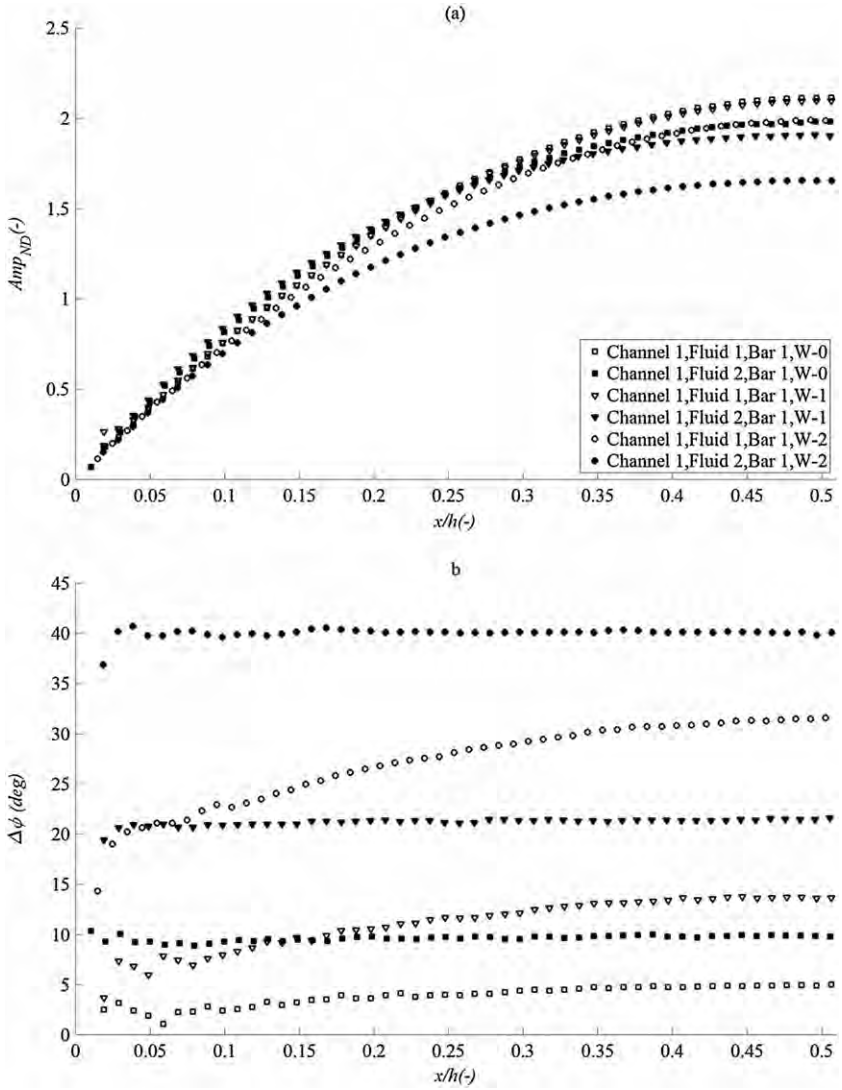

Figure 8. Non-dimensional amplitude (Amp_{ND}) (a), Phase difference ($\Delta\phi$) (b) of Water (empty marker) and 3mg ml^{-1} HA in PBS (full marker) for W-0 (square), W-1 (triangle) and W-2 (circle).

was obtained for W-0 and W-1 flows (Figure 8 (a)). There was an exception for W-2. The bulk flow rate of W-2 was larger than W-0; however, the amplitude profile was not blunter. This behaviour could be explained based on the relaxation time of the polymer contents. Physically, 'relaxation time' means the required time for stress in polymers to reach 1/e of its initial value.[49] Relaxation time (λ) is actually the required time to damp the stress deformation and gain the default configuration or form new networks or entanglements between polymer chains.[43] The longest relaxation time for polymers is in the order of the

DOI: 10.1002/ls

Table IV. Deborah number values for Fluid 2.

Flow name	t_{ch} (s rad^{-1})	Relaxation time (s)	De
W-0	0.22	0.047	0.21
W-1	0.078	0.047	0.60
W-2	0.039	0.047	1.2

critical shear rate inverse. The relaxation time of Fluid 2 was 0.047 s (Figure 4). To assess the rheological behaviour of polymeric solutions according to stress relaxation time, the non-dimensional 'Deborah number' (De) was evaluated.[50,51]

$$De = \frac{Fluid\ characteristic\ time}{Flow\ characteristic\ time}$$

A small De number means the fluid behaves mainly like a viscous material. De number around 1 indicates that the fluid does not have enough time to release from all the previously applied deformations and has viscoelastic behaviour. In this situation, the previous polymer chain state influences the present behaviour. High De number represents more elastic or solid behaviour.[52]

In the middle of each cycle the flow direction changed and thus the stresses direction applied to the fluid. Polymers needed some time to release from their previous applied stresses to regain their default configuration. Then they disentangled and took the new orientation, by flowing the new flow direction. Therefore, half of each cycle period was considered as the characteristic time (t_{ch}) for the flow. Using the Cox–Merz rule previously described, the data from steady shear measurements in Hz used for relaxation time estimation while for calculation of t_{ch}, frequency in rad s^{-1} was considered. Table IV shows the De number for Fluid 2 at W-0, W-1 and W-2.

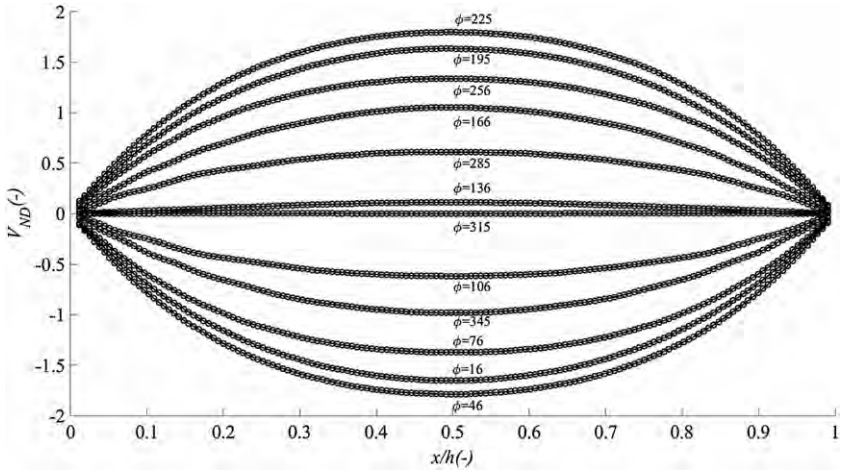

Figure 9. Non-dimensional velocity (V_{ND}) profiles along the non-dimensional channel width (x/h) for HA 3 mg ml^{-1} in PBS in Channel 2, W-2.

DOI: 10.1002/ls

De numbers for W-0 and W-1 were small. Under these two flow conditions, the fluid had enough time to damp the applied stresses from the opposite direction. However for W-2, De was higher than 1. There were still deformations from the stresses applied in the opposite direction remaining in the polymer network which prevented the fluid from reaching the highest possible amplitude and provided the fluid with partially elastic behaviour. This result is compatible with the findings of Zhang et al. The wall strain at W-2 was about 15%.[53] They showed that at this range of strain, HA solution with similar molecular weight and concentration is predominantly viscous and the elastic behaviour increases by increasing strain frequency.[54]

Figure 10 shows the phase difference between the syringe velocities and fluid velocities for Fluid 2 in two different channels. Both Figure 8 (b) and Figure 10 show that for the non-Newtonian Fluid 2, the phase difference between the syringe and fluid velocities increased as a function of the frequency of oscillation and channel aspect ratio.[42,47] Functionality of frequency meant that the phase difference was a function of the response time of the fluid to fluctuations. The disentanglement process was a time-dependent process and more disentanglement took longer time. Therefore, in channels with higher shear rates, the disentanglement density and phase difference increased. The amount of this phase difference could also be estimated from the relaxation time. For flow with a frequency of 1.02 Hz and relaxation time of 0.047 s, one to two relaxation times took about 17 to 33°. Both Channel 1 and Channel 2 had phase differences in this range.

Based on previous work,[5] a different channel material only affects the fluid behaviour very close to the wall. This also seems valid for oscillatory motion, see Figure 11.

2) 3mg ml^{-1} HA in 75% PBS+25% calf serum. The HA solution with concentration of 3 mg ml^{-1} in 75% PBS and 25% bovine calf serum (Fluid 3) and Fluid 2 are presented in Figure 12. Fluid 3 had almost the same behaviour as Fluid 2 except at W-1, although the relaxation times of these two fluids

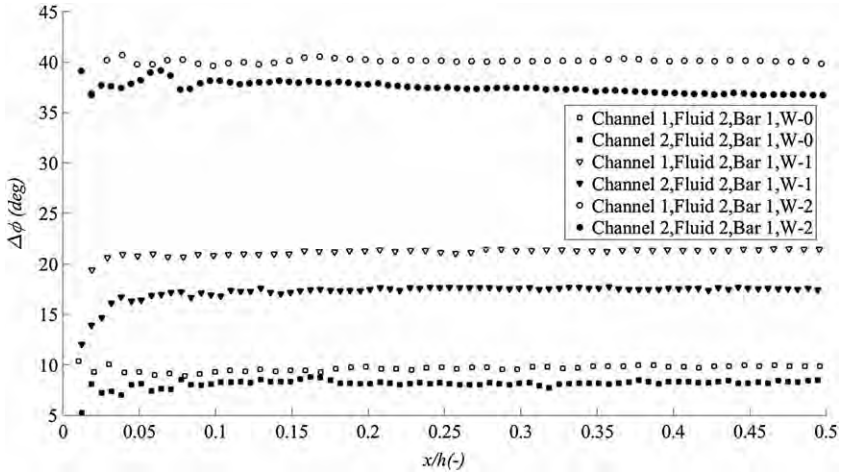

Figure 10. Phase difference ($\Delta\phi$) between bulk and local velocities along the non-dimensional channel width (x/h) for HA 3 mg ml^{-1} solution in PBS in Channel 1 (empty marker) and Channel 2 (full marker) for W-0 (square), W-1 (triangle) and W-2 (circle).

DOI: 10.1002/ls

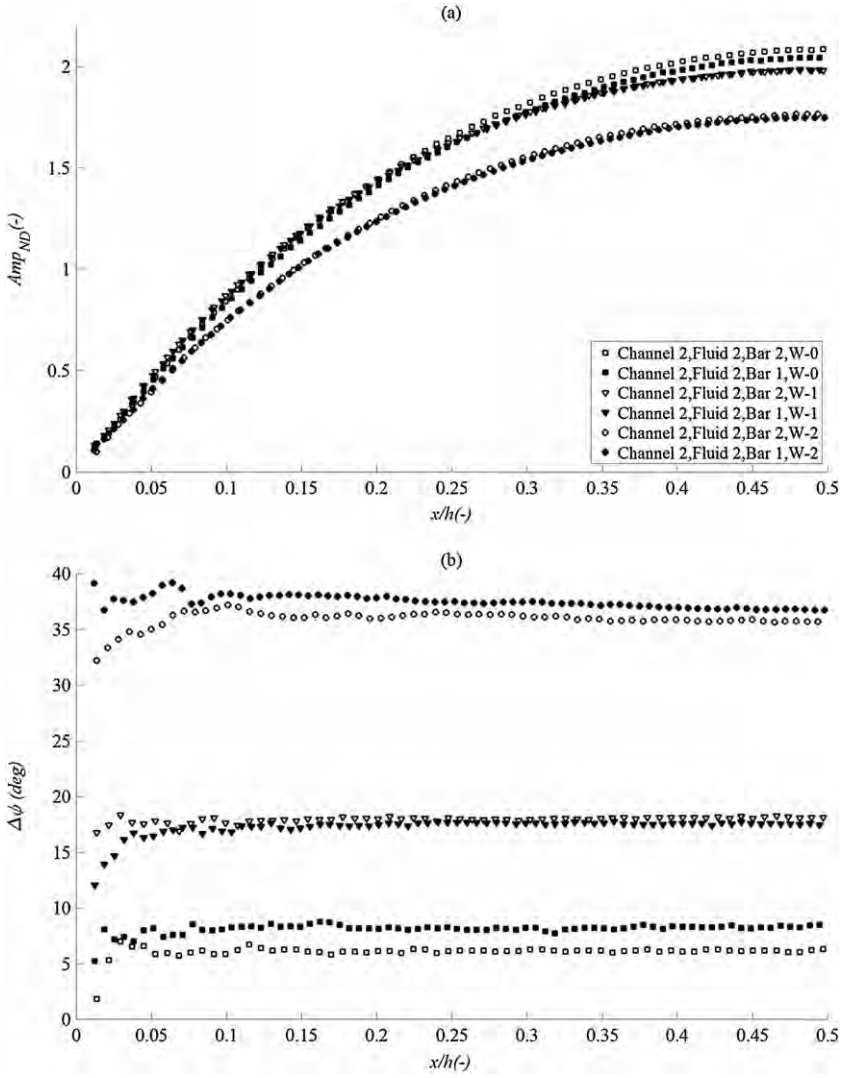

Figure 11. Non-dimensional amplitude (Amp_{ND}) (a), phase difference ($\Delta\phi$) (b) of 3 mg ml^{-1} HA in PBS in Channel 2 with UHMWPE bar material (empty marker) and CoCrMo bar material (full marker) for W-0 (square), W-1 (triangle) and W-2 (circle).

derived from Figure 4 are nearly the same. Many studies suggest that flow shear stress for shear rates less than 1000 s^{-1} induces protein aggregation.[55,56] Most probably the protein aggregation formed a tight network around HA chains which increased the HA chain entanglements.[15] It was not possible to quantify this increment and although it did not affect fluid behaviour at W-0 and W-2, it affected the flow at W-1 significantly. This could be due to non-linear viscoelastic effects of the solution. The shear strain at different W was calculated based on Eq. 10[57]

DOI: 10.1002/ls

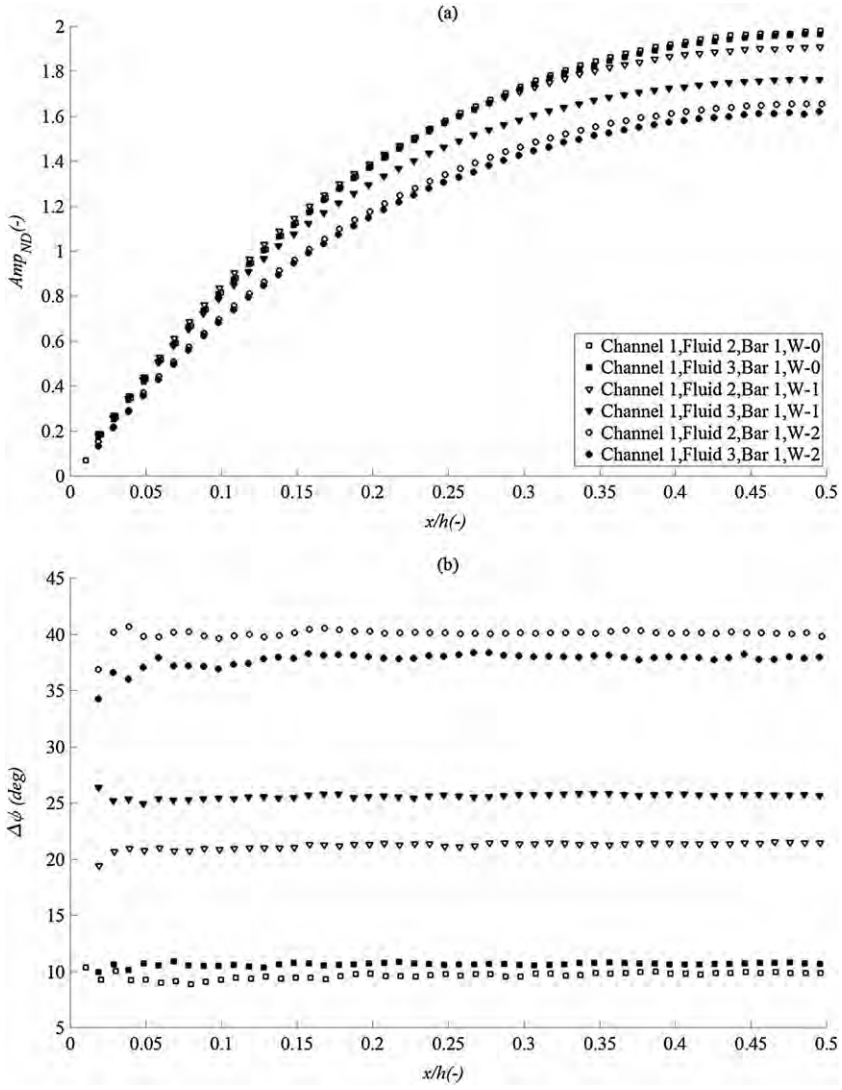

Figure 12. Non-dimensional amplitude (Amp_{ND}) (a), phase difference ($\Delta\phi$) (b) of 3 mg ml^{-1} HA in PBS (empty marker) and 3 mg ml^{-1} HA in 75%PBS + 25% calf serum (full marker) for W-0 (square), W-1 (triangle) and W-2 (circle).

$$\dot{\gamma} = \omega\gamma \tag{10}$$

$\gamma, \dot{\gamma}$ and ω are shear strain, shear rate and strain frequency in rad s^{-1}. The strain amplitudes for Fluid 3 at W-0, W-1 and W-2 were 65.4, 53 and 23, respectively. This amount of shear strain suggested that the viscoelastic behaviour of the fluids was non-linear. Zhang showed that during one cycle of oscillation at high strains with non-linear viscoelastic condition, the HA solution is predominantly viscous with

DOI: 10.1002/ls

some elastic characteristics. They also showed that by increasing the frequency or strain amplitude (non-linear time dependent behaviour), the solution shows increased elastic behaviour. By comparing frequencies and strain amplitudes of three *W*, only in W-1 both the strain and the frequency were rather high. Therefore, this case had more elastic and non-linear viscoelastic behaviour compared to the other two. At W-0 with very small frequency and W-2 with low strain, the change in solution structure did not affect the flow behaviour.[54]

3) 5mg ml^{-1} HA in PBS. Figure 13 shows the behaviour of HA solutions for two different concentrations (Fluid 2 and Fluid 4). *W* had a small value for both of these solutions, indicating the importance of the viscous forces. Figure 13 (a) shows that for W-0, both solutions had a quasi-steady behaviour. Figure 13 (b) shows a larger phase difference for the HA solution of 5 mg ml^{-1} concentration (Fluid 4) in comparison to Fluid 2 for W-0. By increasing the concentration, the polymer coils overlapped, entanglements densified and the relaxation time increased,[58] which explains the increment in phase difference.

For W-1, in contrast to Fluid 2, Fluid 4 did not follow quasi-steady behaviour and behaved similarly to Fluid 2 for W-2. The explanation for this behaviour was also based on the De number value. The longest relaxation time for Fluid 4 was 0.1 s (Figure 4). Table V shows the De value of Fluid 4 for different flows. For W-1, Fluid 4 had a De value around 1, a similar case as for Fluid 2 and W-2.

For W-2, the velocity amplitudes of Fluid 4 dropped extensively compared to previous cases, indicating a different mechanism. As explained earlier, HA has viscoelastic behaviour. At low deformation or strain frequency the fluid behaves as a viscous material; the polymer chains can disentangle, slip along each other, form new entanglements and stable configurations. However by increasing the frequency, there is not enough time for the chain networks to disentangle and move relative to each other. Instead the polymer chains store the mechanical energy and behave as an elastic material.[16] The crossover frequency at which the HA behaviour changes from a viscous material to an elastic one is representative of the disentanglement rate or HA chain mobility. This crossover frequency decreases by increasing the HA molecular weight or concentration in solutions.[21,26,59] Therefore, in the present study, Fluid 4 had a lower crossover frequency than Fluid 2. The frequency of 2.04 Hz (W-2) was higher than the crossover frequency of the HA solution with a concentration of 5 mg ml^{-1} in PBS (1.4 Hz). Thus the polymer solution behaved as an elastic material, absorbed the applied stresses and reduced the mobility and velocity of the flow.

The shear rate increased from the channel centre to the channel wall. There were chain disentanglements near the channel walls for Fluid 4 at W-2 due to the high value of the wall shear rate at this location. This could be one reason for the phase difference reduction away from channel walls to the centre (Figure 13 (b)).

The phase difference for all fluids and all flows suggested that in human articulating joints (natural or artificial) with reciprocating motion of the joint surfaces, SF velocity is not in phase with the motion of the surface. This phase lag depends both on the frequency of the motion and the SF viscous behaviour which itself depends on the HA molecular weight, concentration and HA–protein interactions.

SF of a healthy joint has HA with higher concentration and molecular weight in comparison to the SF of a TJR or injured joint. Results of this study showed that decreasing the shear thinning characteristic or increasing the cross-over frequency could not be the only behavioural difference between the healthy and non-healthy SFs. In fact the whole velocity map changes which enhances the effects of lubricant characteristics on the pressure distribution and the lubricant film thickness. This is in agreement with the numerical studies conducted on lubrication, pressure distribution and film thickness of

DOI: 10.1002/ls

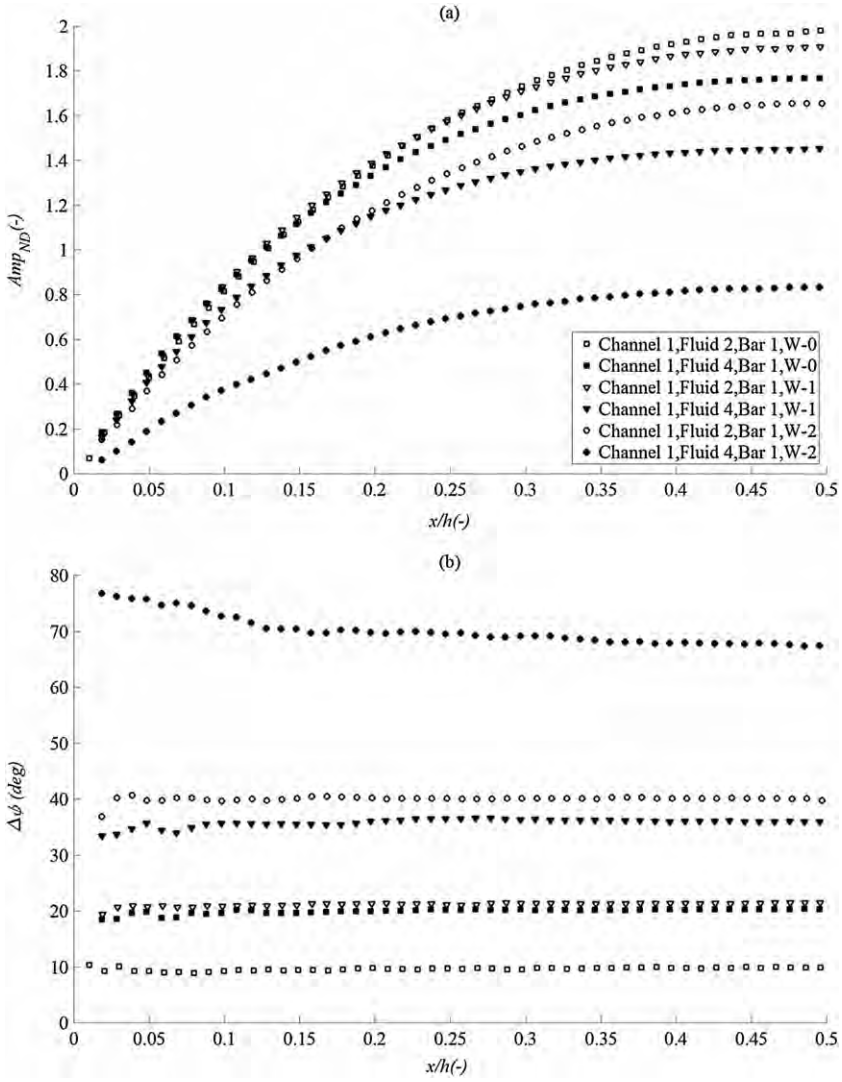

Figure 13. Non-dimensional amplitude (Amp_{ND}) (a), phase difference ($\Delta\phi$) (b) of 3 mg ml^{-1} HA in PBS (empty marker) and 5 mg ml^{-1} HA in PBS (full marker) for W-0 (square), W-1 (triangle) and W-2 (circle).

Table V. Deborah number values for Fluid 4.

Flow name	De
W-0	0.46
W-1	1.28
W-2	2.56

DOI: 10.1002/ls

hip implants with the assumption of viscoelastic shear-thinning behaviour for the lubricant. It is usually suggested that the lubricant behaves as a Newtonian fluid in walking condition in a hip implant under walking condition and a classical EHL model applied to predict the implant performance.[60–62] However, one of the conclusions of the review by Myant and Cann was that the classical EHL model with assumption of SF to be single phase fluid with Newtonian rheology could not be considered as a good basis for designing implants.[63] Tichy et al. studied the effect of non-Newtonian viscoelastic behaviour of SF on the pure squeezing lubrication of the hip implant while Meziane et al. developed the model for the hydrodynamic lubrication.[6,64] Gao et al. improved the previous studies by conducting numerical study on metal hip implant considering EHL transient lubrication for a shear-thinning lubricant under physiological and simulator walking condition.[7] These studies showed that considering the non-Newtonian viscoelasticity of the SF improves minimum film thickness and the pressure distribution inside the implant gap.

The results of this study along with all aforementioned studies suggested that the viscoelasticity and shear-thinning characteristics play key roles in unsteady behaviour of the lubricant.

CONCLUSION

Vastly different behaviour between water as a Newtonian fluid and HA solutions was observed. For the investigated polymeric non-Newtonian fluid, although the Womersely number had a very small value, no annular effect was visible and the velocity profiles kept the blunt shapes; the amplitude profile and phase difference along the channel width changed significantly for different flows. Therefore for non-Newtonian fluid the non-dimensional Deborah number, defined based on the response time of the polymer chains, should also be considered for assessing the fluid behaviour.

At very high shear rates, the non-Newtonian shear thinning fluid behaves like a Newtonian fluid with constant viscosity similar to the solvent. Therefore, usually SF is considered as a Newtonian fluid for simulation of joint performance due to very high shear rates inside the joint gap. However, based on our results under unsteady reciprocating conditions and by increasing the frequency, HA solution (i.e. SF) does not behave in the same way as under steady state conditions. This is due to time-dependent behaviour of the HA polymeric chain and therefore the flow cannot be considered as quasi steady.

The experimental setup developed in this study was suitable for studying the unsteady behaviour of joint lubricant flow which is a polymeric fluid. Simple geometry of the experimental model eliminated the complexity of the geometry and provided the possibility to investigate the SF composition and unsteadiness on the lubricant behaviour. It was concluded that HA concentration and interaction between the HA chains and protein were two of the key parameters in the behaviour. Obtaining resembling to solid trend behaviour at high frequency motion suggested that the velocity inside the implant gap might stay gradientless at some locations. This eliminated the fluid shear forces applied on the studied particles; therefore particles could behave based on the other applied forces such as gravitational force.

ACKNOWLEDGEMENTS

The authors' gratitude goes to the Doctoral Program DocMASE for the financial support, and Kaveh Amiri, Martin Lund and Jan Granström for designing and fabricating the reciprocating pump.

DOI: 10.1002/ls

REFERENCES

1. Fam H, Bryant JT, Kontopoulou M. Rheological properties of synovial fluids. *Biorheology* 2007; **44**(2):59–74.
2. Ingham E, Fisher J. Biological reactions to wear debris in total joint replacement. *Proceedings of the Institution of Mechanical Engineers. Part H, Journal of Engineering in Medicine* 2000; **214**(1):21–37. DOI:10.1243/0954411001535219.
3. Bauer TW, Schils J. The pathology of total joint arthroplasty. *Skeletal Radiology* 1999; **28**(9):483–497.
4. Fam H, Kontopoulou M, Bryant J. Development of a rheological analogue to periprosthetic fluid. *Biorheology* 2005; **42**(4):295–306.
5. Safari A, Emami N, Cervantes MJ. Bio-lubricant flow behaviour in mini-channels. *Lubrication Science* 2016; **28** (4):221–242. DOI:10.1002/ls.1328.
6. Tichy J, Bou-SaĂŻd B. The Phan–Thien and Tanner model applied to thin film spherical coordinates: applications for lubrication of hip joint replacement. *Journal of Biomechanical Engineering* 2008; **130**:021012–021012–6.
7. Gao L, Dowson D, Hewson RW. A numerical study of non-Newtonian transient elastohydrodynamic lubrication of metal-on-metal hip prostheses. *Tribology International* 2016; **93**:486–494.
8. Mazzucco D, Scott R, Spector M. Composition of joint fluid in patients undergoing total knee replacement and revision arthroplasty: correlation with flow properties. *Biomaterials* 2004; **25**(18):4433–4445. DOI:10.1016/j.biomaterials.2003.11.023.
9. Mazzucco D, McKinley G, Scott RD, Spector M. Rheology of joint fluid in total knee arthroplasty patients. *Journal of Orthopaedic Research* 2002; **20**(6):1157–1163.
10. Bingöl A, Lohmann D, Püschel K, Kulicke W. Characterization and comparison of shear and extensional flow of sodium hyaluronate and human synovial fluid. *Biorheology* 2010; **47**(3):205–224.
11. Chiroiu V, Mosneguţu V, Munteanu L, Ioan R. On a micromorphic model for the synovial fluid in the human knee. *Mechanics Research Communications* 2010; **37**(2):246–255. DOI:10.1016/j.mechrescom.2009.12.003.
12. Neville A, Morina A, Liskiewicz T, Yan Y. Synovial joint lubrication—does nature teach more effective engineering lubrication strategies? *Proceedings of the Institution of Mechanical Engineers-Part C: Journal of Mechanical Engineering Science* 2007; **221**(10):1223–1230.
13. Dahl LB, Dahl IM, Engstrom-Laurent A, Granath K. Concentration and molecular weight of sodium hyaluronate in synovial fluid from patients with rheumatoid arthritis and other arthropathies. *Annals of the Rheumatic Diseases* 1985; **44**(12):817–822.
14. Decker B, Mcguckin WF, Mckenzie BF, Slocumb CH. Concentration of hyaluronic acid in synovial fluid. *Clinical Chemistry* 1959; **5**:465–469.
15. Oates KM, Krause WE, Jones RL, Colby RH. Rheopexy of synovial fluid and protein aggregation. *Journal of the Royal Society Interface* 2006; **3**(6):167–174. DOI: L26P34510M528MRK [pii].
16. Balazs EA. The physical properties of synovial fluid and the special role of hyaluronic acid, in *Disorders of the Knee*. JB LippincoU Co., Philadelphia 1974: 63–75.
17. Seller P, Dowson D, Wright V. The rheology of synovial fluid. *Rheologica Acta* 1971; **10**(1):2–7.
18. Safari M, Bjelle A, Gudmundsson M, Hogfors C, Granhed H. Clinical assessment of rheumatic diseases using viscoelastic parameters for synovial fluid. *Biorheology* 1990; **27**(5):659–674.
19. Thurston G, Greiling H. Viscoelastic properties of pathological synovial fluids for a wide range of oscillatory shear rates and frequencies. *Rheologica Acta* 1978; **17**(4):433–445.
20. King R. A rheological measurement of three synovial fluids. *Rheologica Acta* 1966; **5**(1):41–44.
21. Fam H. Effect of composition on periprosthetic fluid rheology and friction in total knee arthroplasty 2010
22. Mo Y, Takaya T, Nishinari K, Kubota K, Okamoto A. Effects of sodium chloride, guanidine hydrochloride, and sucrose on the viscoelastic properties of sodium hyaluronate solutions. *Biopolymers* 1999; **50**(1):23–34.
23. Meyer F, Lohmann D, Kulicke W. Determination of the viscoelastic behavior of sodium hyaluronate in phosphate buffered saline with rheo-mechanical and rheo-optical methods. *Journal of Rheology* (1978-present) 2009; **53**(4):799–818.
24. Fujii K, Kawata M, Kobayashi Y, Okamoto A, Nishinari K. Effects of the addition of hyaluronate segments with different chain lengths on the viscoelasticity of hyaluronic acid solutions. *Biopolymers* 1996; **38**(5):583–591.
25. Cowman MK, Matsuoka S. Experimental approaches to hyaluronan structure. *Carbohydrate Research* 2005; **340**(5):791–809. DOI:10.1016/j.carres.2005.01.022.
26. Fam H, Kontopoulou M, Bryant J. Effect of concentration and molecular weight on the rheology of hyaluronic acid/bovine calf serum solutions. *Biorheology* 2009; **46**(1):31–43.
27. Gibbs DA, Merrill E, Smith KA, Balazs E. Rheology of hyaluronic acid. *Biopolymers* 1968; **6**(6):777–791.
28. Raffel M, Willert CE, Wereley ST, Kompenhans J. *Particle Image Velocimetry A Practical Guide*. Springer 2007.
29. Williams SJ, Park C, Wereley ST. Advances and applications on microfluidic velocimetry techniques. *Microfluidics and Nanofluidics* 2010; **8**(6):709–726. DOI:10.1007/s10404-010-0588-1.

30. Goldman A, Cox R, Brenner H. Slow viscous motion of a sphere parallel to a plane wall—II Couette flow. *Chemical Engineering Science* 1967; **22**(4):653–660.
31. Çarpinlio lu MÖ, Gündo du MY. A critical review on pulsatile pipe flow studies directing towards future research topics. *Flow Measurement and Instrumentation* 2001; **12**(3):163–174.
32. Yakhot A, Arad M, Ben-Dor G. Numerical investigation of a laminar pulsating flow in a rectangular duct. *International Journal for Numerical Methods in Fluids* 1999; **29**(8):935–950.
33. Muto T, Nakane K. Unsteady flow in circular tube: velocity distribution of pulsating flow. *Bulletin of JSME* 1980; **23**(186):1990–1996.
34. Denison EB, Stevenson WH, Fox RW. Pulsating laminar flow measurements with a directionally sensitive laser velocimeter. *AIChE Journal* 1971; **17**(4):781–787.
35. Uchida S. The pulsating viscous flow superposed on the steady laminar motion of incompressible fluid in a circular pipe. *Zeitschrift für angewandte Mathematik und Physik ZAMP* 1956; **7**(5):403–422.
36. Sert C, Beskok A. Numerical simulation of reciprocating flow forced convection in two-dimensional channels. *Transactions-American Society of Mechanical Engineers Journal of Heat Transfer* 2003; **125**(3):403–412.
37. O'Brien V. Pulsatile fully developed flow in rectangular channels. *Journal of the Franklin Institute* 1975; **300**(3):225–230.
38. Fan C, Chao B. Unsteady, laminar, incompressible flow through rectangular ducts. *Zeitschrift für angewandte Mathematik und Physik ZAMP* 1965; **16**(3):351–360.
39. Drake D. On the flow in a channel due to a periodic pressure gradient. *Quarterly Journal of Mechanics and Applied Mathematics* 1965; **18**(1):1–10.
40. Urata E. The frequency response of rectangular ducts. *Proceedings of the Institution of Mechanical Engineers-Part C: Journal of Mechanical Engineering Science* 2014: DOI: 10.1177/0954406214542037.
41. Franke M, Moore E. Dynamic response approximation for noncircular fluid lines. *Journal of Dynamic Systems, Measurement, and Control* 1976; **98**(4):421–424.
42. Ray S, Durst F. Semianalytical solutions of laminar fully developed pulsating flows through ducts of arbitrary cross sections. *Physics of Fluids* (1994-present) 2004; **16**(12):4371–4385.
43. Vazquez M, Schmalzing D, Matsudaira P, Ehrlich D, McKinley G. Shear-induced degradation of linear polyacrylamide solutions during pre-electrophoretic loading. *Analytical Chemistry* 2001; **73**(13):3035–3044.
44. Thurston GB. Viscoelasticity of human blood. *Biophysical Journal* 1972; **12**(9):1205–1217. DOI: S0006-3495(72)86156-3 [pii].
45. Cox WP, Merz EH. Correlation of dynamic and steady flow viscosities. *Journal of Polymer Science* 1958; **28**(118):619–622. DOI:10.1002/pol.1958.1202811812.
46. Zhang Z, Barman S, Christopher G. The role of protein content on the steady and oscillatory shear rheology of model synovial fluids. *Soft Matter* 2014; **10**(32):5965–5973.
47. Ray S, Ünsal B, Durst F, Ertunc Ö, Bayoumi O. Mass flow rate controlled fully developed laminar pulsating pipe flows. *Journal of Fluids Engineering* 2005; **127**(3):405–418.
48. Fam H. Effect of composition on periprosthetic fluid rheology and friction in total knee arthroplasty. PhD Thesis, Queen's University, 2010
49. Roylance D. *Engineering Viscoelasticity*, Vol. **2139**. Department of Materials Science and Engineering–Massachusetts Institute of Technology, Cambridge MA 2001: 1–37.
50. Shaw MT. *Introduction to Polymer Rheology*. John Wiley & Sons 2012.
51. Macosko CW, Larson RG. *Rheology: Principles, Measurements, and Applications*. John Wiley & Sons 1994.
52. Partal P, Franco JM. Non-Newtonian fluids, in *Rheology: Encyclopaedia of Life Support Systems (EOLSS)*. UNESCO.Eolss, Oxford 2010: 96–119.
53. Mackley M, Marshall R, Smeulders J. The multipacks rheometer. *Journal of Rheology* (1978-present) 1995; **39**(6):1293–1309.
54. Zhang Z, Christopher GF. The nonlinear viscoelasticity of hyaluronic acid and its role in joint lubrication. *Soft Matter* 2015; **11**(13):2596–2603.
55. Bekard IB, Dunstan DE. Shear-induced deformation of bovine insulin in Couette flow. *The Journal of Physical Chemistry B* 2009; **113**(25):8453–8457.
56. Bekard IB, Asimakis P, Bertolini J, Dunstan DE. The effects of shear flow on protein structure and function. *Biopolymers* 2011; **95**(11):733–745.
57. Thurston G, Gaertner E. Viscoelasticity of electrorheological fluids during oscillatory flow in a rectangular channel. *Journal of Rheology* (1978-present) 1991; **35**(7):1327–1343.
58. Krause WE, Bellomo EG, Colby RH. Rheology of sodium hyaluronate under physiological conditions. *Biomacromolecules* 2001; **2**(1):65–69.
59. Ambrosio L, Borzacchiello A, Netti P, Nicolais L. Rheological study on hyaluronic acid and its derivative solutions. *Journal of Macromolecular Science, Pure and Applied Chemistry* 1999; **36**(7-8):991–1000.

60. Jalali-Vahid D, Jin Z, Dowson D. Effect of start-up conditions on elastohydrodynamic lubrication of metal-on-metal hip implants. *Proceedings of the Institution of Mechanical Engineers, Part J: Journal of Engineering Tribology* 2006; **220**(3):143–150.
61. Jalali-Vahid D, Jin Z, Dowson D. Elastohydrodynamic lubrication analysis of hip implants with ultra high molecular weight polyethylene cups under transient conditions. *Proceedings of the Institution of Mechanical Engineers-Part C: Journal of Mechanical Engineering Science* 2003; **217**(7):767–777.
62. Jalali-Vahid D, Jagatia M, Jin Z, Dowson D. Prediction of lubricating film thickness in UHMWPE hip joint replacements. *Journal of Biomechanics* 2001; **34**(2):261–266.
63. Myant C, Cann P. On the matter of synovial fluid lubrication: Implications for Metal-on-Metal hip tribology. *Journal of the Mechanical Behavior of Biomedical Materials* 2014; **34**:338–348.
64. Meziane A, Bou-Saïd B, Tichy J. Modelling human hip joint lubrication subject to walking cycle. *Lubrication Science* 2008; **20**(3):205–222.

DOI: 10.1002/ls

Paper C

Viscoelasticity and Shear Thinning Effects on Bio-Polymer Solution and Suspended Particle Behaviors under Oscillatory Curve Couette Flow Conditions

Viscoelasticity and shear thinning effects on bio-polymer solution and suspended particle behaviors under oscillatory curve Couette flow conditions

Alaleh Safari[1], Nazanin Emami[1], Michel J. Cervantes[2,3]
[1]*Biotribology group, Division of Machine Element, Luleå University of Technology, 97187, Luleå, Sweden.*
[2]*Division of Fluid and Experimental Mechanics, Luleå University of Technology, 97187, Luleå, Sweden.*
[3]*Water Power Laboratory, Norwegian University of Science and Technology, 7491, Trondheim, Norway.*

Submitted to Journal of Non-Newtonian Fluid Mechanics

Abstract

Formation of wear particles within total hip replacement (THR) is one of the main causes of its failure. In addition to improving the lubrication and wear resistance of materials used as bearing surfaces, understating of wear particle distribution patterns within lubricants inside an implant gap could be used to improve design parameters and implants' lifespan. In this study, the behaviors of biolubricants (with compositions similar to human joint synovial fluid) and suspended particles were investigated by micro-Particle Image Velocimetry (micro-PIV) in curved mini channels under oscillatory Couette flow conditions. The studied biolubricants had shear thinning viscoelastic characteristics. We found that increasing shear thinning, elasticity or motion frequency levels did not affect the trend behaviors of biolubricant flows due to the low strain values of the experimental conditions applied. However, suspended particles formed strings along flow directions and exhibited cross-stream migration to channel walls. Motion frequency, fluid shear thinning and elasticity characteristics and channel dimensions strongly affected particle behaviors.

Keywords: Viscoelasticity, Unsteady Couette flow, Hyaluronic acid, Particle migration, Particle alignment

Abbreviasions:
THR: Total hip replacement
Micro-PIV: micro-Particle Image Velocimetry
SF: Synovial fluid
HA: Hyaluronic acid
PBS: Phosphate buffer saline

1. Introduction

The dynamics of non-Brownian suspended particles in non-Newtonian viscoelastic fluid flow have been recently studied widely due to their numerous biological and industrial applications [1]. One challenging application that has not yet received much attention is related to the distribution of wear particles in total hip replacements (THRs). Synovial fluid (SF), which lubricates human joints, is a viscoelastic fluid with non-Newtonian shear thinning characteristics. It is composed of proteoglycan (0.05-0.35 $mg.ml^{-1}$), hyaluronan (1-4 $mg.ml^{-1}$) and surface active phospholipids (0.1 $mg.ml^{-1}$), which provide lubricity features [2,3]. The shear thinning and viscoelasticity of SF is attributed to its hyaluronic acid (HA) composition as a linear biopolymer. HA exists in healthy SF at a molecular weight and concentration of 6.7-7.6 MDa and 1.45-4.22 $mg.ml^{-1}$, respectively [4]. However, characteristics of HA in SF of patient with THR, which is called periprosthetic SF, is not the same as healthy SF. THR is one of the most successful surgeries in the 21^{st} century. Most conventional THR design consists of a hard ball made of cobalt chromium (CoCr) alloy or ceramics moving against a soft accetabular cup usually made from ultra-high-molecular-weight polyethylene (UHMWPE). Although UHMWPE shows favorable mechanical and tribological properties for reducing friction, wear particles of this material produced during the THR life-time are the source of bone loss (osteolysis) and implant loosening which eventually cause failure [5]. Distribution patterns of these wear particles within implants' gaps are affected by the special rheological behaviors of the SF, geometrical parameters, particles' sizes, particles interactions and particle-fluid interactions [6,7]. Therefore, understanding these patterns can allow one to optimize design parameters to decrease wear particles and third body wear effects on bearing surfaces. Therefore, the lifespan of the implant and patient life quality are increased.

The specific behaviors of particles within viscoelastic fluid that are not happening in Newtonian fluid include particle migration and string formation along the flow direction. Particle alignment and string formation along the flow direction were first reported by Michele et al. [8]. These authors showed that randomly distributed particles in viscoelastic fluid subjected to shear or pipe flow align and build up strings. They attributed the discrepancy between particle behaviors in Newtonian and viscoelastic fluids to normal stress effects. This behavior was observed when the Weissenberg (Wi) value (defined as the ratio of normal stress to shear stress) reached at least to ten. Further investigations have focused on understanding the effects of parameters such as shear thinning, wall confinement, particle

sizes and flow conditions (shear or pressure driven and steady or unsteady) on the migration and alignment of particles in non-Newtonian viscoelastic fluid flows.

Lyon et al. [9] showed that particles in a fluid flow with an oscillatory motion, cluster rather than forming long strings. Won and Kim [10] conducted studies on both shear thinning and viscoelastic fluids under reciprocating shear flow conditions. They found that although the Wi number may be critical for particle migration, shear thinning is the determinant parameter for particle string structure formation. This observation was later confirmed by Van Loon et al. [7]. The results presented by Van loon et al. showed that while compressive forces originating from normal stress and elasticity effects enhance particle cross-stream migration and particle alignment, shear thinning is necessary for particle strings formation. Moreover, confinement from channel walls was found to improve collision probability levels and facilitate particle alignment. On the other hand, Scirocco et al. [11] showed that when particles are small enough relative to the channel size, gap sizes have no significant effects on alignment. The authors showed that experimental conditions, particle sizes and criteria used to define string formation processes have significant effects on critical Weissenberg number determination (the Wi value at which particle alignment starts), and they confirmed that a critical degree of shear thinning is required to initiate string formation. They also suggested that string formation is a bulk phenomenon that does not necessarily occur along the walls. However, Pasquino et al. [12] suggested that in very weak shear thinning fluids, particle alignment is not a bulk phenomenon and occurs near the walls. Particle strings were found to form when the applied shear rate value is higher than the critical shear rate and are enhanced when the shear rate is increased and the gap size is decreased. Once low shear rates and small particle sizes are involved, short strings of particles can align normal to the flow direction. The authors concluded that different parameters might affect string lengths and alignment directions. Particle sizes, fluid characteristics such as colloidal and hydrodynamic forces, kinetics of string formation and particle migration features were listed as some of the parameters involved. In a later work, the same authors defined an alignment factor for quantifying the effects of shear rates and particle concentrations on the duration and length of string formation. Their results showed that increasing both parameters results in faster and longer particle string formation [13]. Numerical and experimental studies on single particle migration under Couette flow conditions between two concentric cylinders conducted by D’avino et al. [14] showed that under the effects of viscoelasticity forces, particles migrate toward the outer cylinder unless they are very close to the inner cylinder. Higher angular

velocity and shear thinning rates were found to increase the migration rate. Numerical simulations of particle migration under reciprocated confined simple shear flows have shown that increasing the frequency ceases particle migration induced by fluid viscoelasticity and wall confinement [15]. This result is partly in agreement with the results of Lormand and Phillips's [16] study on particle migration within viscoelastic shear thinning fluids in concentric cylinders with oscillatory motion. Lormand's results showed that depending on initial particle positions, migration is directed towards the inner or outer cylinder. Inner migration velocity levels were found to increase with frequency. In Lormand's study, for frequencies larger than 1 Hz, outer migration velocities reached a value of zero and particles did not migrate toward the outer wall. The authors thus proposed that the migration rate is affected by the elasticity parameter [16].

Particles' migration and alignment in non-Newtonian viscoelastic fluid flows are affected by numerous factors: flow conditions (steady state, oscillatory, Couette, Poiseuille, etc.), gap and particle sizes and geometries, shear thinning, elasticity degrees, particle concentrations, etc.

The main objective of the present study was to investigate particle-flow interactions within a cylindrical curve channel mimicking a THR configuration. Various viscoelastic shear thinning HA solutions under an oscillatory Couette flow were investigated via micro particle image velocimetry (micro-PIV). The effects of HA concentration, protein content, motion frequency and gap size were investigated. Distilled water was used as the reference liquid. Potential improvements for THR design were deduced from the results.

2. Materials and Methods

2.1. Experimental Setup

Micro-PIV was used to derive velocity profiles of the polymeric fluid flow. The working principle of micro-PIV is the same as that of PIV but for smaller scales. In this method, tracing particles were added to the fluid. Particles were illuminated with a pulsed light (either laser or LED). Sequences of double frame images were captured by a CCD (charge coupled device) camera mounted on a microscope. The plane of the view was divided into numerous interrogation areas. The displacement of particles between two frames of a double frame image divided by the time difference between each light exposure provided the particle velocity value. According to PIV principles if the density and size of particles are suitable,

particles follow the fluid motion and particle behaviors are representative of fluid behavior [17-19]. Previous studies have included further information on particle suitability evaluations for studying the steady and unsteady behaviors of polymeric solutions [20,21].

Figure 1 shows a schematic view of the experimental setup used. The system included a double pulsed micro-strobe (LED) and a high-speed double frame CCD camera with a spatial resolution of 1,280×1,024 pixels per frame mounted on a microscope with four magnifications (5x, 10x, 20x and 40x). The two pulses had the same time duration (70 to 110 μs) based on the flow speed and channel size. The time between two pulses was set between 150 and 940 μs as a function of the speed amplitude and fluid type. Polystyrene particles (microParticles GmbH, Berlin, Germany) with a density of 1-1.05 $g.cm^{-3}$ and a diameter of 4.89 microns were used at a magnification of 10x.

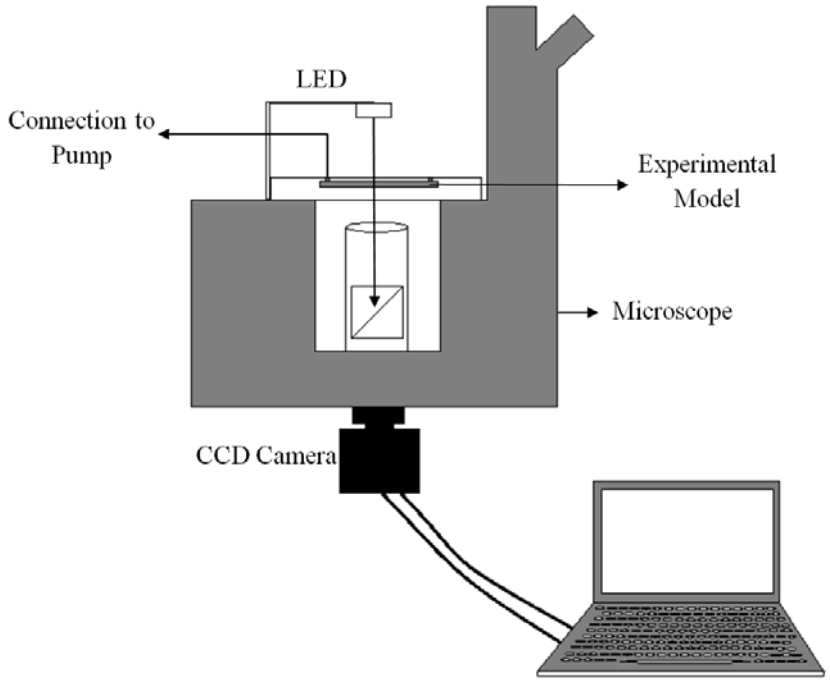

Figure 1 Schematic view of the experimental setup

2.2. Experimental Model

Two curved channels were designed to study particle-flow interactions under constant width and converging-diverging channel conditions. The curved channel consisted of two stainless steel concentric cylinders. To optically access the model, the stainless steel parts were placed inside a Plexiglas frame. The constant-width channel was 1.1 mm wide while the width of the converging-diverging channel ranged from 0.3 to 1.1 mm. The inner wall radius and depth of both channels were set to 21 and 3 mm, respectively. Approximately 3 ml of fluid was stored

in the rectangular storage areas of each model during the measurement period (Figure 2). The channels were sealed with an upper Plexiglas plate. Hereafter, the constant width channel is referred to as the Const Channel and the converging diverging channel is referred to as the Conv Channel.

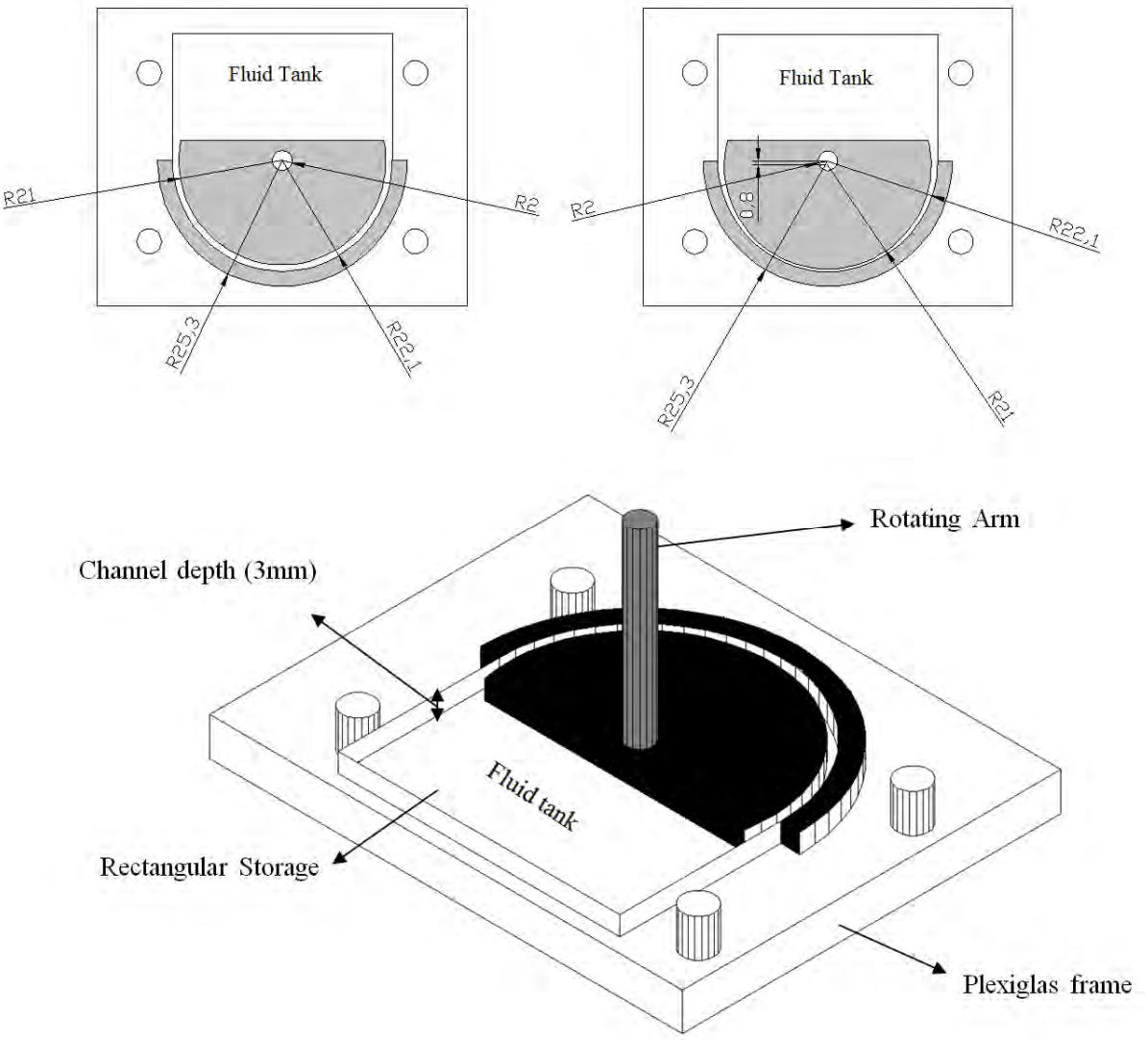

Figure 2 Experimental model

2.3. Reciprocal movement

The inner cylinder was oscillated by a rotating disk powered by an electrical motor in combination with four rotating arms and one pushing arm. Figure 3 presents a schematic view of the oscillatory engine coupled with the experimental model. To determine the angular positioning of the disk, a magnetic encoder and twelve steel teeth (knobs) spaced equally along the periphery of the disk were used. An encoder signal synchronized the micro-PIV and LED, i.e., it acted as a trigger. Images were captured at defined phases. As noted in the

previous study, to achieve statistically significant mean velocity profiles, several velocity maps must be averaged [20]. Under oscillatory conditions, averaging is possible only for images captured at almost the same phase. Image phases were defined based on the positioning of the pushing arm and rotating disk phase. The positioning of pushing arm was defined by a distance laser.

A code developed in LabVIEW controlled the frequency of the rotating disk. Three different frequencies were applied: 0.37, 1.02 and 2.03 Hz. The criteria applied to select the frequency are listed in our previous paper [21]. The rotation amplitude of the inner cylinder was set to 15° (total movement of 30°), which is the average hip joint rotation amplitude in sagittal plane that occurs during walking [22].

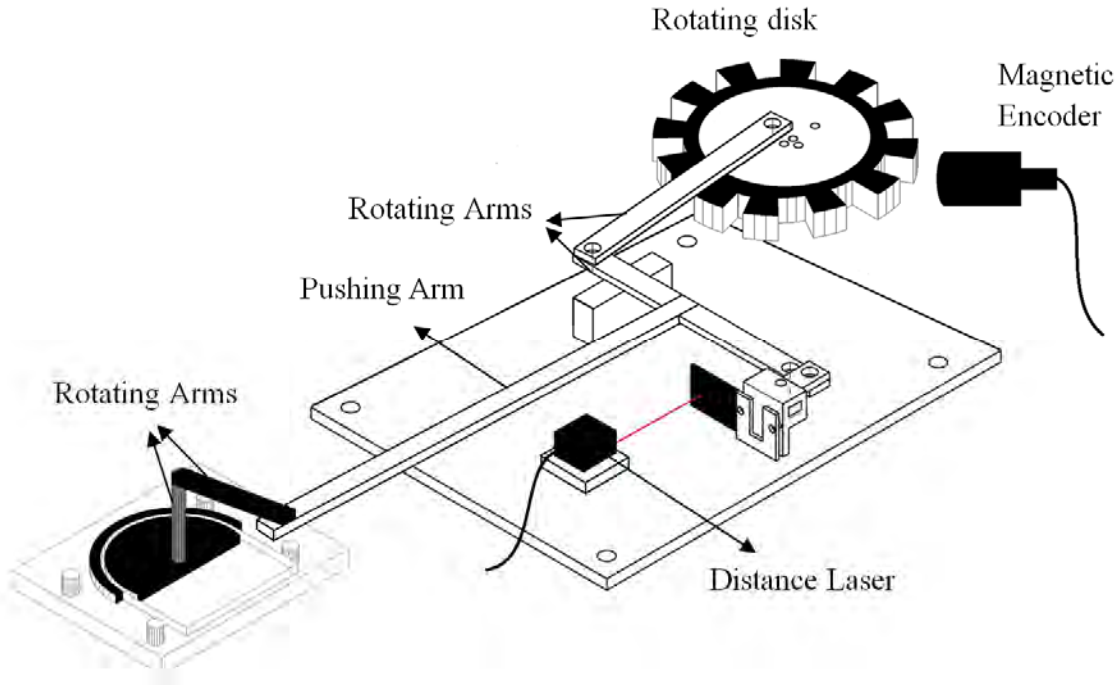

Figure 3 Schematic view of the oscillatory engine

2.4. Experimental Fluid

Distilled water was used as reference Newtonian fluid. The HA solutions investigated were selected to capture periprosthetic fluid characteristics through using a simple composition. Available data suggest that the periprosthetic fluid has a similar composition to that of normal synovial fluid with less viscosity, shear thinning and viscoelastic behavior [23]. To capture characteristics of the periprosthetic fluid and to investigate effects of the different parameters on flow behaviors, three solutions of HA were studied:

1- HA with 1.6-1.8 MDa molecular weight (Sigma Aldrich 53747, St. Louis, Missouri, USA) with a concentration of 3 $mg.ml^{-1}$ in Phosphate Buffer Saline (PBS from Sigma Aldrich, St. Louis, Missouri, USA with 0.15 M concentration).

2- HA with 3 $mg.ml^{-1}$ concentration in a mixture of 75% PBS and 25% bovine calf serum (Sigma Aldrich 12133C).

3- HA with 5 $mg.ml^{-1}$ concentration in PBS.

To minimize bacterial activity, 0.1% (w/v) sodium azide (Sigma Aldrich 71289, St. Louis, Missouri, USA) was added to the HA solutions.

The blending procedures applied to the solutions have been published [20].

Rheological behaviors of the HA solutions were investigated using a Bohlin CVO Rheometer at 25° C under shear rate control (0.05-1570 s^{-1}) with coaxial cylinders (C25) to obtain the variation of viscosity versus the shear rate. The viscoelastic behavior of the HA with 5 $mg.ml^{-1}$ concentration in PBS was investigated using the same Rheometer and cone on plate configuration, which consisted of a stainless steel cone of 1° and 20 mm in diameter. Frequency sweep measurement was performed with the strain value of 2% and strain frequency between 0.07 and 10 Hz. Investigating the viscoelastic behavior of the HA solutions with 3 $mg.ml^{-1}$ was not possible due to the calibration range of the Rheometer used. Table 1 provides a summary of the experimental conditions applied.

Table 1 Experimental conditions

Fluid	**Fluid Name**
Water	Fluid 1
PBS+HA 3 $mg.ml^{-1}$ Solution	Fluid 2
75% PBS+25% Serum+HA 3 $mg.ml^{-1}$ Solution	Fluid 3
PBS+HA 5 $mg.ml^{-1}$ Solution	Fluid 4
Channel Width (*h*)	**Channel Name**
1.1	Const Channel
0.3-1.1	Conv Channel
Flow Frequency (Hz)	**Frequency Acronym**
f =0.37 Hz	*Fr*-0
f=1.02 Hz	*Fr*-1
f= 2.03 Hz	*Fr*-2

3. Theory

A shear flow induced by a flat plate with harmonic oscillatory motion in its own plane is known as Stokes' second problem [24]. Viscous waves generated at the moving wall penetrate into the fluid with a velocity perpendicular to the wall and a penetration depth calculated from Eq. 1 [25]

$$\delta = \sqrt{\frac{2\nu}{\omega}} \qquad \text{Eq. 1}$$

δ, ν and ω represent the penetration depth or Stokes boundary layer thickness, the kinematic viscosity and the frequency of oscillation, respectively.

Figure 4 shows a 2-dimensional view of the experimental model and measurement location. The measurement location was set at 45° with respect to the symmetrical axis of the model. For the Conv Channel, the ratio of the widths of the largest to smallest measurement sections width in a complete cycle was more than 2 at this location. The maximum curvature ratio (ratio of the width of the channel to the inner cylinder radius) of both channels was 0.05. Due to the small field of view and small curvature ratio, it was assumed that curvature effects were negligible in our analytical analysis. The half-circle part (Figure 4) is subjected to oscillatory motion in its own plane at a velocity of $u_x = A\cos(\omega t)$. Assuming a negligible effect of the curvature on the flow, the governing equation for the conservation of momentum for both Const and Conv Channels is given by Eq. 2:

$$\rho \frac{\partial u}{\partial t} = \frac{\partial}{\partial y}\left(\mu \frac{\partial u}{\partial y}\right) - \frac{\partial P}{\partial x} \qquad \text{Eq. 2}$$

where ρ, μ and P represent density, dynamic viscosity and pressure, respectively.

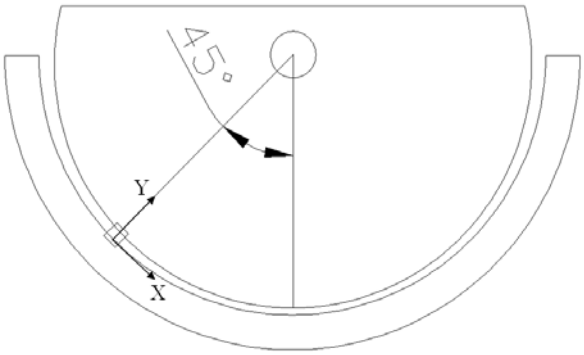

Figure 4 Schematic 2-D view of the experimental model

In Eq. 2, $\frac{\partial P}{\partial x} = 0$ for the Const Channel. The flow induced by a moving wall between two parallel infinite plates was solved by Berker [26]. Berker solved this problem for a moving plane with sinusoidal harmonic motion placed at y=0 and a fixed plane placed at y=h. The boundary conditions and general form of the velocity solution are presented in Eq. 3 and Eq. 4:

$$u(h,t) = 0$$
$$u(0,t) = u_0 \sin(\omega t) \qquad \text{Eq. 3}$$

$$u = f(y)\sin(\omega t) + g(y)\cos(\omega t) \qquad \text{Eq. 4}$$

Eq. 5 is the derived fluid velocity:

$$u = \frac{u_0}{\sin(\beta_1 + \beta_2)}\left(e^{y\sqrt{\omega/2\nu}} \sin\beta_2 .\right.$$
$$\sin(\omega t + y\sqrt{\omega/2\nu} + \beta_1) \qquad \text{Eq. 5}$$
$$\left. + e^{-y\sqrt{\omega/2\nu}} \sin\beta_1 .\right.$$
$$\sin(\omega t - y\sqrt{\omega/2\nu} - \beta_2)$$

where β_1 and β_2 are arbitrary constants.

In the current study, the moving surface was placed at *y*=h with Cosine oscillatory motion. The Berker solution was adapted in this case. The adapted boundary condition and general form of the velocity are presented in Eq. 6 and Eq. 7.

$$u(h,t) = u_0 \cos(\omega t) = u_0 \sin(\omega t - \pi/2)$$
$$u(0,t) = 0 \qquad \text{Eq. 6}$$

$$u = f(y)\sin(\omega t - \frac{\pi}{2}) + g(y)\cos(\omega t - \frac{\pi}{2}) \quad \text{Eq. 7}$$

By adding a phase difference of $-\frac{\pi}{2}$ and replacing "*y*" with "*y*-*h*" in the general solution derived by Berker, the boundary conditions are satisfied.

The final form of the equation obtained for velocity is presented in Eq. 8.

$$\begin{aligned} u = {} & \frac{-u_0}{\sin(\beta_1 + \beta_2)}(e^{(y-h)\sqrt{\omega/2\nu}} \sin\beta_2. \\ & \sin(\omega t + (y-h)\sqrt{\omega/2\nu} + \beta_1 - \frac{\pi}{2}) \\ & + e^{-(y-h)\sqrt{\omega/2\nu}} \sin\beta_1. \\ & \sin(\omega t - (y-h)\sqrt{\omega/2\nu} - \beta_2 - \frac{\pi}{2}) \end{aligned} \quad \text{Eq. 8}$$

The arbitrary constants β_1 and β_2 are obtained from Eq. 9 and Eq. 10.

$$\beta_1 + \beta_2 = 2h\sqrt{\omega/2\nu} \quad \text{Eq. 9}$$

$$\beta_1 = \tan^{-1}\left(\frac{-(\sin(2h\sqrt{\omega/2\nu})}{(e^{2h\sqrt{\omega/2\nu}} - \cos(2h\sqrt{\omega/2\nu})}\right) \quad \text{Eq. 10}$$

Appendix I includes the derivation procedure for β_1 and β_2.

4. Data Analysis

The velocity profiles were derived by applying cross-correlations between two frames of a double frame image. Based on the criteria described in our pervious publication [20], the interrogation area size was set to 16×128 pixels. The border of the analysis was set at two particle diameters from the wall to prevent the large error region.

The distance laser determined the position of the pushing arm at each instant. Connections between the arms were assumed to be solid and sinusoidal movement was transferred to the moving cylinder. The sinusoidal velocity of the moving cylinder was derived from the distance laser signal. The zero phase was defined as the middle position of the pushing arm when moving backward. At least 120 images were captured at each phase. Derived velocity maps were phase resolved and averaged at each phase, i.e., angular resolved. Sinus curves

were fitted at angular resolved velocities along the width of the channel, thus describing the profile in time for the Const Channel. The amplitude and phase of the fluid velocity used in the analysis were derived from the sinus curves. The phase difference between the moving wall and fluid was calculated from Eq. 11.

$$u_{cylinder} = Amp_{u_{cylinder}} \sin(2\pi f + \phi)$$
$$u_{fluid} = Amp_{fluid} \sin(2\pi f + \phi') \qquad \text{Eq. 11}$$
$$\Delta\phi = \phi - \phi'$$

where u, Amp, f and ϕ represent the measured velocity, calculated amplitude, frequency and phase of motion, respectively. The velocity was made dimensionless by dividing it by the maximum amplitude. As the phase acquired for the moving wall was $\phi = -90°$, the cylinder velocity can be written in cos form (Eq. 12).

$$u_{cylinder} = -Amp_{u_{cylinder}} \cos(2\pi f) \qquad \text{Eq. 12}$$

Channel width variations in the Conv Channel made it impossible to use the same procedure for the data analysis. Therefore, results were compared at each phase.

It was noted in reference [20] that at least 300 images are required to have mean velocity variations of less than 0.5%. For this set of measurements, due to CCD camera memory limitations, 120 images were captured at each phase. The relative difference (RD) between the mean velocity obtained from 120 and 300 images was investigated (Eq. 13). Figure 5 shows RD along the channel width. The RD is presented for the case of distilled water at a frequency of 2.03 Hz and for the phase with the cylinder maximum velocity.

$$RD = \frac{\left|\bar{u}_{120} - \bar{u}_{300}\right|}{u_{cylinder}} * 100 \qquad \text{Eq. 13}$$

where $\bar{u}_{120}$ is the mean value of the velocity calculated using 120 images, $\bar{u}_{300}$ is the mean value of the velocity calculated using 300 images and $u_{cylinder}$ is the cylinder velocity of the specific phase. The results show that the maximum relative difference along the channel is less than 1% of the cylinder velocity.

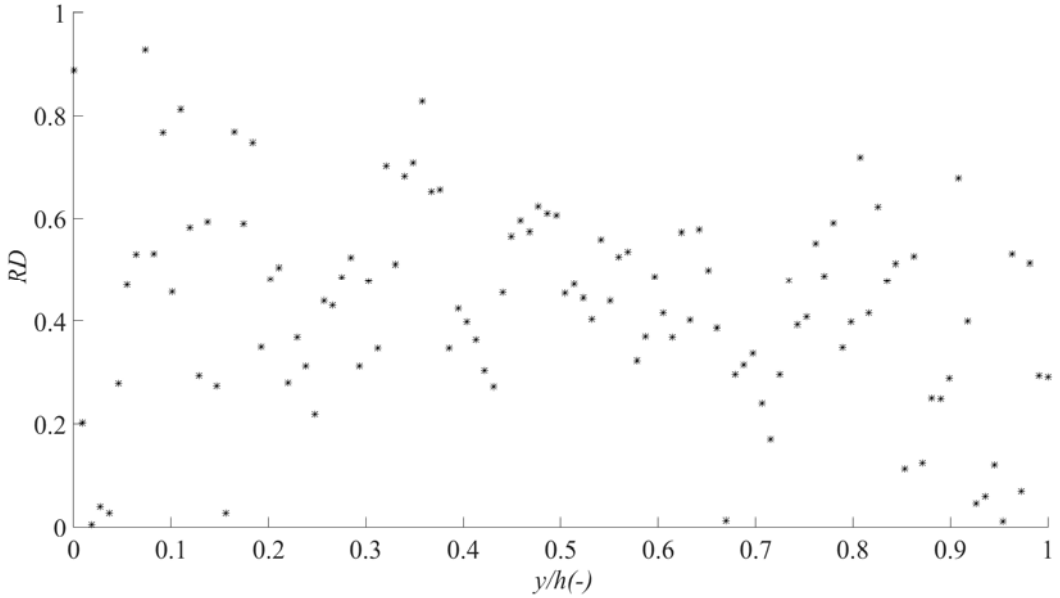

Figure 5 Relative difference in mean velocities obtained from 120 and 300 images along the channel width at f=2.03 Hz.

5. Results and Discussion

5.1. HA Rheology

Figure 6 shows the viscosity versus the shear rate for the three HA solutions investigated. The HA solution with protein content showed higher viscosity compared to the HA solution without protein at low shear rates. As noted by Zhang et al. [27], the rheological behavior of these two solutions is actually the same, and the difference is attributed to the interfacial effects of rheological measurements. The intersection of the two lines fitted on the experimental measurements defines the critical shear rate ($\dot{\gamma}_{critical}$) [28,29]. $\dot{\gamma}_{critical}$ is the shear rate at which the disentanglement of the HA solutions and shear thinning behavior begins. The inverse of $\dot{\gamma}_{critical}$ is equal to the longest relaxation period. The relaxation periods of the higher and lower HA solution concentrations were 0.168 and 0.077 s, respectively.

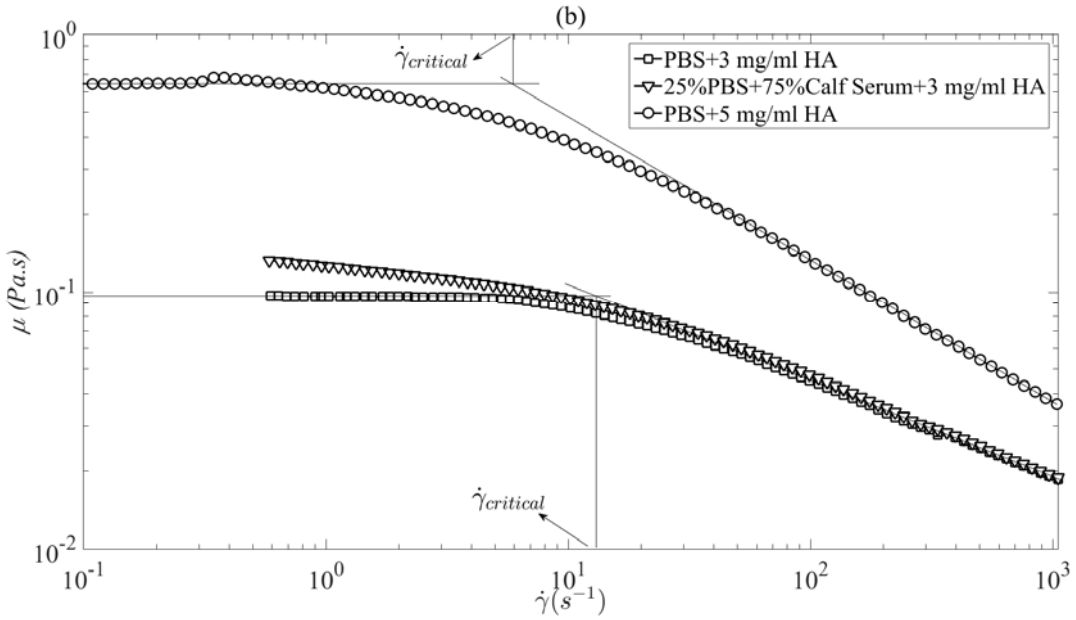

Figure 6 Viscosity (μ) function of the shear rate (γ) for the HA solutions

Figure 7 shows the dynamic moduli versus the strain frequency for the HA solutions with 5 $mg.ml^{-1}$ concentration. The crossover frequency is at 1.1 Hz. At frequencies lower than the crossover frequency, viscosity controls the flow behavior while at higher frequencies the elasticity dominates the viscous effects. For lower HA solution concentrations, the dynamic moduli were not measurable due to instrument limitations. However, it is known that by decreasing the HA concentration, the crossover frequency increases [30].

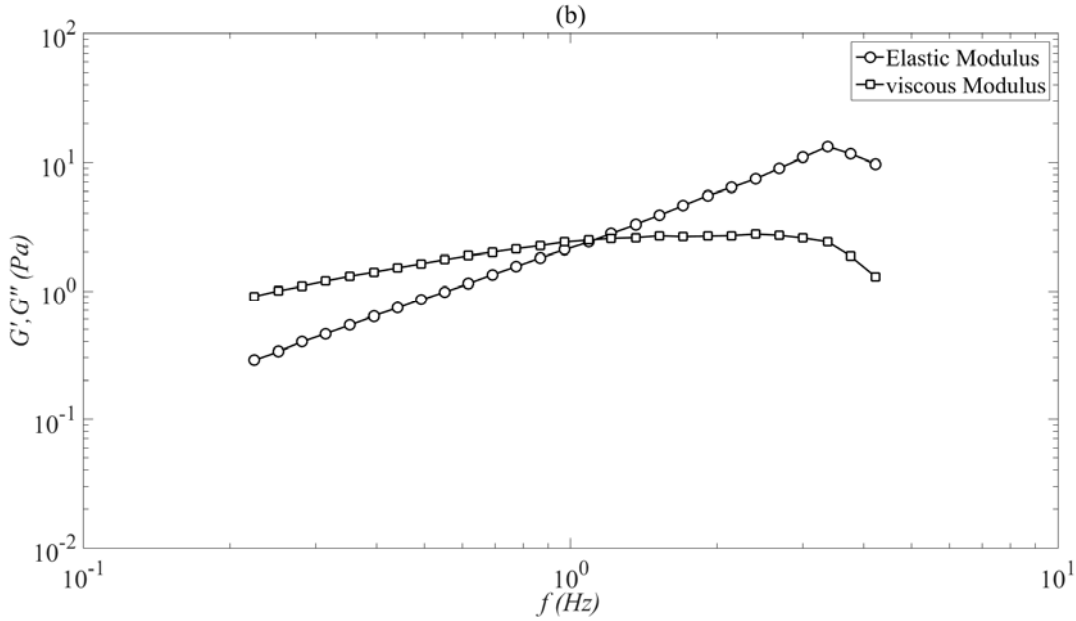

Figure 7 Viscous and elastic moduli (G' and G") versus strain frequency (f) for HA solution with 5 $mg.ml^{-1}$ concentration in PBS

5.2. Channel with constant width

5.2.1. Water behavior

Figure 8 shows the experimental and theoretical results for the amplitude and phase difference profiles along the non-dimensional channel width for distilled water at difference frequencies. The experimental and theoretical results deviate significantly. At Fr-2 and Fr-1, and for the region near the moving wall, the experimental and theoretical results are similar. For the theoretical solution, it was assumed that the parallel plates were infinite. However, this was not the case in the current experiment. Moreover, the curvature effect was assumed to be negligible.

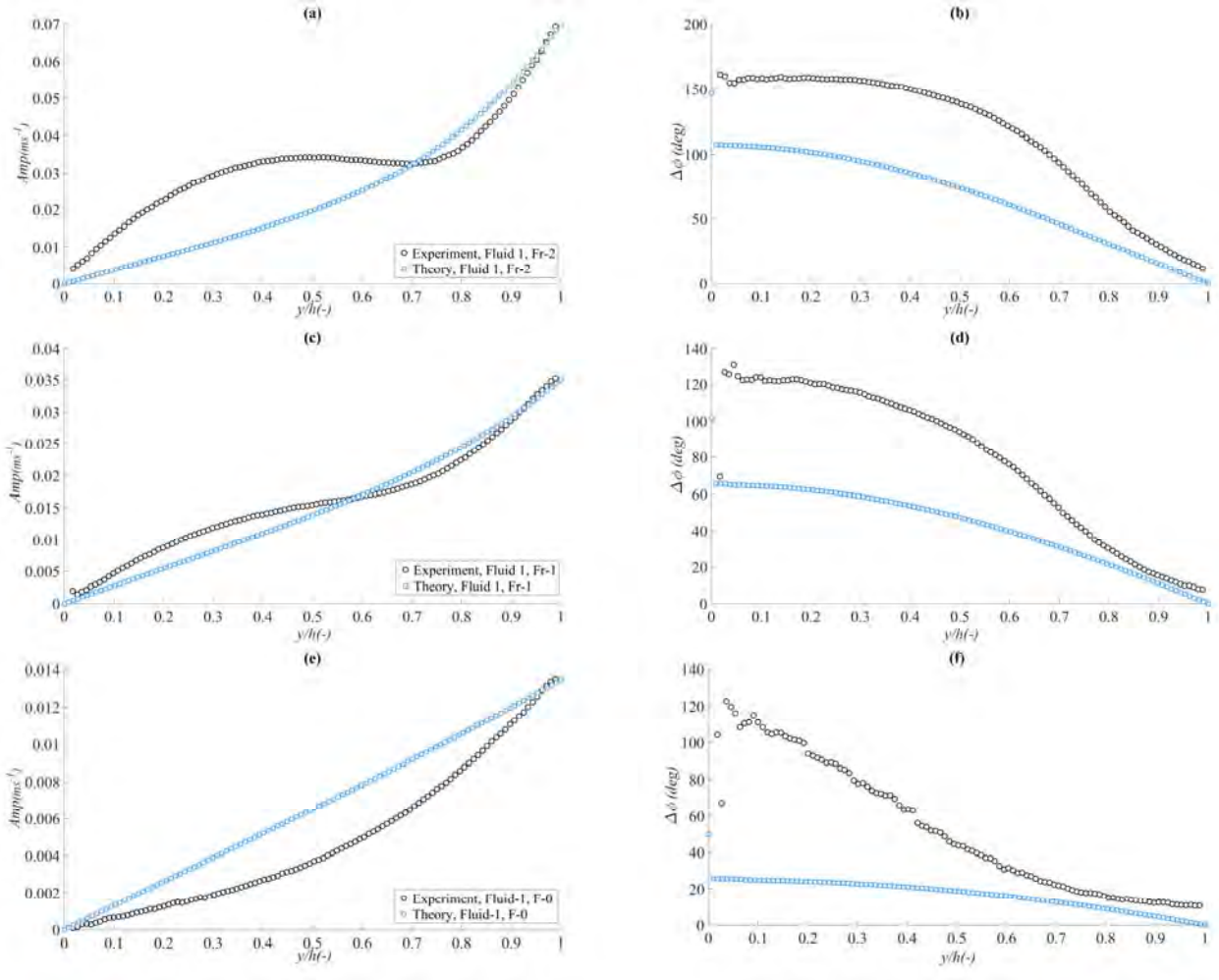

Figure 8 Amplitude (Amp) and phase difference ($\Delta\phi$) of distilled water in the Const Channel for the experimental (black circle) and theoretical solution (blue square) for (a) and (b) Fr-2, (c) and (d) Fr-1, (e) and (f) Fr-0.

To investigate the effect of the side walls and the curvature on induced flow between the two concentric half cylinders, a CFD model was developed in Ansys CFX. The model comported

only the curved channel, i.e., the fluid tank shown in Figure 2 was not included in the numerical domain. A hexahedral mesh consisting of more than 200,000 elements was used to discretize the space with a time step of 0.02 s. Figure 9 shows the analytical, numerical and experimental amplitudes for distilled water at Fr-2. The agreement between the theoretical and numerical results suggests that the difference between the experimental and theoretical results did not originate from the side walls or curvature effects.

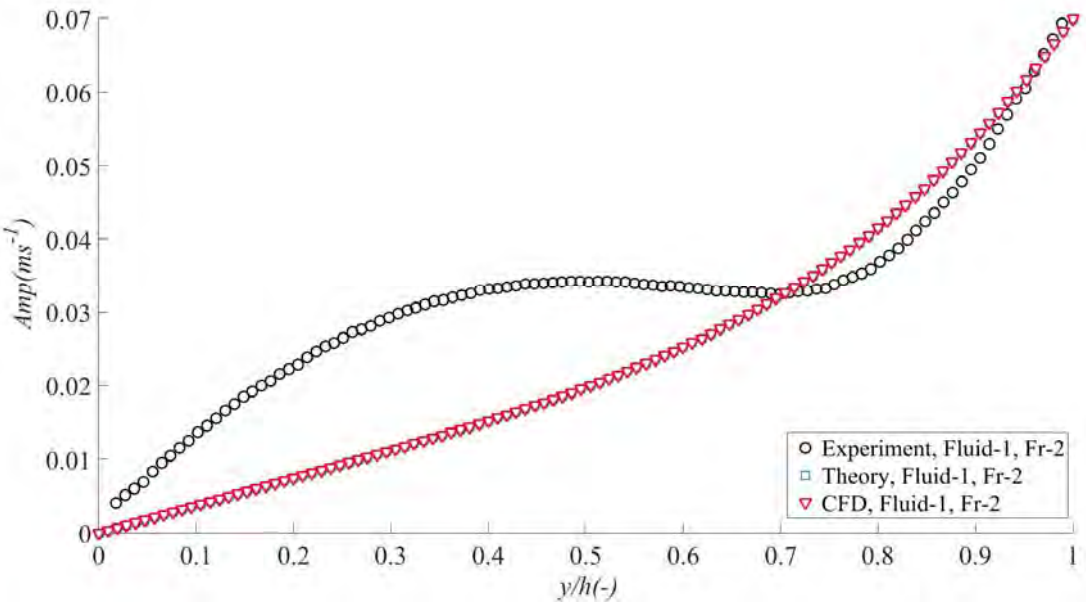

Figure 9 Amplitude (*Amp*) along non-dimensional channel width in the Const Channel for distilled water at frequency of 2.03 Hz.

At Fr-2, the Stokes length (Stokes boundary layer thickness) was 0.4 mm, which was smaller than the width of the channel (1.1 mm). The viscous waves generated at the moving wall only described the fluid behavior in the vicinity of the moving wall. With increasing distance from the inner cylinder, the phase difference increased. Figure 10 shows the experimental and theoretical velocity profiles along Const Channel width for various phases of cylinder motion. Because of small Stokes length, at some phases (e.g. $\phi = 303°$) the flow direction in the vicinity of moving wall was opposite to that of middle of channel. However, the experimental results enhanced this phenomenon.

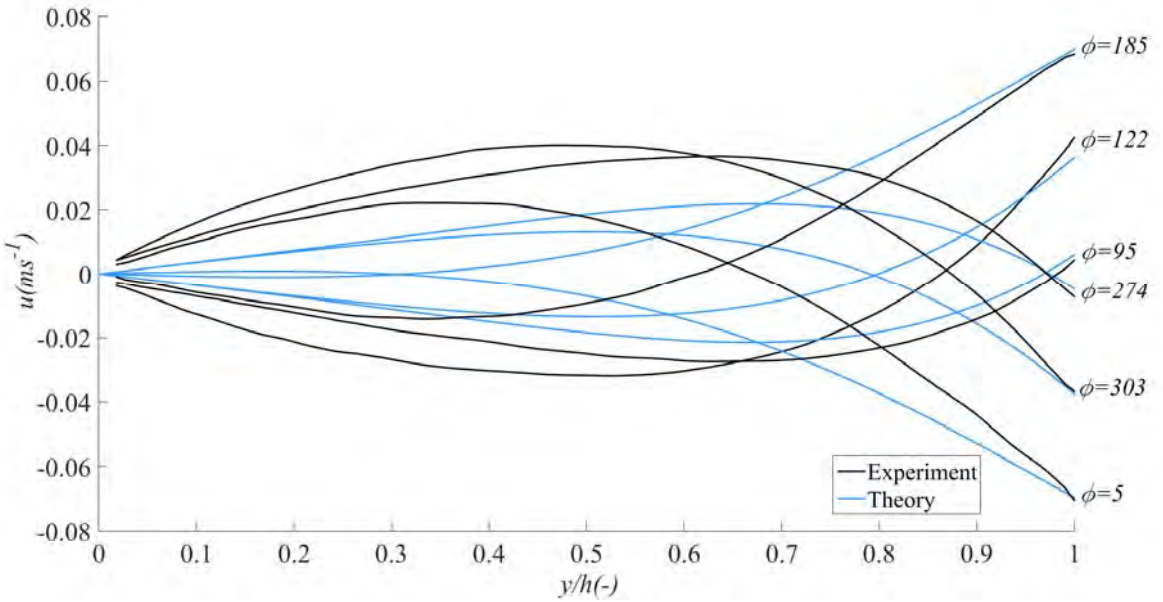

Figure 10 Experimental (black lines) and theoretical (blue lines) velocity profiles along the Const Channel width for distilled water at frequency of 2.03 Hz.

The theoretical solution applies for flows between two infinite parallel plates. However, in the experiments, surfaces were finite and in contact with a fluid tank (Figure 2). Since the flow behavior in fluid tank was not interesting for this study, the PIV data were only collected within the channel. Therefore, there are no results available on velocity maps within fluid tank. However, it is speculated that the difference between experimental and theoretical results can be attributed to a reverse flow generated as the inner disk moved back and forth through the fluid tank (Figure 11).

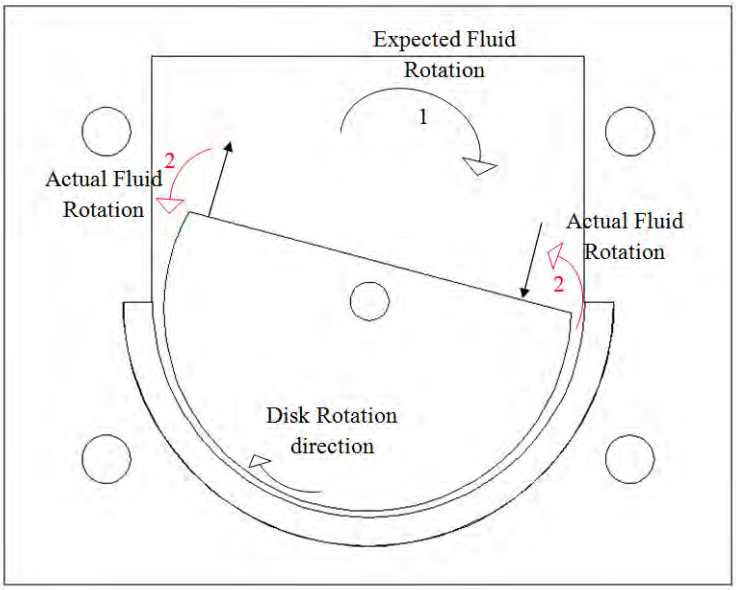

Figure 11 Fluid motion within the experimental model.

Figure 11 shows a schematic of the experimental model and of fluid rotations within the model. The rotation of the inner disk generated fluid rotation within the fluid tank. It was expected that the fluid moved based on the rotation direction shown in Figure 11 with black arrow number 1. However, the fluid might also move and rotate as indicated by the red arrows marked with a number 2. Therefore, a reverse flow that was actually a pressure driven flow may have formed within the channel.

For frequencies of 2.03, 1.02 and 0.37 Hz, Stokes lengths were 0.4, 0.56 and 0.93 mm, respectively. At frequencies of 2.03 and 1.02 Hz, Stokes lengths was smaller than the width of the channel, and therefore the flow near the moving wall (inner cylinder) was controlled by the induced shear flow, and the amplitude profiles of the experimental and theoretical results followed almost the same behavior in that region (Figure 8 (a) and (c)). However, the flow near the fixed wall was controlled by the pressure driven reverse flow. Therefore, different behaviors between the amplitude profiles of the experimental and theoretical results were found.

At a frequency of 0.37 Hz, the Stokes length was comparable to the channel size. Therefore, viscous waves generated at the moving wall (due to shear induced flow) and constant wall (due to pressure driven reverse flow) could control the flow across the entire channel width. The final flow was the superposition of two flows. The reverse flow reduced the absolute value of the velocities induced by the moving surface along the width of the channel. In Figure 12 and at each phase, the absolute values of the experimental velocity profiles along the width of the channel are lower than those of the theoretical velocity profiles. Therefore, the amplitude profile along the width of the channel for the experimental results is lower than that of the theoretical results (Figure 8 (e)).

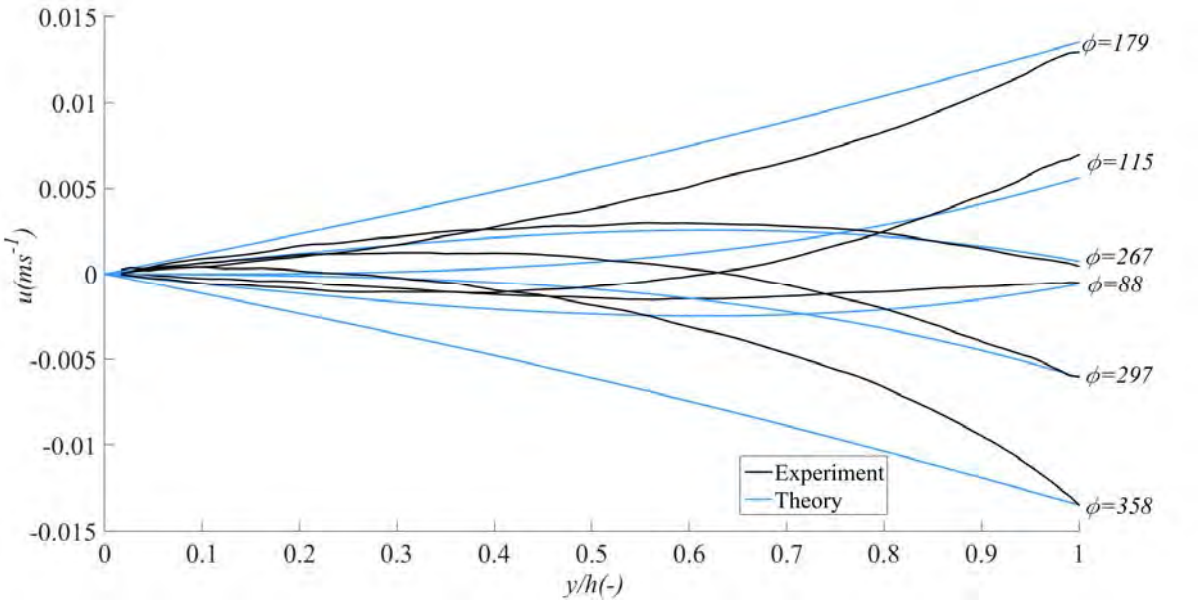

Figure 12 Experimental (black lines) and theoretical (blue lines) velocity profiles along the width of the Const Channel for distilled water at frequency of 0.37 Hz.

5.2.2. HA Behavior

Figure 13 shows velocity profiles along the non-dimensional channel width for the lower concentration of HA solution (Fluid 2) at the highest frequency: f = 2.03 Hz. The HA viscosity at the highest achievable shear rate was roughly 40 times that of distilled water (Figure 6). The penetration depth of the viscous wave was much greater than the width of the channel and viscous forces controlled fluid behavior. At each instant, the velocity profiles maintained steady state conditions.

Figure 14 shows the non-dimensional amplitude and phase difference profiles along the non-dimensional channel width for HA solution with 3 mg.ml^{-1} concentration in PBS (Fluid 2) at different motion frequencies. Different behavior from that of distilled water was observed, as the frequency of motion did not affect the amplitude or phase difference.

For a polymeric solution and under oscillatory motion, the Deborah number (fluid characteristic time to flow characteristic time ratio) shows how viscoelasticity affects the flow. At a Deborah number of close to 1 or higher, elastic forces affect the solution behavior [21]. The Deborah number for lower HA solution concentrations under different frequency of motion conditions is presented in Table 2. Although the Deborah number was large at frequencies of 1.02 and 2.03 Hz, the polymeric solution did not show any variations in

behavior. This suggests that a different mechanism dominated and controlled the flow behavior.

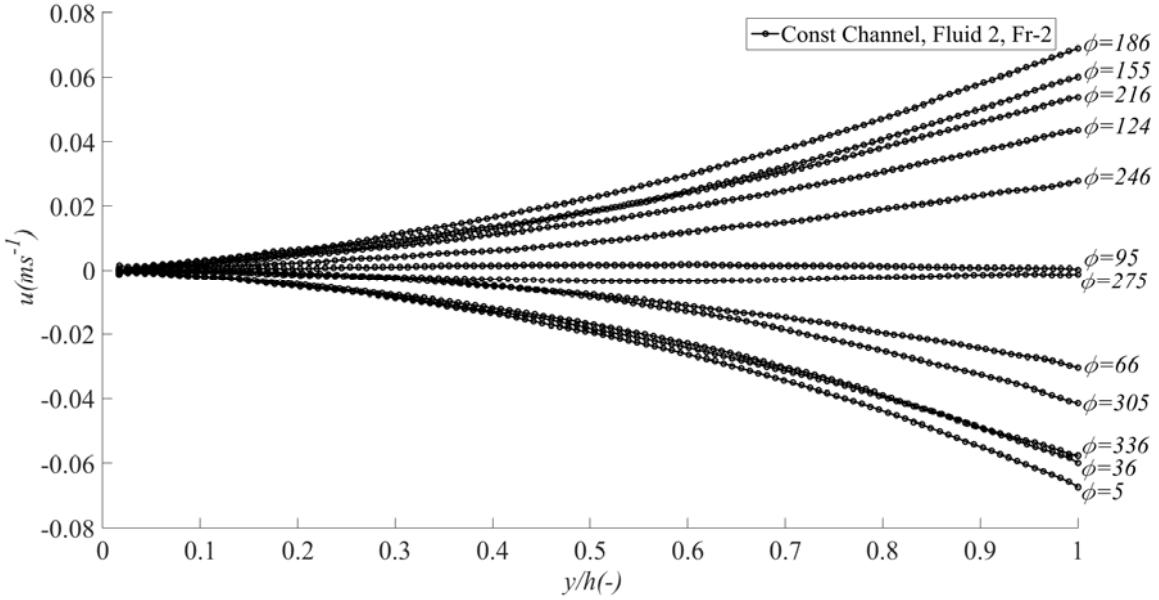

Figure 13 Velocity profiles along the non-dimensional channel width (x/h) for HA solution with concentration of 3 $mg.ml^{-1}$ in PBS for the constant width channel (Fr-2) with the moving wall placed at 1.

The same behavior was observed for HA solutions with and without protein content at frequencies of 1.02 and 2.03 Hz. A comparison of amplitudes and phase differences of HA solutions of different concentrations at different frequencies (Figure 15) shows that almost the same behavior was observed for Fr-0 and Fr-1. Differences between the non-dimensional amplitude profiles shown in Figure 14(a) and Figure 15 (a) for Fr-0 and Fr-1 were less than 1% (as expected based on the section 4. Data Analysis (Figure 5)). However, the difference between non-dimensional amplitude profiles for Fluid 4 at Fr-2 near the moving wall in Figure 15 (a) relative to other amplitude profiles was roughly 4%. At higher HA solution concentrations (5 $mg.ml^{-1}$) and at the highest frequency (Fr-2), a different behavior near the rotating wall was observed (see Figure 16). This suggests that in contrast to previous findings [21], under these conditions the De number did not describe the flow behavior and other fluid characteristics dominated the flow behavior.

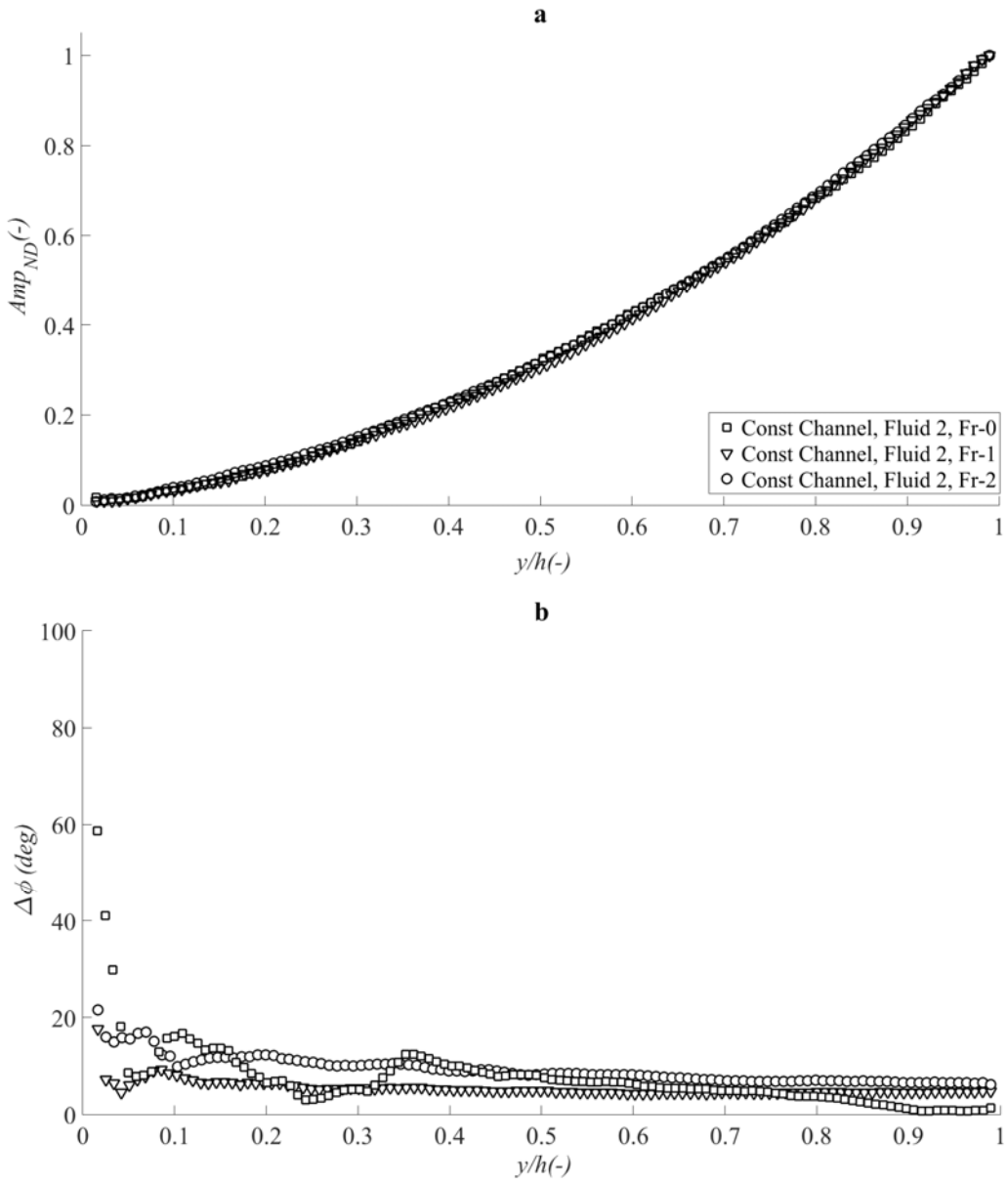

Figure 14 (a) Non-dimensional amplitude (Amp_{ND}) and (b) phase difference ($\Delta\phi$)of HA with 3 $mg.ml^{-1}$ concentration in PBS for the constant width channel at Fr-0 (square), Fr-1 (triangle) and Fr-2 (circle); moving wall is located at 1.

Previous experiments were performed on an unsteady Poiseuille flow [21]. In earlier study, the HA molecular weight was slightly lower (1.4-1.5 MD) than the present study (1.6-1.8 MDa). While the reciprocal frequency and geometric parameters applied in the current and previous experiments were the same [21], the strain had different values (Eq. 14).

$$\dot{\gamma} = \omega\gamma \qquad \text{Eq. 14}$$

where γ, $\dot{\gamma}$ and ω are the shear strain, shear rate and strain frequency, respectively.

A maximum strain value of 8 was reached in the present study, which was much lower than the strain values of 23 to 60 in previous experiments [21]. Therefore, the strain gradient along the width of the channel was smaller.

The critical concentration (the concentration at which entanglement formation starts) for a HA solution with a molecular weight of 1.5 MDa in PBS has been reported to be 2.4 $mg.ml^{-1}$ [31]. This suggests that for all tested HA solutions, HA chains were entangled and formed temporary networks. Applying strain resulted in network disentanglement. On the other hand, the Brownian motion acted towards forming new entanglements. The disentangled chains tended toward aligning with the flow. This combination of opposing forces applied to the HA chains resulted in net force creation on the polymer chains. Based on the coordinated system shown in Figure 4, the contributions of this force to the normal stress in the flow direction (σ_{xx}) were more significant than contributions to the normal force in the y direction (σ_{yy}) [32]. The difference between these two normal stresses is known as the *first normal stress difference* (N_1 in Eq. 15) which is representative of elasticity in viscoelastic fluids.

$$N_1 = \sigma_{xx} - \sigma_{yy} \qquad \text{Eq. 15}$$

Therefore, anisotropy in the HA solution was actually induced by the strain [32,33]. In previous study [21], higher strain generated higher degree of disentanglement and gave rise to the elasticity effect. Moreover, under such high strain values, the viscoelastic behaviors of the HA solutions were non-linear [21].

Under Poiseuille flow conditions [21], the pressure difference applied to the fluid produced flows that also contributed to the normal force in the flow direction (σ_{xx}) and could increase *the first normal stress difference* and enhance the elastic effects. However, when the flow was induced by a moving surface, this pressure effect was not present.

In characterizing viscoelastic non-Newtonian behaviors of a fluid, two non-dimensional parameters are usually evaluated: the Deborah and Weissenberg numbers. The Weissenberg number defines the effect of elastic forces relative to viscous forces. Two equations are typically used to define this parameter (Eq. 16 and Eq. 17) [34].

$$Wi = \dot{\gamma}\lambda \qquad \text{Eq. 16}$$

$$Wi = \frac{N_1}{\sigma_{xy}} \qquad \text{Eq. 17}$$

where λ is the fluid characteristic time, which is usually considered to be the longest relaxation time (inverse of $\dot{\gamma}_{critical}$). N_1 and σ_{xy} represent first normal stress and shear stress, respectively. $\dot{\gamma}$ is the amplitude of the strain rate in an unsteady oscillatory flow. Table 2 shows the Weissenberg number for fluids 2 and 4.

As the Wi number is proportional to the strain value, the present results had considerably lower Wi values in comparison to the previous measurements on unsteady Poiseuille flows [21]. The small Wi and strain values show that the disentanglement density was not considerable.

Discrepancies between Newtonian and non-Newtonian flow velocity profiles under Poiseuille flow originated from variations in the strain along the width of the channel. Variations in the strain value along the width of the channel could be an effective parameter for obtaining different velocity profiles under different measurement conditions as well. However, for the present measurements, variations in strain values along the width of the channel were not considerable. Strain values changed from 1.5 at the outer stationary wall to 8 at the inner channel wall. Therefore, there was not a considerable strain distribution to cause strong velocity deviations between different measurement conditions.

Table 2 Weissenberg and Deborah number values for Fluids 2 and 4.

Fluid	**Frequency**	**Wi**	**De**
Fluid 2	Fr-0	0.23	0.35
	Fr-1	0.63	0.99
	Fr-2	1.25	1.97
Fluid 4	Fr-0	0.49	0.77
	Fr-1	1.36	2.16
	Fr-2	2.72	4.30

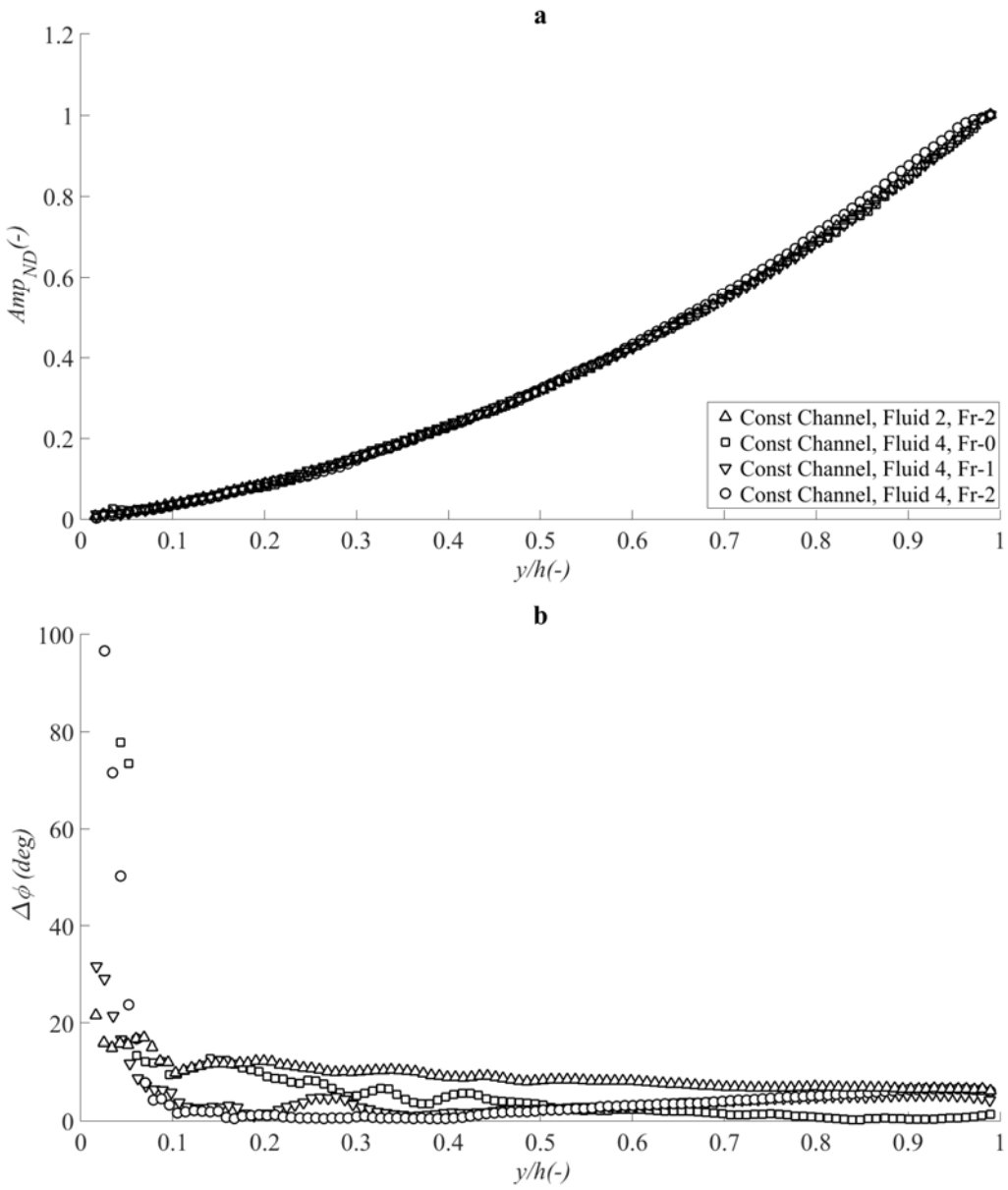

Figure 15 (a) Non-dimensional amplitude (Amp_{ND}) and (b) phase difference ($\Delta\phi$) in constant channel for the HA solution with 3 $mg.ml^{-1}$ concentration at Fr-2 (upward triangle) and for the HA solution with 5 $mg.ml^{-1}$ concentration at Fr-0 (square), Fr-1 (downward triangle), and Fr-2 (circle); the moving wall is located at 1.

Previous studies on particle migration within viscoelastic fluid flows show that elasticity contributes to the migration of particles towards lower shear rate regions and that the migration rate increases with the velocity gradient while shear thinning drives particles in the opposite direction [1,14,35]. This behavior was observed in the present measurements with Fluid 4 at frequency of 2.03 Hz (the most elastic solution with the highest velocity gradient). Therefore, non-dimensional amplitude profiles near the moving wall in this case deviated from the other measurements (Figure 15). The migration of particles resulted in the formation

of a particle-depleted layer in the vicinity of the moving wall. This layer formed gradually and caused gradual decrease in velocity values. As noted in Section 4. Data Analysis, velocity profiles were derived by averaging several velocity maps to obtain reliable velocity fields for each phase. The velocity amplitude based on an average of 60 images is compared to that obtained from 120 images for Fluids 4 and 1 (Figure 16). Fluid 4 variations are explained by gradual particle migration.

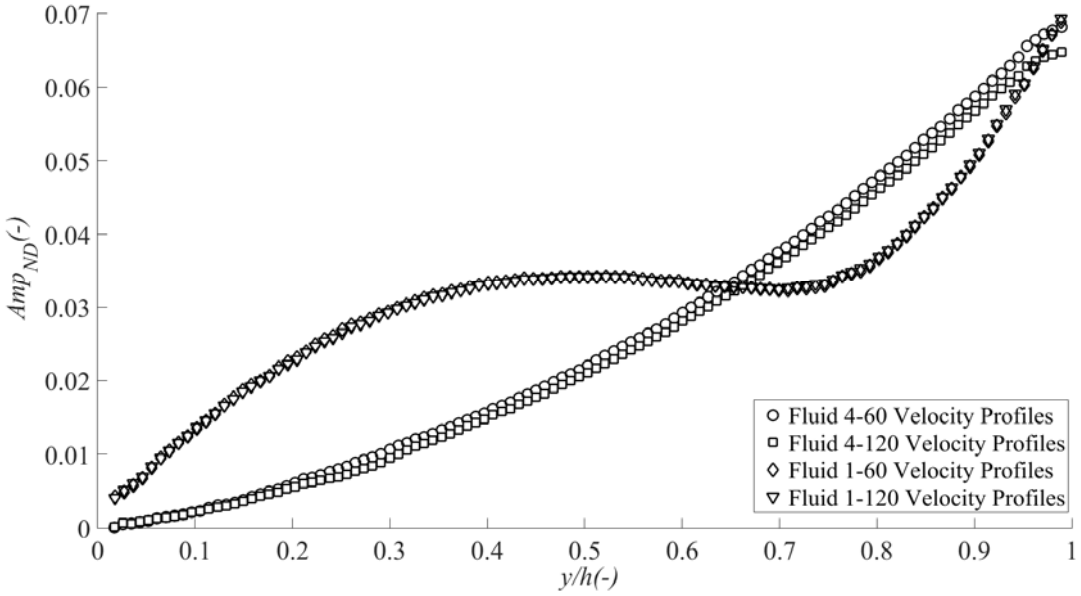

Figure 16 Velocity amplitudes at frequency of 2.03 Hz for the HA solution with 5 $mg.ml^{-1}$ concentration for 60 velocity profiles averaged (circle), for 120 velocity profiles averaged (square, distilled water), for 60 velocity profiles averaged (diamond), and for 120 velocity profiles averaged (triangle); the moving wall is located at 1.

For Fluid 4 flow at frequency of 2.03 Hz, particles aligned near the moving wall and formed strings. These strings were distributed along the width of the channel by flow circulation within the plane of study. Figure 17 (a) shows the random distribution of particles as small white dots and formed strings as white lines, and Figure 17 (b) shows the particle trajectories during the measurement period. Figure 17 (b) was derived by extracting the maximum pixel values for a series of images (image accumulation) and shows that particles followed a specific trajectory. Particle alignment is a known phenomenon found in non-Newtonian shear thinning fluid. Previous studies by Scirocco et al. [11] and Van Loon et al. [7] show that particle alignment is mainly dependent on the shear thinning characteristics of the fluid and that normal stresses create better conditions for particles to approach one another.

Particles in a Newtonian fluid subjected to shearing, rotate to maintain a zero torque balance on their surfaces [1]. To keep the particles in a string directed along a flow direction, each

particle must maintain its rotation and zero torque conditions. In Newtonian fluid, as two particles are draw closer, the fluid leaves the gap between the particles. These two particles in turn attach to one another and tumble, which prevents them from maintaining their rotation. The torque applied to them is non-zero, which results in the separation of the two particles. In shear thinning fluid, as two particles are draw closer to each other, the shear rate inside the small gap increases, resulting in viscosity decline and pressure build up. The squeezing effect due to built-up pressure prevents the two particles from getting too close and maintains a thin layer of fluid between them. This condition helps particles maintain their rotation and zero torque conditions. The formed strings in turn remain stable within the fluid along the flow direction [7].

According to Scirocco et al. [11], once a sufficient degree of shear thinning is achieved, strings form, which may be affected by other parameters thereafter. The critical shear rate value of Fluid 4 was the lowest relative to the other fluids. Within the gap between the two concentric cylinders, the shear rate increased toward the inner cylinder (the moving cylinder). It seems that a frequency of 2.03 Hz provided the sufficient degree of shear thinning for particles to start forming strings in Fluid 4 near the moving wall.

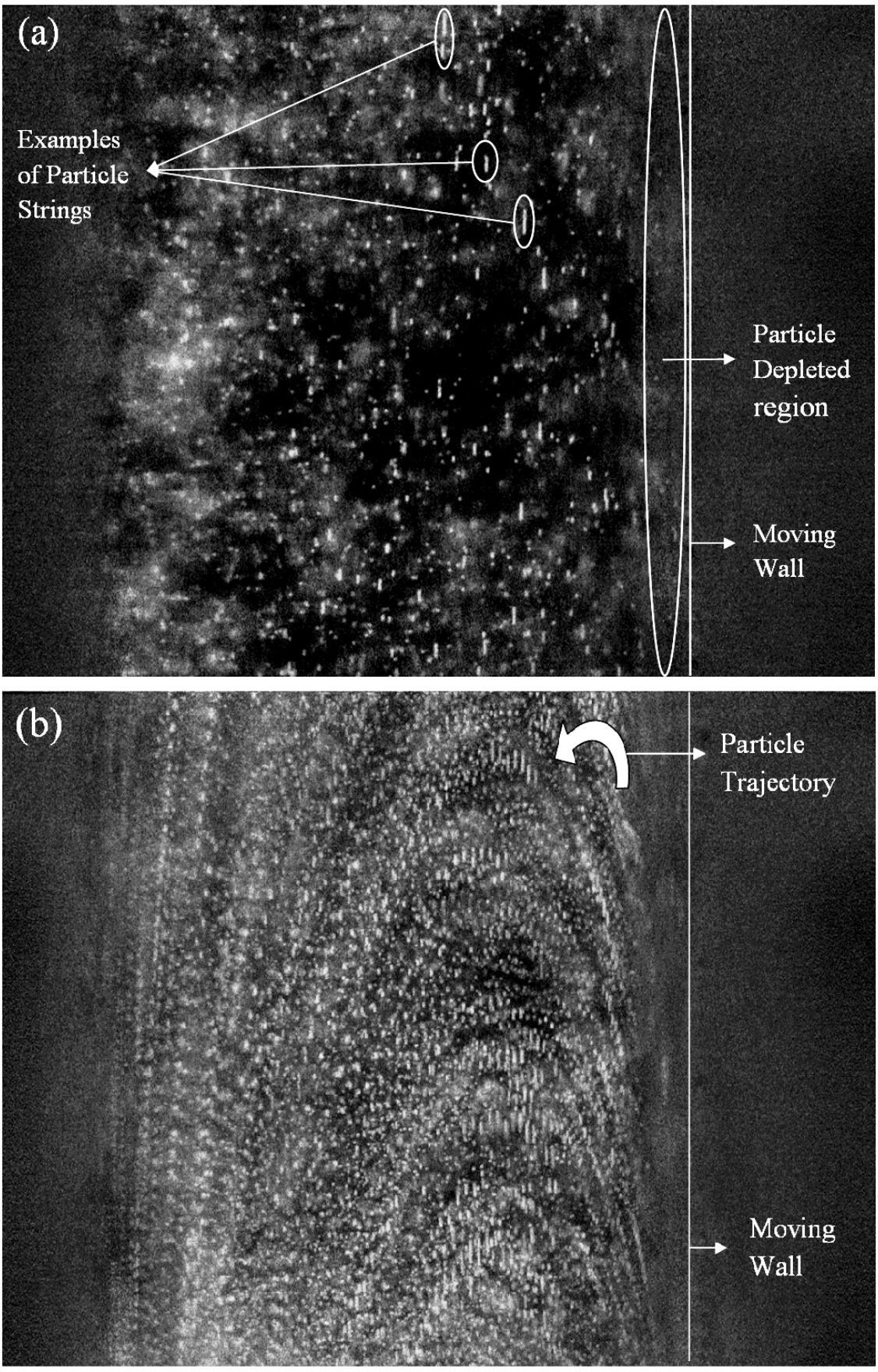

Figure 17- HA solution with 5 $mg.ml^{-1}$ concentration flowing at frequency of 2.03 Hz; (a) particle depleted layer and particle alignment; (b) particle trajectories in the plane of view.

5.3. Channel with variable width

5.3.1. Water Behavior

Variations in channel width at the measurement section of the Conv Channel regarding the phase of movement (ϕ) are shown in Figure 18. The measurement section width decreased from $\phi = 270°$ to $\phi = 90°$ and increased from $\phi = 90°$ to $\phi = 270°$. $\phi = 90°$ and $\phi = 270°$ corresponded to a zero angular velocity when the inner cylinder changed direction. Figure 19 shows the velocity profiles along the width of the measurement section of the Conv Channel at different phases of motion. The measured velocities at phases close to $\phi = 90°$ and $\phi = 270°$ were close to zero and presented very high levels of deviation. Therefore, they are not included in the figure. $\Delta\phi_c$ and $\Delta\phi_d$ represent the phase differences between each phase and that of the smallest and largest measurement section, respectively. Figure 18 shows variations in measurement section width and velocity at the moving wall versus the phase of movement, and $\Delta\phi_c$ and $\Delta\phi_d$ are also shown in this plot.

Figure 19 presents velocity profiles along the width of the measurement section at different phases of movement. A comparison between the positive and negative velocity profiles with similar $\Delta\phi_c$ and $\Delta\phi_d$ values shows that the flow behaved asymmetrically under contraction and expansion modes.

This behavior originated from the pressure gradient (Eq. 2) along the flow direction. During contraction, $\frac{\partial P}{\partial x} > 0$, which produced pressure resistance against the flow and resulted in back flow. However, under the expansion mode, $\frac{\partial P}{\partial x} < 0$, which contributed to the induced flow. However, as noted in a section 5.2.1, the rotation of the inner cylinder in the fluid tank produced excessive flows (e.g., reverse flow) within the channel. This complex final flow behavior could be due to the superposition of different flows.

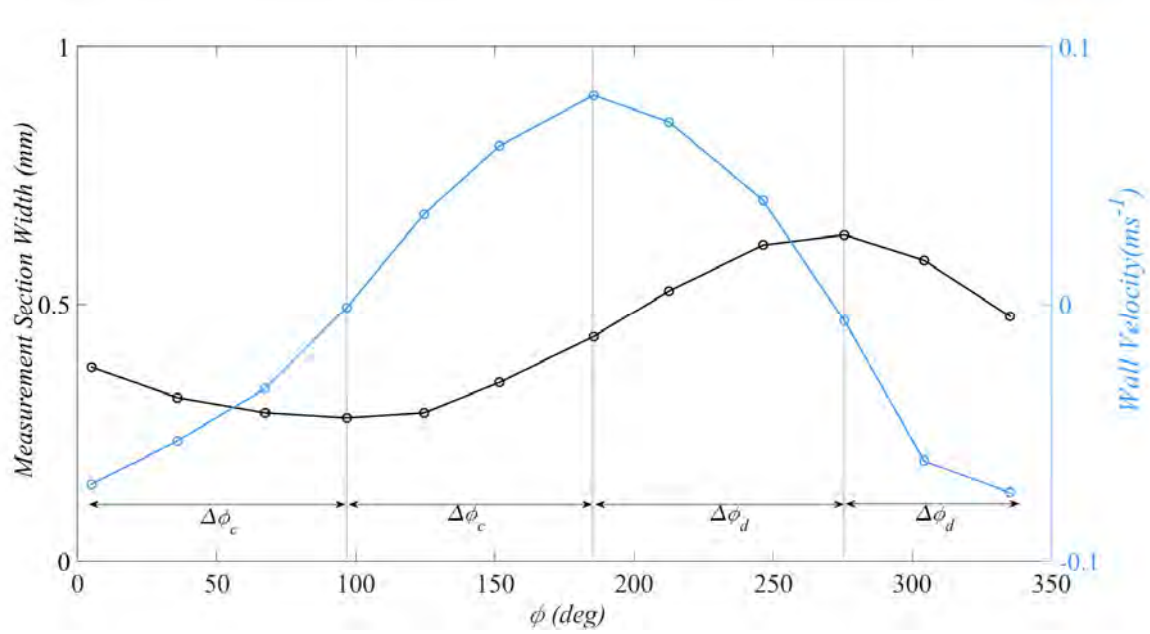

Figure 18- Measurement section width variations in the Conv Channel.

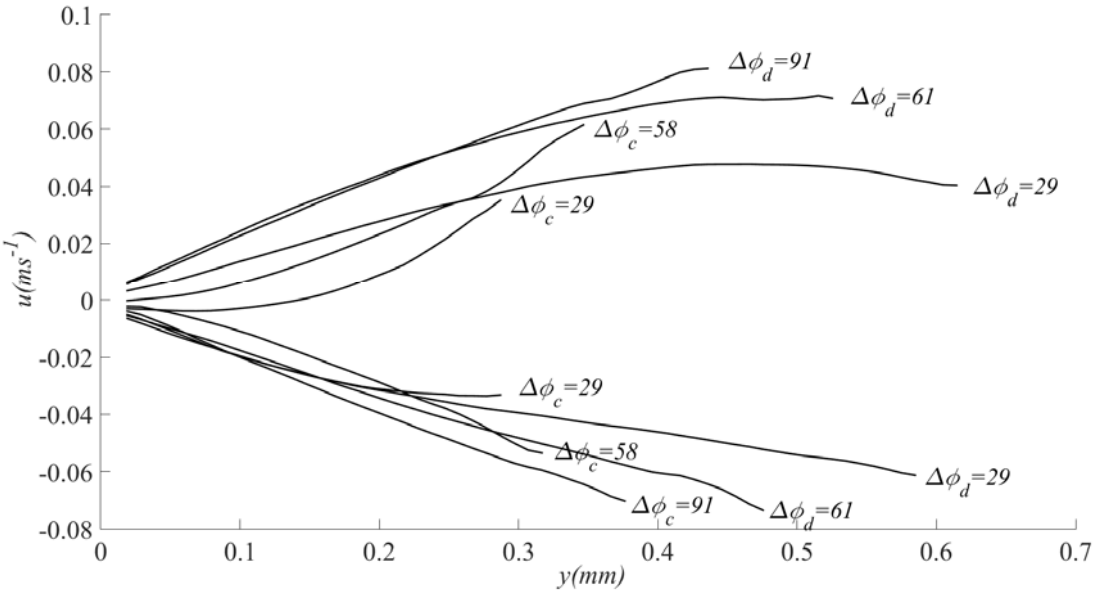

Figure 19 Velocity profiles along the width of the measurement section for distilled water at Fr-2 during contraction (negative velocity profiles) and expansion (positive velocity profiles).

5.3.2. HA behavior

Figure 20 and Figure 21 show the velocity profiles at frequencies of 2.03 and 1.02 Hz, respectively, for water in comparison with HA solutions for measurement section widths exceeding 0.4 mm. At these phases, HA solutions affected the asymmetry of the flow during contraction and expansion. By increasing the HA concentration, the viscosity increased and the effect of the pressure gradient decreased (Eq. 2). Therefore, for the HA solution with

concentration of 5 mg.ml^{-1} and a viscosity of roughly two orders of magnitude of the viscosity of water, the asymmetry between the velocity profiles disappeared as the width of the measurement section increased or decreased.

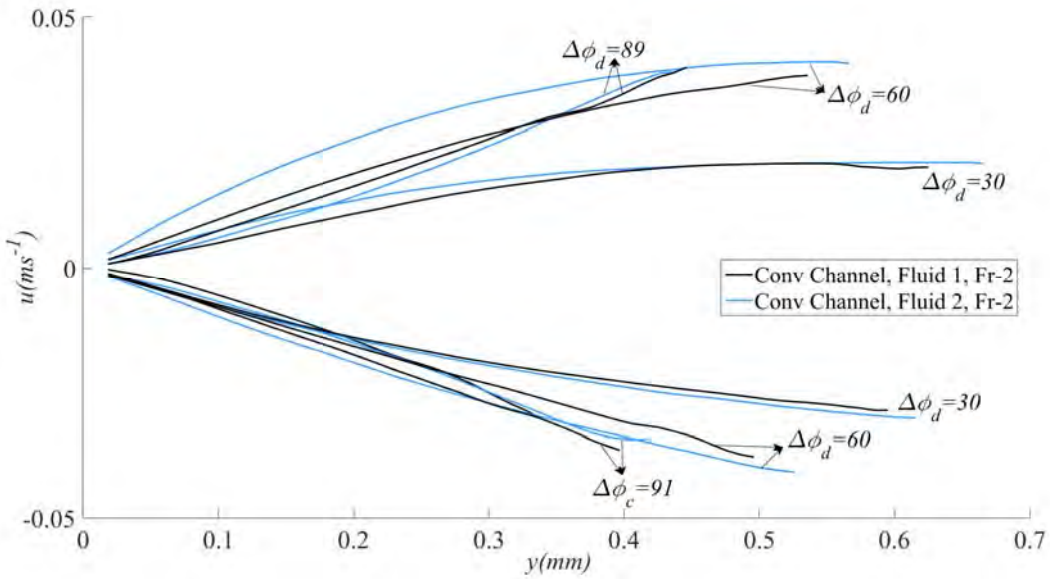

Figure 20 Velocity profiles along the width of the measurement section for distilled water (black) and for the HA solution with 3 mg.ml^{-1} concentration (blue) at Fr-1 under contraction (negative velocity profiles) and expansion (positive velocity profiles) modes.

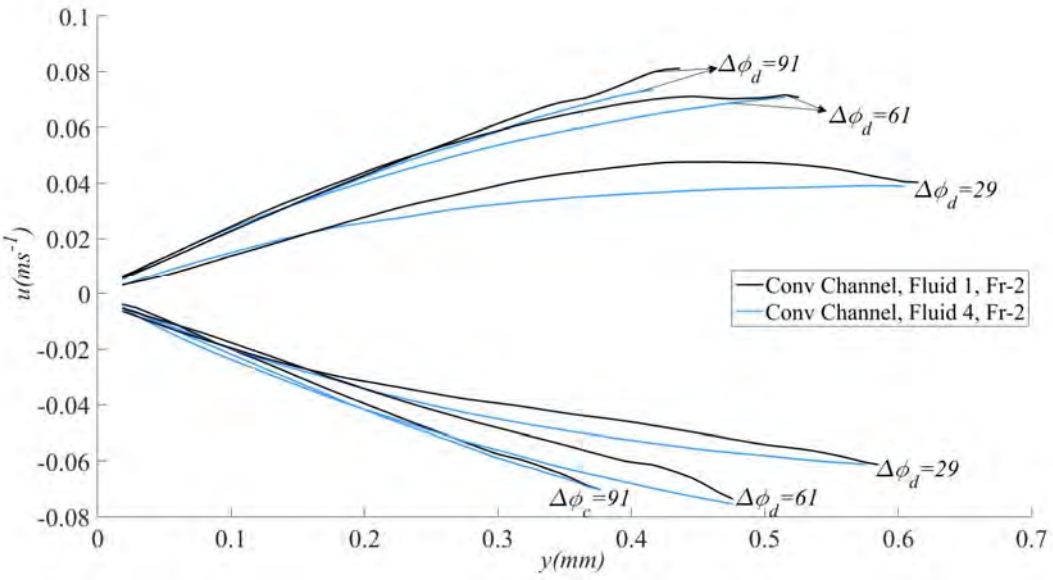

Figure 21 Velocity profiles along the width of the measurement section for distilled water (black) and for the HA solution with 5 mg.ml^{-1} concentration (blue) at Fr-2 under contraction (negative velocity profiles) and expansion (positive velocity profiles) modes.

For measurement section widths of less than 0.4 mm and for Fluid 2 at all frequencies and Fluid 4 at frequencies of 0.37 and 1.02 Hz, particles depleted the region near the moving wall and created large deviations in derived velocity profiles. Figure 22 (a) and (b) show the

particle distribution along the 0.35 mm measurement section for Fluid 2 at start and end of the measurement, respectively. Particles were depleted from the region near the moving wall, which resulted in large deviations in the derived velocity profile of that region (Figure 22 (c)). As noted in a previous section, elasticity caused particle migration to the lower shear rate region. One parameter that affects particle migration is wall confinement [1,14]. Studies performed by D'Avino et al. [14] show that particle cross-streamline migration is heavily affected by curvature in the shear rate and by interactions with confining walls. The results published by Van Loon et al. [7] also show that more confinement (a smaller gap size) enhances both particle migration and string formation. A shear rate distribution around particles forms as a results of different distances from the confinement wall, which in turn results in normal force imbalances and particle migration. When decreasing the channel size, the velocity gradient increases and shear rate variations around particles are enhanced [7]. Therefore, after decreasing the width of the channel in the Conv Channel in comparison with the Const Channel, particles migrated in both HA fluids at all frequencies. At all frequencies, the width of the depletion layer varied from 0.031 to 0.105 mm for different phases of motion. However, Fluid 4 at frequency of 2.03 Hz showed a different particle migration mechanism. At all phases, particles formed strings that traveled to the channel walls. Figure 23 shows the particle distribution in the Conv Channel along the width of the measurement section for Fluid 4 under different conditions. Figure 23 (a) and (b) show the particle distributions at the start and end of the measurement at frequency of 2.03 Hz, respectively, for a measurement section width of 0.7 mm. Random particle distribution was visible at the start of the rotation period. However, after 120 cycles (roughly 1 minute), particle strings formed and migrated towards the inner and outer walls. The same behavior was observed for other phases and at smaller measurement section widths (Figure 23 (c)). At the end of the measurement period, for Fluid 4 at Fr-2 in the Conv Channel, almost all particles participated in string formation, which did not occur for the constant width channel. Decreasing the channel size affected particle string formation in two ways, which in turn resulted in more particle string formation: 1- increased particle collision, 2- increased shear thinning effects. Figure 23 (d) shows that for Fluid 4 at frequency of 1.02 Hz, shorter particle strings formed. By increasing the frequency, the shear rate increased and shear thinning characteristics improved, which in turn directly affected and facilitated particle string formation. Particle alignment was not detected for Fluid 4 at frequency of 0.37 Hz and for Fluid 2 at all frequencies.

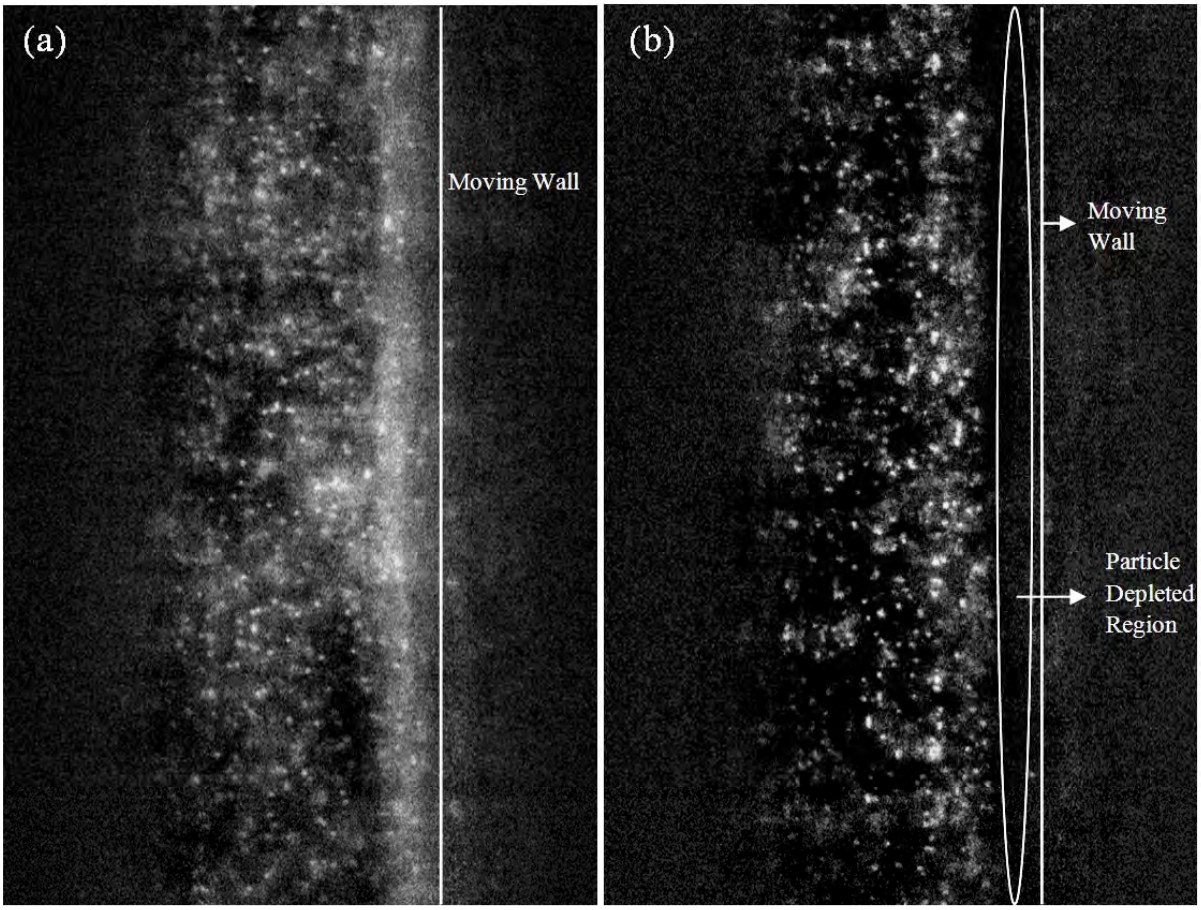

(c)

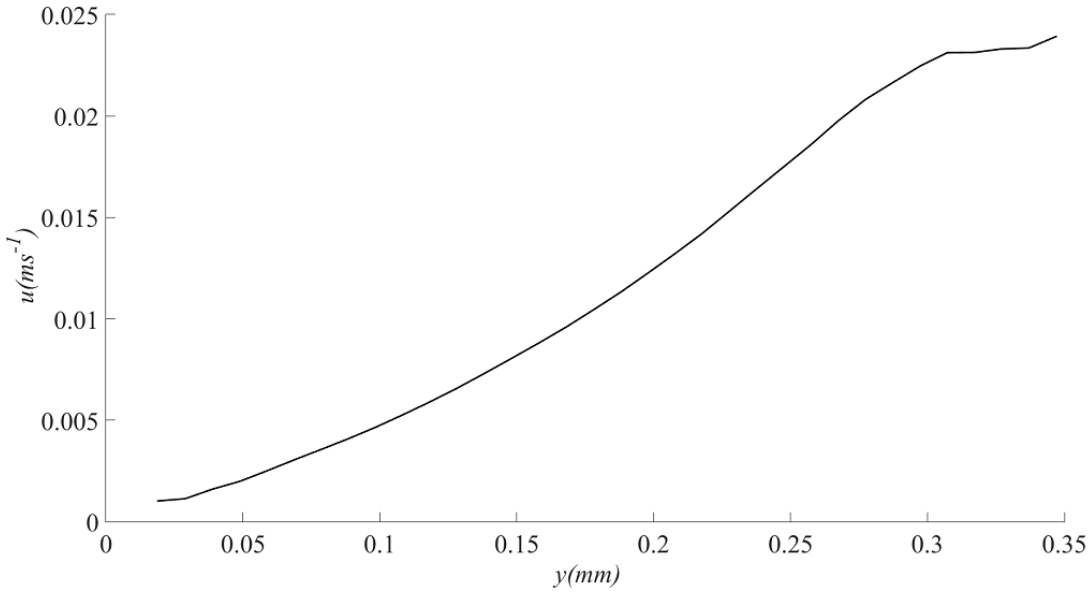

Figure 22 Particle distribution along the Conv Channel for HA solution with 3 $mg.ml^{-1}$ concentration along 0.35-mm-width measurement section at frequency of 1.02 Hz at the (a) start and (b) end of the measurement period; (c) obtained velocity profile for the measurement sections of (a) and (b).

Different behaviors investigated during these measurements are in agreement with previous study results. Lormand and Philips [16] studied particle migration in viscoelastic fluid subjected to flows in concentric cylinders as the inner cylinder moved at a square wave velocity and induced flow. Compared to materials used in the present study, Lormand's fluid was higher in viscosity and had shear thinning characteristics similar to those of Fluid 4. Their results show that for oscillatory flows, particles generally migrate towards the walls and away from the channel center. However, this behavior is strongly dependent on flow characteristics. In Lormand's study once oscillation frequencies exceeded 1 Hz, outward particle migration ceased and particles remained in regions close to the outer cylinder. This behavior in our study was observed for Fluid 2 at all frequencies and for Fluid 4 at frequencies of 0.37 and 1.02 Hz. Particle migration showed similar behavior for Fluid 4 at frequency of 2.03 Hz for all phases. However, for other measurements, migration was only detected across small measurement section widths. This may be attributable to 3-dimensional effects and vorticity within the flow. The results did not show that the formation of a particle-depleted layer near the moving wall resulted in increasing particle density in other channel sections in the plane of view (Figure 23 (d)). This suggests that the migration pattern was 3-dimensional and that understanding the complete mechanism requires 3-dimensional study.

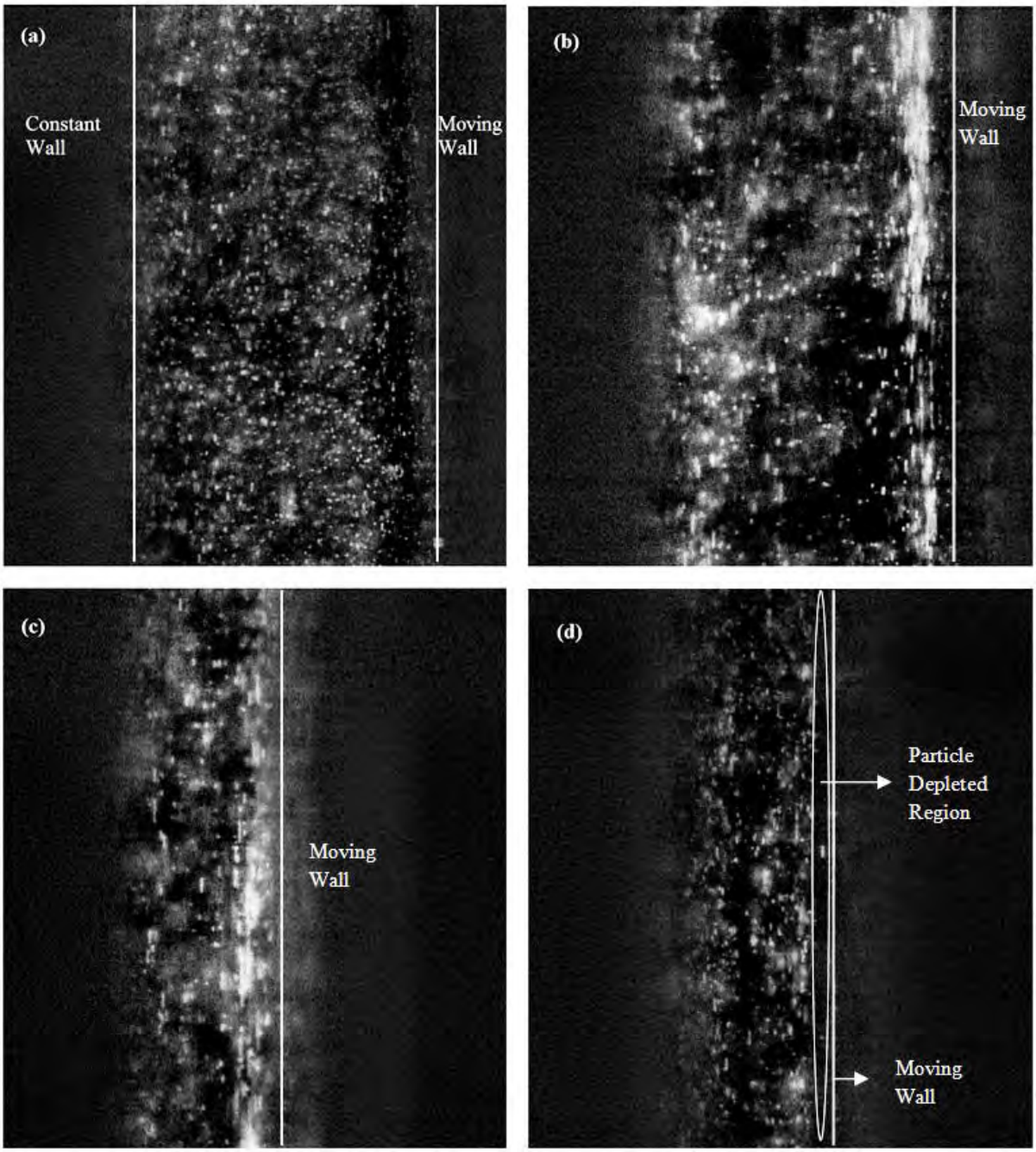

Figure 23 Particle distribution along the Conv Channel for the HA solution with 5 $mg.ml^{-1}$ concentration along the 0.7-mm-wide measurement section at frequency of 2.03 Hz at the (a) start and (b) end of the measurement period; (c) along the 0.36-mm-wide measurement section at frequency of 2.03 at the end of the measurement period and (d) along the 0.32-mm-wide measurement section at frequency of 1.02 at the end of the measurement period.

6. Conclusion

HA solutions and suspending particle behaviors were investigated under unsteady Couette flow conditions within curved channels of constant and variable widths. Micro-PIV was used

as the quantitative flow measurement method. For the unsteady Couette flow measurement inside curve channels, particles did not necessarily follow fluid behavior and showed cross-streaming migration. The selection of fluid and experimental model configurations was designed to simulate flows within THR. The aim was to investigate and understand wear particle distributions within the THR. Our results showed particle alignment/cluster formation and particle migration towards channel walls, which increased by decreasing the distance between walls. Dependent on HA concentrations, particles migrated towards the outer wall alone or to both inner and outer walls. However, the density of particles migrating towards the outer walls was always higher than that of the inner walls. The outer wall in the present study corresponds to the UHMWPE liner surface in THR. The results of the present study suggest that at hip implant frequency of movement (0-0.37 Hz) wear particles are mostly concentrated in regions close to the UHMWPE surface rather than in the metallic/ceramic femoral head. The particle aggregation mechanism near walls can increase third body wear of the implant bearing surfaces, and confinement effects (smaller gap) increase aggregation and wear rates. However, 3-dimensional measurements must be carried out to validate the observed phenomena.

Acknowledgment

The authors' gratitude goes to the Doctoral Program DocMASE for their financial support.

Appendix I

Arbitrary constants β_1 and β_2 are obtained by considering zero velocity at y=0 where the constant wall is placed (Eq. 18 and Eq. 19).

$$u = \frac{-u_0}{\sin(\beta_1 + \beta_2)}\left(e^{-h\sqrt{\omega/2\nu}} \sin\beta_2 .\right.$$
$$\sin\left(\omega t - h\sqrt{\omega/2\nu} + \beta_1 - \frac{\pi}{2}\right) \qquad \text{Eq. 18}$$
$$\left. + e^{h\sqrt{\omega/2\nu}} \sin\beta_1 .\right.$$
$$\sin\left(\omega t + h\sqrt{\omega/2\nu} - \beta_2 - \frac{\pi}{2}\right)$$

$$\Rightarrow u = \frac{-u_0}{\sin(\beta_1+\beta_2)}(e^{-h\sqrt{\omega/2\nu}}$$
$$\sin\beta_2.(\sin(\omega t).\cos(-h\sqrt{\omega/2\nu}+\beta_1-\frac{\pi}{2}))$$
$$+\cos(\omega t).\sin(-h\sqrt{\omega/2\nu}+\beta_1-\frac{\pi}{2}))$$
$$+e^{h\sqrt{\omega/2\nu}}\sin\beta_1.$$
$$(\sin(\omega t).\cos(h\sqrt{\omega/2\nu}-\beta_2-\frac{\pi}{2})$$
$$+\cos(\omega t).\sin(h\sqrt{\omega/2\nu}-\beta_2-\frac{\pi}{2})))=0$$

Eq. 19

Coefficients of $\sin(\omega t)$ and $\cos(\omega t)$ should be zero to obtain zero velocity at each instant, providing us with Eq. 20 to Eq. 22.

$$\begin{cases} 1) \quad e^{-h\sqrt{\omega/2\nu}}\sin\beta_2.\cos(-h\sqrt{\omega/2\nu}+\beta_1-\frac{\pi}{2}) \\ \quad +e^{h\sqrt{\omega/2\nu}}\sin\beta_1.\cos(h\sqrt{\omega/2\nu}-\beta_2-\frac{\pi}{2})=0 \\ 2) \quad e^{-h\sqrt{\omega/2\nu}}\sin\beta_2.\sin(-h\sqrt{\omega/2\nu}+\beta_1-\frac{\pi}{2}) \\ \quad +e^{h\sqrt{\omega/2\nu}}\sin\beta_1.\sin(h\sqrt{\omega/2\nu}-\beta_2-\frac{\pi}{2})=0 \end{cases}$$

$$\Rightarrow \begin{cases} 1) \quad e^{-h\sqrt{\omega/2\nu}}\sin\beta_2.\cos(-h\sqrt{\omega/2\nu}+\beta_1-\frac{\pi}{2}) \\ \quad -e^{h\sqrt{\omega/2\nu}}\sin\beta_1.\cos(h\sqrt{\omega/2\nu}-\beta_2-\frac{\pi}{2}) \\ 2) \quad e^{-h\sqrt{\omega/2\nu}}\sin\beta_2.\sin(-h\sqrt{\omega/2\nu}+\beta_1-\frac{\pi}{2}) \\ \quad -e^{h\sqrt{\omega/2\nu}}\sin\beta_1.\sin(h\sqrt{\omega/2\nu}-\beta_2-\frac{\pi}{2}) \end{cases}$$

Eq. 20

$$\Rightarrow \frac{e^{-h\sqrt{\omega/2\nu}}\sin\beta_2.\cos(-h\sqrt{\omega/2\nu}+\beta_1-\frac{\pi}{2})}{e^{-h\sqrt{\omega/2\nu}}\sin\beta_2.\sin(-h\sqrt{\omega/2\nu}+\beta_1-\frac{\pi}{2})} =$$
$$\frac{-e^{h\sqrt{\omega/2\nu}}\sin\beta_1.\cos(h\sqrt{\omega/2\nu}-\beta_2-\frac{\pi}{2})}{-e^{h\sqrt{\omega/2\nu}}\sin\beta_1.\sin(h\sqrt{\omega/2\nu}-\beta_2-\frac{\pi}{2})}$$

$$\frac{\sin(-h\sqrt{\omega/2\nu}+\beta_1)}{-\cos(-h\sqrt{\omega/2\nu}+\beta_1)}=\frac{\sin(h\sqrt{\omega/2\nu}-\beta_2)}{-\cos(h\sqrt{\omega/2\nu}-\beta_2)} \qquad \text{Eq. 21}$$

$$\tan(-h\sqrt{\omega/2\nu}+\beta_1)=\tan(h\sqrt{\omega/2\nu}-\beta_2)$$
$$\Rightarrow \beta_1+\beta_2=2h\sqrt{\omega/2\nu} \qquad \text{Eq. 22}$$

By replacing β_2 with $2h\sqrt{\omega/2\upsilon}-\beta_1$ in the second part of Eq. 20, β_1 is obtained as Eq. 23.

$$e^{-h\sqrt{\omega/2\nu}}\sin\beta_2.\sin(-h\sqrt{\omega/2\nu}+\beta_1-\frac{\pi}{2})+e^{h\sqrt{\omega/2}}$$
$$\sin\beta_1.\sin(h\sqrt{\omega/2\nu}-\beta_2-\frac{\pi}{2})=0$$
$$\Rightarrow -e^{-h\sqrt{\omega/2\nu}}\sin(2h\sqrt{\omega/2\nu}-\beta_1)$$
$$\cos(-h\sqrt{\omega/2\nu}+\beta_1)$$
$$-e^{h\sqrt{\omega/2\nu}}\sin\beta_1\cos(-h\sqrt{\omega/2\nu}+\beta_1)=0$$
$$\Rightarrow e^{-h\sqrt{\omega/2\nu}}\sin(2h\sqrt{\omega/2\nu}-\beta_1)=-e^{h\sqrt{\omega/2\nu}}\sin\beta$$
$$(\sin(2h\sqrt{\omega/2\nu})\cos\beta_1 \qquad \text{Eq. 23}$$
$$-\cos(2h\sqrt{\omega/2\nu})\sin\beta_1)=$$
$$-e^{2h\sqrt{\omega/2\nu}}\sin\beta_1.$$
$$\sin\beta_1(e^{2h\sqrt{\omega/2\nu}}+\cos(2h\sqrt{\omega/2\nu}))$$
$$=(\sin(2h\sqrt{\omega/2\nu})\cos\beta_1$$
$$\Rightarrow \beta_1=\tan^{-1}\left(\frac{-(\sin(2h\sqrt{\omega/2\nu})}{(e^{2h\sqrt{\omega/2\nu}}-\cos(2h\sqrt{\omega/2\nu})}\right)$$

References

[1] G. D'Avino, P. Maffettone. Particle dynamics in viscoelastic liquids, J.Non Newtonian Fluid Mech. 215 (2015) 80-104.
[2] V. Chiroiu, V. Mosneguţu, L. Munteanu, R. Ioan. On a micromorphic model for the synovial fluid in the human knee, Mech.Res.Commun. 37 (2010) 246-255.
[3] S. Ghosh, D. Choudhury, N.S. Das, B. Pingguan-Murphy. Tribological role of synovial fluid compositions on artificial joints—a systematic review of the last 10 years, Lubr Sci. 26 (2014) 387-410.
[4] L.B. Dahl, I.M. Dahl, A. Engstrom-Laurent, K. Granath. Concentration and molecular weight of sodium hyaluronate in synovial fluid from patients with rheumatoid arthritis and other arthropathies, Ann.Rheum.Dis. 44 (1985) 817-822.
[5] E. Ingham, J. Fisher. Biological reactions to wear debris in total joint replacement, Proceedings of the Institution of Mechanical Engineers, Part H: Journal of Engineering in Medicine. 214 (2000) 21-37.
[6] G. Li, G.H. McKinley, A.M. Ardekani. Dynamics of particle migration in channel flow of viscoelastic fluids, Bulletin of the American Physical Society. 59 (2014).
[7] S. Van Loon, J. Fransaer, C. Clasen, J. Vermant. String formation in sheared suspensions in rheologically complex media: The essential role of shear thinning, Journal of Rheology (1978-present). 58 (2014) 237-254.
[8] J. Michele, R. Pätzold, R. Donis. Alignment and aggregation effects in suspensions of spheres in non-Newtonian media, Rheologica Acta. 16 (1977) 317-321.
[9] M. Lyon, D. Mead, R. Elliott, L. Leal. Structure formation in moderately concentrated viscoelastic suspensions in simple shear flow, Journal of Rheology (1978-present). 45 (2001) 881-890.
[10] D. Won, C. Kim. Alignment and aggregation of spherical particles in viscoelastic fluid under shear flow, J.Non Newtonian Fluid Mech. 117 (2004) 141-146.
[11] R. Scirocco, J. Vermant, J. Mewis. Effect of the viscoelasticity of the suspending fluid on structure formation in suspensions, J.Non Newtonian Fluid Mech. 117 (2004) 183-192.
[12] R. Pasquino, F. Snijkers, N. Grizzuti, J. Vermant. The effect of particle size and migration on the formation of flow-induced structures in viscoelastic suspensions, Rheologica acta. 49 (2010) 993-1001.
[13] R. Pasquino, D. Panariello, N. Grizzuti. Migration and alignment of spherical particles in sheared viscoelastic suspensions. A quantitative determination of the flow-induced self-assembly kinetics, J.Colloid Interface Sci. 394 (2013) 49-54.
[14] G. D'Avino, F. Snijkers, R. Pasquino, M. Hulsen, F. Greco, P. Maffettone, et al. Migration of a sphere suspended in viscoelastic liquids in Couette flow: experiments and simulations, Rheologica acta. 51 (2012) 215-234.
[15] G. d'Avino, P. Maffettone, F. Greco, M. Hulsen. Viscoelasticity-induced migration of a rigid sphere in confined shear flow, J.Non Newtonian Fluid Mech. 165 (2010) 466-474.
[16] B.M. Lormand, R.J. Phillips. Sphere migration in oscillatory Couette flow of a viscoelastic fluid, Journal of Rheology (1978-present). 48 (2004) 551-570.
[17] M. Raffel, C.E. Willert, S.T. Wereley, J. Kompenhans, Particle Image Velocimetry A Practical Guide, 2nd ed., Springer, 2007.
[18] P. Vennemann, R. Lindken, J. Westerweel. In vivo whole-field blood velocity measurement techniques, Exp.Fluids. 42 (2007) 495-511.
[19] R. Lindken, M. Rossi, S. Grobe, J. Westerweel. Micro-Particle Image Velocimetry (micro-PIV): Recent developments, applications, and guidelines, Lab Chip. (2009) 2551.
[20] A. Safari, N. Emami, M.J. Cervantes. Bio-lubricant flow behaviour in mini-channels, Lubr Sci. 28 (2016) 221-242.
[21] A. Safari, M.J. Cervantes, N. Emami. Viscoelastic behaviour effect of hyaluronic acid on reciprocating flow inside mini-channel, Lubr Sci. (2016).
[22] R.C. JOHNSTON, G.L. Smidt. Measurement of hip-joint motion during walking, J.Bone Joint Surg.Am. 51 (1969) 1083-1094.
[23] H. Fam, J.T. Bryant, M. Kontopoulou. Rheological properties of synovial fluids, Biorheology. 44 (2007) 59-74.
[24] L. Ai, K. Vafai. An investigation of Stokes' second problem for non-Newtonian fluids, Numerical Heat Transfer, Part A. 47 (2005) 955-980.
[25] A. Yakhot, M. Arad, G. Ben-Dor. Numerical investigation of a laminar pulsating flow in a rectangular duct, Int.J.Numer.Methods Fluids. 29 (1999) 935-950.
[26] R. Berker. Intégration des équations du mouvement d'un fluide visqueux incompressible, Handbuch der physik. 2 (1963) 1-384.
[27] Z. Zhang, S. Barman, G. Christopher. The role of protein content on the steady and oscillatory shear rheology of model synovial fluids, Soft matter. 10 (2014) 5965-5973.
[28] M. Vazquez, D. Schmalzing, P. Matsudaira, D. Ehrlich, G. McKinley. Shear-induced degradation of linear polyacrylamide solutions during pre-electrophoretic loading, Anal.Chem. 73 (2001) 3035-3044.
[29] A. Bingöl, D. Lohmann, K. Püschel, W. Kulicke. Characterization and comparison of shear and extensional flow of sodium hyaluronate and human synovial fluid, Biorheology. 47 (2010) 205-224.
[30] H. Fam, M. Kontopoulou, J. Bryant. Effect of concentration and molecular weight on the rheology of hyaluronic acid/bovine calf serum solutions, Biorheology. 46 (2009) 31-43.
[31] W.E. Krause, E.G. Bellomo, R.H. Colby. Rheology of sodium hyaluronate under physiological conditions, Biomacromolecules. 2 (2001) 65-69.
[32] R.K. Gupta, Polymer and composite rheology, CRC Press 2000.
[33] J.M. Dealy, J. Wang, Viscosity and Normal Stress Differences, Melt Rheology and its Applications in the Plastics Industry, Springer, 2013, pp. 19-47.

[34] N. Phan-Thien, Understanding viscoelasticity: basics of rheology, Springer Science & Business Media 2013.
[35] M. Jefri, A. Zahed. Elastic and Viscous Effects on Particle Migration in Plane-Poiseuille Flow, Journal of Rheology (1978-present). 33 (1989) 691-708.

Paper D

Effect of Dynamic Loading versus Static Loading on The Frictional Behavior of a UHMEPW Pin in Artificial Biolubricants

Effect of dynamic loading versus static loading on the frictional behavior of a UHMWEP pin in artificial biolubricants

Alaleh Safari[1], Montserrat Espanol[2], Maria Pau Ginebra[2], Michel J. Cervantes[3,4], Nazanin Emami[1]

[1]Biotribology group, Division of Machine Element, Luleå University of Technology, 97187, Luleå, Sweden.
[2] Biomaterials, Biomechanics and Tissue Engineering Group, Dept. of Materials Science and Metallurgy, Technical University of Catalonia, Barcelona, Spain
[3]Division of Fluid and Experimental Mechanics, Luleå University of Technology, 97187, Luleå, Sweden.
[4] Water Power Laboratory, Norwegian University of Science and Technology, Norway.

Submitted to Biosurface and Biotribology Journal

Abstract

To obtain reliable results from in vitro measurements on the tribological behavior of joint implant materials, the parameters of the measurements must simulate in vivo conditions. Although the nature of the load in human joints is dynamic, most of the studies using simple pin-on-disk tribometers were performed with a constant load. The current study focused on investigating the effect of dynamic loading in comparison with static loading in the tribological behavior of ultra-high-molecular-weight polyethylene (UHMWPE) sliding against a cobalt chromium molybdenum (CoCrMo) counter surface with different lubricants, where the effects of hyaluronic acid (HA) and protein content in the lubricants were also investigated. The results suggested that although the dynamic loading did not affect the friction evolution for any of the lubricants, the friction value decreased for the lubricants that did not contain HA. The results showed that higher protein content in the lubricant increased the friction coefficient, however, it provided the highest protection against wear for sliding surfaces.

Keywords

Pin on disk, bio-lubricant, Hyaluronic acid, friction coefficient, bio-tribology

1. Introduction

Long survival rate (low wear) and low coefficient of friction are two of the most important characteristics of a total joint replacement (TJR), which is used in improving mobility and reducing the pain of patients with joint disease or injuries. A low coefficient of friction (COF) in metal on ultra-high-molecular-weight polyethylene (UHMWPE) prostheses and a survival rate of 75% in 20 years make metal on polyethylene (MoP) joint implants the most commonly used type in TJR [1,2]. However, because the oxidation degradation characteristic of UHMWPE decreases the wear resistivity of this material, eventually, excessive production of wear particles will cause implant failure due to aseptic loosening [3,4]. Theoretical studies have shown that the MoP joint operates mainly in boundary or mixed lubrication regime, which intensifies the wear rate due to asperity contacts [5-7]. Moreover, a large number of cyclic loadings leads to material fatigue, and high friction can contribute to joint loosening as a result of the fatigue [8]. To understand the frictional and wear characteristics of a MoP joint, many studies have used different experimental approaches: free and driven pendulum, pin-on -disk, pin-on-plate, and hip or knee simulator under different loads, speed and lubricant conditions [1,4,8-19]. One of the most important factors for obtaining reliable results from the tribological measurements is the composition of the periprosthetic synovial fluid (SF). Although the composition of periprosthetic SF is not fully understood because of ethical issues and the difficulty of accessing SF, recent studies suggested that its composition is similar to the osteoarthritic SF [14,20]. However, the protein content of the periprosthetic SF is higher compare to that of normal SF. The hyaluronic acid (HA) concentration and molecular weight in periprosthetic SF are lower than healthy SF and about 2-3 $mg.ml^{-1}$ and 1.1-1.8 MDa, respectively [21]. Early studies showed that when blood serum was used as the lubricant in tribological measurements, the wear surfaces that were produced resembled implant wear surfaces [22]. Therefore, the ASTM F732 protocol proposed bovine calf serum (BCS) as the best lubricant for bio-tribological measurements [23]. To fully understand the lubrication mechanism of implants, many studies focused on understanding the main component of SF that acts as the lubricant. Sawae et al. [4] investigated the effect of different lubricants on the frictional and wear behavior of a UHMWPE pin with unidirectional sliding against a steel or alumina disk. Their results suggested that the albumin solution behavior as a lubricant was different from that of serum. Although both of them prohibited the transfer of the polymeric surface to the counter surface, the wear mechanism and the frictional behavior were different. Albumin showed a much higher friction compared to serum. This study also

showed that adding HA to the lubricant decreased the COF significantly. Schole et al. [13,24] studied the effect of the non-Newtonian and physiological characteristics of the lubricant on the frictional behavior of different hip joint configurations using a hip simulator. They showed that for ceramic and metal implants, the differences in the COFs between synthetic and physiological lubricants were significant. This difference was negligible for the MoP configuration, with the protein containing lubricant exhibiting a slightly higher COF compared to that of the synthetic lubricant. These studies also suggested that the protein present in SF or calf serum adsorbed onto the implant surfaces, creating a solid-like film that protected the surfaces form wear but could either increase or decrease the friction. The effects of serum concentration on the frictional behavior of different UHMWPE pins sliding against CoCrMo disks were studied by Yao et al. [25]. The results showed that although BCS with different concentrations and bovine SF increased the COF compared to deionized water, human SF provided a lower COF. It was also shown that crosslinking or gamma irradiating the polymer did not affect its sliding COF. The studies of Gispert et al. [14] on the friction and wear behavior of pins from different metals and alumina sliding on a UHMWPE disk with a unidirectional movement and different lubricants showed the importance of adding proteins to the lubricant. The results of this study showed that adding proteins to the lubricant prohibited the transfer of the polymeric layer to the metallic counter surface and improved the lubrication condition. They also concluded that because HA did not affect the surface tension significantly, in contrast to bovine serum albumin (BSA), it did not have a considerable effect on the COF. Chen et al. [15] showed that although albumin adsorbed strongly onto the implant bearing surfaces, thereby improving the boundary lubrication, for the lubricant with 50% BSA, the COF increased significantly compared to water. The results of the studies by Flannery et al. [16] on MoP using a knee simulator also suggested that under the mixed lubrication regime, the adsorption of proteins on the bearing surfaces increased the COF. Fam [18] investigated the frictional behavior of UHMWPE sliding against CoCrMo lubricated with water and serum and determined how the HA concentration affected this behavior in reciprocating pin-on-disk measurements. The main conclusion of this study was that increasing the HA concentration up to 1 $mg.ml^{-1}$ decreased the friction, and for higher concentration HA solutions, the COF remained constant.

The high variability of these results suggested the importance of controlling the measurement parameters, such as lubricant composition, type of motion, load, speed, and roughness. Previous studies showed that the wear rate of UHMWPE is very sensitive to the motion type [26,27] and that the friction can be significantly affected by applying a dynamic load

compared to a steady state load [12,28]. Dynamic loading (either applied as a sudden load variation or a semi-sinusoidal loading profile) is used in pendulum or hip and knee simulators. However, these two methods are a rather complex means of studying the biotribological behavior of implant materials. Using a pin-on-disk with multidirectional motion is the most common and simple method of investigating the tribological behavior of joint implant materials. Almost all measurements using this method have been conducted under steady state loading. However, because joint bearing materials are subjected to cyclic loading, it is crucial to understand how dynamic loading might affect the results in comparison with static loading when tribological behaviors are studied using the pin-on-disk method. Therefore, the main aim of the current study was to understand how dynamic loading might change the frictional behavior of materials in comparison with static loading in the pin-on-disk measurement. Understanding the effect of the loading condition provides an insight into the fact that how valid are the frictional measurements with pin-on-disk and constant load and which parameters affect this validity.

2. Materials and Method

2.1. Materials

GUR 1020 UHMWPE (Ticona/Celanese, USA) blocks were prepared in our laboratory using the compression molding method, and 4×4×4 mm^3 pins were cut out from a pressed UHMWPE block. Each pin was soaked in distilled water for a minimum of two weeks before tribotesting. The average roughness of the pin surface was approximately R_a = 1.5-2 μm.

Chromium Cobalt Molybdenum alloy (CrCoMo) with a mirror polished surface (with average roughness of R_a = 0.005 μm) was used as the counter surface. All samples were cleaned based on the procedure in the ASTM F732 - 00(2011) standard. Table. 1 contains a detailed explanation of the lubricants and the names assigned to each of them.

Distilled water was the reference lubricant used to compare the influence of HA and/or protein in the lubricant. Diluted BCS was chosen as one of the lubricants based on the ASTM F732 standard recommendation and to investigate the protein effect.

The HA content of the SF provides it with shear thinning viscoelasticity behavior. In present study and for the lubricants which contained HA, The concentration and molecular weight of

HA were chosen to capture the HA characteristics in periprosthetic SF (similar shear thinning and viscoelastic behavior).

Table. 1 Lubricants' composition

Lubricant Composition	Lubricant name
Distilled water	**DW**
Diluted BCS: 75% Phosphate Buffer Saline (PBS from Sigma Aldrich, St. Louis, Missouri, USA, with 0.15 M concentration) and 25% BCS (Sigma Aldrich 12133C, St. Louis, Missouri, USA)	**DS**
HA with 1.6-1.8 MDa molecular weight (Sigma Aldrich 53747, St. Louis, Missouri, USA) with concentration of 3 $mg.ml^{-1}$ in PBS	**HA**
HA with 3 $mg.ml^{-1}$ concentration in a mixture of 75% PBS and 25% BCS	**HAS**

2.2. Experimental Methodologies

2.2.1. Tribological characterization (pin-on-disk)

The frictional measurements were performed using a unidirectional Plint TE-67 pin-on-disk tribometer (Phoenix Tribology Ltd, Kingsclere, England). For the steady state condition, a 120-N load was applied on the pin, corresponding to 7.5 MPa of pressure. The dynamic load was applied through a pneumatic system in a sinusoidal pattern at a frequency of 1 Hz, average load of 120 N and amplitude of 40 N. The applied loads were chosen to maintain the pressure in the range of 2 to 10 MPa, based on the ASTM F732 - 00(2011) standard. The frequency of the load was chosen based on the load variation frequency during the normal walking activity [29]. Hereafter, the measurements with steady and dynamic loadings are referred to as Const and Sin, respectively. The sliding velocity was kept constant at 34 $mm.s^{-1}$ to reduce the hydrodynamic effects. This velocity lies in the typical velocity range for hip implants (0-50 $mm.s^{-1}$) [14]. Each measurement was performed for 50,000 cycles at room temperature (25-27°C). Distilled water was added gradually at a constant rate to the lubricant via a syringe pump (kd Scientific model 410 series) to ensure that the concentration of the lubricants remained constant. Each set of measurements was performed at least three times.

The pin viscoelastic thickness deformation was measured by a displacement sensor coupled to the pin holder. Fig. 1 provides a schematic view of the experimental set-up.

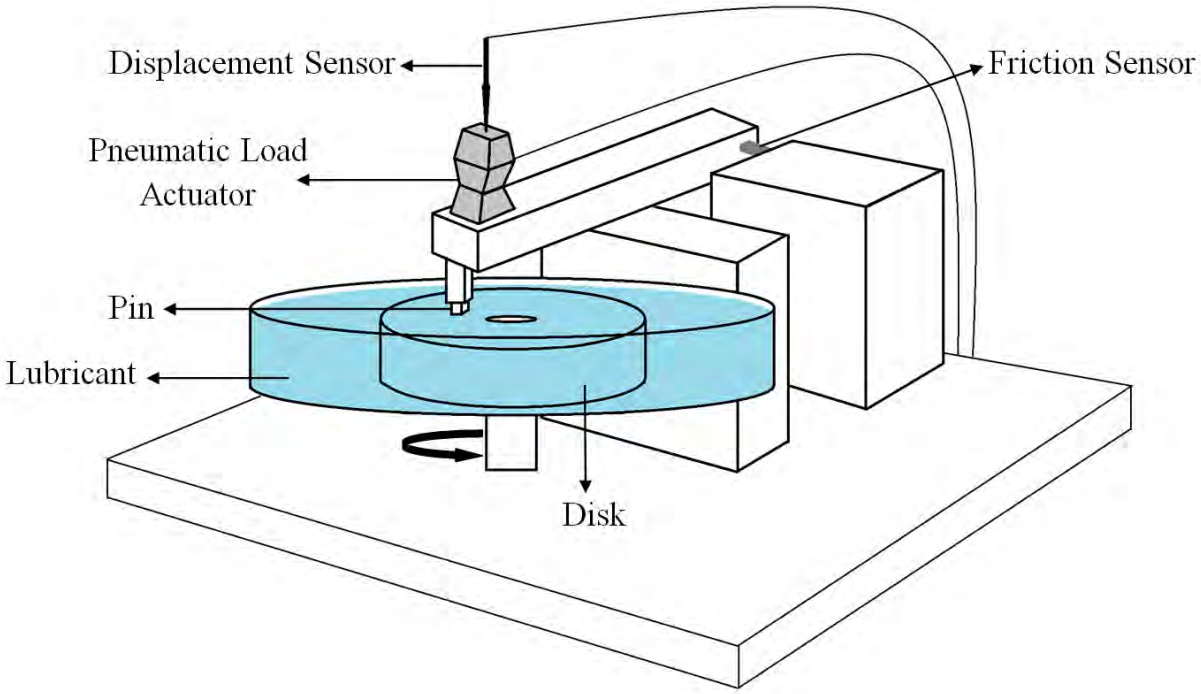

Fig. 1 Schematic of the experimental set-up

Fig. 2 shows the response and decay time of the friction sensor. The response and decay times were approximately 0.7 s and 1.2 s, respectively. These response times are considerably high compared to the load cycle period (1 s). Therefore, the sensor could not capture the total range of friction under dynamic loading conditions. The longer decay time compared to the response time suggested that the mean recorded friction forces had higher values compared to the real situation. Effectively, higher mean values for the recorded Sin friction force were obtained compared to the Const friction force. To correct the recorded friction mean value, sinusoidal loads at a frequency of 1 Hz with defined mean and amplitude values were applied on the friction sensor. By comparing the applied mean value with the recorded one, Eq. (1) was derived for correcting the friction mean value to determine the modified one.

$$F_{\mathrm{mod}} = F_{record} - 0.13*(F_{record\,\max} - F_{record\,\min})$$
$$F_{\mathrm{mod}(mean)} = Average(F_{\mathrm{mod}}) \qquad (1)$$

F represents the friction force. The above equation only corrects the recorded mean value. The mean COF (mean value for sinusoidal COF) was derived by dividing the modified mean friction by the mean applied load (120 N).

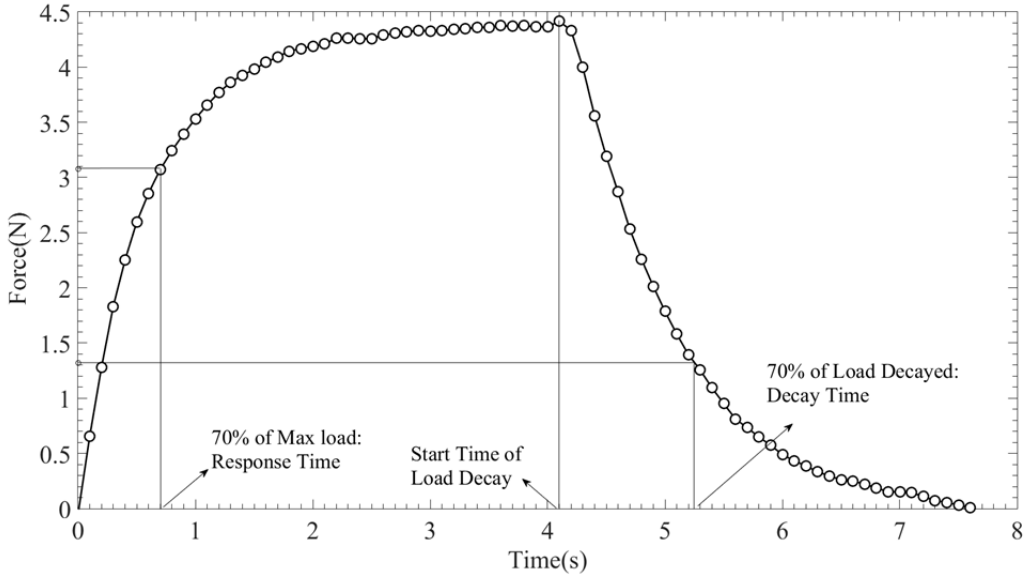

Fig. 2 Step response and decay time of the friction load sensor

2.2.2. Rheological Measurement

The variation of the HA solution's viscosity vs shear rate was investigated using a Bohlin CVO Rheometer at 25ºC under shear rate control (0.05-1570 s^{-1}) with coaxial cylinders (C25).

2.2.3. SEM and EDS

Scanning electron microcopy (SEM) images of the pins and the disks before and after the measurements were captured using a JEOL JSM-7001F microscope.The pin surfaces were coated with platinum/palladium (80/20). No special treatment was used on the disk surfaces. The pin surfaces were also analyzed using energy-dispersive X-ray spectroscopy (EDS) to investigate the chemical elemental composition on the surfaces of the pins.

2.2.4. Topographical Analysis

The topography of the surfaces of the pins and disks was captured and analyzed using optical interferometry (Zygo NewView 7300) before and after the tribotest.

2.2.5. Crystallinity

Differential scanning calorimetry (DSC) was used to investigate whether tribotesting affected the degree of crystallinity of the UHMWPE pins (tested in different lubricants). The degree of

crystallinity was also measured on aged UHMWPE pins (aged in distilled water at 37°C temperature for 2 months).

3. Results

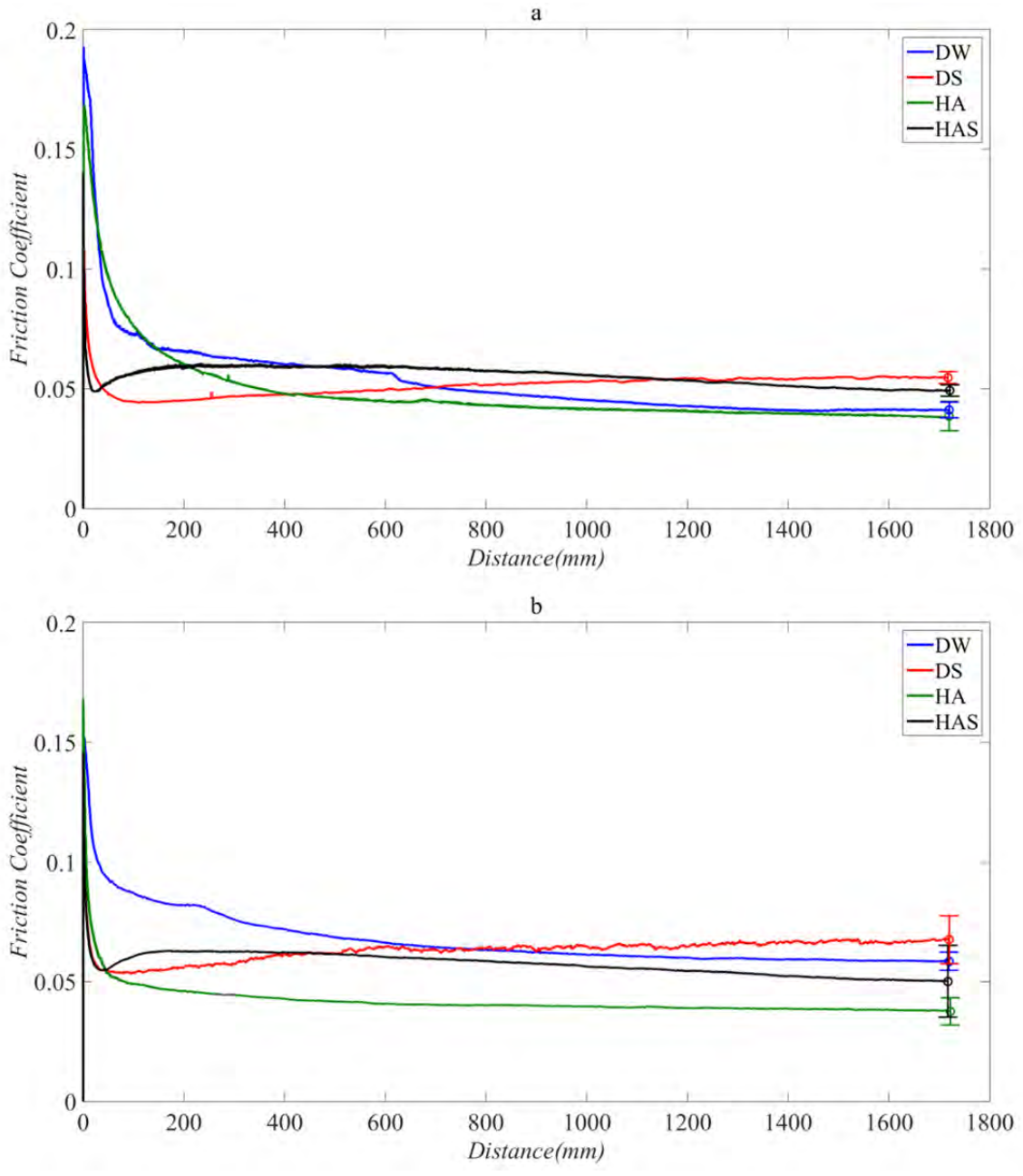

Fig. 3 Friction coefficient vs. sliding distance for four different lubricants under a) sinusoidal pattern load and b) constant load with error bars for 90% confidence interval

Fig. 3 shows the evaluation of the friction coefficient with increasing sliding distance. To compare the results between constant load and sinusoidal load conditions, the mean value of the sinusoidal COF is presented in Fig. 3(a). For each lubricant, the variation of the COF followed nearly the same trend under both dynamic sinusoidal and steady state constant loads. The error bars present 90% confidence interval for the last hour of measurement. Because of the rather high pressure, the polymer pin underwent elastic deformation during the running-in period, resulting in decreases in the surface roughness and the COF. Fig. 4 represents the pin thickness variation during the running-in period caused by elastic effects. The error bars present 90% confidence interval for the last hour of measurement.

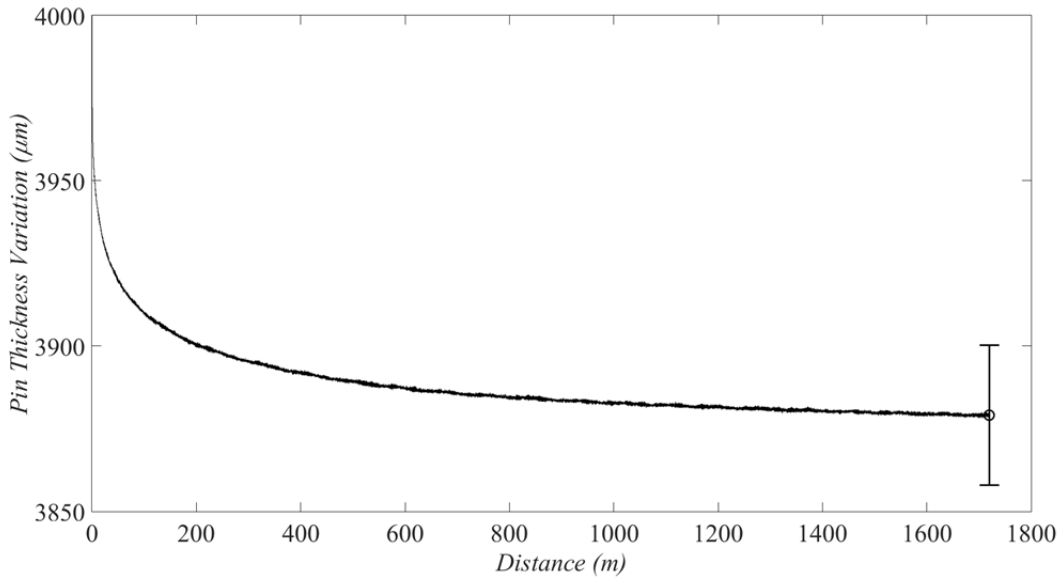

Fig. 4 Pin elastic deformation during a pin-on-disk measurement for the distilled water lubricant under steady state loading with error bars for 90% confidence interval

After the viscoelastic deformation phase, the COF trend was varied for different lubricants. The viscosities of these lubricants were different. This difference was one of the reasons for obtaining the different trends and values for the COF. The diluted BCS viscosity is 0.002-0.0025 Pas (two to three times the value for distilled water). Increment of COF in with BCS as lubricant compared to distilled water could be due to protein adsorption on the contact surfaces (Fig. 6); for diluted BCS, a white circle of the adsorbed protein was visible at the end of the test, thus verifying protein adsorption. Fig. 5 shows the average viscosity variation as a function of shear rate and the error bars for 90% confidence interval for HA solutions. To estimate the viscosity at higher shear rate it is possible to fit a mathematical model and extrapolate. Power law model is the simplest model which is usually fitted on the shear

thinning region of the double logarithmic plot of the viscosity vs. shear rate for HA solution (Eq. (2)) [30].

$$\mu = m\dot{\gamma}^{n-1} \qquad (2)$$

μ, $\dot{\gamma}$, m and n are viscosity, shear rate, consistency and power indices, respectively. n-1 is the slope of the line fitted on the shear-thinning region of the double logarithmic plot of the viscosity vs. shear rate and "m" is the intercept of the fitted line with shear rate of 1 s^{-1}. "n" and "m" had the value of 0.618 and 0.26, respectively. By considering the average roughness of the surfaces and the sliding velocity of the pin, the average shear rate exerted on the HA solution was about 23,000 s^{-1}. The viscosity of the HA solution at this shear rate was 0.0056 (more than 6 times of the distilled water viscosity at 25°C).

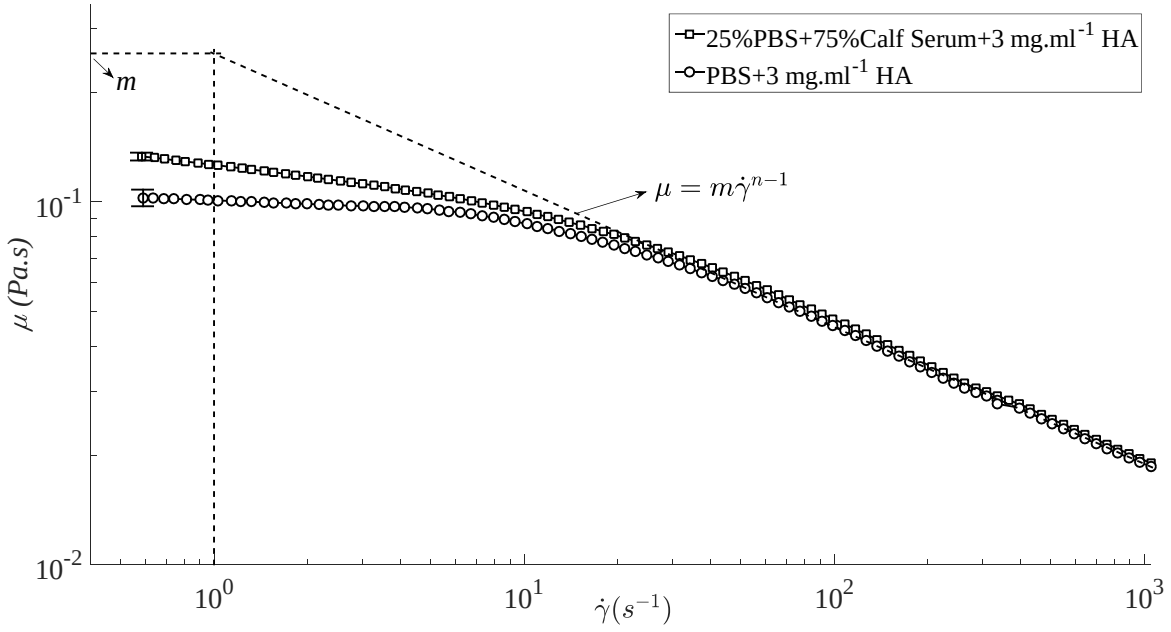

Fig. 5 Viscosity (μ) as a function of the shear rate ($\dot{\gamma}$) for the HA solutions with error bars for 90% confidence interval

The value of the COF after the running-in period placed between 0.2 and 0.75. Under constant load condition and by increasing the viscosity in HA solution, compared to distilled water, the COF decreased. These suggested that the active lubrication mechanism was mixed lubrication [14,16,31].

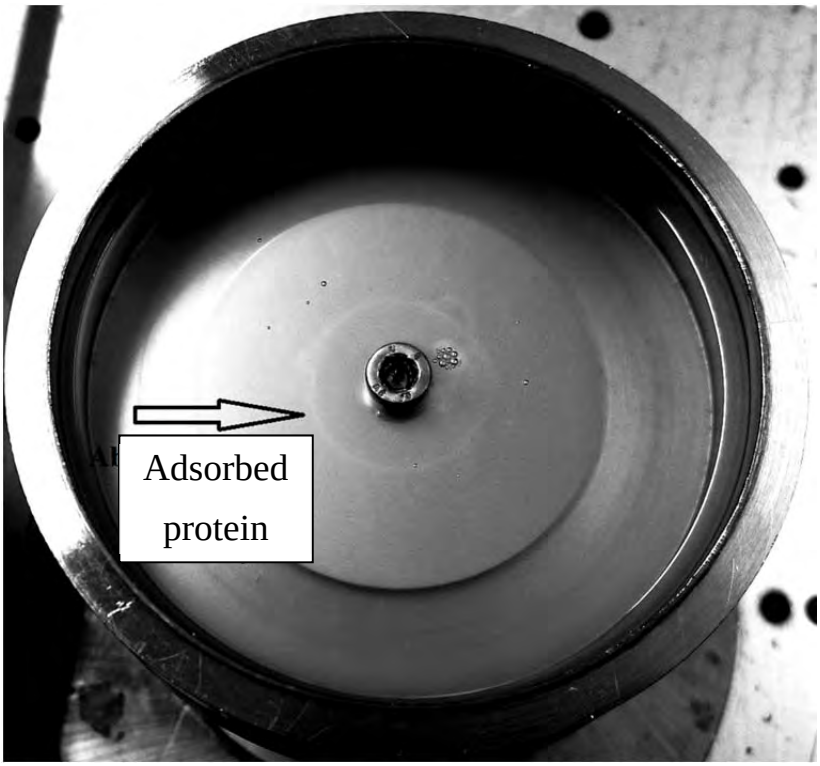

Fig. 6 The lubricant bath condition after measurement with diluted BCS

The average COF for the last hour of measurements and the error bars (standard deviation for 3 measurements) for 90% confidence interval are presented in Fig. 7. The difference between steady state and dynamic COFs was significant for non-HA-containing lubricants. Statistical analysis (one-way ANOVA) performed on the COF values for steady state and dynamic loadings and in the case of non-HA solution lubricants led to a value of $p<0.03$. However, for the HA-containing lubricants, the difference between COFs of static and dynamic loadings was not statistically significant.

For diluted BCS lubricant containing HA, the COF had a higher value compared to HA solution in PBS and a lower value compared to dilute BCS. Examination of the COF evolution for HAS over time (Fig. 3) showed that at the beginning of the measurement, the frictional behavior was similar to dilute BCS (rapid decreasing of COF at the start of measurement and gradual increasing of COF afterward). However, at the middle of the measurement the COF value started to decrease gradually and the frictional behavior moved towards the frictional behavior with HA in PBS.

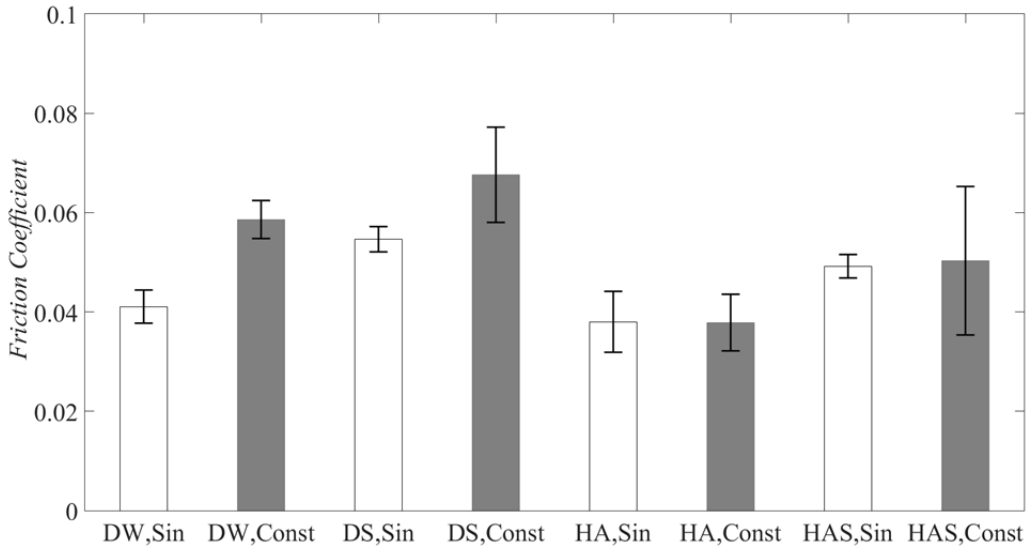

Fig. 7 Average friction coefficients after a sliding distance of 1700 meters for all test conditions

Table. 2 shows the crystallinity values for pin surfaces (before and after tribo-testing) with different lubricants. With distilled water as the lubricant, compared to the other lubricants, a trend of a decrease in the crystallinity value was observed. However, the amount of decrease is not significant. Therefore, different lubricants or testing conditions had no significant effect on the degree of crystallinity.

Table. 2 Crystallinity values of the pin samples before and after measurement at different conditions

Sample	**Crystallinity**
Control pin	48.55 ± 2.32
DW, Sin	46.43 ± 4.51
DW, Const	47.49 ± 0.98
DS, Sin	46.43 ± 0.89
DS, Const	50.24 ± 0.12
HA, Sin	51.44 ± 0.60
HA, Const	51.07 ± 0.30
HAS, Sin	49.33 ± 1.30
HAS Const	50.70 ± 0.65

Fig. 8 shows the SEM images from the CoCrMo disks before measurement (Fig. 8(a)) and after measurements at constant load with diluted BCS, HA solution in PBS, and HA solution in diluted BCS as lubricants (Fig. 8 (b), Fig. 8 (c), and Fig. 8 (d), respectively). The black spots on the disk surfaces correspond most probably to the Mo-rich undissolved particles [14]. No wear sign or tracks were visible in Fig. 8 (b) and (d). In Fig. 8 (c), the pin tracks might be related to the early stages of wear.

Fig. 9 shows the SEM images of the wear tracks on the CoCrMo disks with distilled water as the lubricant at two different magnifications. Fig. 9 (a) corresponds to the constant load condition, and Fig. 9 (c) represents the disk surface after the dynamic load measurement. The shape of the tracks suggested that abrasive wear was the dominant wear mechanism for both loading conditions.

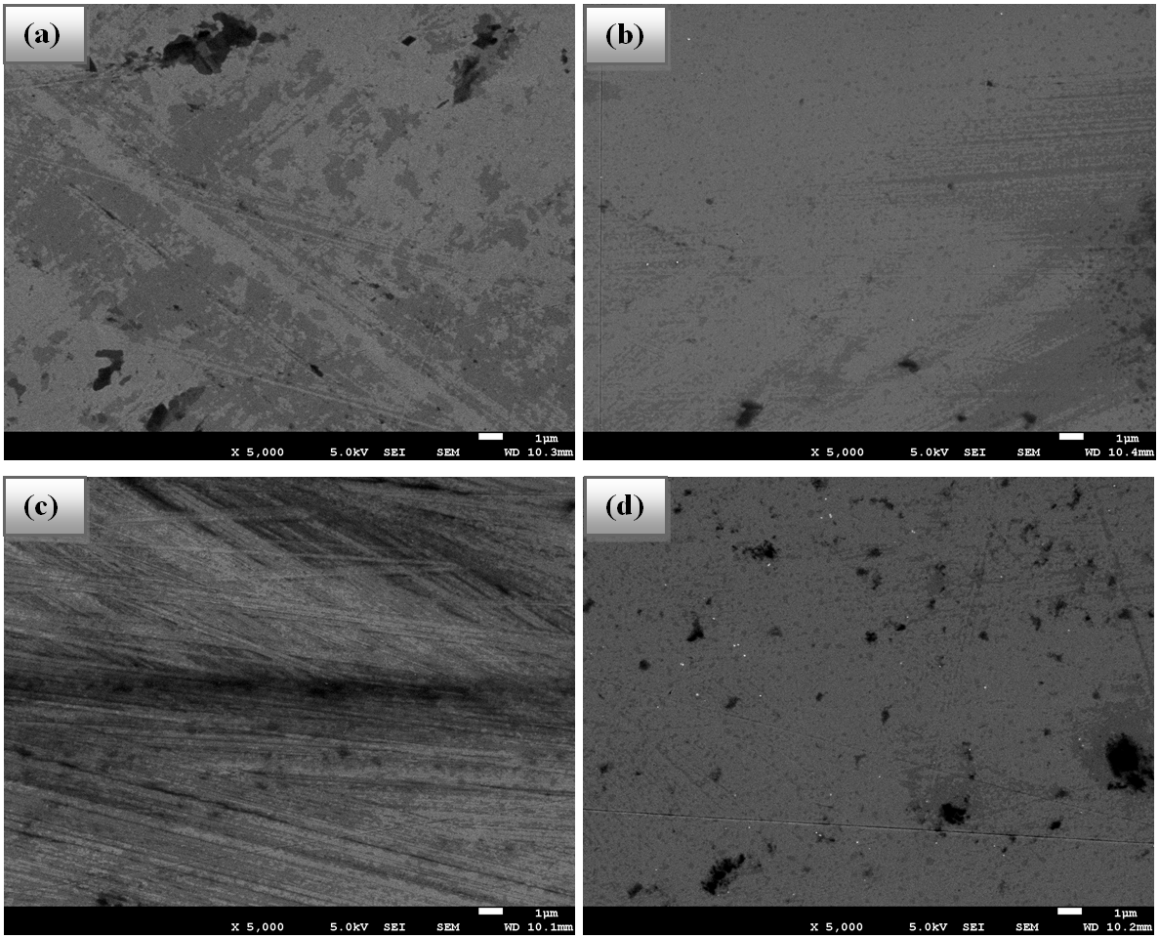

Fig. 8 SEM images of the CoCrMo disk surface at a magnification of 5000× (a) before the pin-on-disk measurements and after the pin-on-disk under constant load conditions with (b) diluted BCS, (c) HA solution 3 $mg.ml^{-1}$ concentration in PBS, and (d) HA solution 3 $mg.ml^{-1}$ concentration in diluted BCS

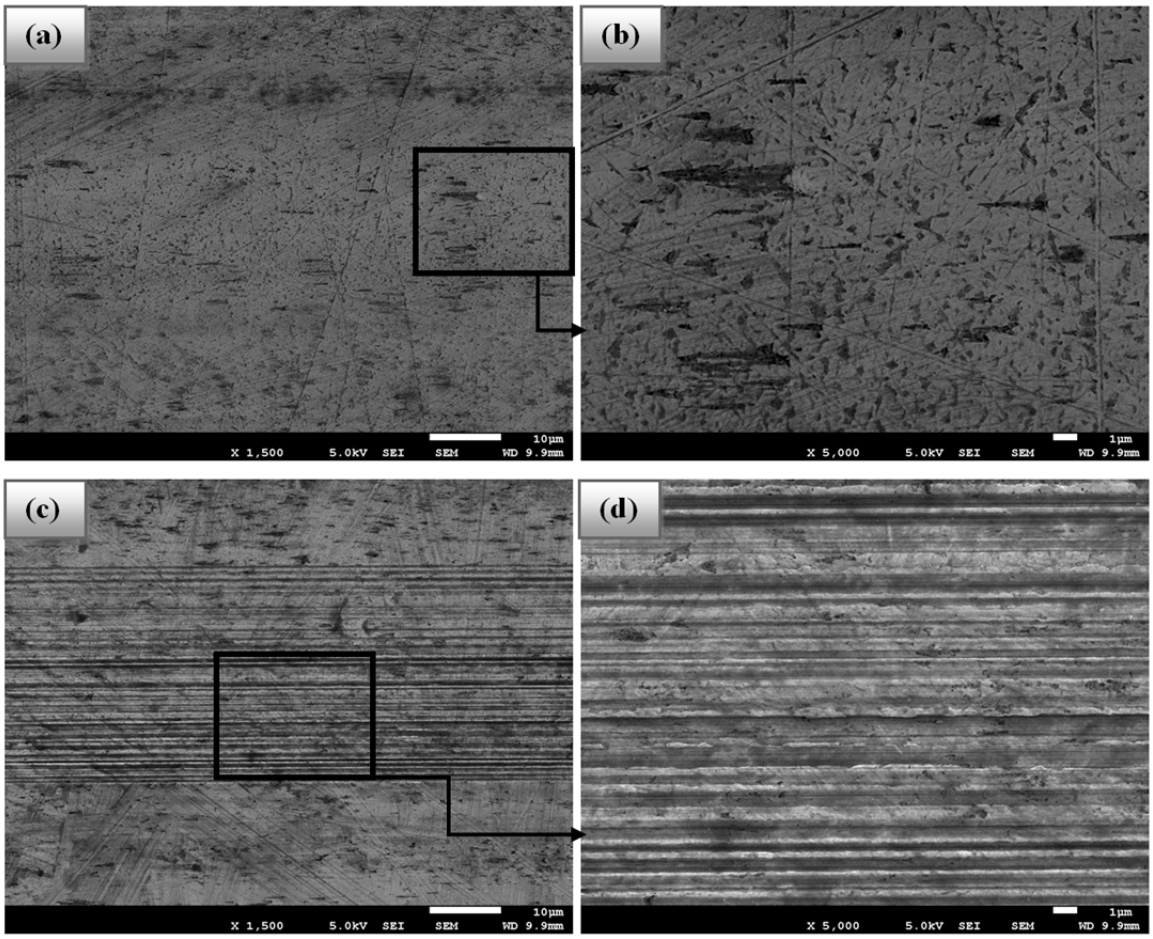

Fig. 9 SEM images of CoCrMo disk surfaces after tribo-testing with distilled water as the lubricant (a) under constant load conditions at a magnification of 1500×, (b) under constant load conditions at a magnification of 5000×, (c) under sinusoidal load conditions at a magnification of 1500×, and (d) under sinusoidal load conditions at a magnification of 5000×

Fig. 10 (a) is the pin surface before measurements, Fig. 10 (b), (c) and (d) show the pin surface after pin-on-disk measurements under constant load conditions with lubricants of distilled water, HA solution in PBS and diluted BCS, respectively. The arrows show the sliding direction tracks on the pins when the lubricant was distilled water or the HA solution in PBS; these tracks were absent for the BCS-containing lubricants.

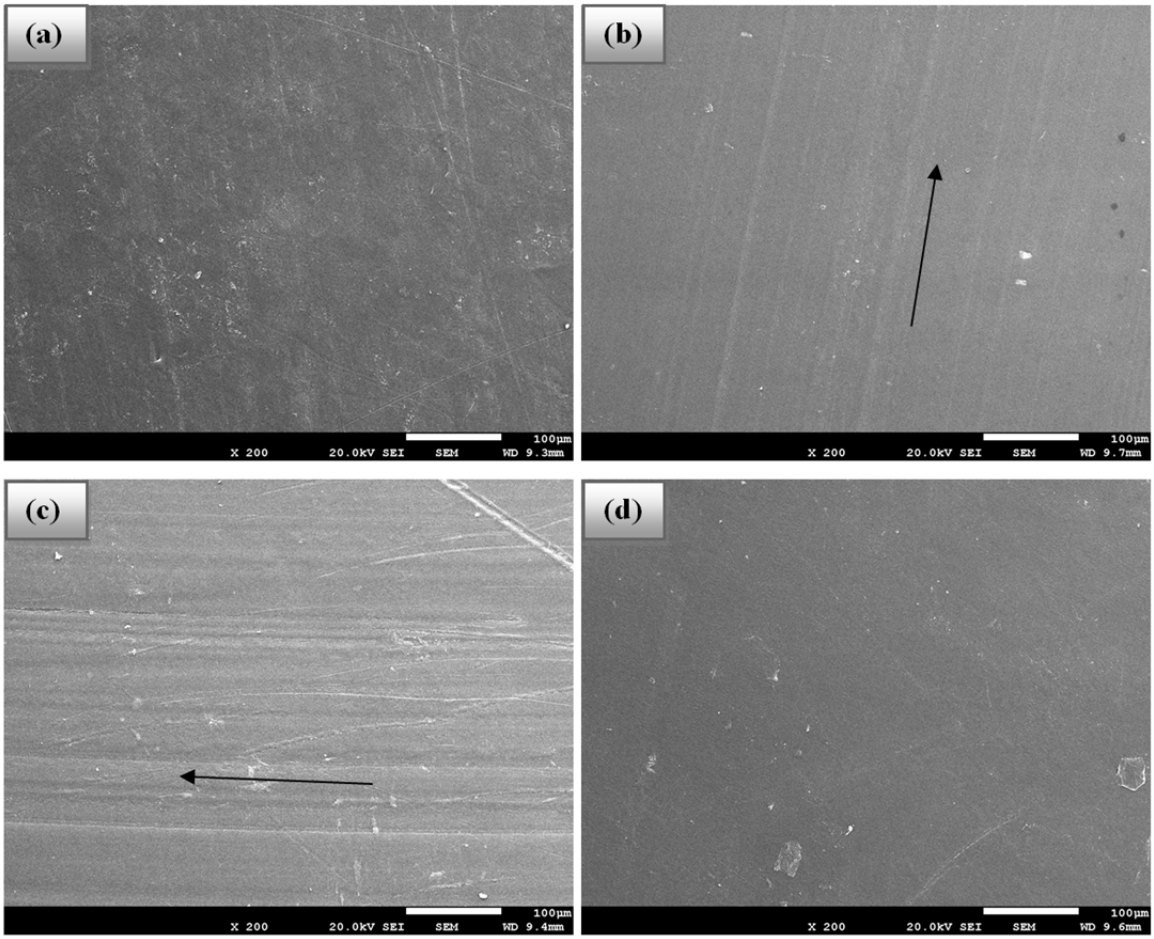

Fig. 10 SEM images of the UHMWPE pin surface (a) before pin-on-disk measurements and after pin-on-disk measurements under constant load conditions with (b) distilled water, (c) HA solution 3 mg.ml^{-1} concentration in PBS, and (d) diluted BCS; the arrows show the sliding direction

Fig. 11 and Fig. 12 show the EDS analysis of the pin surfaces with distilled water and HA in PBS solution as lubricants. For the pin with distilled water as the lubricant, Co and Cr particles are observed at the pin surface. The chemical composition of the CoCrMo discs was Co (65.74 wt%), Cr (27.11 wt%), Mo (5.52 wt%), Mn (0.78 wt%), N (0.194 wt%), Fe (0.07 wt%), Ni (0.06 wt%), Si (0.59 wt%), C (0.04 wt%), W (< 0.02 wt%), Cu (< 0.01 wt%), P (< 0.003 wt%), and S (< 0.0005 wt%). From the three main elements of the disks (Co, Cr, and Mo) only Cr could be detected at the pin surface with HA solution in PBS as the lubricant. The other available elements at the pin surface in Fig. 12 belonged to the disk composition, but their concentrations in the metal alloy were low. Further investigation using electron backscatter revealed that these elements were embedded into the pin surfaces; after the

polymer surfaces softened under the high temperature produced during the sliding process, these elements penetrated into the polymer surface. None of the main components of the disk composition (Cr, Co, or Mo) could be found at the pin surfaces with diluted BCS or HA solution in diluted BCS as lubricants.

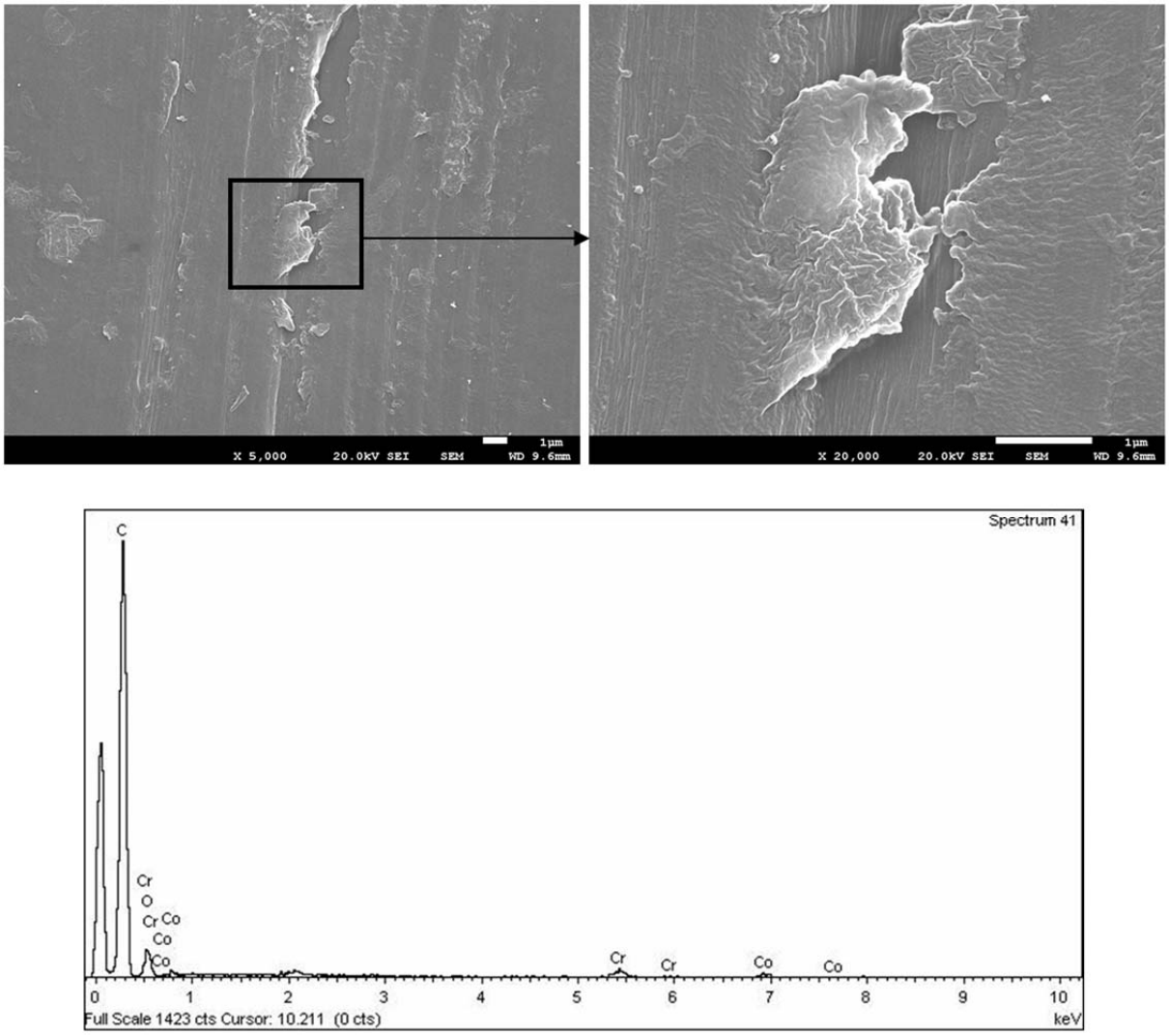

Fig. 11 SEM and EDS of pins lubricated with distilled water

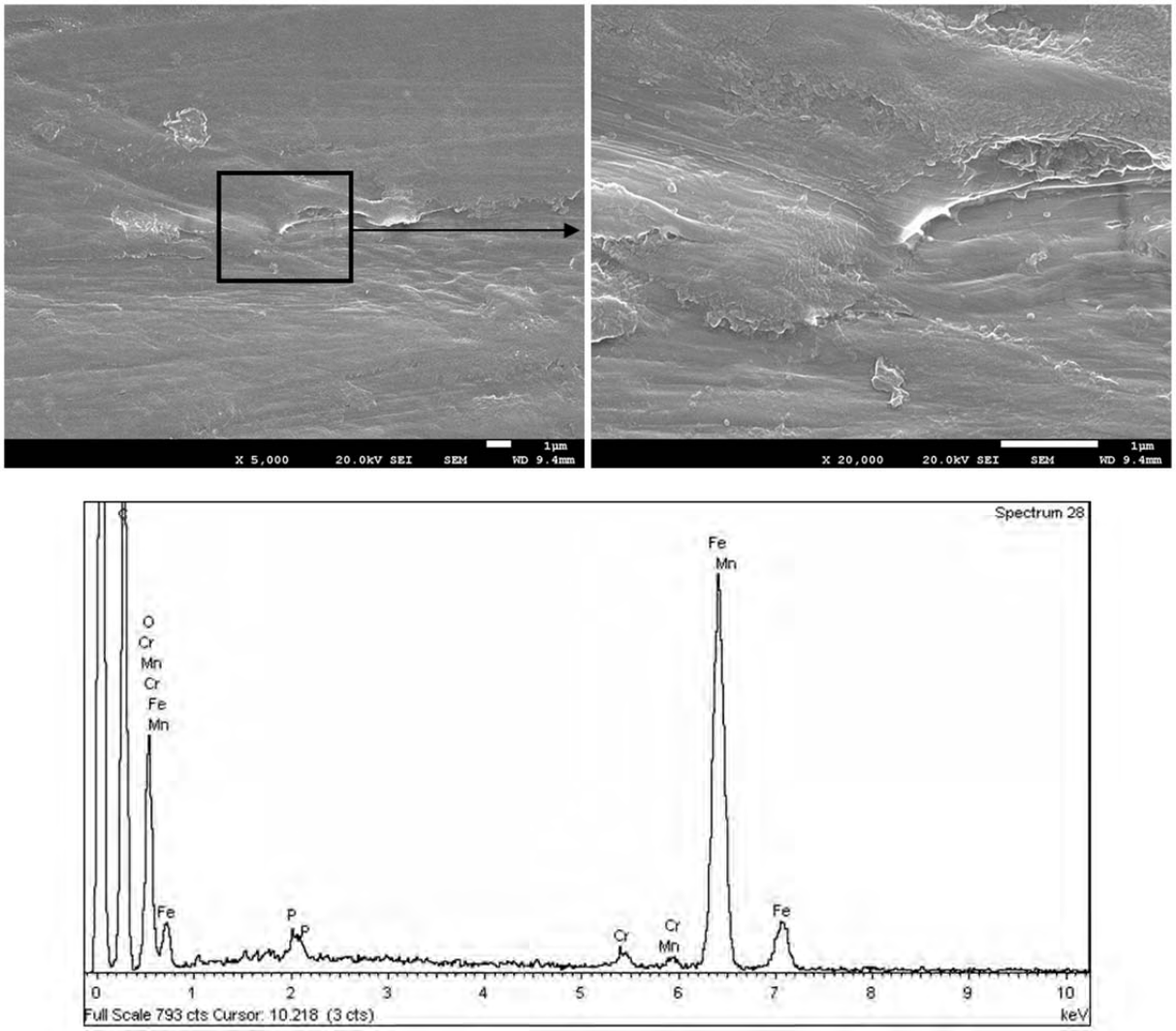

Fig. 12 SEM and EDS of pins lubricated with HA solution in PBS

4. Discussion

Decrease in the COF by adding HA to the solution has been reported before by many authors [4,14,18]. HA has very low adsorption on UHMWPE surface and previous studies showed that HA has poor functionality as boundary lubricant and although it improves the friction condition, it cannot work as the boundary lubricant [32-34]. Therefore, in current study adding HA to the lubricant decreased the COF by increasing the viscosity and improving the hydrodynamic effect. This suggested that the active lubrication mechanism was mixed lubrication.

Increasing the load during dynamic loading pushed the counter surface asperities close to each other. Distilled water as the lubricant was trapped between the asperities and then squeezed out gradually from smaller gap regions to larger gaps. Gradual depletion of the water and fluid resistivity against depletion resulted in the development of the hydrodynamic built-up pressure and the micro-squeeze effect [35,36]. The built-up pressure contributed to the load supported by the fluid film and improved the frictional behavior. Under static and dynamic loading conditions, the COF was not significantly different for the lubricants containing HA. HA higher viscosity improved the hydrodynamic effect, which resulted in fewer asperity contacts compared to that of distilled water. Therefore, the surfaces were more protected from rubbing against each other, and in contrast to water lubrication, the contact surfaces stayed smooth. Fig. 9 (a) and (b) shows the abrasive wear damaged the surface of the disk when distilled water was the lubricant. While Fig. 8 (c) shows early stages of wear and smoother disk surface when the lubricant was HA solution in PBS. With lower surface roughness for the HA solution in comparison with water, the micro-squeeze effect became negligible and almost no difference was visible between the COFs of the static and dynamic loadings. However, decreasing the COF and improving the friction, did not necessarily improve the wear condition. The SEM images of the disk surfaces with distilled water as the lubricant (Fig. 9) show that dynamic loading deteriorated the wear condition. Based on the hypothesis suggested by Barbour et al. [2], under high stress condition and constant load, the produced wear particles were trapped between the surface asperities and were prohibited from deteriorating the wear condition. However, under dynamic load and during the load decreasing phase, the asperities were separated, thereby providing the opportunity for the wear debris to slide along the surfaces and contribute to wear. Grooves of 2-body abrasive wear were visible for both loading conditions. The wear tracks on the disk surface when dynamic load applied represented sliding of the wear particles along the disk surface, which was absent for the measurement at constant load.

When BCS was used as the lubricant, the COF was found to increase compared to water. Increasing of the COF in presence of BCS in comparison with water was also reported by Yao et al. [25]. As stated by Scholes and Unsworth [13] and later verified by Flannery et al. [16], when UHMWPE moved against CoCrMo in a protein-containing lubricant, the protein was adsorbed on both surfaces and formed a solid lubricant on the sliding surfaces. Protein-to-protein rubbing against each other acted as a bridge between the two surfaces and increased the friction coefficient. Fig. 6 shows the white circle layer of adsorbed protein between the pin and the disk after 14 hours of measurement. Fig. 3 shows that for diluted BCS, the COF value

decreased quickly after the measurement, although it continued to gradually increase afterward. The gradual increment of COF was most probably related to the gradual protein adsorption during the measurement. Therefore increasing the COF in the presence of diluted BCS compared to distilled water was related to the protein adsorbed layer. The dynamic loading, resulted in the decrease in the COF in comparison with static loading with diluted BCS as lubricant. Increasing the load during dynamic loading resulted in higher surface asperity contacts, which might broke the adsorbed protein layer at some spots and resulted in a decrease in the COF. By adding HA to the diluted BCS, the COF decreased gradually and the differences between COFs of static and dynamic loading disappeared. The adsorbed protein layer was not visible for diluted BCS with HA at the end of the measurement. Results of the study of Serro et al. [34] on the adsorption of albumin on UHMWPE showed that in presence of HA, the albumin adsorption slightly reduced. The concentration of the HA in that study was 0.5 $mg.ml^{-1}$ which is rather low compared to the current study [34]. They did not investigate the effect of HA concentration on the albumin adsorption. However, it is visible from current study's results that by increasing the HA concentration, the protein adsorption reduced considerably. Consequently COF decreased and the frictional behavior moved towards that of the HA solution in PBS.

Fig. 10 (b) and (c) shows that ripple-shaped tracks at the surfaces of the pins with distilled water and HA solution in PBS. When the soft surface of a pin contacted the hard disk surface, these could be created via abrasive wear, or as mentioned by other authors, they were produced as a result of plastic strain accumulation [37]. Bragdon et al. [38] stated that for unidirectional motion, these ripples formed a result of polymer chains orientation due to exerted friction forces at the polymer surface [38,39]. These ripple shapes were absent when diluted BCS used as the lubricant (Fig. 10 (d)). This also confirms that in presence of protein, the friction forces were not exerted on the pin surface and the protein-protein rubbing was the source of high friction value.

In most of the tribological studies of the TJR materials with pin-on-disk or pin-on-plate setup, the load is kept constant and based on ASTM 732 protocol, BCS used as the lubricant. However, the results of the present study suggested that variable load affect the frictional behavior of the BCS. It should be noted that this study was conducted by unidirectional motion pin on disk setup to provide the simplest motion. There are numerous tribological studies which are focused on the detail of the wear behavior of the TJR materials [2,22,39-42], therefore this study only addressed frictional behavior. However, the effect of the loading condition on the wear factor is the subject of future studies. The other parameter which was

not included in this study was crosslinking of the UHMWPE pins. Crosslinking of Polyethylene molecular chains are performed to improve the wear resistance of UHMWPE [3]. Since current study only focused on frictional behavior, the pins from virgin UHMWPE without crosslinking were used. Moreover, Yao et al. [25] study on the effect of crosslinking on the frictional behavior of the UHMWPE showed no statistical difference between friction coefficient when non-irradiated and highly crosslinked UHMWPE were used.

5. Conclusion

The tribological behavior of a UHMWPE pin sliding against a CoCrMo disk was investigated under steady state and dynamic loading conditions with different lubricants. The COF values calculated from tribotest results and SEM, EDS and DSC were used to evaluate how different measurement conditions affected the pins and disks. The crystallinity of the polymeric pin was not affected by the use of different lubricants and different loading condition. The results suggested that the friction evolution over time for static and dynamic loading follows the same trend and only depends on the lubricant type. Only the non-HA lubricants showed variation in the COF values between static and dynamic loadings, with dynamic loading resulting in a decreased COF. Moreover, although the presence of protein in the lubricant increased the COF value, it provided the strongest protection for the bearing surfaces against wear. Almost all of the tribological studies of TJR materials using pin-on-disk or pin-on-plate setup are performed with constant load. However, the results of the current study showed that for tribological study of the TJR materials using the pin-on-disk or pin-on-plate method, the combination of the lubricant constituents with the loading condition plays a significant role in the frictional behavior.

Acknowledgment

The authors' gratitude goes to the Doctoral Program DocMASE for their financial support.

References

[1] S. Scholes, A. Unsworth, A. Goldsmith. A frictional study of total hip joint replacements, Phys.Med.Biol. 45 (2000) 3721.
[2] P.M. BARBOUR, D. Barton, J. Fisher. The influence of stress conditions on the wear of UHMWPE for total joint replacements, J.Mater.Sci.Mater.Med. 8 (1997) 603-611.

[3] S.S. Moreno. Investigation of Carbon Reinforced UHMWPE Nanocomposites for Use in Orthopaedics, Luleå University of Technology, PhD thesis, 2015.
[4] Y. Sawae, T. Murakami, J. Chen. Effect of synovia constituents on friction and wear of ultra-high molecular weight polyethylene sliding against prosthetic joint materials, Wear. 216 (1998) 213-219.
[5] C. Brockett, S. Williams, Z. Jin, G. Isaac, J. Fisher. Friction of total hip replacements with different bearings and loading conditions, Journal of Biomedical Materials Research Part B: Applied Biomaterials. 81 (2007) 508-515.
[6] Z.M. Jin, D. Dowson, J. Fisher. Analysis of fluid film lubrication in artificial hip joint replacements with surfaces of high elastic modulus, Proc.Inst.Mech.Eng.H. 211 (1997) 247-256.
[7] D. Jalali-Vahid, M. Jagatia, Z. Jin, D. Dowson. Prediction of lubricating film thickness in UHMWPE hip joint replacements, J.Biomech. 34 (2001) 261-266.
[8] S.C. Scholes, A. Unsworth. Comparison of friction and lubrication of different hip prostheses, Proc.Inst.Mech.Eng.H. 214 (2000) 49-57.
[9] A. Unsworth, D. Dowson, V. Wright. The frictional behavior of human synovial joints—Part I: Natural joints, Journal of Lubrication Technology. 97 (1975) 369-376.
[10] A. Unsworth, D. Dowson, V. Wright, D. Koshal. The Frictional Behavior of Human Synovial Joints—Part II: Artificial Joints, Journal of Lubrication Technology. 97 (1975) 377-381.
[11] A. Unsworth, M. Pearcy, E. White, G. White. Soft layer lubrication of artificial hip joints, Mechanical Engineering Publications,. (1987) 715-724.
[12] T. Gore, G. Higginson, R. Kornberg. Some evidence of squeeze-film lubrication in hip prostheses, Eng.Med. 10 (1981) 89-95.
[13] S.C. Scholes, A. Unsworth. The effects of proteins on the friction and lubrication of artificial joints, Proc.Inst.Mech.Eng.H. 220 (2006) 687-693.
[14] M. Gispert, A. Serro, R. Colaco, B. Saramago. Friction and wear mechanisms in hip prosthesis: Comparison of joint materials behaviour in several lubricants, Wear. 260 (2006) 149-158.
[15] X. Chen, Z. Jin, J. Fisher. Effect of albumin adsorption on friction between artificial joint materials, Proc.Inst.Mech.Eng.Part J. 222 (2008) 513-521.
[16] M. Flannery, E. Jones, C. Birkinshaw. Analysis of wear and friction of total knee replacements part II: Friction and lubrication as a function of wear, Wear. 265 (2008) 1009-1016.
[17] M. Roba. Interaction of synovial fluid components with artificial hip-joint materials. (2009).
[18] H. Fam. Effect of composition on periprosthetic fluid rheology and friction in total knee arthroplasty, (2010).
[19] A. Ruggiero, R. D'Amato, E. Gómez. Experimental analysis of tribological behavior of UHMWPE against AISI420C and against TiAl6V4 alloy under dry and lubricated conditions, Tribol.Int. 92 (2015) 154-161.
[20] L.E. Guenther, B.W. Pyle, T.R. Turgeon, E.R. Bohm, U.P. Wyss, T.A. Schmidt, et al. Biochemical analyses of human osteoarthritic and periprosthetic synovial fluid, Proc.Inst.Mech.Eng.H. 228 (2014) 127-139.
[21] H. Fam, J.T. Bryant, M. Kontopoulou. Rheological properties of synovial fluids, Biorheology. 44 (2007) 59-74.
[22] H. McKellop, I. Clarke, K. Markolf, H. Amstutz. Wear characteristics of UHMW polyethylene: a method for accurately measuring extremely low wear rates, J.Biomed.Mater.Res. 12 (1978) 895-927.
[23] P. Kumar, M. Oka, K. Ikeuchi, K. Shimizu, T. Yamamuro, H. Okumura, et al. Low wear rate of UHMWPE against zirconia ceramic (Y-PSZ) in comparison to alumina ceramic and SUS 316L alloy, Journal of Biomedical Materials Research Part A. 25 (1991) 813-828.
[24] S. Scholes, A. Unsworth, R. Hall, R. Scott. The effects of material combination and lubricant on the friction of total hip prostheses, Wear. 241 (2000) 209-213.
[25] J. Yao, M. Laurent, T. Johnson, C. Blanchard, R. Crowninshield. The influences of lubricant and material on polymer/CoCr sliding friction, Wear. 255 (2003) 780-784.
[26] D. Xiong, S. Ge. Friction and wear properties of UHMWPE/Al 2 O 3 ceramic under different lubricating conditions, Wear. 250 (2001) 242-245.
[27] R. Hall, A. Unsworth. Friction in hip prostheses, Biomaterials. 18 (1997) 1017-1026.
[28] A. Unsworth. The effects of lubrication in hip prostheses, Phys.Med.Biol. 23 (1978) 253.
[29] D. Dowson, C. McNie, A. Goldsmith. Direct experimental evidence of lubrication in a metal-on-metal total hip replacement tested in a joint simulator, Proc.Inst.Mech.Eng.Part C. 214 (2000) 75-86.
[30] R. Barbucci, S. Lamponi, A. Borzacchiello, L. Ambrosio, M. Fini, P. Torricelli, et al. Hyaluronic acid hydrogel in the treatment of osteoarthritis, Biomaterials. 23 (2002) 4503-4513.
[31] Z. Jin, M. Stone, E. Ingham, J. Fisher. (v) Biotribology, Current Orthopaedics. 20 (2006) 32-40.
[32] C. Myant, P. Cann. On the matter of synovial fluid lubrication: Implications for Metal-on-Metal hip tribology, journal of the mechanical behavior of biomedical materials. 34 (2014) 338-348.

[33] D.P. Chang, N.I. Abu-Lail, F. Guilak, G.D. Jay, S. Zauscher. Conformational mechanics, adsorption, and normal force interactions of lubricin and hyaluronic acid on model surfaces, Langmuir. 24 (2008) 1183-1193.
[34] A. Serro, K. Degiampietro, R. Colaço, B. Saramago. Adsorption of albumin and sodium hyaluronate on UHMWPE: a QCM-D and AFM study, Colloids and Surfaces B: Biointerfaces. 78 (2010) 1-7.
[35] S. Kato, N. Sato, T. Matsubayashi. Some considerations on characteristics of static friction of machine tool slideway, Journal of Lubrication Technology. 94 (1972) 234-247.
[36] E. Marui, S. Kato, T. Matsubayashi, A. Kobayashi, S. Senda, M. Ozawa. On the squeeze effect of lubricant between two rough surfaces, Journal of tribology. 109 (1987) 696-703.
[37] M. Gispert, A. Serro, R. Colaço, E. Pires, B. Saramago. The effect of roughness on the tribological behavior of the prosthetic pair UHMWPE/TiN-coated stainless steel, Journal of Biomedical Materials Research Part B: Applied Biomaterials. 84 (2008) 98-107.
[38] C. Bragdon, D. O'Connor, J. Lowenstein, M. Jasty, W. Syniuta. The importance of multidirectional motion on the wear of polyethylene, Proc.Inst.Mech.Eng.Part H J.Eng.Med. 210 (1996) 157-165.
[39] H. Marrs, D. Barton, R. Jones, I. Ward, J. Fisher, C. Doyle. Comparative wear under four different tribological conditions of acetylene enhanced cross-linked ultra high molecular weight polyethylene, J.Mater.Sci.Mater.Med. 10 (1999) 333-342.
[40] T. Joyce, A. Unsworth. Wear studies of all UHMWPE couples under various bio-tribological conditions, Journal of Applied Biomaterials and Biomechanics. 2 (2004) 29-34.
[41] A. Wang, A. Essner, G. Schmidig. The effects of lubricant composition on in vitro wear testing of polymeric acetabular components, Journal of Biomedical Materials Research Part B: Applied Biomaterials. 68 (2004) 45-52.
[42] A. Galvin, L. Kang, J. Tipper, M. Stone, E. Ingham, Z. Jin, et al. Wear of crosslinked polyethylene under different tribological conditions, J.Mater.Sci.Mater.Med. 17 (2006) 235-243.